GROWTH RELATED PHENOMENA IN MBE FILMS OF INGAASP ON INP SUBSTRATES

By

TATSUYA OKADA, B.ENG.

M.ENG.

A Thesis

Submitted to the School of Graduate Studies

in Partial Fulfilment of the Requirements

for the Degree

Doctor of Philosophy

McMaster University

GROWTH RELATED PHENOMENA IN MBE FILMS

DOCTOR OF PHILOSOPHY (1996) McMaster University

(Materials Science and Engineering) Hamilton, Ontario

TITLE: Growth Related Phenomena in MBE Films of InGaAsP on InP substrates

AUTHOR: Tatsuya Okada, B.Eng. (Kyoto University, Kyoto, Japan)

M.Eng. (Kyoto University, Kyoto, Japan)

SUPERVISOR: Professor G.C.Weatherly

NUMBER OF PAGES: xviii, 228

Abstract

Heteroepitaxial growth of $In_{1-x}Ga_xAs_yP_{1-y}$ alloy thin films on InP(001) substrates using molecular beam epitaxy (MBE) is technologically important for the fabrication of optoelectronic devices. Recent progress in MBE, for example the use of hydride gas sources such as AsH_3 and PH_3 has improved the control of the P to As ratio and added more versatility to this thin film growth technique. In this thesis, transmission electron microscopy (TEM) studies of some unique growth-related phenomena occurring in $In_{1-x}Ga_xAs_yP_{1-y}$ films grown with gas-source MBE are described. The experiments were intended to understand the growth mechanism of the films and the characteristics of structural "defects", rather than to obtain practical knowledge which can directly be applied to the manufacturing of optoelectronic devices.

The initial stage of strain relaxation in compressively-strained $InAs_yP_{1-y}$ ternary alloy films was studied. The compressive misfit strain in 190Å thick films ranged from –0.96% to –2.43% ($0.30 \le y \le 0.77$). Both TEM and cathodoluminescence imaging revealed the existence of new types of misfit dislocations aligned close to [100] and [010] directions generated from heterogeneous dislocation sources at the $InAs_yP_{1-y}$ / InP (001) interfaces. The new types of misfit dislocations were found to be pure edge in character, formed probably by slip on {011} planes. Contrast profiles were computed for misfit dislocations parallel and adjacent to one of the free surfaces of a plan-view TEM foil by taking into account the significantly modified elastic fields associated with such misfit dislocations. The calculated profiles were useful when Burgers vectors of misfit dislocations generated from a dislocation source were analyzed.

A composition modulation occurring only along the [110] direction with a small wavelength (100Å) was repeatedly observed in 3000Å thick $In_{1-x}Ga_xAs_yP_{1-y}$ alloy films

having a wide range of nominal composition being lattice-matched to InP. This modulation is different from the "classical" spinodal decomposition along elastically soft [100] and [010] directions with long-wavelength (1000-1500Å), commonly observed in $In_{1-x}Ga_xAs_yP_{1-y}$ films grown by liquid phase epitaxy. A simple free energy argument including the effect of constraint from the InP substrate suggests that the observed modulation is not directly caused by the minimization of free energy but is driven by kinetic processes occurring at the surface of growing films.

The morphological instability of a strained film surface was also studied. Cross-sectional TEM investigation revealed the coexistence of prominent composition modulation and surface undulation in tensile-strained $In_{1-x}Ga_xAs_yP_{1-y}$ films. The surface morphology of the strained films showed a clear correlation with the degree of the composition modulation, occurring predominantly along the [110] direction. When the film was under tension, the surface undulation developed at relatively low strains (as low as 0.5%); on the other hand, films with the same magnitude of compressive strain did not exhibit any surface undulation. In addition, the surface undulation was composition dependent; it was enhanced as the degree of composition modulation increased. These features distinguish the present morphological instability induced by the inherent composition modulation from the "classical" three-dimensional island growth mode of compressively strained films having strains larger than 2%.

Acknowledgements

I am grateful to Professor G.C.Weatherly for his support and encouragement throughout the Ph.D. program.

I would also like to appreciate Professor D.A.Thompson at the Department of Engineering Physics for helpful discussion. Thin film growth was conducted by Dr.B.J.Robinson and Mr.S.McMaster at the Centre for Electrophotonic Materials and Devices. Photoluminescence measurements were done by Mr.R.R.LaPierre, a graduate student at the Department of Engineering Physics. Drs. R.V.Kruzelecky and A.Perovic are acknowledged for their help in cathodoluminescence and energy dispersive x-ray analysis.

For the first two years of my Ph.D. program I was financially supported by Ontario Centre for Materials Research Graduate Scholarship Program. A scholarship was supplied by the Department of Materials Science and Engineering for the next two years. In the fifth year Professor Weatherly arranged me a research assistantship.

Finally I would like to thank Dr.S.Miura, Professor Emeritus of Kyoto University for introducing me to Professor Weatherly to give me a chance to study in Canada when I was depressed after having quitted my first job. I believe that my five year study in Canada helped me to find the right direction in my life.

Table of contents

List of Tables and Figures

critical thickness h_c, the strained layer is energetically favourable and the misfit between the film and the substrate is totally accommodated by elastic distortion of the thin film.

Fig.2.1.3 A cross-grid configuration of misfit dislocations at the interface caused by (a/2)<110>-{111} slip (a). Thompson's tetrahedron is shown for a reference (b).

Fig.2.1.4 The critical thickness as a function of misfit f calculated from eq.(2.1.9). The Poisson's ratio ν and magnitude of Burgers vector were taken as 0.284 and 4.15Å, respectively.

Fig.2.1.5 The stacking sequence of zinc-blende structure along the [111] direction. Atoms with different size indicate that they are not on the same height along the projected direction.

Fig.2.1.6 III-V compound semiconductor with zinc-blende structure viewed along [1 $\bar{1}$0] direction (a) and [110] direction (b) to explain the conventional 'shuffle-set' cut and 'glide-set' cut to create 60° dislocations.

Fig.2.1.7 Abrupt kink model of dislocation motion on a {111} slip plane. The dislocation creates a minimum kink pair at A and expands it to move a distance d towards the next potential valley. Dotted lines represent three sets of Peierls potential valleys on this slip plane.

Fig.2.2.1 Free energy diagram (a) and phase diagram (b) for a binary alloy of elements A and B with miscibility gap. Note that a small fluctuation starting from the nominal composition x_0 continues without energy barrier; the alloy is unstable. On the other hand, if the starting composition is x_0', a small composition fluctuation leads to an increase in free energy of the system. Such an alloy is termed a metastable alloy.

Fig.2.2.2 Chemical spinodal for $In_{1-x}Ga_xAs_yP_{1-y}$ alloy at 470°C.

Fig.2.2.3 Glas' step-by-step procedures to solve elastic fields associated with a phase-

Fig.4.3.2 Experimental (g= $\bar{2}20$ (a) and g=2 $\bar{2}0$ (b)) and computed (c,d) bright field images of a misfit near-edge dislocation aligned close to [010] direction. The solid lines are based on the present calculation showing good agreement with the experimental image, while the image dislocation method leads to a poorer match.

Fig.4.3.3 Dark field image intensity profiles of a 60°α dislocation in TEM foils with thickness 3, 4 or $6\xi_{220}$. The diffraction vector g=220 and the Burgers vector b=(a/2)[0 $\bar{1}$1] or (a/2)[$\bar{1}$01] ((111) slip) were used.

Fig.4.3.4 Plan-view TEM dark field image of one of the cross-shaped dislocation sources in the sample #225 (g= $\bar{2}20$). The crystallographic coordinate system used in this analysis and the Burgers vectors of <100> misfit dislocations are shown in the micrograph.

Fig.4.3.5 Schematic representation of cross-slip of a pure screw segment from (111) plane to (011) plane leaving [1 $\bar{1}$0] MD and [100] MD at the interface.

Fig.4.3.6 Plan-view TEM of typical dislocation sources in sample #239. (a) A spherical particle (pointed by a triangle marker) seems to have acted as a dislocation nucleation source. (g=2 $\bar{2}0$) (b) A short segment of <100> misfit dislocation (arrowed) is ejected from the "non-planar growth" region. (g= $\bar{2}20$)

Fig.5.2.1 Structure of the samples with 3000Å thick $In_{1-x}Ga_xAs_yP_{1-y}$ layer lattice-matched to InP.

Fig.5.2.2 The nominal composition of the $In_{1-x}Ga_xAs_yP_{1-y}$ layers lattice-matched to InP.

Fig.5.2.3 [1 $\bar{1}$0] cross-sectional dark field TEM images of samples #940, #935, #950, #945, #933 and #746. Reflection vectors g=±004 (left side) and g=±220 (right side) were used (marker=0.1μm).

Fig.5.2.4 [110] cross-sectional dark field TEM images of samples #940, #935, #950, #945, #933 and #746. Reflection vectors g=±004 (left side) and g=±2 $\bar{2}$0 (right side) were used (marker=0.1μm).

Fig.5.2.5 [1 $\bar{1}$0] cross-sectional dark field TEM images of samples #886, #878 and #880 with x=0.37, y=0.80. Reflection vectors g=±004 (left) and g=±220 (right) were used (marker=0.1μm).

Fig.5.2.6 [110] cross-sectional dark field TEM images of samples #886, #878 and #880. Reflection vectors g=±004 (left) and g=±2 $\bar{2}$0 (right) were used (marker=0.1μm).

Fig.5.2.7 Plan-view dark field images of #945 (x=0.285, y=0.630) under (a) g=400, (b) g=0 $\bar{4}$0, (c) g=2 $\bar{2}$0 and (d) g= $\bar{2}$ $\bar{2}$0 (marker=0.3μm).

Fig.5.2.8 Dark field image, g=400 of plan-view sample #945 and the selected area diffraction pattern (in the inset) taken exactly at [001] zone axis.

Fig.5.3.1 PL linewidth [a] and integrated intensity [b] as a function of the As content y for various $In_{1-x}Ga_xAs_yP_{1-y}$ lattice-matched layers. Measurements were conducted at room temperature (300K) and low temperature (11K). The solid lines in [a] are theoretical linewidths and the lines in [b] are for reference. The points (a) to (f) correspond to the samples examined using [1 $\bar{1}$0] and [110] cross-section TEM in Section 5.2. (After LaPierre (1994).)

Fig.5.3.2 PL spectra for samples (a) #940, (d) #945 and (f) #746 (after LaPierre (1994)).

Fig.5.3.3 Strain energy densities for [100] and [110] modulations. The dashed line is calculated for an isotropic material using the Voigt average.

Fig.5.3.4 Thermodynamic critical temperatures of $In_{1-x}Ga_xAs_yP_{1-y}$ alloy film lattice-

matched to (001) InP for [100] and [110] modulations. The modulation is assumed to occur along $\Delta x = -\Delta y$.

Fig.5.3.5 Critical temperatures when the modulation occurs along $\Delta x = -2.1\Delta y$.

Fig.6.2.1 Structure of #421. The layers T1-T5 with the composition of $In_{0.7}Ga_{0.3}As_{0.2}P_{0.8}$ are under 1.5% tensile strain. The marker layers M1-M4 are 20Å thick $In_{0.7}Ga_{0.3}As_{0.648}P_{0.352}$ being lattice-matched to InP. All layers are separated by 200Å thick InP spacer layers.

Fig.6.2.2 Structure of samples #501 and #502. All layers are separated by 1200Å thick InP spacer layers.

Fig.6.2.3 Composition of strained layers in #421, #501 and #502.

Fig.6.2.4 [1 $\bar{1}$0] cross-sectional dark field images of #421 taken with **g**=00 $\bar{4}$ (a) and **g**=220 (b). The marker is 0.1μm.

Fig.6.2.5 [110] cross-sectional dark field images of #421 taken with **g**=00 $\bar{4}$ (a) and **g**= $\bar{2}$20 (b). The marker is 0.1μm.

Fig.6.2.6 [1 $\bar{1}$0] cross-sectional dark field images of sample #501 taken with **g**=004 (a) and **g**=220 (b). The marker is 0.1μm.

Fig.6.2.7 [110] cross-sectional dark field images of sample #501 taken with **g**=004 (a) and **g**= $\bar{2}$20 (b). The marker is 0.1μm.

Fig.6.2.8 [1 $\bar{1}$0] cross-sectional dark field images of sample #502 taken with **g**=00 $\bar{4}$ (a) and **g**=220 (b). The marker is 0.1μm.

Fig.6.2.9 [110] cross-sectional dark field images of sample #502 taken with **g**=00 $\bar{4}$ (a)

Fig.A3 An edge dislocation $\mathbf{b}_2$ in an infinite body.

Fig.A4 Coordinate system used to compute TEM diffraction intensity profiles of misfit dislocations.

Fig.B1.1 Coordinate system X,Y,Z used for elasticity calculation of [100] modulation. The periodic lines schematically represent the modulation occurring along the X-direction ([100] in the crystal).

Fig.B2.1 Coordinate system X,Y,Z used for elasticity calculation of [110] modulation. The periodic lines schematically represent the modulation occurring along the X-direction ([110] in the crystal).

Chapter 1

Introduction

Heteroepitaxy is the growth of a film on a dissimilar substrate. The film and substrate are termed (lattice-)mismatched when their unconstrained unit cells are not of the same size (they may also have different crystal structures). Mismatched heteroepitaxy has been an active research area for more than 25 years. The major finding of the early studies of lattice-mismatched heteroepitaxy was that thin films can be grown coherent to the mismatched substrates without introducing misfit dislocations to the film/substrate interface when the film thickness is below a critical thickness (Jesser and Matthews (1967 and 1968)). The critical thickness is a function of lattice-mismatch between the film and the substrate and its detailed derivation based on strain energy calculation will be reviewed in subsection 2.1.1 of this thesis. A coherent thin film is under strain and this is termed strained layer heteroepitaxy.

At first, the study of lattice-mismatched heteroepitaxy seems to have been driven by scientific curiosity. But during the last 10 to 15 years, optoelectronic devices which can be created using semiconductor heterostructures, especially structures incorporating strained layer components, have added practical interest to the study. The use of strained layer structures has two major advantages over conventional lattice-matched semiconductor devices in which each component material must have the same lattice-constant as the substrate. Firstly, the use of strained layers allows us new material combinations, e.g. $Si_{1-x}Ge_x$ alloys on Si substrates and $In_{1-x}Ga_xAs_yP_{1-y}$ alloys of wide composition range grown on InP or GaAs substrates, which are not allowed within the lattice-match limitation. There are only a limited number of suitable combinations of lattice-matched materials as long as we use commercially available high-quality semiconductor substrates such as Si, Ge, GaAs

and InP. Secondly, the axial strain (typically 1-2%) built in the strained layers introduces new physical effects which significantly modify the electronic properties of semiconductors and improve the device performance (O'Reilly (1989)).

The material system which I studied in this thesis was $In_{1-x}Ga_xAs_yP_{1-y}$ ($0 \le x \le 1$, $0 \le y \le 1$) alloy thin films grown on InP (001) substrates. The $In_{1-x}Ga_xAs_yP_{1-y}$ alloy has the zinc-blende (sphalerite) structure shown in Fig.1.1.

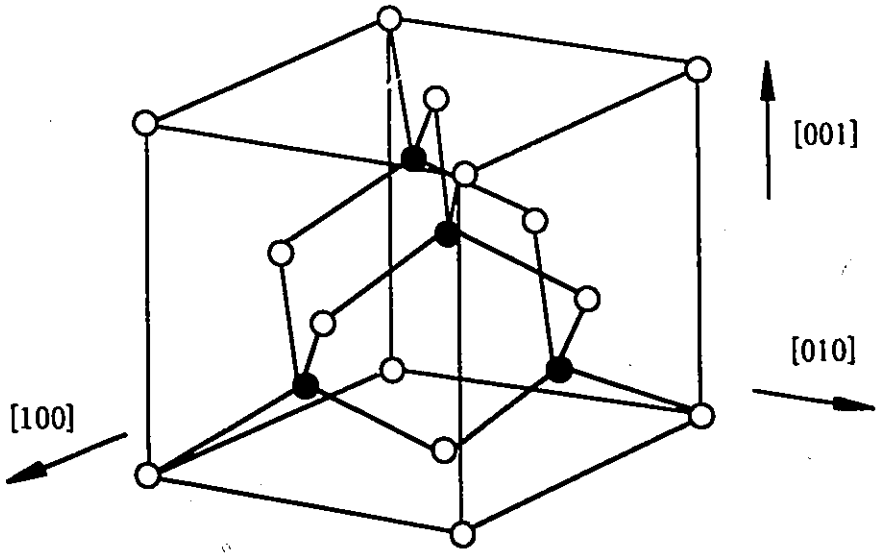

Fig.1.1 A unit cell of zinc-blende structure. In $In_{1-x}Ga_xAs_yP_{1-y}$ alloys, group III atoms (In or Ga) occupy open circles and group V atoms (As or P) occupy solid circles.

This structure consists of two fcc sublattices which are shifted relative to each other by a quarter of the <111> body diagonal and then superimposed. Each sublattice has a different group of atoms (i.e. group III or group V). Although there are 4 different elements in a quaternary $In_{1-x}Ga_xAs_yP_{1-y}$ alloy, the composition of the alloy is specified by two

composition parameters x (Ga content in group III) and y (As content in group V) due to the stoichiometry between group III and group V elements. The composition of an alloy can be represented as a point in the diagram shown in Fig.1.2.

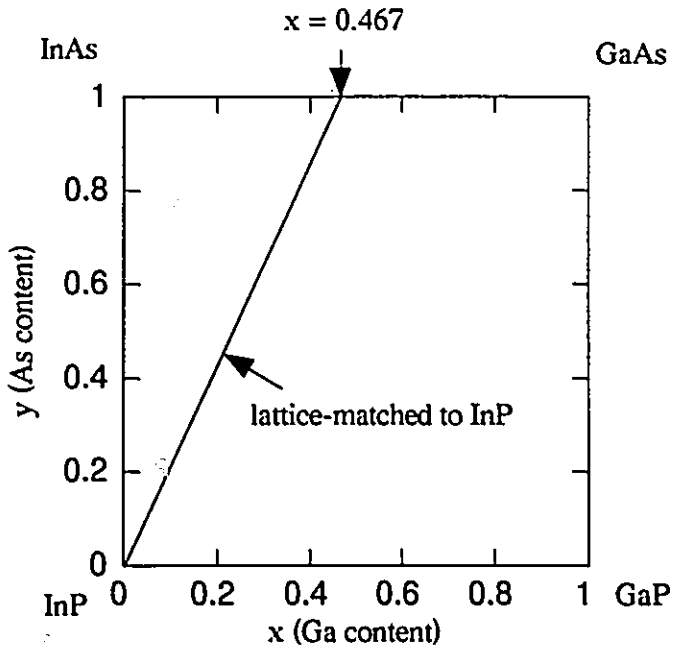

Fig.1.2 Composition diagram for $In_{1-x}Ga_xAs_yP_{1-y}$ alloy. The straight line represents the alloy compositions which have the same lattice-constant as InP (lattice-matched to InP).

The four corners of the diagram are InP (x=0, y=0), InAs (x=0, y=1), GaAs (x=1, y=1) and GaP (x=1, y=0). In this diagram the straight line connecting the origin (InP) and the $In_{0.533}Ga_{0.467}As$ alloy represents the alloy compositions which have the same lattice-constant as InP, that is, they are lattice-matched to InP.

The lattice-constant of $In_{1-x}Ga_xAs_yP_{1-y}$ alloys is known to follow Vegard's law (Nahory et al. (1978)).

$$a(In_{1-x}Ga_xAs_yP_{1-y}) = (1-x)y\,a(InAs) + (1-x)(1-y)\,a(InP) + xy\,a(GaAs)$$
$$+x(1-y)\,a(GaP) = 5.8688 - 0.4176x + 0.1896y + 0.0125xy\ (Å) \qquad (1.1)$$

The lattice-constants are represented by functions "a" and the values for InAs, InP, GaAs and GaP are 6.0584Å, 5.8688Å, 5.6533Å and 5.4512Å, respectively (Adachi (1982)). The misfit f of such an alloy film with respect to an InP substrate is defined by

$$f = (a(InP) - a(In_{1-x}Ga_xAs_yP_{1-y}))/a(In_{1-x}Ga_xAs_yP_{1-y}). \qquad (1.2)$$

The misfit between the InP substrate and the alloy film is accommodated by elastic deformation and/or by misfit dislocations formed at the interface. Throughout this thesis, the lattice-constants used to calculate the lattice-mismatch or misfit strain are based on the values at room temperatures and modification considering the difference in thermal expansion coefficients between the InP substrate and the film material will not be presented. The thermal mismatch strain is usually small compared to the typical strains considered in this thesis. The maximum strain due to the thermal expansion difference occurs between InP substrate and GaAs film and its magnitude is about 0.09% at 470°C.

In the present thesis, studies on the growth of $In_{1-x}Ga_xAs_yP_{1-y}$ alloy films heteroepitaxially deposited on InP (001) substrates using gas-source molecular beam epitaxy (MBE) will be described. Transmission electron microscopy (TEM) has been extensively used as a major experimental tool to obtain direct evidence for some unique growth-related phenomena occurring in these thin films. Throughout the thesis, the emphasis is put on views from materials science rather than from practical interest for fabricating devices. The construction of this thesis is described below.

In Chapter 2 some fundamental phenomena related to heteroepitaxy of III-V compound semiconductors are reviewed. They are the mechanism of strain relaxation via introduction of misfit dislocations, the "classical" spinodal decomposition in In_{1-}

$_xGa_xAs_yP_{1-y}$ alloys and the surface morphological instability of highly strained films. Experimental techniques and related background theories including MBE and TEM are reviewed in Chapter 3. Experimental results and discussions are presented in Chapters 4 to 6 for each subject. The summary of major findings is given in Chapter 7.

In Chapter 4, studies on the initial stage of strain relaxation in compressively-strained $InAs_yP_{1-y}$ ternary alloy films grown on InP (001) substrates are described. The compressive misfit strain in 190Å thick films ranged between –0.96% and –2.43% ($0.30 \le y \le 0.77$). Both TEM and cathodoluminescence imaging revealed the existence of new types of misfit dislocations aligned close to [100] and [010] directions in addition to the expected misfit dislocations along [1 $\bar{1}$0] and [110] directions. The new types of misfit dislocations were found to be pure edge in character, formed probably by slip on {011} planes. Contrast profiles were computed for misfit dislocations parallel and adjacent to one of the free surfaces of a plan-view TEM foil by taking into account the significantly modified elastic field associated with such dislocations. The computed profiles were useful when Burgers vectors of misfit dislocations generated from a dislocation source were analyzed.

In Chapter 5, studies on the composition modulation in 3000Å thick $In_{1-x}Ga_xAs_yP_{1-y}$ alloy films having a wide range of nominal composition being lattice-matched to InP are described. In our MBE-grown films, composition modulation occurring only along the [110] direction with small wavelength (~100Å) was repeatedly observed by using cross-sectional and plan-view TEM. This modulation is different from "classical" spinodal decomposition occurring along elastically soft [100] and [010] directions with long wavelength (1000-1500Å), which is commonly observed in $In_{1-x}Ga_xAs_yP_{1-y}$ alloy films grown by liquid phase epitaxy. A simple free energy argument for composition-modulated thin films, including the effect of constraint from the substrate suggests that the observed

modulation is not directly caused by the minimization of free energy but is driven by kinetic process occurring at the free surface of growing films.

In Chapter 6, studies on morphological instability of strained layer surface are described. Our cross-sectional TEM investigations of strained $In_{1-x}Ga_xAs_yP_{1-y}$ alloy thin films revealed prominent composition modulations and surface undulations only in the $[1\ \bar{1}0]$ cross-section, not in the [110] cross-section. Surface morphology shows clear correlation with the degree of the composition modulation occurring predominantly along the [110] direction in the strained layers. This surface undulation associated with composition modulation was observed only in tensile-strained layers. When the layer is under tension, the surface undulation can be observed at relatively small strain (as low as 0.5%), on the other hand, layers with the same magnitude of compressive strain did not exhibit surface undulation. In addition, the surface undulation is composition dependent; it is enhanced as the degree of composition modulation is increased. This surface morphological instability induced by the inherent composition modulation in $In_{1-x}Ga_xAs_yP_{1-y}$ alloys is distinctive from the "conventional" three dimensional island growth of highly strained films.

Chapter 2

Review

2.1 Strain relaxation via introduction of misfit dislocations (plastic relaxation)

2.1.1 Critical thickness for the introduction of misfit dislocations

A) Strain relaxation of mismatched layers

Consider a thin film deposited on a dissimilar substrate having a different lattice-constant as shown in Fig.2.1.1(a).

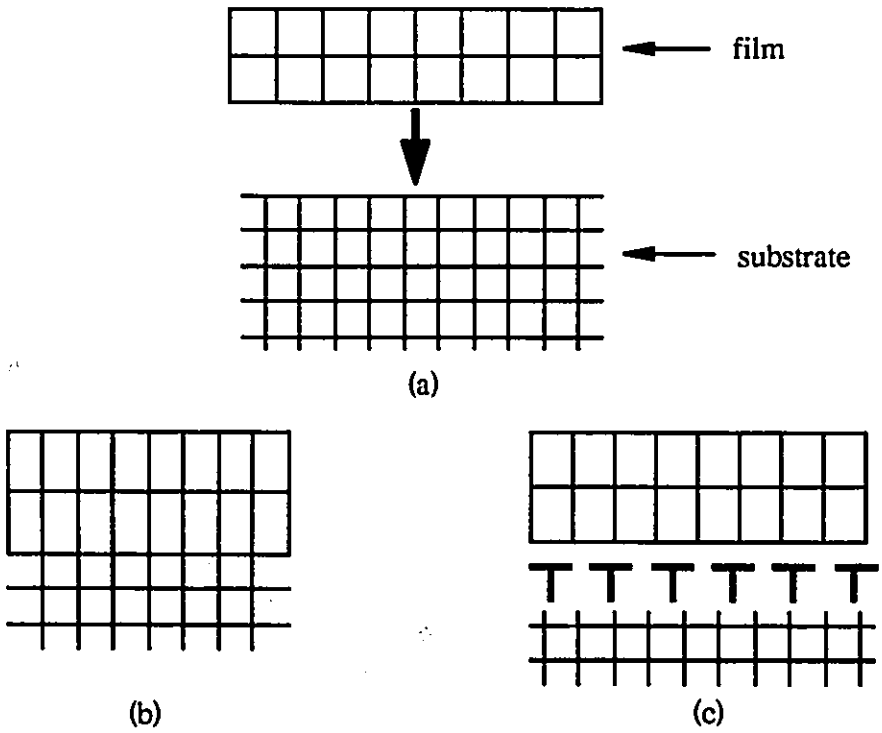

Fig.2.1.1 Mismatched heteroepitaxial growth of a planar thin film on a dissimilar substrate (a). The misfit may be totally accommodated by tetragonal distortion of the film material (b) or some of the misfit may be taken by misfit dislocations (c).

The film may remain coherent to the substrate (i.e. totally strained state through tetragonal distortion of the thin film (Fig.2.1.1(b)) or some of the mismatch may be accommodated by misfit dislocations (Fig.2.1.1(c)). In this example, since the equilibrium lattice-constant of the film a_f is larger than that of the substrate a_s, the film is under biaxial compression. The total misfit f is defined by

$$f = \frac{a_s - a_f}{a_f} = \varepsilon + \delta \qquad (2.1.1)$$

where ε is the elastic strain in the film and δ is the part of the misfit relieved by misfit dislocations. When the deposited film is much thinner than the substrate, almost all of the elastic strain is confined in the film (Hirth and Evans (1986)). If some of the misfit is taken by misfit dislocations at the interface, the dislocation spacing S is

$$S = b_{eff}/\delta \qquad (2.1.2)$$

where b_{eff} is the effective Burgers vector which contributes to relieve the mismatch: this is the projection of the pure edge component of a dislocation Burgers vector onto the interface plane.

The stored strain energy in the tetragonally distorted film increases linearly with the film thickness, whereas the energy required to create a dislocation is large because it involves the energy for breaking a line of bonds. Once present, the dislocation energy increases slowly with the layer thickness h as ln(h). A comparison of the strain energy per unit area E_e stored in a totally strained film, with the strain energy E_{dis} per unit area of a dislocation network relieving the misfit is schematically shown in Fig.2.1.2.

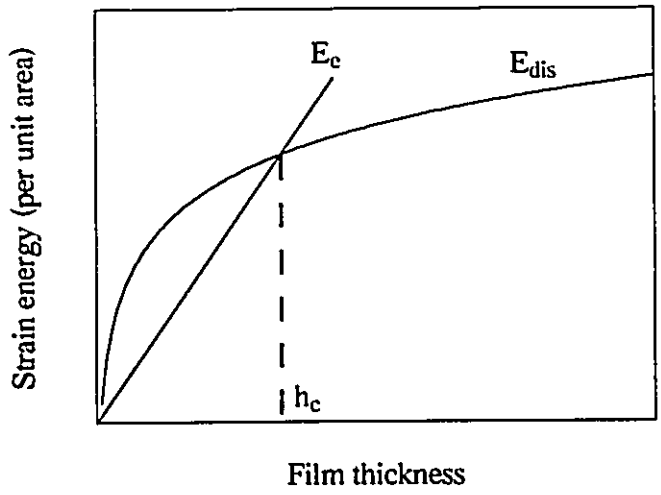

Fig.2.1.2 Schematic comparison of the strain energy of a totally strained film E_c with the energy stored in a dislocation network E_{dis}. When the film thickness h is smaller than the critical thickness h_c, the strained layer is energetically favourable and the misfit between the film and the substrate is totally accommodated by elastic distortion of the thin film.

There will thus be a certain thickness h_c, termed the critical thickness, below which the fully strained state is favoured and a totally strained film without misfit dislocations is realized. If the film thickness exceeds the critical thickness, it becomes energetically favourable to relieve a part of the misfit via misfit dislocations. This phenomenon is called strain relaxation or plastic relaxation.

In semiconductors with the zinc-blende structure, the usual slip systems are (a/2)<110>-{111}. Therefore, for a lattice-mismatched layer grown on a (001) substrate, the misfit dislocations at the interface form a cross grid configuration with two sets of parallel dislocations lying along [1 $\bar{1}$0] and [110] directions as shown in Fig.2.1.3 (a).

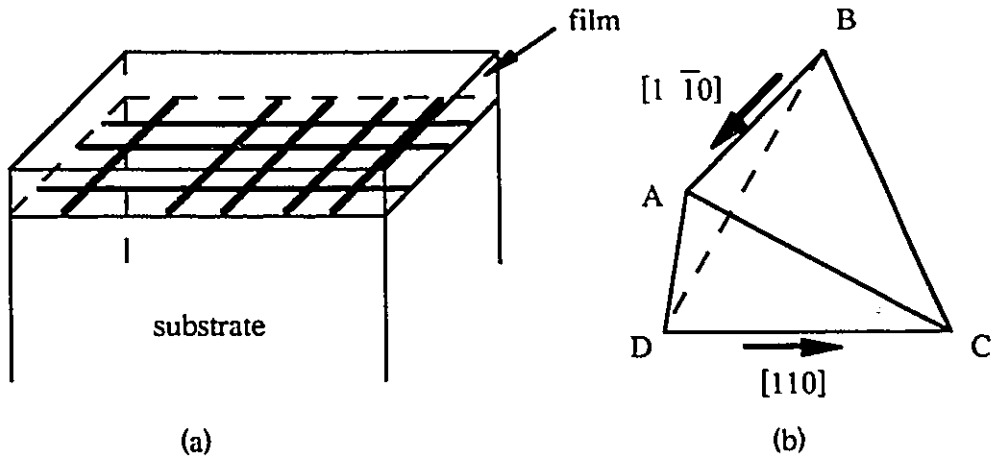

Fig.2.1.3 A cross-grid configuration of misfit dislocations at the interface caused by (a/2)<110>-{111} slip (a). Thompson's tetrahedron is shown for a reference (b).

Slip on ABC and BAD planes form dislocations along BA ([1 $\bar{1}$0]) at the interface. If the film is under compression, the extra half-plane of the misfit dislocations lies in the substrate. The Burgers vectors of misfit dislocations which contribute to strain relaxation are in CA and CB directions on the ABC plane, and AD and BD directions on the BAD plane, expressed using Thompson's notation. Similarly, for misfit dislocations lying along DC ([110]), the possible Burgers vectors are BC and BD on the BCD plane, and CA and DA on the ACD plane. In each case the Burgers vector makes an angle of 60° with the dislocation line direction. Such dislocations are called 60° dislocations.

B) Critical thickness calculation based on energy balance model

In the following, a classical method for critical thickness calculation, the energy balance method will be reviewed (Matthews (1975)). In this energy balance approach, the optimum elastic strain ε^* is first derived as a function of the film thickness h by minimizing

the total strain energy of the system E_e+E_{dis}. The critical thickness h_c is then calculated from the condition $\varepsilon^*=f$ which means that at and below this thickness it is energetically favourable for the misfit f between the film and the substrate to be accommodated only by the elastic strain. For simplicity the following calculations are limited to isotropic elasticity which is a good approximation for $In_{1-x}Ga_xAs_yP_{1-y}$ alloys.

Consider a X,Y,Z-coordinate system in which the Z-axis is parallel to the growth direction and the X and Y-axes are in the film/substrate interface plane. The film is under biaxial strain $\varepsilon_{XX}=\varepsilon_{YY}=\varepsilon$. From $\sigma_{ZZ}=0$, the strain in the growth direction of the film is derived for an isotropic material as $\varepsilon_{ZZ}=-2\nu\varepsilon/(1-\nu)$ where ν is the Poisson's ratio. The biaxial stresses in the film are $\sigma_{XX}=\sigma_{YY}=2\mu(1+\nu)\varepsilon/(1-\nu)$ where μ is the shear modulus. The elastic energy W per unit volume is calculated as

$$W = \int_0^{\varepsilon_{ij}} \sigma_{ij} d\varepsilon_{ij} = 2\int_0^{\varepsilon} \frac{2\mu(1+\nu)}{1-\nu}\varepsilon d\varepsilon = \frac{2\mu(1+\nu)}{1-\nu}\varepsilon^2. \qquad (2.1.3)$$

Therefore, the elastic energy per unit area of the film with thickness h is given by

$$E_e = \frac{2\mu(1+\nu)}{1-\nu} h\varepsilon^2. \qquad (2.1.4)$$

Misfit dislocations may be introduced to the interface to relieve a part of the misfit f. Assuming that the film and the substrate have the same elastic constants μ and ν, two orthogonal sets of misfit dislocations have strain energy per unit area of

$$E_{dis} = 2(1/S)\frac{\mu b^2(1-\nu\cos^2\alpha)}{4\pi(1-\nu)}\{\ln(R/b) + 1\} \qquad (2.1.5)$$

where the factor 2 accounts for the two sets of dislocations, 1/S is the number of dislocations per unit length along the interface, b is the magnitude of the Burgers vector, R is the outer cut-off radius and α is the angle between the Burgers vector and the dislocation line. Using eqs.(2.1.1) and (2.1.2) we can rewrite eq.(2.1.5) in the form

$$E_{dis} = 2\frac{f-\varepsilon}{b_{eff}}\frac{\mu b^2(1-\nu\cos^2\alpha)}{4\pi(1-\nu)}\{\ln(R/b)+1\}. \qquad (2.1.6)$$

The optimum value of the strain ε^* is derived from the minimization of the total strain energy of the system. From $\frac{\partial}{\partial\varepsilon}(E_e + E_{dis}) = 0$, we obtain

$$\varepsilon^* = \frac{(b/b_{eff})b(1-\nu\cos^2\alpha)}{8\pi(1+\nu)h}\{\ln(R/b)+1\}. \qquad (2.1.7)$$

When S/2 is larger than the film thickness h, the cut-off radius R is taken as h. The part of the strain relieved by misfit dislocations is zero until $\varepsilon^* = f$. Thus the critical thickness h_c is calculated from

$$h_c = \frac{(b/b_{eff})b(1-\nu\cos^2\alpha)}{8\pi(1+\nu)f}\{\ln(h_c/b)+1\}. \qquad (2.1.8)$$

For strain relaxation by 60° misfit dislocations, b_{eff} becomes (1/2)b and $\cos^2\alpha$ equals 1/4. We finally obtain the formulation of critical thickness as

$$h_c = \frac{b(1-\nu/2)\{\ln(h_c/b)+1\}}{4\pi(1+\nu)f}. \qquad (2.1.9)$$

An alternative approach to the critical thickness calculation can be performed by considering the balance of forces acting on a dislocation which preexists in the substrate and threads through the thin film as the film grows. This force balance method gives an equivalent result to the energy balance calculation eq.(2.1.9).

Matthews and coworkers conducted a lot of pioneering theoretical and experimental work on the critical thickness. However, when we use their theoretical prediction of critical thickness, we should be careful not to be confused by their inconsistent expressions and many minor errors contained in their original papers. For example, in Matthews et al. (1970) $\cos\lambda=1/2$ and $\cos\phi=\sqrt{2}/\sqrt{3}$ were mistaken as $1/\sqrt{2}$ and $1/\sqrt{3}$,respectively and in Matthews et al. (1976) $\cos\phi$ was taken as 2/3. In these examples, λ and ϕ are the angles which appear in the force balance method and $\cos\lambda\cos\phi$ represents the Schmidt factor of the slip system on which the segment of the dislocation threading through the film slips to form a misfit dislocation at the interface.

Figure 2.1.4 is the critical thickness calculated from eq.(2.1.9). The Poisson's ratio ν was taken as 0.284 which is the Voigt average for InP and the magnitude of the Burgers vector b=4.15Å was used.

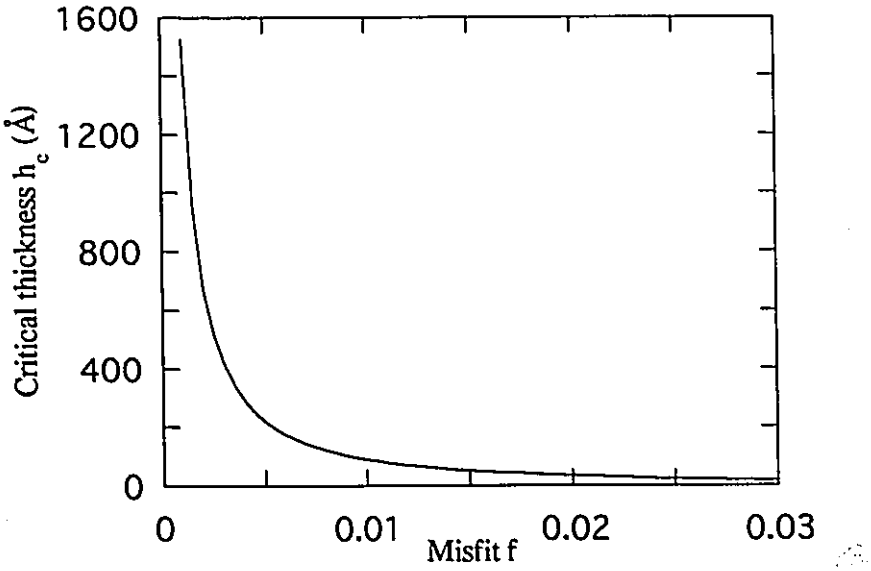

Fig.2.1.4 The critical thickness as a function of misfit f calculated from eq.(2.1.9). The Poission's ratio ν and magnitude of Burgers vector were taken as 0.284 and 4.15Å, respectively.

C) Practical limitations on the determination of critical thickness

In recent years many attempts have been done on theoretically more rigorous treatments of the critical thickness. They include approaches which take account of the dissociation of dislocations (Marée et al. (1987), Zou and Cockayne (1993)), the dislocation-dislocation interaction (Jain et al. (1992)) and the modified elastic fields of misfit dislocations due to the free surface of the thin film (Dynna et al. (1994)). Although these approaches are very interesting topics in materials science, they do not have big advantages over the conventional critical thickness calculations. This is because the experimental determination of the exact critical thickness at which the first misfit dislocation is formed at the interface is very difficult and the evaluation of the validity of various

theories is not easy unless the predicted results have large differences. Experimental techniques available at the present stage do not possess the ability to detect the first dislocation introduced at an interface of wide area. We should also note that the complete strain relaxation does not occur when the film thickness reaches the critical thickness. Strain relaxation will take place continuously as the film thickness increases. Therefore, if the resolution of an experimental technique is low as in x-ray diffraction, the relaxation can not be detected until it becomes sufficiently large and this thickness can easily be confused as the critical thickness. Other techniques such as transmission electron microscopy (TEM) with high resolution to detect individual dislocation can investigate only a limited area of the interface and may easily miss the onset of strain relaxation.

Because theoretical or experimental determination of critical thickness is not the main subject of this thesis, the modified treatments of critical thickness will not be reviewed further. When necessary, the most conservative expression eq.(2.1.9) is going to be used for critical thickness.

2.1.2 Relaxation in $In_{1-x}Ga_xAs_yP_{1-y}$ alloys

A) Polarity (α or β nature) of 60° dislocations in III-V compound semiconductors

$In_{1-x}Ga_xAs_yP_{1-y}$ alloys have the zinc-blende structure as already shown in Fig.1.1. Its stacking sequence along <111> direction is ···AaBbCcAa··· where A,B,C atoms and a,b,c atoms belong to different groups. The spacing between Aa, Bb, Cc is wider than that of aB, bC,cA as seen in Fig.2.1.5.

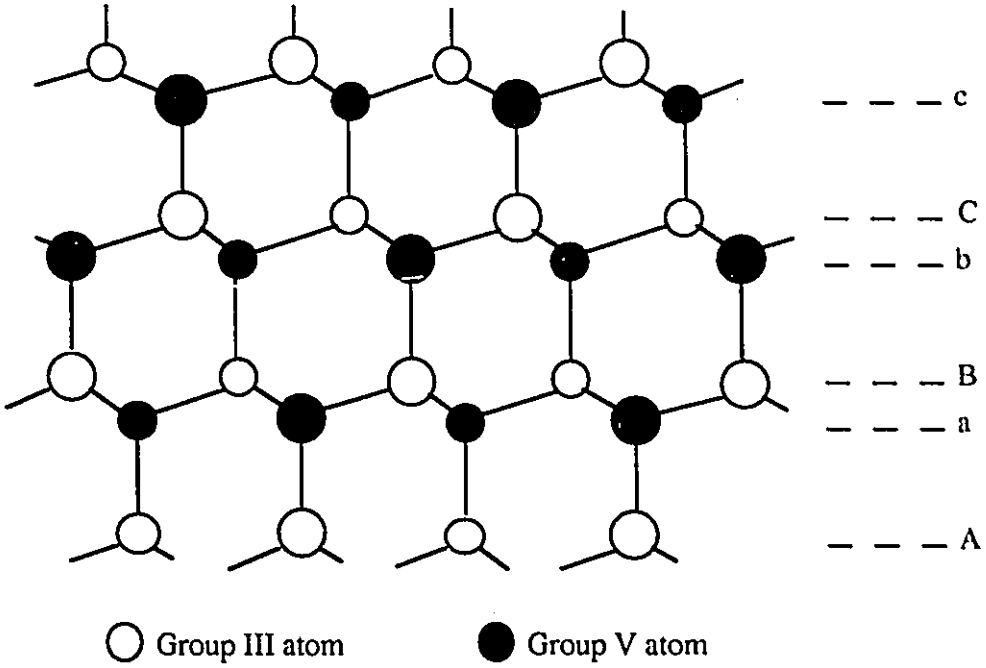

Fig.2.1.5 The stacking sequence of zinc-blende structure along the [111] direction. Atoms with different size indicate that they are not on the same height along the projected direction.

In this structure the Burgers vectors of slip dislocations are (a/2)<110> type and the most commonly observed slip planes are {111} planes. Here, the definition of the polarity (α or β nature) of 60° dislocations is introduced using a ball-and-stick model of cross-sectional views of the crystal along [1 $\bar{1}$0] and [110] directions (Fig.2.1.6 (a) and (b)).

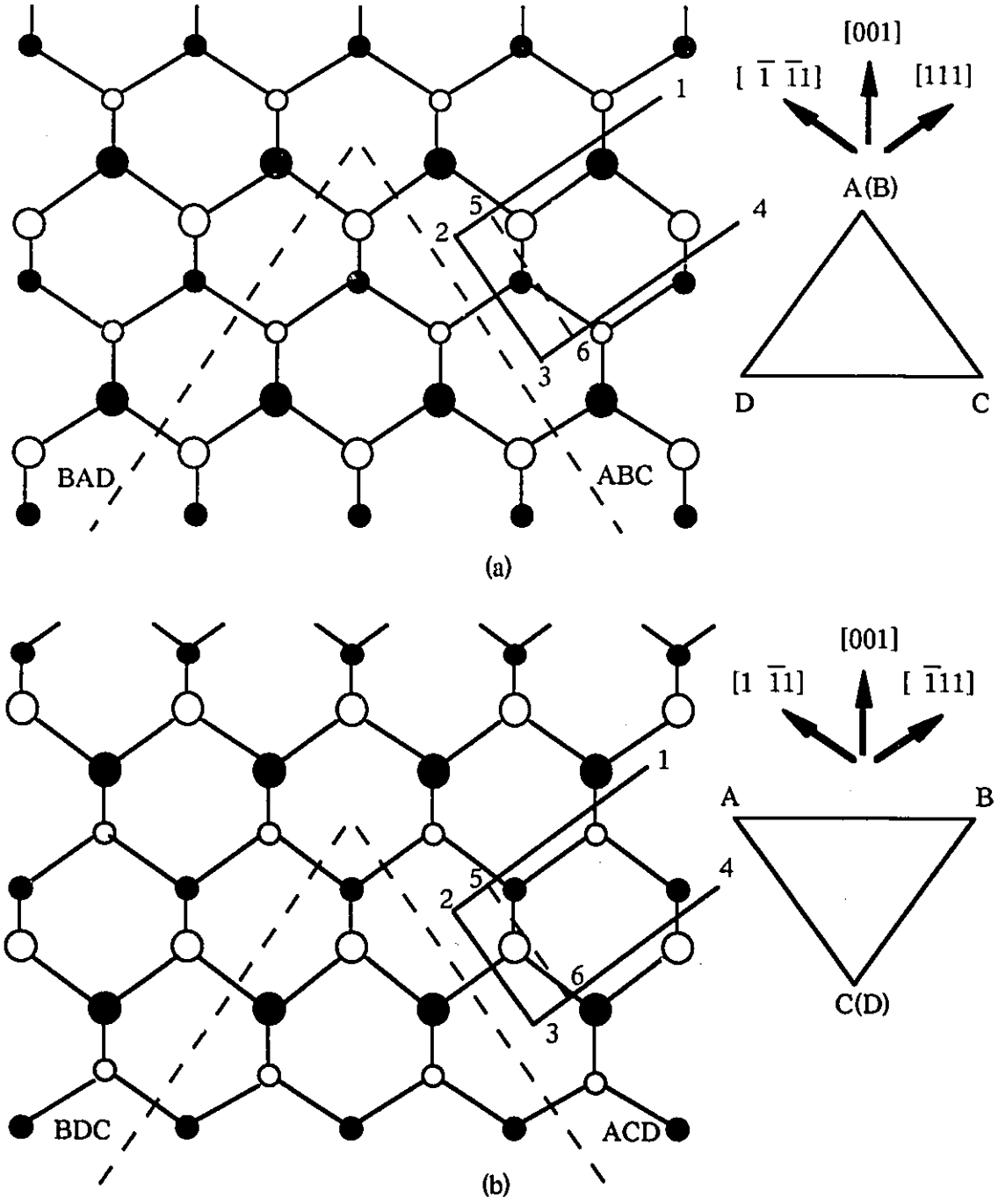

Fig.2.1.6 III-V compound semiconductor with zinc-blende structure viewed along [1 $\bar{1}$0] direction (a) and [110] direction (b) to explain the conventional 'shuffle-set' cut and 'glide-set' cut to create 60° dislocations.

The geometrical way to introduce a dislocation in a perfect crystal is to remove some material from the crystal and then paste the newly generated surfaces together. In Fig.2.1.6 the removal of material along 1-2-3-4 or 1-5-6-4 and subsequent restoration of atom bonds result in the creation of a 60° dislocation. Conventionally, it was believed that the cut is made along 1-2-3-4, that is, widely spaced III-V bonds (i.e. Aa, Bb or Cc) are cut at the slip plane 2-3. Under this assumption, the polarity of a 60° dislocation was defined by the nature of the terminating atoms of the extra half-plane of the dislocation. In Fig.2.1.6 (a), the terminating atoms are group III if the cut is made using the conventional 1-2-3-4 path. In this case the resulting dislocation is termed a 60° α dislocation. The dislocation created by the 1-2-3-4 cut in Fig.2.1.6 (b) is called a 60° β dislocation because its terminating atoms are group V.

However, today, it is generally accepted that the narrowly spaced III-V bonds (i.e. aB,bC or cA) rather than wider bonds are cut at the slip plane. This drastic change of view is supported by experimental observations using high-resolution weak-beam TEM method (Cockayne and Hons (1979)). In most semiconducting crystals almost all glide dislocations are found to be dissociated into leading and trailing partial dislocations which bound a ribbon of stacking fault. Since stacking fault planes in these crystals exist between narrowly spaced bonds (aB,bC or cA), it is more likely that the narrower bonds are first cut by the slip plane and a subsequent dissociation occurs on the same plane. This process does not require complex rearrangement of atoms around the dislocation core. On the contrary, if the dislocation starts from the conventional 1-2-3-4 cut, atoms around the core need to be rearranged on a large scale (shuffling) for the dissociation into partials. The dislocations associated with the conventional 1-2-3-4 cut and the new 1-5-6-4 cut are sometimes called 'shuffle-set' and 'glide-set' dislocations, respectively. We should note that the type of terminating atoms of the extra half-plane is reversed depending on whether

we use 'shuffle-set' or 'glide-set' definition. Therefore, the distinction between α and β dislocations should be done depending on whether the extra half-plane exists on the positive side or negative side of the slip plane. We define that both shuffle-set cut 1-2-3-4 and glide-set cut 1-5-6-4 give an α dislocation in Fig.2.1.6 (a) and in (b) both cuts give a β dislocation.

The above concept of dislocation polarity (α or β) can be applied to misfit dislocations introduced at the mismatched heteroepitaxial interface. When the equilibrium lattice-constant of the deposited film a_f is larger than that of the substrate a_s, the misfit dislocations at the interface must have a 'downward' extra half-plane to relieve the compressive strain as shown in Fig.2.1.6. Therefore, the misfit dislocations aligned along $[1\ \bar{1}0]$ and [110] directions are different in nature; α dislocations are formed along the $[1\ \bar{1}0]$ direction and β dislocations are aligned along the [110] direction. When the film is under tension ($a_f < a_s$), the dislocations along the $[1\ \bar{1}0]$ direction are β type and α dislocations are aligned parallel to the [110] direction.

The slip planes and Burgers vectors are summarised for all possible 60° misfit dislocations in Table 2.1.1. The dislocation line directions are taken as $[1\ \bar{1}0]$ and [110], and Thompson's notation is used.

Table 2.1.1

The slip plane and Burgers vector of 60° misfit dislocations when thin film is under compression ($a_f > a_s$) or under tension ($a_f < a_s$).

	Compression ($a_f > a_s$)	Tension ($a_f < a_s$)
Along [1 $\bar{1}$ 0]	Slip plane Burgers vector (111) ··· (a/2)[0 $\bar{1}$ 1] CA (1) (a/2)[$\bar{1}$ 01] CB (2) ($\bar{1}$ $\bar{1}$ 1) ·· (a/2)[$\bar{1}$ 0 $\bar{1}$] AD (3) (a/2)[0 $\bar{1}$ $\bar{1}$] BD (4)	Slip plane Burgers vector ($\bar{1}$ $\bar{1}$ $\bar{1}$) ·· (a/2)[01 $\bar{1}$] AC (a/2)[10 $\bar{1}$] BC (11 $\bar{1}$)·····(a/2)[101] DA (a/2)[011] DB
Along [110]	Slip plane Burgers vector (1 $\bar{1}$ 1) ···· (a/2)[10 $\bar{1}$] BC (5) (a/2)[0 $\bar{1}$ $\bar{1}$] BD (6) ($\bar{1}$ 11) ···· (a/2)[0 $\bar{1}$ 1] CA (7) (a/2)[101] DA (8)	Slip plane Burgers vector ($\bar{1}$ 1 $\bar{1}$) ···· (a/2)[$\bar{1}$ 01] CB (a/2)[011] DB (1 $\bar{1}$ $\bar{1}$) ···· (a/2)[01 $\bar{1}$] AC (a/2)[$\bar{1}$ 0 $\bar{1}$] AD

B) Dissociation of 60° dislocations

Dissociation of a 60° dislocation nucleating as a half-loop from the surface of strained film is discussed by De Cooman and Carter (1989). The sequence of partials,that

is, whether each partial is leading or trailing can be determined using the convention by Hirth and Lothe (1982); viewing the perfect dislocation from outside the Thompson's tetrahedron and along the positive sense of the line, the intrinsic stacking fault arrangement is achieved by placing the Greek-Roman partial on the viewer's left and Roman-Greek partial on the right. The dissociations of 60° dislocations are summarized in Table 2.1.2 using Thompson's notation.

Table 2.1.2

Dissociation and sequence of partials of 60° dislocations nucleating from the surface of strained film.

	Compression	Tension
Along [1 $\bar{1}$0](BA)	(1) CA → δA + Cδ	(1) AC → δC ÷ Aδ
	(2) CB → δB + Cδ	(2) BC → δC + Bδ
	(3) AD → Aγ + γD	(3) DA → Dγ + γA
	(4) BD → Bγ + γD	(4) DB → Dγ + γB
Along [110](DC)	(5) BC → αC + Bα	(5) CB → αB + Cα
	(6) BD → αD + Bα	(6) DB → αB + Dα
	(7) CA → Cβ + βA	(7) AC → Aβ + βC
	(8) DA → Dβ + βA	(8) AD → Aβ + βD

We should note that 30° partials are the leading dislocations trailed by 90° (pure edge) partials when the film is under compression. In contrast, for films under tension, 90° partials nucleate first followed by 30° partials. Considering that the Schmidt factor for 90° partials is twice as large as that for 30° partials (i.e. 0.4714 vs. 0.2357), the leading 30° partial in a compressed film can be overtaken by the trailing 90° partial to recombine into a 60° perfect dislocation. On the other hand, when the film is under tension, it is likely that the 90° partial leaves the 30° partial behind, forming a stacking fault ribbon between them. A number of processes in a crystal such as twinning or certain phase transformations can occur by such independent nucleation and glide of partial dislocations (De Cooman et al. (1989), Wegscheider and Cerva (1993)).

C) The mobilities of α and β dislocations and anisotropy in misfit dislocation densities

The major characteristics of dislocation mobilities experimentally observed in III-V compound semiconductors are summarized as follows (Mihara and Ninomiya (1975), Kuesters et al. (1986), Zafrany et al. (1992), Yonenaga and Sumino (1993 a, b)).

(i) The velocity of a dislocation v can be expressed as a function of the shear stress τ and temperature T in a form,

$$v = v_0(\tau/\tau_0)^m \exp(-E_a/kT) \qquad (2.1.10)$$

where v_0 and τ_0 are constants, k is the Boltzman's constant, E_a is the activation energy and m takes a value between 1 and 2.

(ii) The dislocation velocities are greatly affected by the doping of crystal.

(iii) The velocity of α dislocations is usually observed to be greater than that of β dislocations.

In III-V semiconductors, an abrupt kink model is assumed to describe dislocation motion on a slip plane at low temperatures ($<T_M/2$). As schematically shown in Fig.2.1.7, a dislocation has to overcome the primary Peierls potentials by creating a minimum kink pair at point A and expanding it sideways overcoming the secondary Peierls potential barriers because on {111} slip planes, there are 3 sets of Peierls potentials aligned along the three <110> directions.

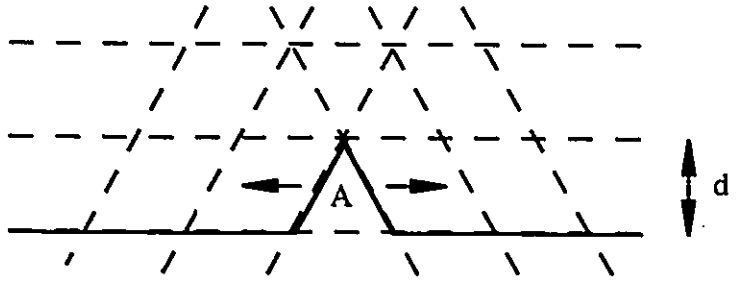

Fig.2.1.7 Abrupt kink model of dislocation motion on a {111} slip plane. The dislocation creates a minimum kink pair at A and expands it to move a distance d towards the next potential valley. Dotted lines represent three sets of Peierls potential valleys on this slip plane.

At the present time there is no theory which can describe dislocation motion in an explicit way, due to the complexity of the phenomenon involving the electronic state of the dislocation core which is believed to play an important role in the dislocation motion. The experimentally confirmed large difference in the mobilities between α and β dislocations is attributed to the different charges at their cores. However quantitative agreement is very difficult because the electronic state of the dislocation core is also sensitive to other factors such as impurity level and doping of the crystal.

In mismatched heteroepitaxy of III-V compound semiconductors, the anisotropy of misfit dislocation densities between [1 $\bar{1}$0] and [110] directions is generally observed at the initial stage of strain relaxation (Abrahams et al. (1972), Kavanagh et al. (1988), Roth et al. (1992), Morris et al. (1992)). The dislocation density is much higher in the <110> direction along which α type dislocations are formed, compared with the other <110> direction. This is usually attributed to the large difference in mobilities of α and β dislocations (De Cooman et al. (1989)).

2.2 Spinodal decomposition in $In_{1-x}Ga_xAs_yP_{1-y}$ alloys

2.2.1 Phase instability in a binary alloy

A) Chemical spinodal

Phase separation in a binary alloy of elements A and B with a miscibility gap can be explained using a free energy diagram approach as shown in Fig.2.2.1.

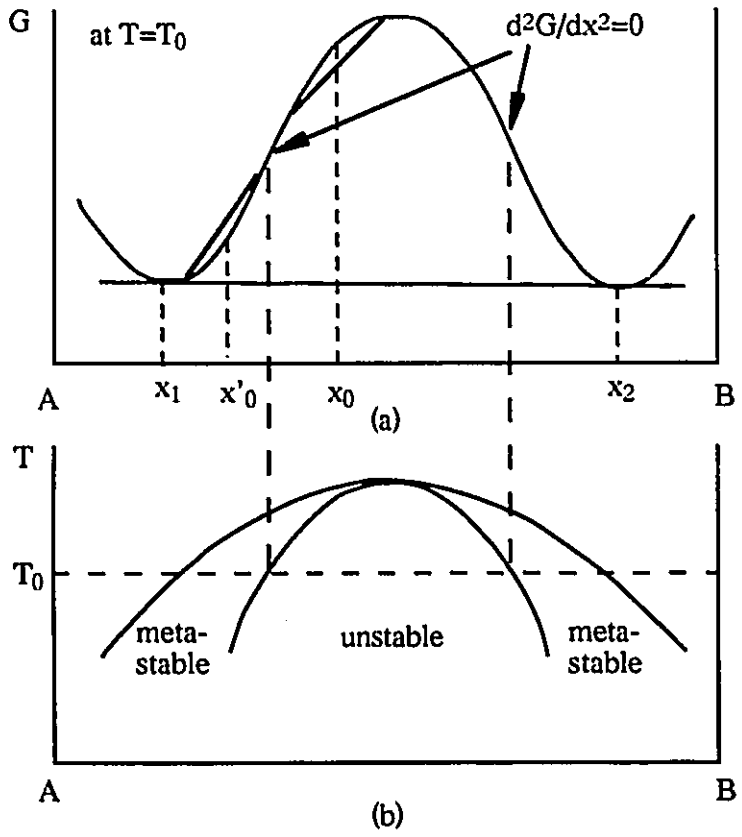

Fig.2.2.1 Free energy diagram (a) and phase diagram (b) for a binary alloy of elements A and B with miscibility gap. Note that a small fluctuation starting from the nominal composition x_0 continues without energy barrier; the alloy is unstable. On the other hand, if the starting composition is x'_0, a small composition fluctuation leads to an increase in free energy of the system. Such an alloy is termed a metastable alloy.

In this figure, the mole fraction of element B in the alloy is taken as the variable x. At temperature T_0, alloys with nominal composition between x_1 and x_2 have a driving force to be separated into two phases as evident from the common tangent construction. Such alloys can be classified into unstable and metastable alloys. A small composition fluctuation imposed on an alloy with nominal composition x_0 at which the free energy curve is convex ($d^2G/dx^2<0$), results in a decrease in total free energy. Elements A and B can diffuse against the composition gradient enhancing the initial composition fluctuation (up-hill diffusion). If the starting composition is x_0' at which the curve is concave ($d^2G/dx^2>0$), the alloy is metastable, because a small composition fluctuation leads to an increase in the free energy of the system. For the phase separation to occur continuously, nucleation and growth of new phases are needed to create a composition gradient for normal down-hill diffusion. In a binary phase diagram the boundary of the unstable region is defined by the locus of $d^2G/dx^2=0$ and is usually called the chemical spinodal.

B) Coherent spinodal --- strain stabilization

Cahn(1961) modified the above argument to include strain energy in a bulk material caused by composition fluctuation when the molar volume of the alloy is dependent on its composition. Suppose that a small composition fluctuation from the nominal value of x_0 occurs along the X-direction following,

$$x - x_0 = A\cos(\alpha X) \qquad (2.2.1)$$

where x is a local composition, A is the amplitude of composition fluctuation and $2\pi/\alpha(=\lambda)$ is its wavelength.

Let us consider an elastically isotropic material in which the stress-free molar

volume is given by

$$V(x) = V_0\{1+3\eta(x-x_0)\} = V_0\{1+3A\eta\cos(\alpha X)\} \qquad (2.2.2)$$

where the stress-free strain is a pure dilatation

$$\varepsilon_{ij} = \delta_{ij} A\eta\cos(\alpha X) \qquad (2.2.3)$$

(δ_{ij} is the Kronecker's delta) and η is the linear expansion per unit composition change. In a bulk material, the total strain which is the sum of the stress-free strain $A\eta\cos(\alpha X)$ and the subsequent elastic strain ε^E_{ij} is suppressed in the Y and Z directions. Therefore

$$\varepsilon^E_{YY} = \varepsilon^E_{ZZ} = -A\eta\cos(\alpha X) \quad \text{and} \quad \varepsilon^E_{XX} = \frac{2\nu}{1-\nu} A\eta\cos(\alpha X). \qquad (2.2.4)$$

The stresses developed in the bulk material after phase modulation are

$$\sigma_{XX} = 0 \quad \text{and} \quad \sigma_{YY} = \sigma_{ZZ} = -\frac{EA\eta}{1-\nu}\cos(\alpha X) \qquad (2.2.5)$$

where E is the Young's modulus. The local elastic energy per unit volume is

$$\frac{1}{2}\sigma_{ij}\varepsilon^E_{ij} = \frac{EA^2\eta^2}{1-\nu}\cos^2(\alpha X). \qquad (2.2.6)$$

The average elastic energy per unit volume is derived by integrating the above local energy over one period of modulation, following

$$\frac{1}{V}\int\frac{1}{2}\sigma_{ij}\varepsilon^E_{ij}dV = \frac{1}{\lambda}\int_0^{\lambda}\frac{EA^2\eta^2}{1-\nu}\cos^2(\alpha X)\,dX = \frac{EA^2\eta^2}{2(1-\nu)}. \qquad (2.2.7)$$

Taking account of the contributions from the elastic energy and the composition gradient, the Gibbs free energy of the bulk material with composition fluctuation can be written as

$$G = \int_V \{g(x) + \frac{EA^2\eta^2}{1-\nu}\cos^2(\alpha X) + \varkappa(\nabla x)^2\}dV \qquad (2.2.8)$$

where $g(x)$ is the Gibbs free energy of a unit volume of homogeneous material with composition x and $\varkappa(\nabla x)^2$ is the increase in free energy due to the composition gradient. The difference in free energy ΔG between the starting homogeneous alloy (with composition x_0) and the alloy with composition fluctuation is

$$\Delta G = \int_V \{g(x) + \frac{EA^2\eta^2}{1-\nu}\cos^2(\alpha X) + \varkappa(\nabla x)^2\}dV - \int_V g(x_0)dV. \qquad (2.2.9)$$

Using a Taylor expansion around x_0 for $g(x)$

$$g(x) = g(x_0) + (x-x_0)(\frac{\partial g}{\partial x})_{x_0} + \frac{1}{2}(x-x_0)^2(\frac{\partial^2 g}{\partial x^2})_{x_0} + \cdots \qquad (2.2.10)$$

and $\nabla x = \frac{dx}{dX} = -A\alpha\sin(\alpha X)$, we obtain

$$\Delta G \propto A^2\{\frac{1}{2}(\frac{\partial^2 g}{\partial x^2}) + \frac{E\eta^2}{1-\nu} + \varkappa\alpha^2\}\frac{\lambda}{2}. \qquad (2.2.11)$$

$$\therefore \frac{\Delta G}{V} = \frac{A^2}{4}\{(\frac{\partial^2 g}{\partial x^2})_{x_0} + \frac{2E\eta^2}{1-\nu} + 2\kappa\alpha^2\} \qquad (2.2.12)$$

Cahn defined the stability limit as $\Delta G/V=0$. By taking $\alpha \rightarrow 0$ (infinite wavelength of the fluctuation), we obtain

$$(\frac{d^2 g}{dx^2})_{x_0} + \frac{2E\eta^2}{1-\nu} = 0 \qquad (2.2.13)$$

as the new stability limit. By comparing with the old definition for the chemical spinodal, we note that the system is stabilized due to the introduction of the coherent strain energy term. This effect is called strain stabilization. The spinodal calculated from eq.(2.2.13) is termed the coherent spinodal for a bulk material.

2.2.2 Phase instability in $In_{1-x}Ga_xAs_yP_{1-y}$ alloys

A) Chemical spinodal in $In_{1-x}Ga_xAs_yP_{1-y}$ alloys

Onabe (1982) calculated the chemical spinodal of $In_{1-x}Ga_xAs_yP_{1-y}$ alloy, based on the regular solution approximation for a solid solution (Jordan and Ilegems (1975)). The free energy G is expressed as

$$\begin{aligned} G = {} & \omega_{InP}(1-x)(1-y) + \omega_{InAs}(1-x)y + \omega_{GaP}x(1-y) + \omega_{GaAs}xy \\ & + \alpha_{InP-GaP}(1-x)x(1-y) + \alpha_{InAs-GaAs}(1-x)xy \\ & + \alpha_{InP-InAs}(1-x)(1-y)y + \alpha_{GaP-GaAs}x(1-y)y \\ & + RT\{(1-x)\ln(1-x) + x\ln x + (1-y)\ln(1-y) + y\ln y\} \qquad (2.2.14) \end{aligned}$$

where the ω values are the sum of the first and second nearest-neighbour interaction energies of a binary compound, α values are the ternary interaction parameters, R is the gas constant and T is the absolute temperature. The spinodal limit of a ternary alloy with two independent parameters x and y is defined by

$$\frac{\partial^2 G}{\partial x^2}\frac{\partial^2 G}{\partial y^2} - \left(\frac{\partial^2 G}{\partial x \partial y}\right)^2 = 0 \qquad (2.2.15)$$

(Meijering (1950)). Substituting eq.(2.2.14) into eq.(2.2.15), we find

$$\begin{aligned}&[RT - 2(1-x)x\{(1-y)\alpha_{InP-GaP} + y\alpha_{InAs-GaAs}\}]\\ &\times [RT - 2(1-y)y\{(1-x)\alpha_{InP-InAs} + x\alpha_{GaP-GaAs}\}]\\ &- (1-x)x(1-y)y(\omega_Q + \alpha_Q)^2 = 0 \qquad (2.2.16)\end{aligned}$$

where ω_Q is given by 3688+0.92T (cal/mol) and

$$\alpha_Q = (1-2x)(\alpha_{InAs-GaAs} - \alpha_{InP-GaP}) + (1-2y)(\alpha_{GaP-GaAs} - \alpha_{InP-InAs}).$$

The values of α are 3500, 3000, 400, 400 (cal/mol) for InP-GaP, InAs-GaAs, InP-InAs and GaP-GaAs, respectively (Panish and Ilegems (1972)). The chemical spinodal for the $In_{1-x}Ga_xAs_yP_{1-y}$ alloy at 470°C calculated using eq.(2.2.16) is shown in Fig.2.2.2.

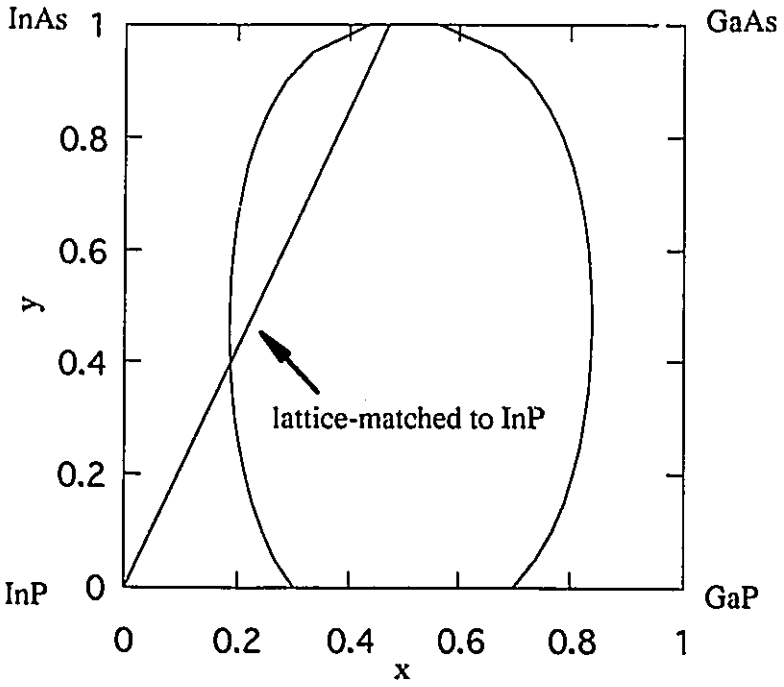

Fig.2.2.2 Chemical spinodal for $In_{1-x}Ga_xAs_yP_{1-y}$ alloy at 470°C.

We should note that the work done by Onabe and another equivalent result (Stringfellow(1982a)) are based only on chemical free energy and do not take account of the effect of elastic energy.

B) Coherent spinodal in $In_{1-x}Ga_xAs_yP_{1-y}$ alloys considering bulk strain stabilization

Stringfellow (1982b) calculated the coherent spinodal in $In_{1-x}Ga_xAs_yP_{1-y}$ alloys considering the bulk strain energy associated with newly formed InAs-rich and GaP-rich regions having different lattice-constants. The following derivation of coherent strain energy is based on an approximation which takes the value of $a_{GaAs}-a_{InAs}-a_{GaP}+a_{InP}$ as

zero. The exact value is 0.0125Å, little different from zero. This assumption enables us to avoid using a lot of undefined and unclear variables in Stringfellow's original paper.

First, the local lattice parameter a is expanded in a Taylor series about the average lattice-constant a_0 of the starting homogeneous alloy

$$a = a_0 + \frac{\partial a}{\partial x}(x-x_0) + \frac{\partial a}{\partial y}(y-y_0) + \cdots \qquad (2.2.17)$$

where x_0 and y_0 are the composition parameters for the starting alloy. The strain energy per unit volume is proportional to $(a_0-a)^2/a_0^2$ and, therefore, the average strain energy per unit volume W can be written under the assumption of small amplitude of the fluctuation in a form,

$$W \propto \frac{1}{V}\frac{E}{1-\nu}\int_V \{\eta_A^2(x-x_0)^2+\eta_B^2(y-y_0)^2+2\eta_A\eta_B(x-x_0)(y-y_0)\}dV \qquad (2.2.18)$$

where $\eta_A=(1/a_0)(\partial a/\partial x)$ and $\eta_B=(1/a_0)(\partial a/\partial y)$. If the local chemical free energy per unit volume is G(x,y), the total free energy G′ is written as

$$G'(x,y)=G(x,y)+\frac{E\eta_A^2}{1-\nu}(x-x_0)^2+\frac{E\eta_B^2}{1-\nu}(y-y_0)^2+\frac{2E\eta_A\eta_B}{1-\nu}(x-x_0)(y-y_0). \qquad (2.2.19)$$

Substituting G′ in eq.(2.2.19) for G in the stability condition eq.(2.2.15), we obtain

$$\left.\begin{aligned}
\frac{\partial^2 G'}{\partial x^2} &= \frac{\partial^2 G}{\partial x^2} + \frac{2E\eta_A^2}{1-\nu} \\
\frac{\partial^2 G'}{\partial y^2} &= \frac{\partial^2 G}{\partial y^2} + \frac{2E\eta_B^2}{1-\nu} \\
\frac{\partial^2 G'}{\partial x \partial y} &= \frac{\partial^2 G}{\partial x \partial y} + \frac{2E\eta_A\eta_B}{1-\nu}
\end{aligned}\right\}. \qquad (2.2.20)$$

Stringfellow used the delta lattice parameter (DLP) model to calculate the chemical free energy of the alloy G^S (cal/mol)

$$G = N_v G^S = N_v[-Ka^{-2.5} + RT\{x\ln x + (1-x)\ln(1-x) + y\ln y + (1-y)\ln(1-y)\}] \qquad (2.2.21)$$

where N_v is the number of moles per unit volume and K is an empirical parameter equal to 1.15×10^7 (cal/mol)$Å^{2.5}$. Using (2.2.21), the derivatives in the right hand side of eq.(2.2.20) become

$$\left.\begin{aligned}
\frac{\partial^2 G}{\partial x^2} &= N_v\{-8.75K(\frac{\partial a}{\partial x})^2 a^{-4.5} + \frac{RT}{x(1-x)}\} \\
\frac{\partial^2 G}{\partial y^2} &= N_v\{-8.75K(\frac{\partial a}{\partial y})^2 a^{-4.5} + \frac{RT}{y(1-y)}\} \\
\frac{\partial^2 G}{\partial x \partial y} &= N_v\{-8.75K(\frac{\partial a}{\partial x})(\frac{\partial a}{\partial y})a^{-4.5}\}
\end{aligned}\right\}. \qquad (2.2.22)$$

Using eq.(1.1)

$$\left.\begin{aligned}\frac{\partial a}{\partial x} &= a_{GaP} - a_{InP} + Dy = -0.4176 + 0.0125y \\ \frac{\partial a}{\partial y} &= a_{InAs} - a_{InP} + Dx = 0.1896 + 0.0125x\end{aligned}\right\} \qquad (2.2.23)$$

where $D = a_{GaAs} - a_{InAs} - a_{GaP} + a_{InP} = 0.0125$ (Å). As noted earlier, it is a reasonable approximation to take D as zero because this causes relatively small errors in $\partial a/\partial x$ and $\partial a/\partial y$. We take

$$\left.\begin{aligned}\frac{\partial a}{\partial x} &= a_0 \eta_A \approx a_{GaP} - a_{InP} = \Delta a_A \\ \frac{\partial a}{\partial y} &= a_0 \eta_B \approx a_{InAs} - a_{InP} = \Delta a_B\end{aligned}\right\}. \qquad (2.2.24)$$

The stability condition becomes

$$\left(\frac{\partial^2 G^S}{\partial x^2} + S\Delta a_A^2\right)\left(\frac{\partial^2 G^S}{\partial y^2} + S\Delta a_B^2\right) - \left(\frac{\partial^2 G^S}{\partial x \partial y} + S\Delta a_A \Delta a_B\right)^2 = 0 \qquad (2.2.25)$$

where $S=2E/(1-\nu)a_0^2N_v$. Introducing $M=8.75Ka_0^{-4.5}$,we can rewrite eq.(2.2.22) as

$$\left.\begin{aligned}\frac{\partial^2 G^S}{\partial x^2} &= \frac{RT}{x(1-x)} - M\Delta a_A^2 \\ \frac{\partial^2 G^S}{\partial y^2} &= \frac{RT}{y(1-y)} - M\Delta a_B^2 \\ \frac{\partial^2 G^S}{\partial x \partial y} &= -M\Delta a_A \Delta a_B\end{aligned}\right\}. \qquad (2.2.26)$$

Here we used the fact that the lattice parameter difference from the starting a_0 is very small. Substituting eq.(2.2.26) into eq.(2.2.25), we finally obtain an expression

$$T = \frac{(M-S)\{x(1-x)\Delta a_A^2 + y(1-y)\Delta a_B^2\}}{R} \qquad (2.2.27)$$

for a given alloy composition x and y. If the growth temperature is higher than the value calculated from eq.(2.2.27), the alloy is stable against phase separation. The temperature T(x,y) may be termed the critical temperature against phase separation.

Now let us compare the critical temperatures for (i) the chemical spinodal by putting the strain term S=0 in eq.(2.2.27) and for (ii) the coherent spinodal with non-zero S. For the chemical spinodal in which the strain stabilization effect is ignored the critical temperature is calculated as T_{chem}=1010K for an alloy with x=y=0.5. On the other hand, if the strain effect is taken into account, the critical temperature becomes negative in the absolute temperature scale because in the $In_{1-x}Ga_xAs_yP_{1-y}$ alloy the value of S is larger than M for x=y=0.5. This implies that the $In_{1-x}Ga_xAs_yP_{1-y}$ alloy is stable against phase separation at any temperature due to strain stabilization.

However the above prediction is controversial because there is considerable experimental evidence for phase separation in $In_{1-x}Ga_xAs_yP_{1-y}$ alloys. TEM contrast related to phase separation along elastically soft [100] and [010] directions with a wavelength typically 1000-1500Å or 100-200Å has been observed in $In_{1-x}Ga_xAs_yP_{1-y}$ alloy films grown by liquid phase epitaxy (LPE) (Henoc et al. (1982), Mahajan et al. (1984), Ueda et al. (1984a), Norman and Booker (1985), Ishikawa et al.(1990), McDevitt et al. (1992)). The growth temperature used for LPE is typically 630-650°C. Similar TEM contrast was observed in $In_{1-x}Ga_xAs_yP_{1-y}$ films deposited using vapour phase epitaxy (VPE) (Chu et al. (1985)) and in $In_{1-x}Ga_xAs$ ternary films grown with molecular beam

epitaxy (MBE) (Peiró et al. (1991 and 1993)) with lower growth temperatures, typically 450-550°C. Stringfellow's coherent spinodal calculation is not appropriate to estimate the effect of strain stabilization in thin films grown on substrates because his theory is based on elastic fields in an infinitely large bulk material.

C) Strain stabilization in thin films

Glas (1987) first calculated the elastic fields of a system in which a thin film material deposited on a semi-infinite substrate experiences a phase modulation. Glas' approach following step-by-step procedures similar to Eshelby (1957) is schematically shown in Fig.2.2.3. In stage I, the thin film material is divided into independent cubes and a lattice-constant, sinusoidally varying with the position along the modulation direction X, is given to each cube following $a_0\{1-\varepsilon_0 \cos(\alpha X)\}$. Then external forces are applied to each cube to give it the substrate lattice parameter a_0. In stage II these cubes are assembled on the substrate. This process changes the nature of some of the external forces applied in stage I. In the final stage III, the system is relaxed by cancelling the forces applied in stage I.

Glas solved the problem for an elastically isotropic material. In Chapter 5 of this thesis his approach will be extended to materials with cubic or tetragonal symmetry to discuss the critical temperatures for composition modulation along <100> direction and <110> direction.

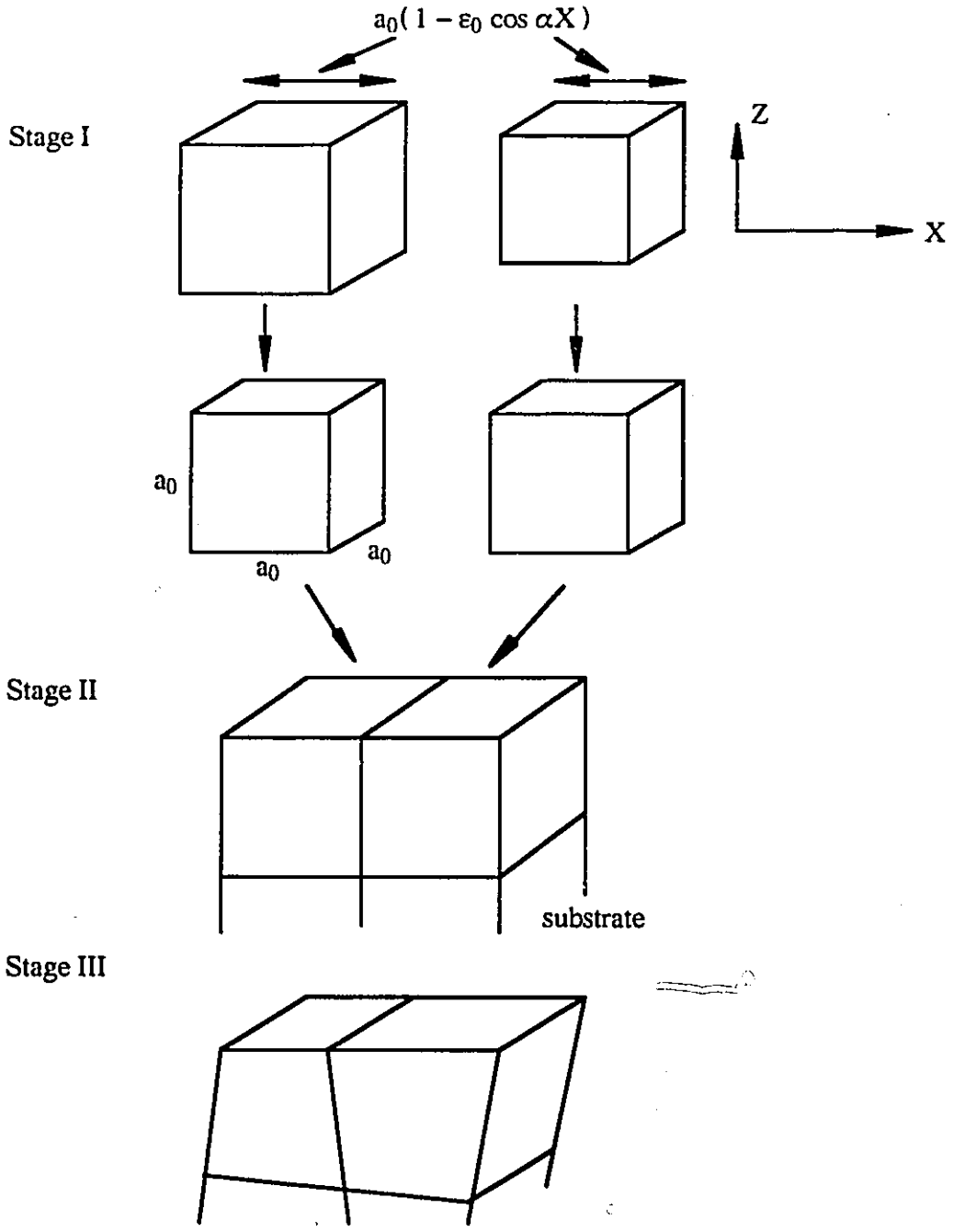

Fig.2.2.3 Glas' step-by-step procedures to solve elastic fields associated with a phase-modulated thin film deposited on a semi-infinite substrate.

In his paper Glas found that the elastic energy w_E stored in a unit volume of the phase modulated thin film with thickness h is considerably reduced with respect to the elastic energy in a bulk material following,

$$w_E = w_{bulk}[1-(1+\nu)\{1-\exp(-\alpha h)\}^2/\alpha h] \qquad (2.2.28)$$

where w_{bulk} is the elastic energy in a bulk material $(1/2)E\varepsilon_0^2/(1-\nu)$. Equation (2.2.28) is plotted in Fig.2.2.4 for a Poisson's ratio $\nu=1/3$.

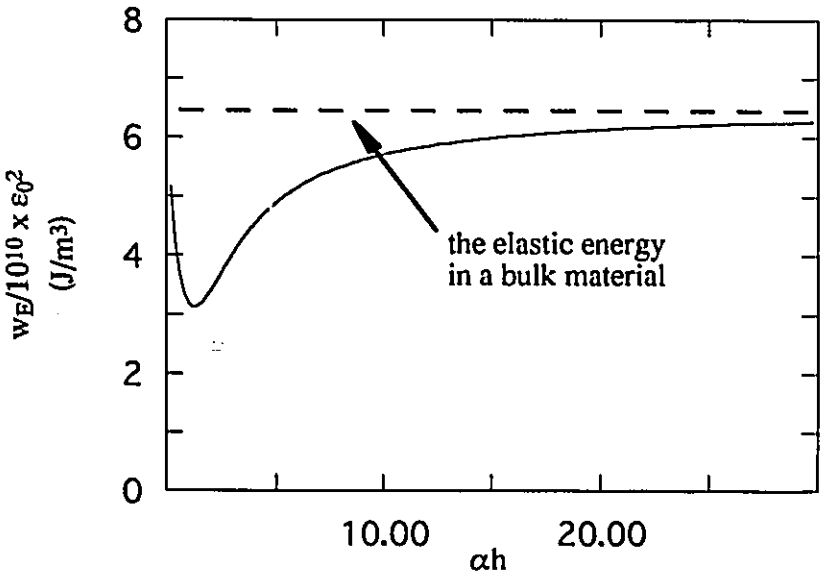

Fig.2.2.4 The elastic energy w_E stored in a unit volume of a phase-modulated thin film with thickness h deposited on a semi-infinite substrate. The elastic energy is considerably reduced at around $\alpha h=1$.

It is clear that the elastic energy in thin film is reduced to about 43% of the bulk elastic

energy at around $\alpha h=1$. This is due to the elastic relaxation which occurs toward the growth direction (Z-axis) at this thickness.

Glas calculated the critical temperature T_c for $In_{1-x}Ga_xAs$ films above which the alloy becomes stabilized against phase separation and compared it with other critical temperatures T_{chem} and T_{bulk} for chemical spinodal (without strain stabilization) and coherent spinodal (strain stabilization in bulk material), respectively. These values are T_c=320K, T_{chem}=730K and T_{bulk}=–140K for x=0.5. A considerable improvement is achieved by evaluating elastic energy in thin films. However, even this result is still not consistent with experimental observation. For example, coarse and fine phase modulations were observed in $In_{1-x}Ga_xAs$ thin films grown at 515°C (Peiró et al. (1993)). The estimated critical temperature T_c=320K is low compared with this result.

Ipatova et al. (1993) calculated the strain energy associated with alloy composition fluctuations in the epitaxial film grown on the (001) substrate taking into account the anisotropy of elastic moduli. In their analysis, composition modulation not only in the direction parallel to the free surface but also in the growth direction was considered. They showed that the minimum strain energy corresponds to the short-wavelength fluctuation parallel to the [100] (or [010]) direction localized near the free surface of the film. It is apparent that the strain energy is reduced with respect to Glas' case since the constraint by the substrate can be ignored. The critical temperature calculated for this "softest" modulation was, however, 430K for $In_{1-x}Ga_xAs$ alloys, which is still low to explain observations.

It is apparent that none of the existing theories based on thermodynamic stability arguments can quantitatively account for all experiments. This suggests that the kinetic factors at the surface of growing films are important in the development of composition modulation.

2.3 Surface morphological instability of strained films

2.3.1 Classical growth modes in heteroepitaxy

In the previous sections it has been tacitly assumed that the growth of a heteroepitaxial film proceeds at constant thickness everywhere. In reality this is not always true. A film deposited heteroepitaxially on a substrate may lose the uniformity of thickness due to a roughening of the surface. This phenomenon may become a major obstacle to practical application of heteroepitaxial structures because surface (or interface when buried by subsequent layers) undulations caused by roughening may provide preferred sites for defect formation e.g. dislocations and stacking faults (Androussi et al. (1995)). The thickness uniformity is considered to be closely related to the growth mode of heteroepitaxy.

The names of the three classical growth modes were assigned by Bauer (1958): Frank-van der Merwe (FM) mode for monolayer-by-monolayer growth (also designated as two-dimensional (2D) growth), Volmer-Weber (VW) mode (also known as three-dimensional (3D) growth) for a growth which is initiated by island formation on a substrate, and Stranski-Krastanow(SK) mode in which the growth starts with the completion of one monolayer or a few monolayers (FM growth) followed by island formation (VW growth) on the flat surface. These three modes are shown schematically in Fig.2.3.1.

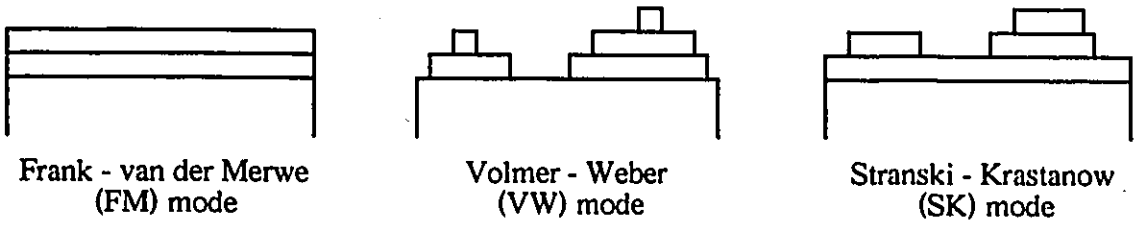

Fig.2.3.1 Three classical growth modes.

A very simple equilibrium criterion for 2D or 3D mode at the initial stage of growth can be derived with reference to Fig.2.3.2 in which a substrate is partly covered by a monolayer (ML) or by a double layer (DL) of film material.

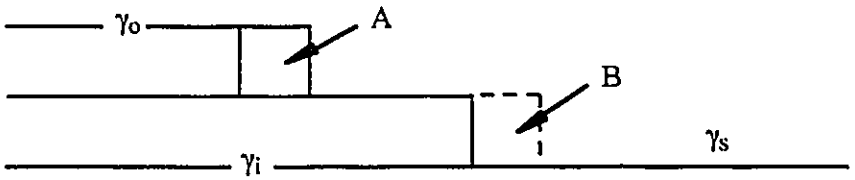

Fig.2.3.2 A substrate partly covered by a monolayer (ML) or by a double layer (DL) of film material. The surface free energies of the film and the substrate are γ_o and γ_s, respectively and their interface energy is designated as γ_i.

We assume that the surface free energies of the film and the substrate are γ_o and γ_s, respectively and their interface energy is γ_i. If the free energy of the system is decreased by transferring material from A to B, 2D(FM) growth is energetically favoured at the initial stage. On the other hand, an increase in the free energy results in 3D(VW) growth:

$$\left.\begin{array}{l} \Delta\gamma = \gamma_o + \gamma_i - \gamma_s \leq 0 \quad \text{favours FM growth} \\ \Delta\gamma > 0 \quad \text{favours VW growth} \end{array}\right\}. \qquad (2.3.1)$$

These simple criteria (2.3.1), referred to as Bauer's criteria are based on many assumptions and simplifications.

(i) Appropriate growth conditions and thermal equilibrium are assumed.

(ii) The surface energies are assumed to be isotropic and the macroscopic value of

the surface energy is assigned to that of a very thin film.

(iii) The surface energy of the film is considered to be unaffected by the proximity to the substrate.

(iv) The effect of lattice-mismatch between the film and the substrate and strain relaxation by misfit dislocations are not considered.

Bauer's criteria (2.3.1) can be rewritten in terms of adhesion energies. If ε_{oo} is the work per unit area required to separate the film material into two halves (the energy of adhesion) and ε_{ss} is the corresponding value for the substrate material, we get

$$\varepsilon_{oo} = 2\gamma_o \quad \text{and} \quad \varepsilon_{ss} = 2\gamma_s. \qquad (2.3.2)$$

The interface energy γ_i, the excess energy after joining the film and substrate is given by

$$2\gamma_i = \varepsilon_{oo} + \varepsilon_{ss} - 2\varepsilon_{os} \qquad (2.3.3)$$

where ε_{os} is the adhesion energy of film and substrate materials. Substituting eq.(2.3.3) into Bauer's criteria, we obtain

$$\left.\begin{array}{ll} \Delta\gamma = \varepsilon_{oo} - \varepsilon_{os} \le 0 & \text{FM growth} \\ \Delta\gamma \ge 0 & \text{VW growth} \end{array}\right\}. \qquad (2.3.4)$$

The rewritten criteria (2.3.4) apply only to the interface between the first film layer and the substrate. After the substrate is covered, the energy difference $\Delta\gamma$ is redefined by $\Delta\gamma = \varepsilon_{oo} - \varepsilon_{os}'$ where ε_{os}' is the bonding strength between the layer covering the substrate and the next overlayer. For the FM growth mode to continue, the condition $\Delta\gamma \le 0$ must be

fulfilled for each overlayer. This will be the case only when the film and substrate materials are very similar. If for some reason $\Delta\gamma$ changes to positive, we have a transition of growth mode from FM to SK (island formation on a flat film). The main reason for this growth mode transition is attributed to the influence of the substrate on the nature of the electronic configurations in the film material, although it is not fully understood in a quantitative manner (van der Merwe (1993)).

The effects of lattice-mismatch and strain relaxation on growth mode transition can be explained using Fig.2.3.3.

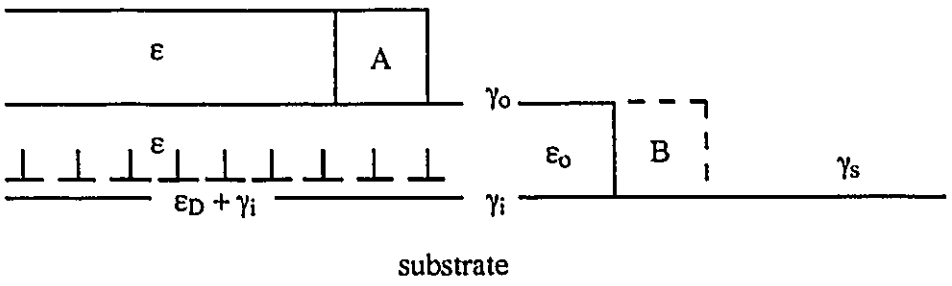

Fig.2.3.3 A substrate partly covered by a monolayer (ML) or by a double layer (DL). The lattice-mismatch between the substrate and the DL is assumed to be above the critical value for introducing misfit dislocations at the interface. The ML is below the critical thickness. The expressions ε_o, ε_D and ε represent the strain energies per unit area, of the ML which is fully strained, of the misfit dislocations and of the residual strain in each monolayer of the DL, respectively.

Consider a case in which a fully strained monolayer (ML) is energetically stable but a double layer (DL) exceeds the critical thickness for the introduction of misfit dislocations at the film /substrate interface, i.e.

$$2\varepsilon + \varepsilon_D < 2\varepsilon_o \qquad (2.3.5)$$

where ε_o is the strain energy density per unit area in a fully strained ML, ε_D is the strain energy due to the misfit dislocations and ε is the residual strain energy density in each monolayer of the DL when the misfit dislocations are present. By transferring material from A to B, we obtain

$$\Delta\gamma = \Delta\gamma_o + 2\varepsilon_o - (2\varepsilon + \varepsilon_D) > \Delta\gamma_o \qquad (2.3.6)$$

where $\Delta\gamma_o$ is the energy term given by eq.(2.3.4). Therefore, the introduction of misfit dislocations tends to promote 3D growth on a flat ML and is considered to trigger the growth mode transition. Some researchers conducted reflection high energy electron diffraction (RHEED) experiments during MBE growth of strained films and reported the simultaneous occurrence of an abrupt reduction in RHEED intensity which indicates the onset of island formation and a change in RHEED streak separation due to the change in the lattice-constant at the growing surface (Elman et al. (1989), Nakao and Yao (1989) , Whaley and Cohen (1990) and Anan et al. (1992)). They considered that the change in the surface lattice-constant was caused by the formation of misfit dislocations at the film(island)/substrate interface and concluded that the transition to SK growth occurred simultaneously with the introduction of misfit dislocations when the strained film exceeded the critical thickness.

However, recent TEM observations of strained films after the onset of island formation show that the films can undergo the transition to island morphology without the help of misfit dislocations (Eaglesham and Cerullo (1990), Guha et al. (1990), Guha et al. (1991), Snyder et al. (1991), Hansson et al. (1992), Androussi et al. (1994), Dutartre et al. (1994)). The islands observed in TEM are dislocation-free up to some size and strong TEM contrast around the islands indicates the existence of local lattice bending (Eaglesham

and Cerullo(1990)). High resolution TEM shows that the relaxation of the lattice towards the unconstrained lattice-constant occurs at the surface of the dislocation-free islands (Guha et al. (1991)). This "elastic relaxation", i.e. relaxation of lattice strain via elastic deformation, is ignored in the classical theory for the 2D to 3D growth mode transition. The interpretation of RHEED experiments which concluded that the growth mode transition and misfit dislocation formation occurred simultaneously should be reexamined because the observed change in RHEED streak spacing might have been caused by elastic relaxation of the lattice at the dislocation-free island surface.

2.3.2 Models of surface morphological instability in strained films

In this subsection, some theoretical approaches to understand the evolution of island-like surface morphology in strained bodies will be reviewed. In order to handle the problem within the range of linear elasticity, the onset of island formation is interpreted as the morphological instability problem of a strained body with a small undulation imposed on its originally flat surface.

Consider first a semi-infinite solid with a flat surface subject to a uniform uniaxial compressive stress in the direction parallel to the surface. This applied stress results in uniform strain throughout the solid and the strain energy density is also uniform. Consider now the same solid but with an undulated surface. When the surface is undulated, the stress distribution in the solid becomes nonuniform. There is an elastic stress relaxation at the peaks of the undulation and a stress concentration at the valleys. In a schematic example Fig.2.3.4, since we assume that the solid is originally compressed, the lattice spacing becomes larger when relaxed. The stress relaxation at the peaks occurs because the peaks are less supported by the surrounding material and are more able to relax toward the stress-free state. In contrast, the valleys become stress concentration sites (Gao (1991)).

The variation in strain energy density formed along the surface drives instability. Similar to the mass transport from regions of high curvature to low curvature, strain energy variation drives mass transport from regions of higher energy density (valleys) to lower energy density (peaks). The peaks grow at the expense of the valleys. This enhances the strain energy variation along the surface and leads to a sustained growth of the undulation.

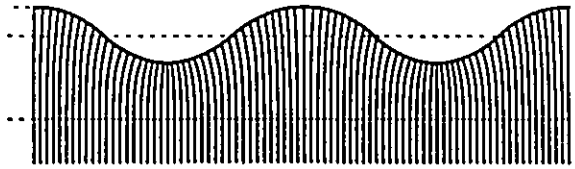

Fig.2.3.4 Schematic representation of nonuniform distribution of lattice distortion in a stressed body with a sinusoidal surface undulation.

Srolovitz (1989) derived approximate expressions for the stress state of a semi-infinite body with a sinusoidally undulated surface under a uniaxial stress σ using Airy's stress function method. For stability analysis, he used Mullins' equation which describes the change in surface profile h(x,t) with time t. When the surface morphological evolution is controlled by surface diffusion,

$$\frac{\partial h}{\partial t} = \frac{D_s \Omega \delta}{kT} \frac{\partial^2 \mu}{\partial s^2} \qquad (2.3.7)$$

where D_s is the surface diffusivity, Ω is the atomic volume, δ is the number of atoms per unit area, kT is the thermal energy, s is the distance along the surface and $\mu(x)$ is the chemical potential including a strain energy density variation along the surface (Mullins (1957)). Assuming that the magnitude of the undulation is much smaller than its

wavelength, Srolovitz concluded that $\lambda_0=\pi E\gamma/\sigma^2$ is the critical wavelength for morphological instability where γ is the isotropic surface energy and E is the Young's modulus. If the wavelength of an undulation is larger than λ_0, the undulation has a positive growth rate.

A more sophisticated approach was conducted by Spencer et al. (1993). They first derived fundamental equations which describe the morphological instability of a growing film. Their theory can evaluate the effects of the growth conditions and of a substrate having different elastic constants from the film, both of which had been ignored in previous theories. They found that the rate of the undulation evolution is very sensitive to the surface diffusivity and a low temperature stabilizes a flat morphology. They also pointed out that elastically stiffer substrates have a stabilizing effect.

Another approach to this instability problem is a static one in which the average elastic energy density in a stressed body with surface undulation is considered without taking account of the film growth or diffusion of matter along the surface (Pidduck et al. (1992) and Grilhe (1993)).

Pidduck et al. (1992) assumed that the strain within the film having a sinusoidal undulation at the surface can be represented as a single value averaged over the film thickness. However, they simply assumed that the strain was a sinusoidal function 180° out of phase with respect to the surface undulation. The calculated critical wavelength above which the average elastic energy density in the undulated film becomes lower than that of the flat film, contains an unknown parameter, i.e. the magnitude of the varying strain. The physical basis of their model is unclear.

Grilhe (1993) estimated the elastic fields in an undulated body by representing them with the elastic fields of imaginary surface dislocations. He derived an appropriate surface

dislocation distribution which satisfies the traction-free condition at the surface and found the critical wavelength $\lambda_0=2\pi\mu\gamma/(1-\nu)\sigma^2$ which is in good agreement with Srolovitz's result. This surface dislocation method was originally developed by Marcinkowski and Das (1974) to approximate the elastic fields around a crack. Although this method may provide quite similar results as the exact solutions, we should note that this theory ignores the singularity of elastic fields at the dislocation position (corresponding to the undulated surface in Grilhe's analysis) and can be justified only when the result shows a good agreement with other more exact methods.

All the theoretical works described so far in this subsection have treated the film as a single component material. Recently, Guyer and Voorhees (1995) expanded the stress driven instability problem of a growing film to an alloy film composed of two species. They assumed that the lattice parameter of the film material is a function of its composition and therefore both misfit strain with respect to the substrate and variation in the film composition induce stresses in the film. In their analysis, the local composition in the film is modified by the variation in local elastic state caused by the development of non-planar film surface morphology. It should be noted that the application of this approach is limited to a system with no spontaneous composition variation when local thermodynamic equilibrium is reached without kinetic barrier. They found that under certain conditions determined by the combination of misfit strain, composition strain and film growth rate, tensile strain can completely stabilize the surface morphology of growing film, whereas, the same magnitude of compressive strain has destabilizing effect. This result is opposite to what we have observed in $In_{1-x}Ga_xAs_yP_{1-y}/InP$ strained system as will be described in Chapter 6. This is because their approach does not include the effect of spontaneous composition modulation occurring in this system.

Chapter 3

Experimental techniques

In this chapter, experimental techniques and related background theories employed in this thesis will be reviewed.

3.1 Molecular beam epitaxy

Molecular beam epitaxy (MBE) is a thin film growth technique in which each element of the film is supplied from a source cell in a form of a beam of atoms or molecules impinging on a substrate in a vacuum chamber with background pressure generally lower than 10^{-10} Torr. In such a high vacuum environment, the mean free path, i.e. the distance travelled by a molecule before colliding with another molecule, is much larger than the spacing between the source cells (evaporation cells or cracker cells) and the substrate. Therefore, molecules evaporated from sources do not experience any chemical or physical reaction until they reach the substrate.

The general features of MBE are summarized below.

(i) Because of the very low growth rate (usually about 1 μm/hr) a very precise control over the film thickness is possible.

(ii) Since the appropriate growth temperature for MBE is usually lower than that of other growth techniques such as metal organic chemical vapour deposition (MOCVD) by about 100°C, the thermal damage to the crystal and the interdiffusion at the heterointerface can be minimized.

(iii) The abrupt composition change at heterointerfaces can be achieved simply by the operation of a mechanical shutter in front of each cell.

(iv) In-situ monitoring of the growth is possible by using reflection high energy electron diffraction (RHEED).

In MBE growth of III-V compound semiconductors such as $In_{1-x}Ga_xAs_yP_{1-y}$ alloys, the sticking coefficients of group III elements (In or Ga) are near unity under appropriate conditions, which means that almost all the group III atoms reaching the substrate are incorporated into the growing film. On the other hand, the sticking behaviour of group V elements (As or P) is more complex because they are usually supplied as beams of dimers (As_2 or P_2) or tetramers (As_4 or P_4). Dimers or tetramers have to be dissociated into atoms before sticking to group III atoms on the surface and some of the group V atoms may recombine into molecules which re-evaporate back into the environment. Molecular beams of dimers are more favourable because dimers have higher sticking coefficient than tetramers. The sticking coefficient of tetramers does not exceed 0.5. Stoichiometry of III-V compounds is achieved by providing a sufficiently large flux of group V molecules so that all group III atoms on the surface can react with group V atoms. The growth rate is controlled by the rate of impingement of group III atoms because the excess group V atoms are usually not incorporated into the film.

The desired In to Ga ratio in $In_{1-x}Ga_xAs_yP_{1-y}$ alloys can be achieved through the control of the group III flux ratio because the sticking coefficients of both In and Ga are close to unity. However, control of the P to As ratio is not as easy due to the fact that incorporation ratio of these two elements are so different and dependent on growth conditions. Since the incorporation of As is more favoured, a higher P/As ratio is necessary in the flux than the designated P/As ratio in the film material (Panish and Sumski (1984), Huet and Lambert (1986), Tappura et al. (1991) and Lambert et al. (1991)).

The control over the P to As flux ratio which is generally very difficult with conventional group V sources using evaporation from solid P and As can be improved by

introducing hydride gases (PH_3 and AsH_3) to generate P_2 or As_2 beams. These hydrides are cracked in a cracker cell heated to 1000°C, following $2MH_3 \rightarrow M_2 + 3H_2$ where M represents P or As. Figure 3.1.1 is a schematic diagram of the McMaster MBE system used for $In_{1-x}Ga_xAs_yP_{1-y}$ thin film growth in this study.

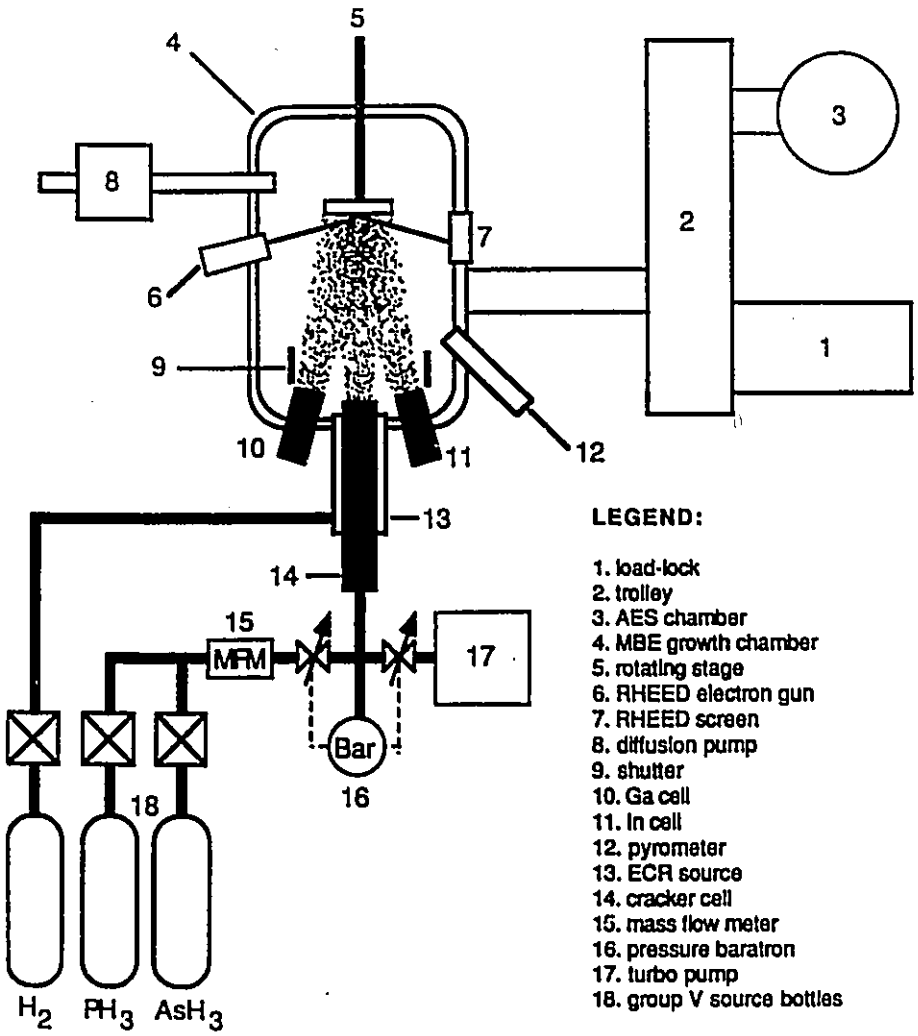

Fig.3.1.1 McMaster MBE system (after LaPierre (1994)).

An InP wafer usually having dimensions of 15×15×0.4mm mounted on a sample holder is first evacuated in the load-lock(1) then transferred to the Auger electron spectroscopy chamber(3) where the wafer is degassed at 350-400°C. After the degassing step, the sample is transferred to the main growth chamber(4) where the temperature is raised to the growth temperature, typically 470°C, under a P_2 overpressure which prevents the preferential evaporation of P from InP wafer. The oxide layer formed on the InP wafer is removed with the help of an electron cyclotron resonance plasma of hydrogen for about 2 minutes (Hofstra et al. (1993)). Usually an InP buffer layer about 500Å thick is deposited first on a substrate to ensure a clean and flat surface for subsequent heteroepitaxial growth. All epitaxial growth is commenced after achieving a clean group V stabilized surface showing a (2×4) streaky RHEED pattern.

3.2 Composition determination of $In_{1-x}Ga_xAs_yP_{1-y}$ alloy films

Since an $In_{1-x}Ga_xAs_yP_{1-y}$ alloy has two degrees of freedom for its stoichiometry, two independent measurements are needed to determine x and y. In this subsection, the composition determination method using the lattice-mismatch measurement from double crystal x-ray diffraction and the bandgap measurement from photoluminescence experiment is reviewed (Macrander and Lau (1991)).

3.2.1 Double crystal x-ray diffraction

Lattice-mismatch was determined by measuring the spacing of (004) peaks with x-ray double crystal diffraction method using Bede Scientific Instruments QC1 double crystal diffractometer. A schematic diagram of the system is shown in Fig.3.2.1.

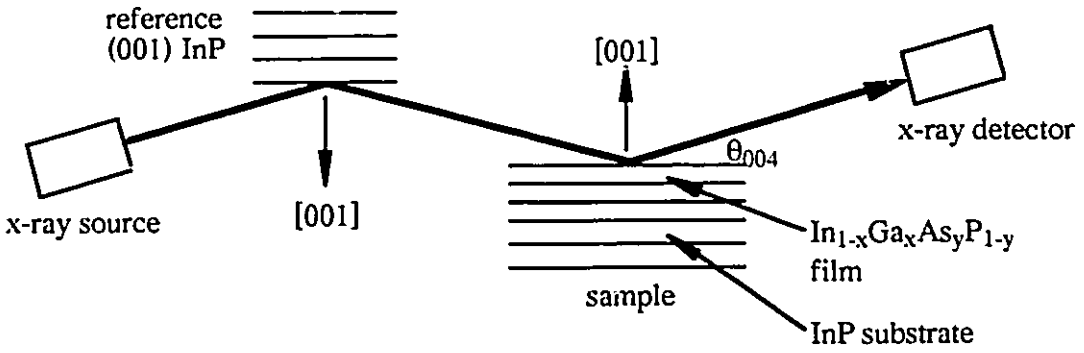

Fig.3.2.1 Double crystal x-ray diffractometer.

The X-rays are first collimated and monochromated by the reference InP single crystal with <001> normal orientation. The sample is illuminated by the monochromated x-ray beam and the diffraction intensity is measured by the x-ray detector. Strong double diffraction occurs when the reference crystal and the sample are set parallel to each other and satisfy the Bragg condition. The Bragg angle θ_{004} for InP (004) planes is 31.68° when we use CuKα_1 x-ray with wavelength 1.541Å. If the $In_{1-x}Ga_xAs_yP_{1-y}$ thin film deposited on the (001) InP substrate has a different (004) plane spacing due to the tetragonal distortion, the second diffraction intensity peak from the thin film can be detected by rotating the sample by a specific angle $\Delta\theta$ from the first parallel position. We can formulate the first and second Bragg conditions as

$$\left.\begin{aligned} 2a_{004}\sin\theta_{004} &= \lambda \quad \text{for InP} \\ 2(a_{004}+\Delta a_{\perp})\sin(\theta_{004}+\Delta\theta) &= \lambda \quad \text{for thin film} \end{aligned}\right\} \qquad (3.2.1)$$

where a_{004} and $(a_{004}+\Delta a_{\perp})$ are the (004) plane spacings for InP and tetragonally distorted $In_{1-x}Ga_xAs_yP_{1-y}$ thin film, respectively. The wavelength of the x-rays is λ. Since $\Delta\theta$ is much smaller than θ_{004} (about 0.01 radian for 1% lattice-mismatch), we obtain

$$\frac{\Delta a_{\perp}}{a_{004}} = -(\cot\theta_{004})\Delta\theta. \qquad (3.2.2)$$

The lattice-mismatch is defined by $\{(a_0+\Delta a)-a_0\}/a_0$ where a_0 and $(a_0+\Delta a)$ are the equilibrium lattice-constants of InP and $In_{1-x}Ga_xAs_yP_{1-y}$ film material, respectively. The lattice-mismatch $\Delta a/a_0$ can be related with the tetragonal strain $\Delta a_{\perp}/a_{004}$ along the [001] direction using

$$\frac{\Delta a}{a_0} = \frac{C_{11}}{C_{11}+2C_{12}}\left(\frac{\Delta a_{\perp}}{a_{004}}\right) \qquad (3.2.3)$$

where C_{11} and C_{12} are the elastic moduli of the film material. Combining eqs.(3.2.2) and (3.2.3), we obtain

$$\frac{\Delta a}{a_0} = -\frac{C_{11}}{C_{11}+2C_{12}}(\cot\theta_{004})\Delta\theta. \qquad (3.2.4)$$

As will be shown, the lattice-mismatch $\Delta a/a_0$ and the elastic moduli C_{11} and C_{12} are functions of composition parameters x and y. Therefore, if the sample rotation angle $\Delta\theta$ is measured, eq.(3.2.4) can be used as one of the equations to determine the film composition.

3.2.2 Photoluminescence

Figure 3.2.2 is a schematic diagram of the McMaster photoluminescence (PL) system used for bandgap measurements.

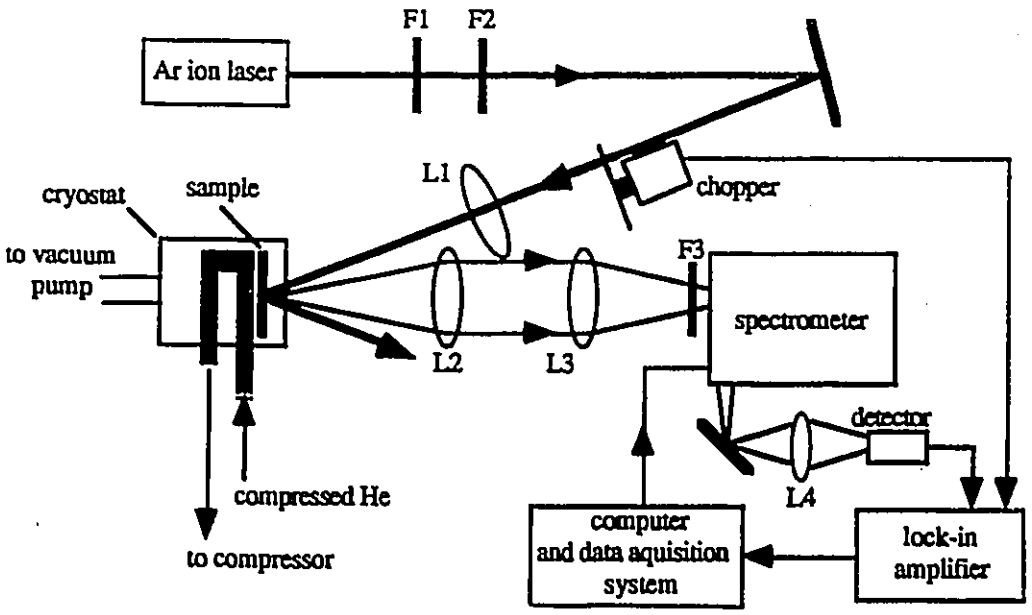

Fig.3.2.2 McMaster photoluminescence system (after LaPierre (1994)).

The sample is excited by a 4880Å Ar^+ laser. Electron-hole pairs in excess of the thermal equilibrium concentration created by exciting photons, may recombine and emit light corresponding to the smallest transition energy between the conduction and valence bands. This phenomenon is called photoluminescence. A mechanical chopper is used to modulate the laser light to increase the sensitivity by lock-in technique. The sample can be cooled using a liquid He cold stage to enhance the PL signal intensity. If we use the peak position

of $In_{1-x}Ga_xAs_yP_{1-y}$ PL spectra as the bandgap $E_g(x,y)$ as conducted by Kuphal (1984), we can estimate the film composition parameters x and y using Kuphal's empirical equation

$$E_g = 1.35 + 0.668x - 1.068y + 0.758x^2 + 0.078y^2 - 0.069xy - 0.322x^2y + 0.03xy^2 \qquad (3.2.5)$$

where E_g is measured in eV. However, eq.(3.2.5) cannot be directly applied to alloy composition determination because it is based on data obtained from lattice-matched samples. For strained films the bandgap shifts due to strain have to be estimated using deformation potential coefficients.

The dependence of the bandgap shift on lattice-mismatch $\Delta a/a_0$ is expressed as

$$\left.\begin{aligned} \Delta E_{lh} &= \{-2a^d(\frac{C_{11}-C_{12}}{C_{11}}) + b^d(\frac{C_{11}+2C_{12}}{C_{11}})\}(\frac{\Delta a}{a_0}) \\ \Delta E_{hh} &= \{-2a^d(\frac{C_{11}-C_{12}}{C_{11}}) - b^d(\frac{C_{11}+2C_{12}}{C_{11}})\}(\frac{\Delta a}{a_0}) \end{aligned}\right\} \qquad (3.2.6)$$

(Asai and Oe (1983)). ΔE_{lh} is the change in the energy gap between the conduction band and the light hole valence band and ΔE_{hh} is that between the conduction band and the heavy hole valence band. Coefficients a^d and b^d are hydrostatic and shear deformation potentials, respectively. The experimentally measured emission energy hν equals the smallest transition energy from the conduction to valence band, which is obtained from

$$\left.\begin{array}{l}(h\nu =)\, E_g + \Delta E_{lh} \quad \text{when } (\Delta a/a_0) \text{ is positive} \\ \text{or} \\ (h\nu =)\, E_g + \Delta E_{hh} \quad \text{when } (\Delta a/a_0) \text{ is negative}\end{array}\right\}. \qquad (3.2.7)$$

As will be shown, the deformation potential coefficients a^d and b^d are functions of the composition parameters x and y. Therefore, if we know whether the $In_{1-x}Ga_xAs_yP_{1-y}$ film is under compression or tension from x-ray diffraction, we can use either of eq.(3.2.7) for composition determination.

3.2.3 Composition determination from x-ray and PL data

From eq.(1.1) the lattice-mismatch ($\Delta a/a_0$) can be written as a function of x and y.

$$\frac{\Delta a}{a_0} = (-0.4176x + 0.1896y + 0.0125xy)/5.8688 \qquad (3.2.8)$$

The elastic moduli C_{11} and C_{12} become

$$\left.\begin{array}{l}C_{11} = 102.2 + 39x - 18.91y - 3.49xy \quad (\text{GPa}) \\ C_{12} = 57.6 + 4.93x - 12.31y + 3.61xy \quad (\text{GPa})\end{array}\right\}. \qquad (3.2.9)$$

The deformation potential coefficients are

$$\left.\begin{array}{l}a^d = 0.35y - 3.25x - 0.52xy - 6.35 \quad (\text{eV}) \\ b^d = 0.20y + 0.35x - 0.25xy - 2.0 \quad (\text{eV})\end{array}\right\}. \qquad (3.2.10)$$

Equations (3.2.4) through (3.2.10) are the complete set of equations to determine x and y

from $\Delta\theta$ and $h\nu$ measured from x-ray diffraction and photoluminescence, respectively. These can be solved using Newton's method.

The constant lattice-mismatch lines for misfits of $\pm 1\%$ and the constant PL wavelength (= constant bandgap energy) lines are drawn in a composition diagram. (Fig.3.2.3)

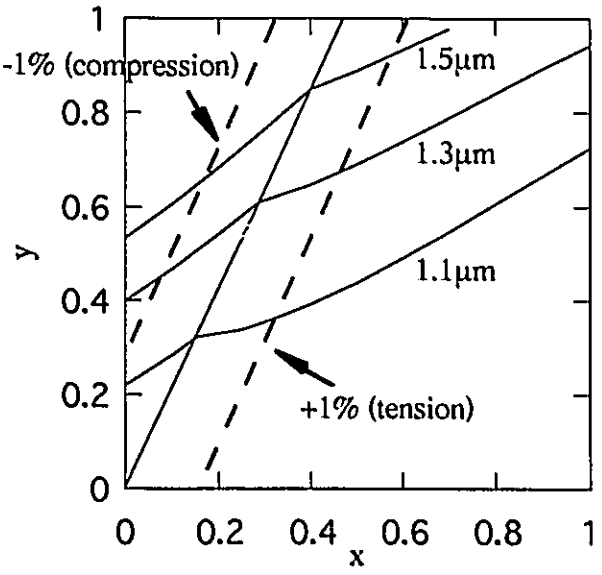

Fig.3.2.3 Constant lattice-mismatch lines and constant PL wavelength lines.

We should note that the constant wavelength lines are kinked at the lattice-match line due to the crossing of the light and heavy hole valence bands.

3.3 Transmission electron microscopy (TEM)

3.3.1 Sample preparation technique

Throughout this research, TEM was most extensively used to characterize growth related phenomena such as misfit dislocations, phase modulation and surface morphology in $In_{1-x}Ga_xAs_yP_{1-y}/InP$ heteroepitaxial systems. For a successful TEM observation, the most important thing is to prepare high quality TEM samples having a wide observable area without severe bending. Three kinds of TEM samples with different geometry were prepared for TEM studies: [1 $\bar{1}$0] cross-section, [110] cross-section and (001) plan-view samples.

After the MBE growth of epitaxial layers on a substrate, preparation of cross-section samples starts from cutting two strips of about $4\times1\times0.4mm^3$ out of a wafer by cleaving along {110} planes (Fig.3.3.1(a)). These strips are glued together with the epitaxial sides face-to-face to make the central part of the cross-section sample. The most critical issue for the preparation of cross-section samples is to select an appropriate glue which has almost the same thinning rate as InP in the final Ar ion-milling stage. For this purpose, I found M-Bond® 610 and EPO-TEK® H22E epoxy glues are appropriate. After the completion of the central part, the "dummy" parts are attached to both sides of the central part to make a "sample raft" of about $4\times4\times1mm^3$ (Fig.3.3.1.(b)). We should note that the normal of the sample raft is the [1 $\bar{1}$0] or [110] direction of the starting wafer. After mechanical thinning of the sample raft to about 0.5mm thickness, a 3mm diameter disc is cut from the raft using an ultrasonic disc cutter. The edge of the disc should be covered with glue to protect the sample from edge chipping. Then the disc is polished down to 200μm thickness (Fig.3.3.1.(c)). The thinned disc is dimpled from both sides using a dimpler with 3μm diamond paste until the centre of the disc is 40-50μm thick and

subsequently polished with 1μm diamond paste to get very smooth surfaces. The final thinning until perforation is conducted using Ar ion-milling with liquid N_2 cold stage. If the thinning rate of the central glue layer is larger or smaller than that of InP, we cannot get a thin area suitable for TEM observation in the region which is very close to the central glue layer. This makes it difficult to characterize phenomena which occur close to the surface of the epi-wafer. Small differences in the thinning rate between InP and the epoxy glue can be adjusted by thinning InP with chemical etching in bromine-methanol solution before ion-milling or by using a two-speed sample rotation stage during ion-milling.

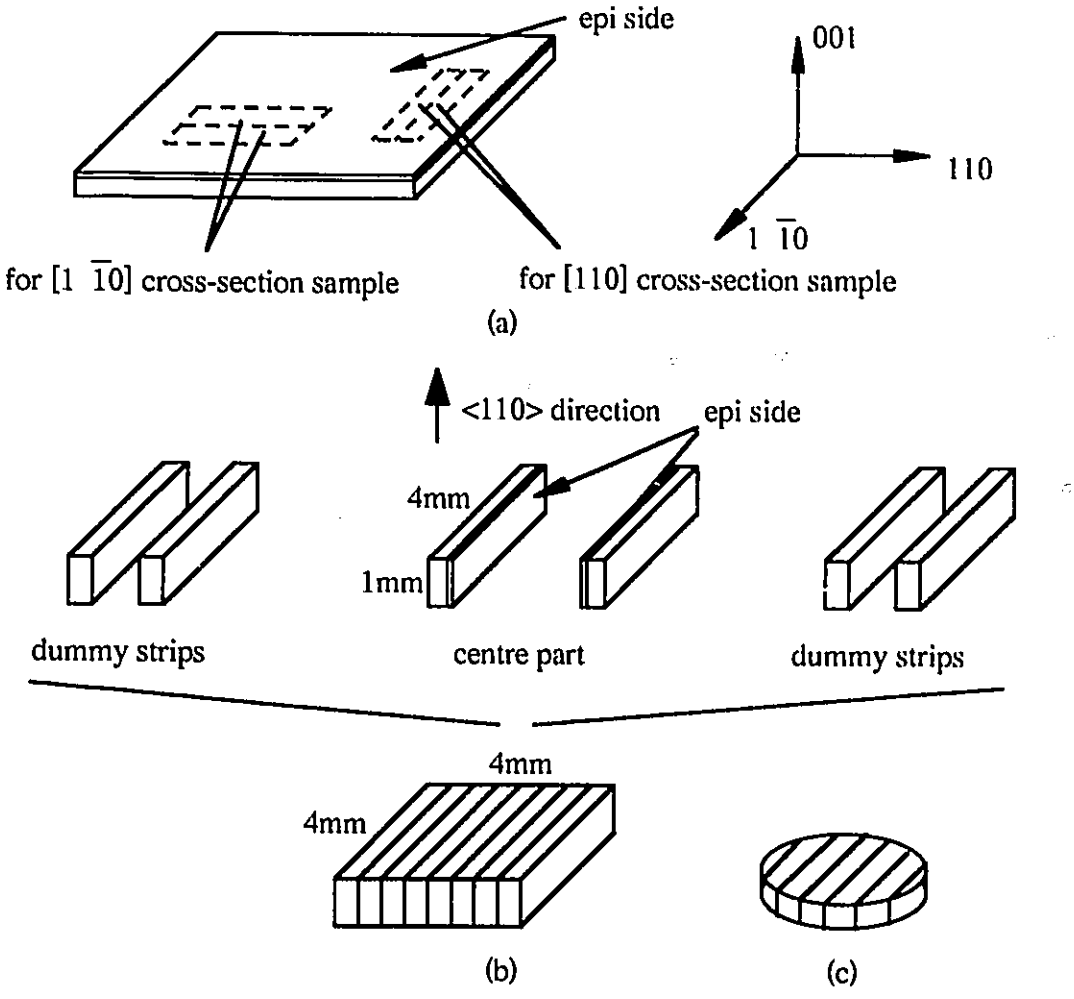

Fig.3.3.1 <110> cross-section TEM sample preparation.

The sample preparation procedures are much simpler for (001) plan-view samples. A small square piece of about $2\times2\times0.4mm^3$ cleaved from the wafer is attached to a Cu grid with the epitaxial surface. The sample is mechanically thinned from the substrate side until the wafer thickness is reduced to 50μm and then polished with 1μm diamond paste. The final thinning can be done using Ar ion-milling or chemical thinning with 2vol.%Br_2 in methanol solution. The yield of plan-view samples is not high because a small bending may result in chipping of the thinned area. This becomes a very serious problem when the $In_{1-x}Ga_xAs_yP_{1-y}$ film has a high strain and severe bending of the thinned region is very likely to occur.

3.3.2 Two-beam dynamical theory for TEM contrast

In this subsection two-beam dynamical theory for TEM image contrast is briefly reviewed. In practice, TEM observation is usually conducted by tilting a sample so that the transmitted beam and one diffraction beam are very intense. Therefore, two-beam theory is an appropriate simplification to explain TEM contrast effects. Two beam images are formed by placing an objective aperture around the spot representing the beam in the direct transmission direction or the spot representing one of the diffracted beams. (In normal operation of the microscope, the incident beam is tilted so that the diffracted beam passes along the optic axis of the microscope in order to avoid abberation of electromagnetic lenses.) When the spot selected in this way is magnified, it forms either a bright field image (direct beam) or a dark field image (diffracted beam). Several theoretical approaches have been proposed to describe the physical process of imaging in TEM on the assumption that only two beams are excited in the crystal. One of these is the kinematical theory (Hirsch et al. (1960)). In this theory, it is assumed that the interaction between the electrons and the crystal is weak, so that only a small number of the incident electrons are scattered into the

diffracted beam. The probability that the electrons in the diffracted beam will be scattered again either into other directions or back into the transmission direction is neglected. This type of theory has the advantage of simplicity and has some applications to very thin crystals or to crystals which are oriented away from the Bragg condition. However, it has been shown to be a poor approximation for many of the observed effects in TEM.

The two-beam dynamical theory, in contrast, takes full account of the scattering of electrons from the main beam into the diffracted beam and the subsequent scattering from the diffracted beam back into the main beam.

Consider an electron beam incident on a crystal which is oriented close to the Bragg condition for a particular set of planes. As the beam passes through the crystal, it will generate a diffracted beam which, in turn, can be re-diffracted back into the incident direction. This dynamic exchange of electrons between the incident and diffracted beams may occur several times if the crystal is thick. Here we define T and S to be the amplitude of the electron waves in the directions of the incident beam and diffracted beam, respectively. Both T and S are the functions of position in the crystal.

The formulation of two-beam dynamical theory (Howie and Whelan (1961)) uses a column approximation in which the crystal is divided into parallel columns, having dynamic exchange of electrons between T and S within a column, but no exchange of electrons between columns. The intensity of a TEM image can be computed point by point (i.e. column by column). This column approximation is reasonable in TEM because Bragg angles involved in electron diffraction are very small.

The equations which are used to describe the two-beam dynamical diffraction of electrons in an isolated column of a crystal are a pair of coupled first-order differential equations,

$$\left.\begin{aligned}\frac{dT}{dZ} &= (\pi i/\xi_0)T + (\pi i/\xi_g)S\exp(2\pi isZ + 2\pi i\mathbf{g}.\mathbf{R}) \\ \frac{dS}{dZ} &= (\pi i/\xi_0)S + (\pi i/\xi_g)T\exp(-2\pi isZ - 2\pi i\mathbf{g}.\mathbf{R})\end{aligned}\right\} \qquad (3.3.1)$$

where g is the diffraction vector normal to the diffracting planes, Z is the coordinate taken down into the column, **R** is the displacement field at depth Z, s is a parameter representing the deviation of the crystal orientation from the exact Bragg condition, ξ_0 is a parameter which represents the mean refractive index of the crystal and ξ_g is a parameter called the extinction distance, which is a measure of the periodic distance in the crystal over which the diffracted beam builds up and dies away.

In order to obtain results from the theory which are in agreement with observation, the quantities $1/\xi_0$ and $1/\xi_g$ in eq.(3.3.1) have to be replaced by the complex quantities $1/\xi_0 + i/\xi_0'$ and $1/\xi_g + i/\xi_g'$, respectively.

$$\left.\begin{aligned}\frac{d\Gamma}{dZ} &= \pi i(1/\xi_0 + i/\xi_0')T + \pi i(1/\xi_g + i/\xi_g')S\exp(2\pi isZ + 2\pi i\mathbf{g}.\mathbf{R}) \\ \frac{dS}{dZ} &= \pi i(1/\xi_0 + i/\xi_0')S + \pi i(1/\xi_g + i/\xi_g')T\exp(-2\pi isZ - 2\pi i\mathbf{g}.\mathbf{R})\end{aligned}\right\} \qquad (3.3.2)$$

The new parameters ξ'_0 and ξ'_g introduce the phenomena of normal absorption and anomalous absorption into the theory. Before contrast calculations are made, eq.(3.3.2) can be reduced to a more convenient form by multiplying T and S by suitable phase factors. This is possible because in image contrast the concern is with electron intensities, i.e. $|T|^2$

and $|S|^2$ at the exit surface of the TEM sample and these are independent of the phase chosen for T and S. Eq.(3.3.2) is rewritten by introducing

$$\left.\begin{aligned} T' &= T\exp(-\pi iZ/\xi_0) \\ S' &= S\exp(2\pi isZ - \pi iZ/\xi_0 + 2\pi i\mathbf{g}.\mathbf{R}) \end{aligned}\right\} \qquad (3.3.3)$$

and by taking a new normalized coordinate $z=Z\pi/\xi_g$

$$\left.\begin{aligned} \frac{dT'}{dz} &= -(\xi_g/\xi_0')T' + (i-\xi_g/\xi_g')S' \\ \frac{dS'}{dz} &= (i-\xi_g/\xi_g')T' + \{-\xi_g/\xi_0' + 2is\xi_g + 2\pi i\frac{d(\mathbf{g}.\mathbf{R})}{dz}\}S' \end{aligned}\right\}. \qquad (3.3.4)$$

In eq.(3.3.4) the ratio ξ_g/ξ'_0 is known as the normal absorption coefficient and will be denoted P. The ratio ξ_g/ξ'_g is the anomalous absorption coefficient and will be denoted Q. The term $s\xi_g$ is a dimensionless measure of the deviation from the exact Bragg condition and will be designated w. By neglecting the phase difference between T and T′, and S and S′, we obtain

$$\left.\begin{aligned} \frac{dT}{dz} &= -PT + (i-Q)S \\ \frac{dS}{dz} &= (i-Q)T + \{-P + 2iw + 2\pi i\frac{d(\mathbf{g}.\mathbf{R})}{dz}\}S \end{aligned}\right\}. \qquad (3.3.5)$$

This is the formulation of the two-beam dynamical theory based on a column

approximation and will be applied to the calculation of image intensity profiles of misfit dislocations in Chapter 4.

Chapter 4

Strain relaxation in $InAs_yP_{1-y}$ ternary alloy films

4.1 Introduction

The study of group IV and III-V semiconductor strained films has been of great interest since the pioneering work by Matthews and Blakeslee (1974 and 1975) demonstrated the importance of the concept of critical thickness in controlling strain or in strain relaxation during film growth or post-growth annealing. In order to exploit the improved electronic or optical properties of semiconductor strained films, it is important to understand how the structure might relax by introducing misfit dislocations (MDs) when the film thickness exceeds the critical thickness. The most extensively studied systems in this field are $Si_{1-x}Ge_x$/(001)Si and $In_{1-x}Ga_xAs$/(001)GaAs or InP.

In the group IV semiconductors strain relaxation is observed to occur predominantly by the nucleation and propagation of (a/2)<011> 60° dislocations gliding on {111} planes provided that the film grows in the two-dimensional layer-by-layer mode rather than the island formation mode. The misfit dislocation densities along the two <110> directions ([1 $\bar{1}$0] and [110]) are approximately the same. On the other hand, in the group III-V compound semiconductor crystals, the rate of strain relaxation is known to be highly anisotropic and in extreme cases only a single set of MDs lying parallel to the easy-glide direction in the film is found. As reviewed in Section 2.1, this anisotropy is usually attributed to the polar nature (α or β) of 60° dislocations contributing to strain relaxation and their different mobilities. In III-V compound semiconductors which have the zinc-blende structure, the easy-glide 60°α dislocations have been reported to be more

mobile than difficult-glide 60°β dislocations by at least one order of magnitude. This factor along with the sense of the pure edge component of the 60° MDs, i.e. the downward or upward direction of extra half-plane required to relieve strain, can explain the observed high anisotropy in strain relaxation. For lattice-mismatched systems such as $In_{1-x}Ga_xAs$ on (001)GaAs and $InAs_yP_{1-y}$ on (001)InP in which the lattice-constant of the deposited film material is larger than that of the substrate, 60° MDs must have a downward extra half-plane to relieve the compressive strain developed in the film. As described in Section 2.1, a large anisotropy is expected in the strain relaxation behaviour between [1 $\bar{1}$0] and [110] directions at the initial stage of strain relaxation. Easy-glide 60°α MDs formed along [1 $\bar{1}$0] direction are expected to have a much higher density than difficult-glide 60°β MDs aligned along [110] direction.

Compared with the extensively studied $In_{1-x}Ga_xAs$ on (001)GaAs or InP systems, there have been relatively few investigations conducted for the strain relaxation in $InAs_yP_{1-y}$ ternary alloy films deposited on InP(001) substrates. The main reason may stem from the fact that a precise control over the ratio of group V elements (As and P) is very difficult with conventional source cells using evaporation from solid As and P in molecular beam epitaxy (MBE). As reviewed in Section 3.1, this difficulty may be overcome by introducing gas-source MBE in which hydride gases (AsH_3 and PH_3) are used to generate molecular beams of As_2 and P_2, although the composition control is still difficult for alloys with high P content, typically $0.8<1-y$, due to the different incorporation behaviour of As and P.

In this chapter studies on the initial stage of strain relaxation in $InAs_yP_{1-y}$ ternary alloy films on InP(001) substrates grown by gas-source MBE are described. Plan-view

and cross-sectional transmission electron microscopy (TEM) and scanning electron microscopy (SEM)/ cathodoluminescence (CL) techniques were employed to investigate the misfit dislocation configurations at the $InAs_yP_{1-y}$/InP interfaces. TEM observations were conducted with a Philips CM12 electron microscope operating at 120kV. CL scanning imaging was performed at room temperature using a Philips 505 SEM. A 20kV primary electron beam was employed to excite the sample surface; the resulting luminescence from the sample surface was detected by an InGaAs detector with a photo-response wavelength extending up to about 1.9 μm. The resolvable point to point contrast due to non-radiative recombination centres was about 0.5 μm with this setup. Misfit dislocations could be readily detected for alloy composition of $y \leq 0.75$, although the dislocation contrast became weaker as y increased due to lower detector sensitivity.

In addition to the expected anisotropic strain relaxation along $[1\ \bar{1}0]$ and [110] directions, new types of misfit dislocations aligned close to [100] and [010] directions were found in $InAs_yP_{1-y}$ films for the first time. From conventional **g.b** analysis in plan-view TEM, they were found to be pure edge in nature, formed probably by slip on {011} planes.

When a misfit dislocation lies parallel and adjacent to one of the free surfaces of a plan-view TEM foil as in the present case, the contrast of the dislocation is significantly modified due to the effect of the free surface. In order to compute intensity profiles of TEM contrast for such MDs, the local lattice rotation associated with dislocations being parallel and adjacent to the free surface of a semi-infinite body was solved in Appendix A using two independent methods, based on the use of the Papkovich-Neuber potential or Head's solution. These were found to provide equivalent results. The computed intensity profiles were useful when we analyzed Burgers vectors of MDs generated from a dislocation source.

4.2 Results

4.2.1 Growth of $InAs_yP_{1-y}$ films

In order to evaluate the uniformity in thickness and composition of $InAs_yP_{1-y}$ films, three samples #345,#343 and #284 were examined using cross-sectional TEM. All samples had the same structure shown in Fig.4.2.1.

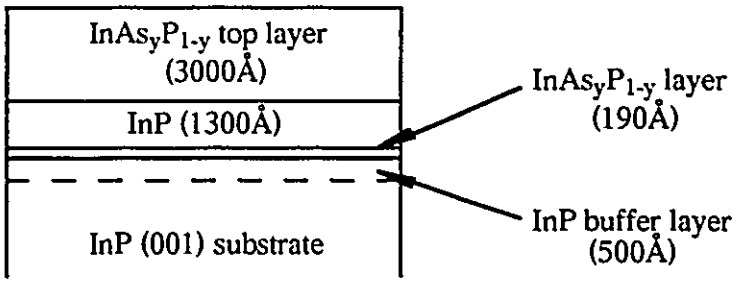

Fig.4.2.1 The structure of #345,#343 and #284.

A 190Å thick $InAs_yP_{1-y}$ layer was grown on the 500Å thick InP buffer layer, followed by a 1300Å thick InP layer and a 3000Å thick $InAs_yP_{1-y}$ top layer. The growth temperature, As content (y) and misfit strain under fully strained state for the 190Å thick layers in these samples are shown in Table 4.2.1.

Table 4.2.1 Growth temperature, As content (y) and misfit strain for 190Å thick $InAs_yP_{1-y}$ layers in samples #345, #343 and #284.

	Growth temperature	As content (y)	Misfit strain
#345	515°C	0.47	-1.50%
#343	460°C	0.49	-1.58%
#284	475°C	0.58	-1.87%

Here we concentrate our attention on the growth features of 190Å thick $InAs_yP_{1-y}$

layers. These layers are about twice as thick as the critical thickness for misfit dislocation introduction. [1 $\bar{1}$0] and [110] cross-sectional TEM photographs are shown only for the sample #343 in Fig.4.2.2 because all 190Å thick layers in these samples exhibited quite similar contrast features.

When observed with g=±004 (Fig.4.2.2(a,c)), strong strain contrast is clearly recognized on both sides of the $InAs_yP_{1-y}$ layer, which can be explained by local lattice bending at the TEM sample surfaces (Perovic et al. (1991)). There is no evidence of either island formation or surface roughening in the layers. The layer thickness is uniform throughout the observable area in cross-sectional TEM. The disturbed contrast is caused by misfit dislocations. In addition, other series of samples (which will be described in 4.2.2) having 190Å thick $InAs_yP_{1-y}$ films ($0.3 \leq y \leq 0.77$) at the top of the structure examined using optical and scanning electron microscopy showed a smooth and featureless surface morphology over a wide range of misfit strain (–0.96% to –2.43%). When the g vector is taken parallel to the interface, that is, g=±220 in [1 $\bar{1}$0] cross-section and g=±2 $\bar{2}$0 in [110] cross-section (Fig.4.2.2(b,d)), the $InAs_yP_{1-y}$ layers exhibited a very weak and uniform contrast which implies that there is no phase modulation in these layers. As will be discussed in Chapter 5, phase modulation can be detected from a periodically varying TEM contrast which appears for g vectors parallel to the interfaces even if the magnitude of the modulation is very small. Furthermore a conventional coherent spinodal calculation (Fig.2.2.2) tells us that the $InAs_yP_{1-y}$ ternary alloy is the most stable against phase separation among all ternary alloys in the $In_{1-x}Ga_xAs_yP_{1-y}$ system. These results strongly suggest that the growth of $InAs_yP_{1-y}$ alloy films proceeded in two-dimensional layer-by-layer mode without phase separation, at least until the initial stage of strain relaxation, even for highly strained films (≤2.5%).

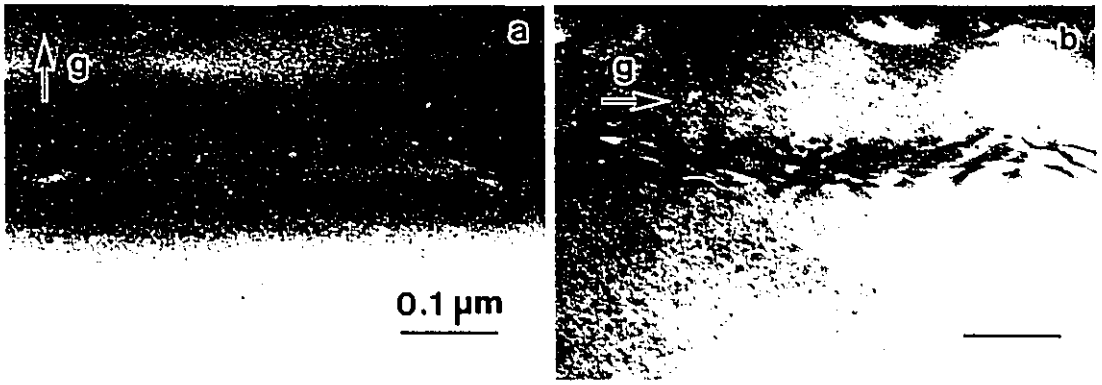

[1 $\bar{1}$0] cross-section

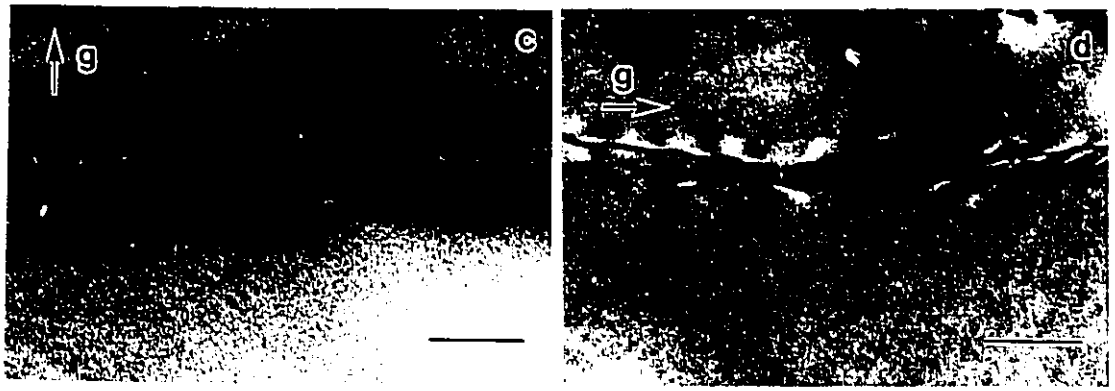

[110] cross-section

Fig.4.2.2 [1 $\bar{1}$0] and [110] cross-sectional bright field (BF) and dark field (DF) TEM of the 190Å thick $InAs_yP_{1-y}$ layer in sample #343. Note that the micrographs were not taken from the same area. The marker is 0.1μm. ((a) g=004 (BF) (b) g=220 (DF) (c) g=004 (BF) (d) g= $\bar{2}$20 (DF))

The micrographs taken for samples tilted about 5° from the exact <110> position (Fig.4.2.2(b,d)) reveal misfit dislocations at the interfaces. Misfit dislocation contrast which makes large angles with the <110> directions are new types of MDs aligned close to <100> directions at the interface and will be described in detail in the following part of this chapter.

4.2.2 Misfit dislocation configuration at $InAs_yP_{1-y}$/InP interfaces

In order to observe the misfit dislocation configuration at the $InAs_yP_{1-y}$/InP interfaces, a series of samples were prepared systematically varying the As content from y=0.30 to 0.77, corresponding to a misfit between –0.96% and –2.43%. The growth was conducted at 470°C with a growth rate of 0.75 μm/hr (2Å/sec) for all the samples. The structure of the sample is shown in Fig.4.2.3. A 190Å-thick $InAs_yP_{1-y}$ film is deposited on the 500Å-thick InP buffer layer. The As content (y), misfit strain under fully strained state and critical thickness for misfit dislocation introduction are summarized in Table 4.2.2.

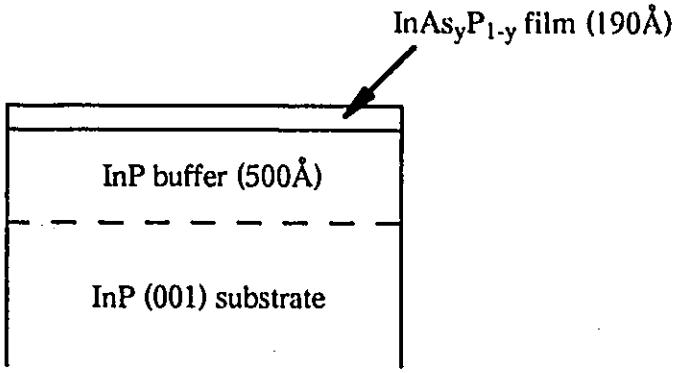

Fig.4.2.3 Structure of the samples examined by CL imaging and plan-view TEM.

Table 4.2.2 Summary of As content (y), misfit strain and critical thickness of 190Å thick $InAs_yP_{1-y}$ films in the samples examined by CL and plan-view TEM.

	As content (y)	Misfit strain	Critical thickness
#427	0.30	-0.96%	106Å
#225	0.48	-1.53%	57Å
#239	0.53	-1.68%	50Å
#424	0.66	-2.09%	36Å
#405	0.75	-2.37%	30Å
#428	0.77	-2.43%	29Å

These samples were examined using SEM/CL imaging technique from the epilayer surface and plan-view TEM from the substrate side. A variety of different misfit dislocations were found by CL and TEM. In the following an abbreviated form is adopted to describe these dislocations; e.g. [1 $\bar{1}$0] or [100] MDs is used for misfit dislocations lying along [1 $\bar{1}$0] or [100] direction.

CL images for #225(y=0.48), #424(y=0.66) and #405(y=0.75) are shown in Fig.4.2.4. Clear dislocation contrast is observed in these CL images. We should note the possibility that straight contrast in the CL images may correspond to several dislocations gliding on a set of parallel planes, due to the low image resolution of this technique. By varying the misfit strain in the films with their thickness fixed at 190Å, a transition in the strain relaxation stages is captured in Fig.4.2.4.

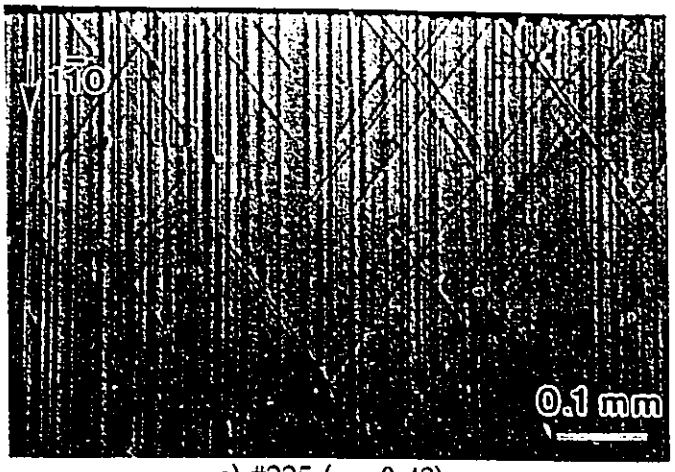

a) #225 (y = 0.48)

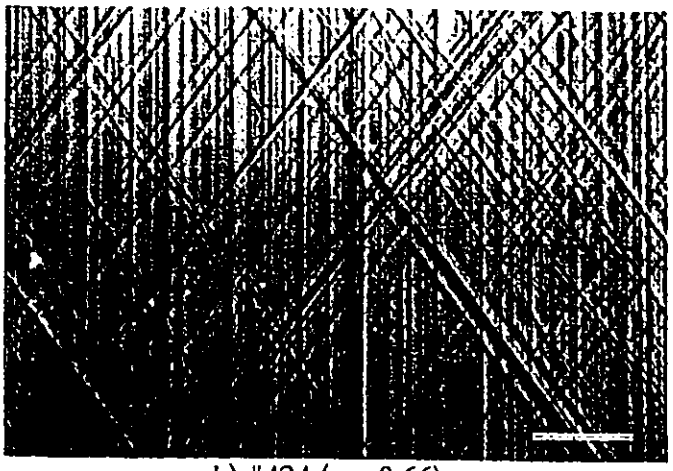

b) #424 (y = 0.66)

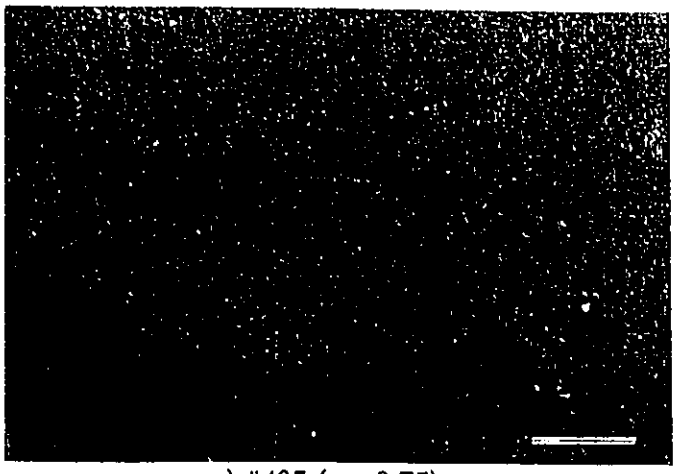

c) #405 (y = 0.75)

Fig.4.2.4 CL images for samples #225, #424 and #405. The marker is 0.1mm.

The initial relaxation occurs by the propagation of α dislocations along the easy-glide direction [1 $\bar{1}$0]. This accounts for the high density of [1 $\bar{1}$0] traces. Relaxation of the film in the orthogonal [110] direction requires dislocation glide on the difficult-glide {111} slip planes. Apparently this is not a favourable glide system in $InAs_yP_{1-y}$ films, since only very short dislocation segments are observed in the [110] direction (Fig.4.2.4 (a)). Instead, as the CL images clearly demonstrate, strain relaxation of the film along the [110] direction involves the activation of fresh dislocation sources lying at the centre of each "cross". Each arm of the cross makes an angle of about ±38° with the [1 $\bar{1}$0] direction, i.e. it runs close to the exact [100] or [010] directions. In the following text, these new types of MDs are going to be termed (near-)<100> MDs. Near-<100>MDs become more prevalent as the As content increases. The low contrast of the CL image for #405 (y=0.75) is caused by a lower detector sensitivity for larger wavelength range.

In order to characterize the new types of MDs lying close to <100> directions, plan-view TEM observation was conducted. Near-<100> MDs were observed in all samples except for #427 (y=0.30) in which no dislocations were found. The <100> MDs showed a fine-scale zigzag configuration. They were composed of both <110> MD segments and near-<100> MD segments which overall make an angle of about ±40° with the [1 $\bar{1}$0] direction. The misfit dislocation configuration in #405 (y=0.75) is shown in Fig.4.2.5. We can clearly recognize four sets of MDs lying along easy-glide [1 $\bar{1}$0], difficult-glide [110] and near-[100] and [010] directions. Stereo microscopy confirmed that all dislocations lie at the $InAs_yP_{1-y}$ interface. Each dislocation except those parallel to the g vector is associated with characteristic dark-light-dark or light-dark-light diffraction contrast. This contrast is caused by the modified displacement fields of MDs which are

parallel and adjacent to one of the free surfaces of a plan-view TEM foil. This contrast feature will be discussed in Section 4.3 and used to analyze Burgers vectors of MDs generated from a source structure.

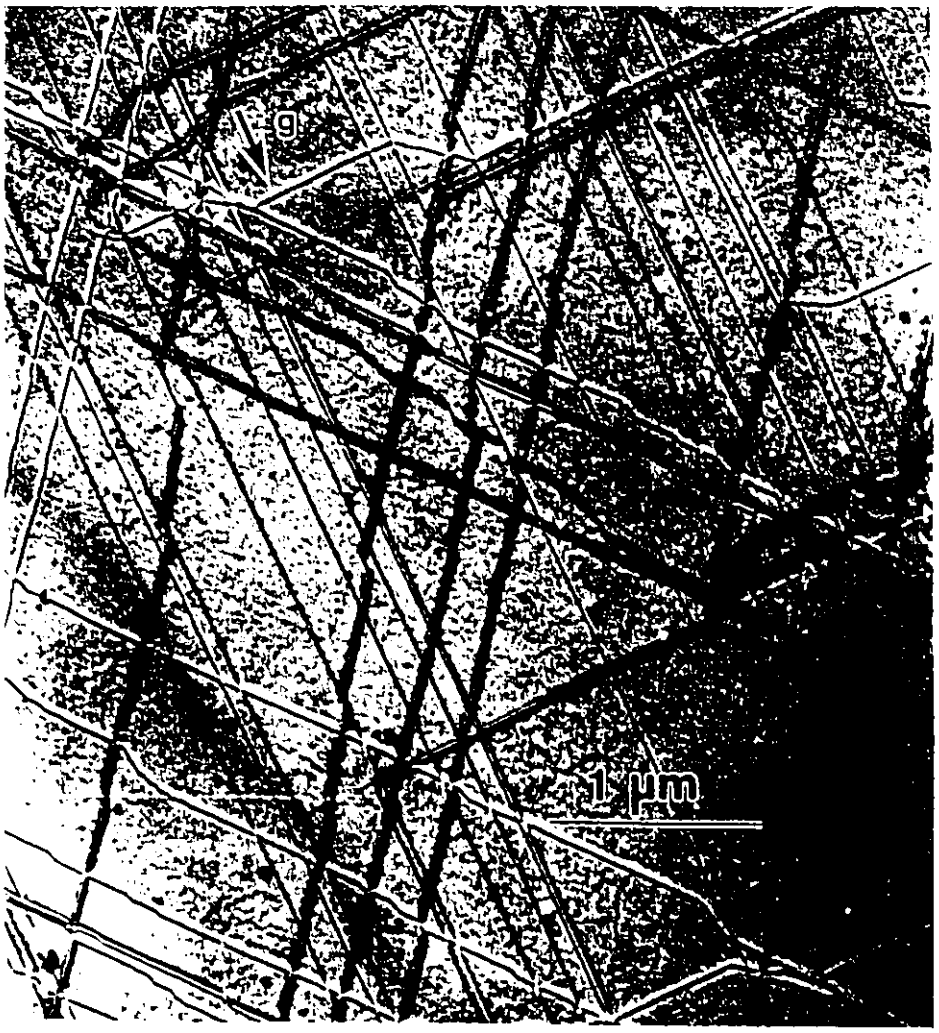

Fig.4.2.5 Misfit dislocations in #405 (y=0.75) observed in bright field plan-view TEM (g=2 $\bar{2}$0).

The near-<100>MDs become almost invisible when g vector is taken (nearly) parallel to the dislocation direction as shown in Fig.4.2.6. Only weak residual contrast is recognized when g=040.

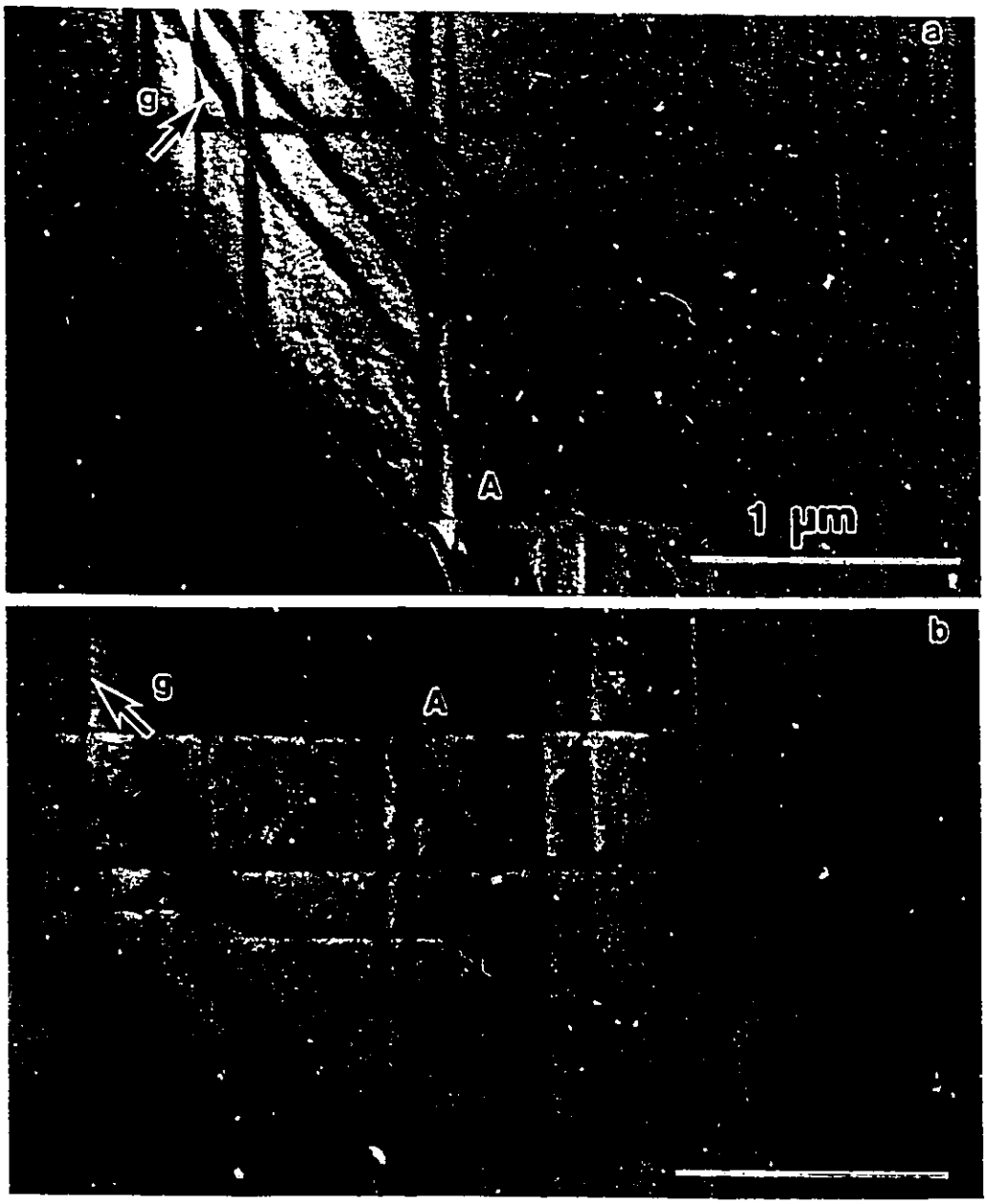

Fig.4.2.6 Bright field images of #405 (y=0.75) taken with g= $\bar{4}00$ (a) and g=040 (b). The mark "A" designates the same position in each image. The marker is 1μm.

From this simple **g.b** analysis it is suggested that these new types of MDs are near-pure edge in nature. If we assume that the Burgers vectors of these dislocations are (a/2)<011> type, the corresponding slip planes defined by the normal **b×l** are {011} planes. Schematic representations of both the "conventional" and "new" type slip systems are shown in Fig.4.2.7.

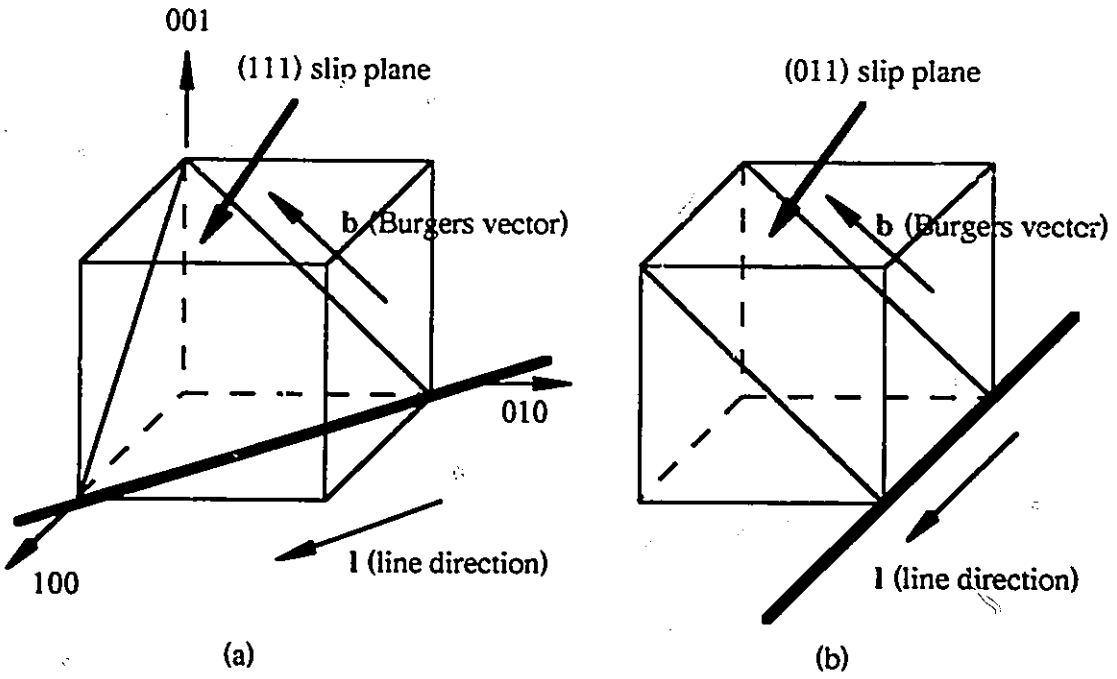

Fig.4.2.7 Schematic representation of conventional {111} slip (a) and new {011} slip (b).

In this example [1 $\bar{1}$0] and [100] MDs are formed on the interface as a result of slip on (111) and (011) planes, respectively. The MDs are represented by thick lines and their Burgers vectors and line directions are taken so that these dislocations can compensate the

compressive strain in the deposited film. Four possible slip systems acting on {011} planes in compressively strained films are listed in Table 4.2.3.

Table 4.2.3 Possible {011} slip systems in compressively strained films.

Along [100]	Slip plane	Burgers vector
	(01 $\bar{1}$)	(a/2)[0 $\bar{1}$ $\bar{1}$]
	(0 $\bar{1}$ $\bar{1}$)	(a/2)[0 $\bar{1}$1]
Along [010]	(10 $\bar{1}$)	(a/2)[101]
	($\bar{1}$0 $\bar{1}$)	(a/2)[10 $\bar{1}$]

The inverse of the average dislocation spacing 1/S for [1 $\bar{1}$0], [110] and <100> ([100] and [010]) MDs determined from plan-view TEM images as a function of the As content (y) is plotted in Fig.4.2.8. This plot can be interpreted as a measure of the strain relaxation. It was not easy to determine large and irregular dislocation spacings for [110] and <100> MDs in low As (y<0.6) samples. The data points which were determined from a small number of measurements (less than three) are parenthesized in this figure. The difference in the dislocation spacings among [1 $\bar{1}$0], [110] and <100> MDs decreases as the strain relaxation progresses. However, in all cases, the strain was only partially relaxed in these as-grown structures, since even in the highest strained sample (y=0.79) only about 10% of the original elastic misfit strain has been relaxed by misfit dislocations. This is

associated with the kinetic limitation to strain relaxation which depends on the rate of dislocation glide and activation of suitable sources in the material.

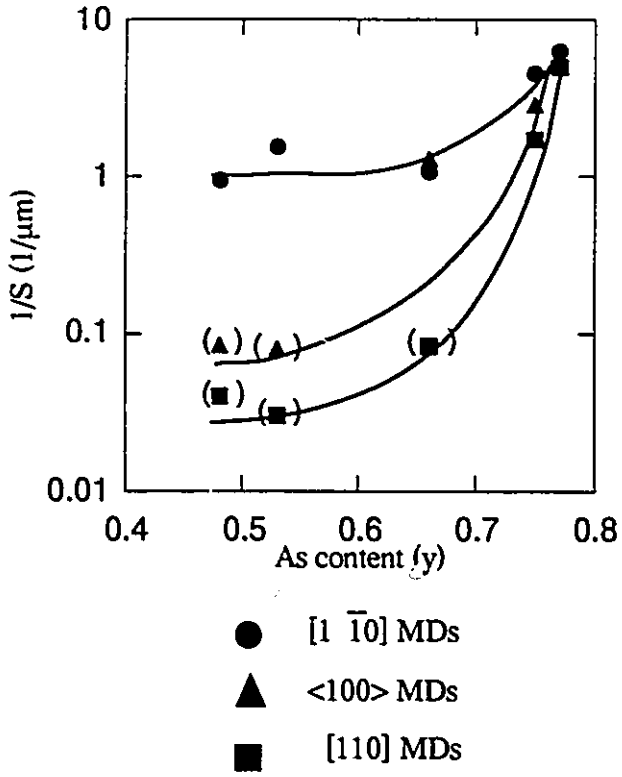

Fig.4.2.8 Plot of inverse dislocation spacing (1/S) for [1 $\bar{1}$0], [110] and <100> misfit dislocations determined from plan-view TEM. Parentheses are applied to data points which were determined from small number of measurements (less than three).

4.3 Discussion

4.3.1 <100> misfit dislocations in other strained systems

Recently, misfit dislocations lying along <100> directions at (001) interfaces have been observed using TEM in other compressively-strained heterostructures such as GaAs/$In_{0.1}Ga_{0.9}As$/GaAs (Kightley et al. (1991)), GaAs/$In_{0.25}Ga_{0.75}As$/GaAs (Zou et al. (1994)), (Al)GaAs/$In_{1-x}Ga_xAs$/GaAs (Bonar et al. (1990 and 1992)) and $Ge_{1-x}Si_x$/Si (Albrecht et al. (1993)). They all reported misfit dislocations running close to the <100> directions with near-pure edge character. Because pure edge dislocations are more effective in relieving strain than 60° dislocations, strain relaxation via pure edge dislocations is energetically more favourable. However, since {011} planes which correspond to the glide plane for near-pure edge misfit dislocations are not the conventional slip planes in zinc-blende structures, some of the above researchers claimed that the new types of <100> MDs were formed by a climb mechanism. Kightley et al. (1991) speculated that a pure edge dislocation segment threading through the strained layer expanded into it through climb, forming a pair of pure edge dislocation dipoles at the top and bottom interfaces. Zou et al. (1994) considered that such threading segments were initially locked at the interface and subsequent climb was triggered when the growth temperature was increased from 500°C ($In_{0.25}Ga_{0.75}As$) to 600°C (GaAs cap). In the former example, a pair of <100> misfit dislocation segments at the top and bottom interfaces seen in their micrographs are relatively short (<0.5μm), forming a dislocation dipole connected by a threading segment. These short dislocation dipoles may have been formed by climb.

On the other hand, Bonar et al. (1992) reported that the <100> MDs propagated with velocities of the order of μm/sec at 450°C and tens of μm/sec at 600°C when annealed in a TEM and concluded that such high dislocation velocities were due to glide rather than climb. In the present $InAs_yP_{1-y}$/InP system, as shown in the CL image Fig.4.2.4(a), some

of the arms of <100> MDs expanding from dislocation sources exceed 0.2mm. If we assume that these arms started expanding when the layer thickness reached the critical thickness of 57Å, the average propagation velocity of the <100> MD arm can be estimated as about 3μm/sec at the growth temperature of 470°C. This value is in good agreement with Bonar et al. (1992).

Albrecht et al. (1993) calculated critical thicknesses for various possible slip planes such as {011}, {100} and {113} taking into account the Peierls stresses for these planes. They concluded that {011} slip may occur if the strain is considerably high, typically larger than 2.5%. In our example, the {011} slip seems to have been activated even when the misfit strain was relatively small (1.53% compression for #225). However, I think that the possibility of the {011} slip mechanism in $InAs_yP_{1-y}$ films is not in conflict with this prediction because, at the present stage, there is no reliable data for Peierls stresses in III-V semiconductor crystals. The formula for Peierls stresses used by Albrecht et al. was originally developed for metal crystals. In the following discussion, it is assumed that the new types of <100> MDs were formed by {011} slip mechanism as suggested from their high mobility.

4.3.2 Diffraction contrast from misfit dislocations

As clearly seen in the plan-view TEM photographs, characteristic dark/light diffraction contrast is associated with each misfit dislocation which is parallel and adjacent to one of the free surfaces of the TEM foil. It is helpful to analyze such diffraction contrast for determining the Burgers vectors of misfit dislocations operating from cross-shaped source structures.

Two independent calculations starting from the Papkovich-Neuber potential method (Weeks et al. (1968)) and Head's solution (Head (1953)) have been used in Appendix A to

find the modified local lattice rotation associated with a dislocation in a semi-infinite body. The plan-view observation of the $InAs_yP_{1-y}$/InP interfaces was conducted from the substrate side only; that is, the misfit dislocations lay close to the bottom surface of the foil. For a typical TEM foil used in this study, prepared for plan-view imaging by thinning from the substrate side only, the foil thickness is in the range of $3\text{-}6\xi_{220}$ and the dislocation lies at about $0.36\xi_{220}$ from the bottom surface of the foil. ξ_{220} is the extinction distance of the 220 reflection, estimated to be 530Å for 120kV electrons in InP. For this geometry, both Papkovich-Neuber method and Head's solution which assume the specimen is a semi-infinite body, should provide a reasonable approximation to solve the local lattice rotation caused by a misfit dislocation, as long as the dislocations at the interface are not too closely spaced. Both methods were confirmed to provide the equivalent result. The derived expressions for $d/dx(\mathbf{g}.\mathbf{R})$ (see Appendix A) were used in the two-beam dynamical theory for diffraction contrast calculation (Howie and Whelan (1961), see Section 3.3), assuming both InP substrate and $InAs_yP_{1-y}$ are elastically isotropic with Poisson's ratio $\nu=0.284$ which is the Voigt average for InP. For image intensity computation the normal and anomalous absorption coefficients P and Q in eq.(3.3.5) were taken as 0.1 and all quantities with the dimension of length were normalized by the extinction distance ξ_{220}. For numerical integration of a pair of differential equations (eq.(3.3.5)) to obtain bright field and dark field image intensities $|T|^2$ and $|S|^2$, respectively, a computer program given by Head et al. (1973) was modified for a dislocation parallel to the TEM foil surface which could not be handled by the original program.

Two types of misfit dislocations are considered; one is the usual 60° dislocation running parallel to <110> directions and the other is the near pure edge dislocation aligned

close to <100> directions at the (001) interface.

As already described in section 2.1, the 60° dislocations which relax the compressive strain in the $InAs_yP_{1-y}$ films can slip on both (111) and ($\bar{1}$ $\bar{1}$1) planes. The resulting misfit dislocations at the interface lies along the easy-glide [1 $\bar{1}$0] direction. There are two possible Burgers vectors for each slip plane, that is, **b**=(a/2)[0 $\bar{1}$1] and (a/2)[$\bar{1}$01] for (111) slip and **b**=(a/2)[$\bar{1}$0 $\bar{1}$] and (a/2)[0 $\bar{1}$ $\bar{1}$] for ($\bar{1}$ $\bar{1}$1) slip. Each Burgers vector can be resolved into a screw component $\mathbf{b}_s$, an edge component $\mathbf{b}_1$ which is parallel to the free surface and a second edge component $\mathbf{b}_2$ which is perpendicular to the free surface. For [1 $\bar{1}$0] misfit dislocations, the following decompositions are found:

<u>(111) slip</u>

(a/2)[0 $\bar{1}$1] = (a/4)[1 $\bar{1}$0] + (a/4)[$\bar{1}$ $\bar{1}$0] + (a/2)[001]

(a/2)[$\bar{1}$01] = (a/4)[$\bar{1}$10] + (a/4)[$\bar{1}$ $\bar{1}$0] + (a/2)[001]

<u>($\bar{1}$ $\bar{1}$1) slip</u>

(a/2)[$\bar{1}$0 $\bar{1}$] = (a/4)[$\bar{1}$10] + (a/4)[$\bar{1}$ $\bar{1}$0] + (a/2)[00 $\bar{1}$]

(a/2)[0 $\bar{1}$ $\bar{1}$] = (a/4)[1 $\bar{1}$0] + (a/4)[$\bar{1}$ $\bar{1}$0] + (a/2)[00 $\bar{1}$]. (4.3.1)

If the operating reflection **g** is perpendicular to the dislocation line, e.g. **g**=±220 for a 60°α dislocation, the screw component does not contribute to the diffraction contrast and an identical image is found for either dislocation on the same slip plane. Figure 4.3.1 (a,b) show typical dark field TEM images of a 60° α dislocation when the **g** vector is taken to be 220 or $\bar{2}$ $\bar{2}$0, respectively.

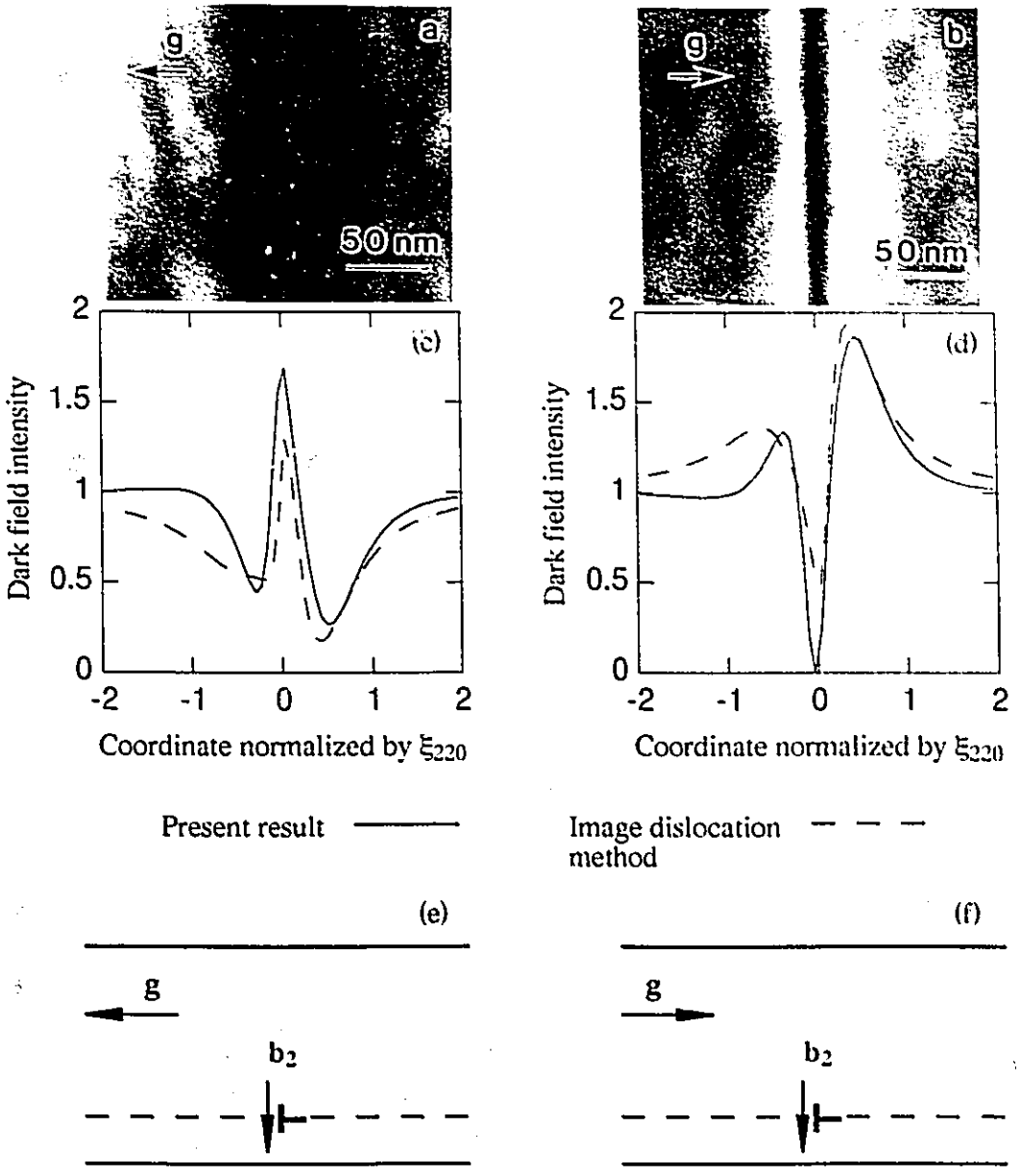

Fig.4.3.1 Dark field images of a 60°α dislocation showing reversal of contrast from (a) g=220 to (b) g= $\bar{2}\ \bar{2}0$ conditions. The computed image contrast (solid lines in (c) and (d)) based on the present calculation shows a good agreement with the experimental images, while the image dislocation method leads to a poorer match. The sense of the edge component $\mathbf{b}_2$ relative to g defines the nature of the dark-light-dark (e) or light-dark-light contrast (f) seen in the dark field image.

The sample in Fig.4.3.1 is oriented at the exact Bragg condition (w=0) and the foil thickness is about $4\xi_{220}$. A dark-light-dark or light-dark-light contrast is associated with the dislocation, which reverses with $\pm\mathbf{g}$ diffraction vectors. We should note that the contrast is asymmetric with the dark or light side bands having different widths. The solid lines in Fig.4.3.1 (c,d) designated as "Present result" are the computed dark field intensity profiles based on the calculations in Appendix A which take into account the effect of the free surface adjacent to the misfit dislocation in a rigorous manner. The image intensity is normalized by the background intensity calculated $10000\xi_{220}$ away from the dislocation. Figure 4.2.1(e,f) represents the orientation of the edge component $\mathbf{b}_2$ of the dislocation with respect to the g vector when seen along the dislocation line. A misfit dislocation close to the bottom surface of the foil displays a light-dark-light contrast in the dark field image when the g vector points towards the extra half-plane of the edge component $\mathbf{b}_2$ as in Fig.4.2.1(f). The bright field image is complementary to the dark field image. The slip plane of the misfit dislocation in Fig.4.3.1 is determined to be (111), i.e. the Burgers vectors of this 60°α dislocation is (a/2)[0 $\bar{1}$1] or (a/2)[$\bar{1}$01].

Following the method first suggested by Howie and Whelan (1962), the TEM contrast using the image dislocation method was also calculated. A 60° image dislocation was placed at the mirror symmetry position with respect to the free surface and the theoretical dark field intensity profile was computed for the modified displacement field. As mentioned in Appendix A, unlike the case of a pure screw dislocation, a traction at the free surface can not be compensated by a simple image dislocation method for a pure edge dislocation. The dashed lines in Fig.4.3.1(c,d) represent the profiles calculated by the image dislocation method. It is clear that the present calculation exhibits narrower profiles and provides a better match with the experimental images.

For **g** vectors perpendicular to the dislocation line direction, the TEM diffraction contrast is determined by the combination of $\mathbf{g}.\mathbf{b}_1$ and $\mathbf{g}.\mathbf{b}_2\times\mathbf{l}$ in eq.(A42). The calculated image intensity profiles of [1 $\bar{1}$0] MD with **b**=(a/2)[0 $\bar{1}$1] or (a/2)[$\bar{1}$01] ((111) slip) for **g**=±220 becomes equivalent to the profiles of [110] MD with **b**=(a/2)[0 $\bar{1}$1] or (a/2)[101] (($\bar{1}$11) slip) for **g**=± $\bar{2}$20 diffraction, because in both cases the values of $\mathbf{g}.\mathbf{b}_1$ and $\mathbf{g}.\mathbf{b}_2\times\mathbf{l}$ are the same, $\mp$1 and ±√2, respectively. Similarly, the profiles of [1 $\bar{1}$0]MD with **b**=(a/2)[$\bar{1}$0 $\bar{1}$] or (a/2)[0 $\bar{1}$ $\bar{1}$] (($\bar{1}$ $\bar{1}$1) slip) for **g**=±220 are equivalent to [110] MD with **b**=(a/2)[10 $\bar{1}$] or (a/2)[0 $\bar{1}$ $\bar{1}$] ((1 $\bar{1}$1) slip) for **g**= $\bar{2}$20 since both cases have $\mathbf{g}.\mathbf{b}_1$= $\mp$1 and $\mathbf{g}.\mathbf{b}_2\times\mathbf{l}$ = $\mp$√2.

Similar contrast effects are observed for the new types of misfit dislocations with near-pure edge character under {220} type diffraction conditions where the **g** vectors make an angle of about 45° with the dislocation line. Figure 4.3.2(a,b) are bright field TEM images of a near-edge dislocation aligned close to the [010] direction under **g**=± $\bar{2}$20. These micrographs were again taken at a relatively thick region of the sample (~$4\xi_{220}$) with the exact Bragg condition (w=0). The contrast behaviour is well explained by the simulated intensity profiles (solid lines in Fig.4.3.2(c.d)). The dark-light-dark or light-dark-light features are less pronounced than the 60° dislocation images. For comparison, the image intensity profiles computed using a simple image dislocation method are shown as dashed lines in Fig.4.3.2(c,d). Again, the image dislocation method shows poorer matching, since the dark/light triple feature is almost lost. The Burgers vector of this near-edge dislocation is determined as (a/2)[10 $\bar{1}$].

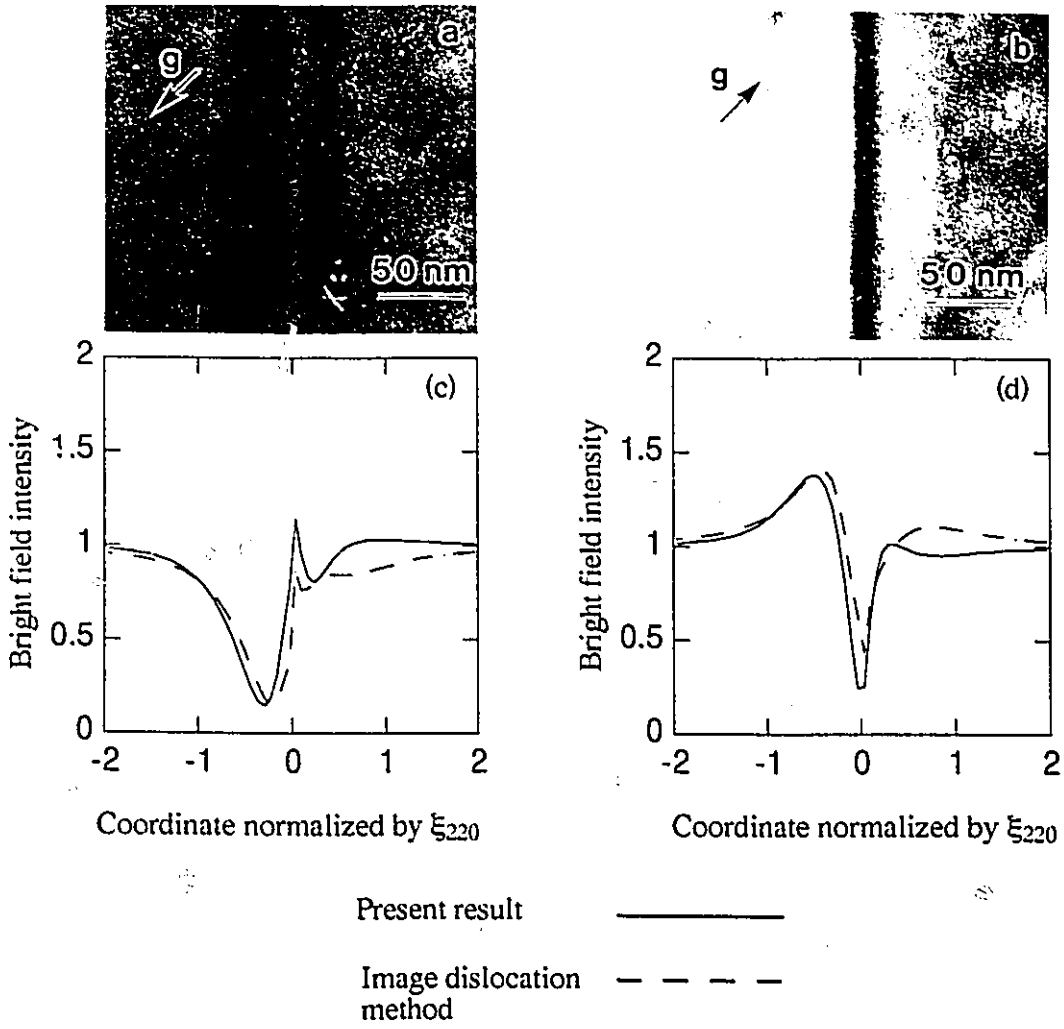

Fig.4.3.2 Experimental (g= $\bar{2}20$ (a) and g=2 $\bar{2}0$ (b)) and computed (c,d) bright field images of a misfit near-edge dislocation aligned close to [010] direction. The solid lines are based on the present calculation showing good agreement with the experimental image, while the image dislocation method leads to a poorer match.

The image intensity profile of a near edge misfit dislocation is determined by the combination of $\mathbf{g}.\mathbf{b}_s$, $\mathbf{g}.\mathbf{b}_1$ and $\mathbf{g}.\mathbf{b}_2\times\mathbf{l}$ terms in eq.(A42), although the effect of the $\mathbf{g}.\mathbf{b}_s$ term is very small. Considering the small angle deviation from the exact <100> direction, typically 5°, the equivalence of misfit dislocation images of these near-<100> MDs are summarized below;

(1) The images of [100] MD with $\mathbf{b}=(a/2)[0\ \bar{1}1]$ under $\mathbf{g}=\pm 220$ (or $\mathbf{g}=\pm\ \bar{2}20$) are equivalent to those of [010] MD with $\mathbf{b}=(a/2)[101]$ under $\mathbf{g}=\ \bar{+}220$ (or $\mathbf{g}=\pm\ \bar{2}20$).

(2) The images of [100] MD with $\mathbf{b}=(a/2)[0\ \bar{1}\ \bar{1}]$ under $\mathbf{g}=\pm 220$ (or $\mathbf{g}=\pm\ \bar{2}20$) are equivalent to those of [010] MD with $\mathbf{b}=(a/2)[10\ \bar{1}]$ under $\mathbf{g}=\ \bar{+}220$ (or $\mathbf{g}=\pm\ \bar{2}20$).

For both 60° and near-edge dislocations the characteristic contrast observed with {220} reflections is unaffected by the total thickness of the sample as long as the observations are conducted in a relatively thick region of the TEM foil ($>3\xi_{220}$). In addition, the calculations show that the width of the dislocation image is virtually unchanged when the thickness of the foil is varied over a wide range ($3\text{-}6\xi_{220}$) as presented in Fig.4.3.3. In this example, simulated dark field image intensities of a 60° α dislocation are shown for three TEM foil thickness, 3,4 or $6\xi_{220}$ under the same diffraction condition. We note that the dark-light-dark feature is enhanced as the foil thickness is decreased while the width of the dislocation image is virtually unchanged.

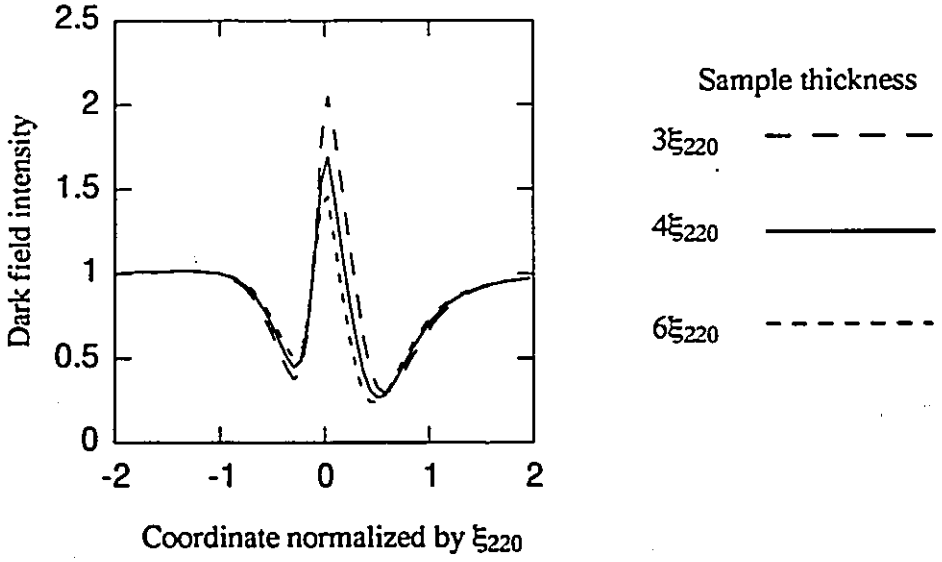

Fig.4.3.3 Dark field image intensity profiles of a 60° α dislocation in TEM foils with thickness 3,4 or $6\xi_{220}$. The diffraction vector **g**=220 and the Burgers vector **b**=(a/2)[0 $\bar{1}$1] or (a/2)[$\bar{1}$01] ((111) slip) were used.

4.3.3 Analysis of dislocation sources

The image intensity analysis can be applied to characterize the Burgers vectors of the dislocations generated at the cross-shaped dislocation sources. Figure 4.3.4 is a dark field image (**g**= $\bar{2}20$) of the dislocations ejected from a source in the sample #225. The coordinate system used to define the orientation of the foil is marked in the figure. The dislocations lie close to the exit surface of the foil and the [001] direction points from the top to bottom surface. The dislocations comprising the arms of the cross can be characterized from their dark-light-dark or light-dark-light contrast features in this single micrograph. Their Burgers vectors are shown in the figure. It is clear that four different near-edge dislocations are activated from this source. These dislocations are highly jogged as they cross-slip from $\{111\}_A$ (easy glide) to {011} or sometimes to $\{111\}_B$ (difficult glide). Since only screw dislocations can cross-slip, the leading arm of each dislocation (not visible in Fig.4.3.4) must be a pure screw segment. The slip plane of the 60°β dislocation aligned along the [110] direction is determined as (1 $\bar{1}$1) (**b**=(a/2)[10 $\bar{1}$] or (a/2)[0 $\bar{1}$ $\bar{1}$]) from its light(wider)-dark-light(narrower) contrast. The other dislocation running along the [110] direction was found to be a pure edge dislocation, because it became invisible when observed with **g**=±220. This sessile edge dislocation is presumably formed by a reaction of the type

$$(a/2)[10\ \bar{1}] + (a/2)[0\ \bar{1}1] = (a/2)[1\ \bar{1}0]$$

or

$$(a/2)[0\ \bar{1}\ \bar{1}] + (a/2)[101] = (a/2)[1\ \bar{1}0] \qquad (4.3.2)$$

between two 60°β dislocations gliding on (1 $\bar{1}$1) and ($\bar{1}$11).

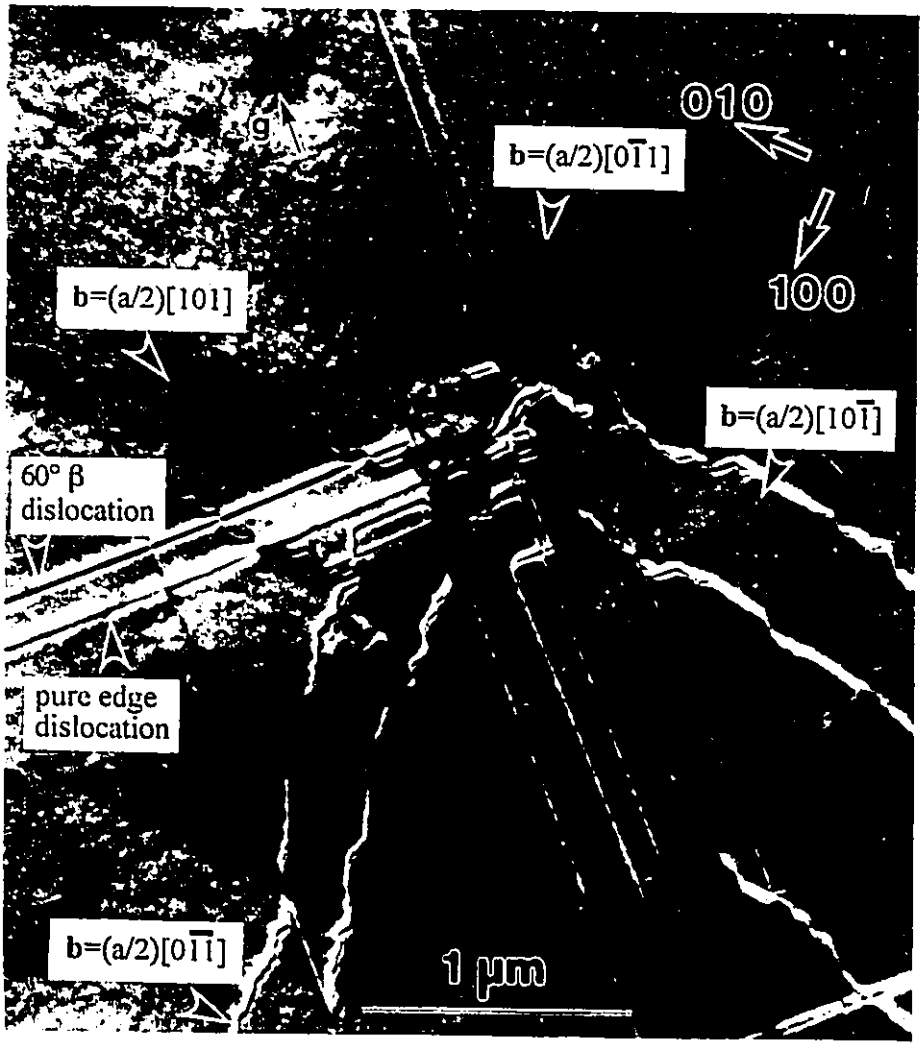

Fig.4.3.4 Plan-view TEM dark field image of one of the cross-shaped dislocation sources in the sample#225 (g= $\bar{2}$20). The crystallographic coordinate system used in this analysis and the Burgers vectors of <100> misfit dislocations are shown in the micrograph.

The misfit dislocations left at the $InAs_yP_{1-y}$/InP interface change their directions from <110> to <100> as the threading arm of the dislocation loop with pure-screw character cross-slips from the normal {111} plane to {011} plane as schematically shown in Fig.4.3.5. In this example, a screw segment of a dislocation loop with $\mathbf{b}=(a/2)[0\ \bar{1}1]$ cross-slips from $(111)_A$ to (011), changing the direction of the misfit dislocation segment at the interface from $[1\ \bar{1}0]$ to [100].

The line direction and Burgers vector of misfit dislocations involved in the cross-slip process can be defined by following two simple rules:

(1) The dislocation line direction along the dislocation loop is fixed by defining the line direction of the 60° dislocation segments as $[1\ \bar{1}0]$ for α dislocations and [110] for β dislocations.

(2) The Burgers vector is determined by noting that the extra half-plane of the misfit dislocation points toward the substrate side in order to relieve the compressive strain in the $InAs_yP_{1-y}$ film.

There are eight possible cross-slips from {111} to {011} relevant to the present problem. They are summarized in Table 4.3.1 using abbreviated form.

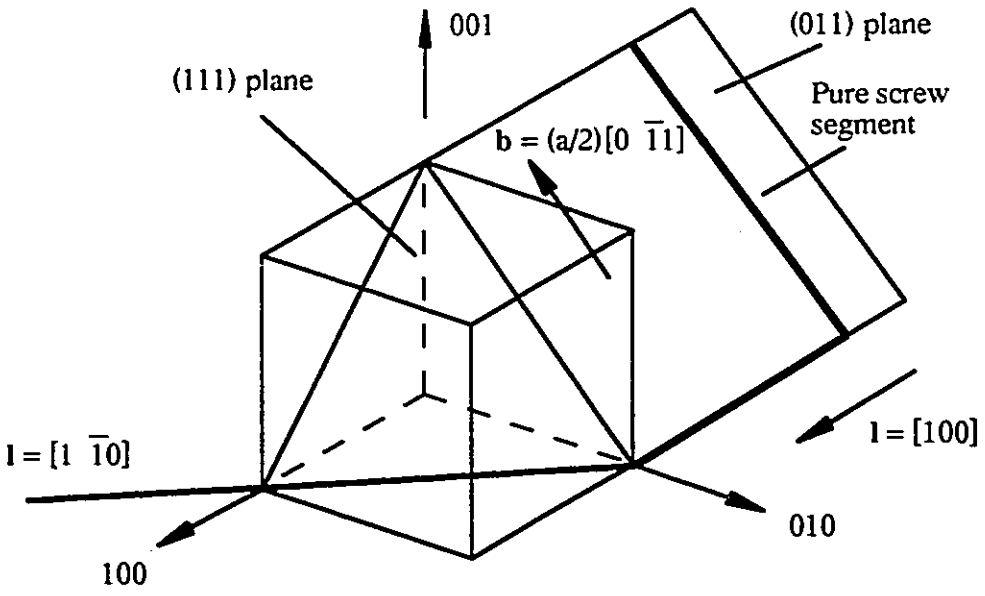

Fig.4.3.5 Schematic representation of cross-slip of a pure screw segment from (111) plane to (011) plane leaving [1 $\bar{1}$0] MD and [100] MD at the interface.

Table 4.3.1 Eight possible cross-slip modes from {111} to {011}.

Burgers vector	Slip plane	Misfit dislocation
(a/2)[0 $\bar{1}$1]	$(111)_A \rightarrow (011)$	60°$\alpha \rightarrow$[100] edge
(a/2)[$\bar{1}$01]	$(111)_A \rightarrow (101)$	60°$\alpha \rightarrow$[0 $\bar{1}$0] edge
(a/2)[0 $\bar{1}$ $\bar{1}$]	$(\bar{1}\ \bar{1}1)_A \rightarrow (0\ \bar{1}1)$	60°$\alpha \rightarrow$[100] edge
(a/2)[$\bar{1}$0 $\bar{1}$]	$(\bar{1}\ \bar{1}1)_A \rightarrow (\bar{1}01)$	60°$\alpha \rightarrow$[0 $\bar{1}$0] edge
(a/2)[0 $\bar{1}$ $\bar{1}$]	$(1\ \bar{1}1)_B \rightarrow (0\ \bar{1}1)$	60°$\beta \rightarrow$[100] edge
(a/2)[10 $\bar{1}$]	$(1\ \bar{1}1)_B \rightarrow (101)$	60°$\beta \rightarrow$[010] edge
(a/2)[0 $\bar{1}$1]	$(\bar{1}11)_B \rightarrow (011)$	60°$\beta \rightarrow$[100] edge
(a/2)[101]	$(\bar{1}11)_B \rightarrow (\bar{1}01)$	60°$\beta \rightarrow$[010] edge

The true nature of dislocation sources in $InAs_yP_{1-y}$/InP system is unclear, but from plan-view TEM observations, it is suggested that they are heterogeneous in nature (Dodson (1988)). Many heterogeneous nucleation sites for misfit dislocations were found in sample #239. Typical examples are presented in Fig.4.3.6. Figure 4.3.6 (a) shows misfit dislocations ejected into [110], [1 $\bar{1}$0] and near-[100] directions from a spherical particle (arrowed in the micrograph) having a diameter of 300Å. Although the composition of the particle was not determined, the particle may be a P-rich region, in excess of the regular stoichiometry. It is known that such precipitates are usually formed after annealing of InP grown by low temperature gas-source MBE (Claverie et al. (1993)). A "non-planar region" can also act as a dislocation source (Fig.4.3.6(b)). In this figure dislocations are generated from a "non-planar region" (approximately 0.4μm×0.25μm in dimensions) into [1 $\bar{1}$0] and [110] directions. From a **g.b** analysis, a short segment (about 0.1μm long) marked in the micrograph was confirmed to be a pure edge misfit dislocation developing along the [$\bar{1}$00] direction. This "non-planar growth region" is convex towards the InP substrate side ([00 $\bar{1}$] direction).

The examples of dislocation sources presented in this subsection are from samples #225 and #239. In the samples with larger As content (higher compressive strain in the $InAs_yP_{1-y}$ film), it was difficult to identify the nucleation sites for misfit dislocations because of the high-density of misfit dislocations.

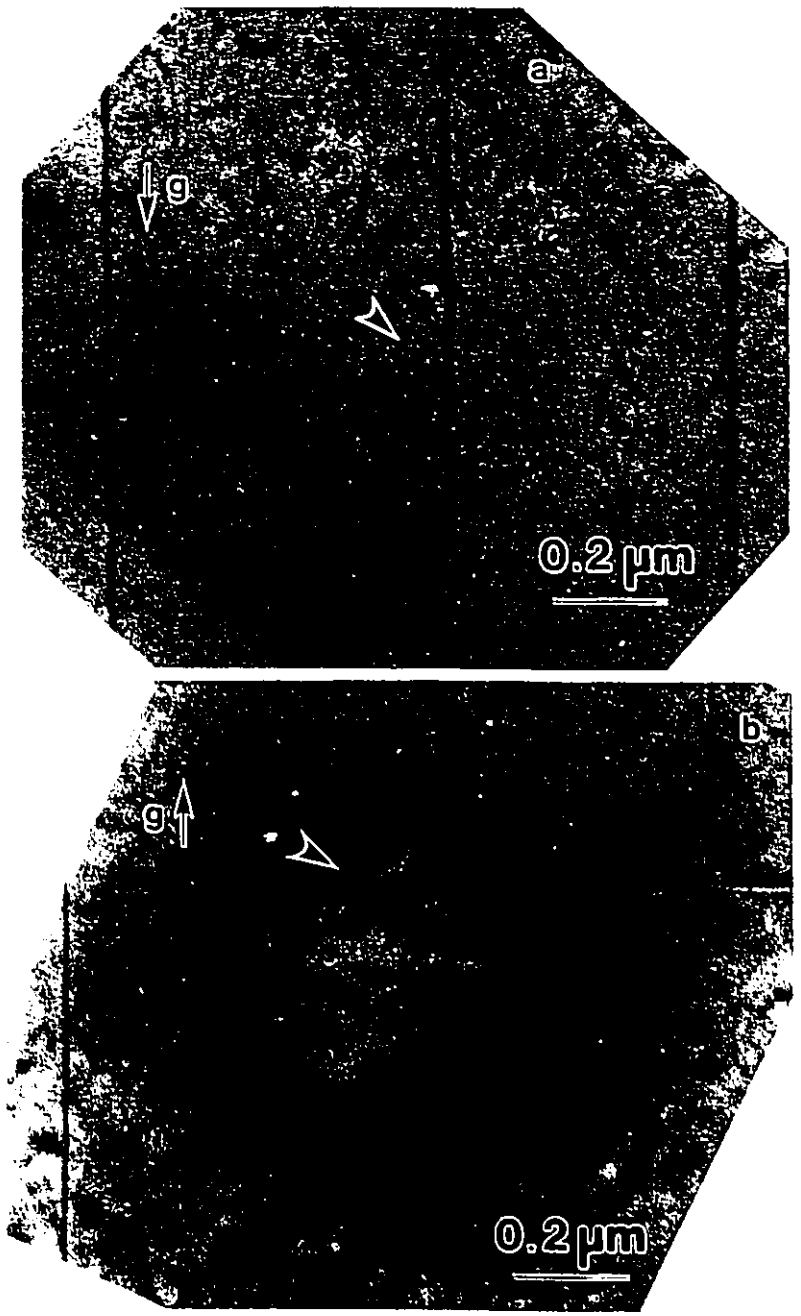

Fig.4.3.6 Plan-view TEM of typical dislocation sources in sample #239. (a) A spherical particle (pointed by a triangle marker) seems to have acted as a dislocation nucleation source. (g=2 $\bar{2}$0) (b) A short segment of <100> misfit dislocation (arrowed) is ejected from the "non-planar growth" region. (g= $\bar{2}$20)

Chapter 5

Composition modulation in lattice-matched $In_{1-x}Ga_xAs_yP_{1-y}$ layers

5.1 Introduction

For optical communication using silica based optical fibres, the $In_{1-x}Ga_xAs_yP_{1-y}$ alloys play a very important role. When lattice-matched to InP, their bandgap range of 0.92 - 1.6μm enables the fabrication of semiconductor lasers which match the wavelengths of minimum dispersion (1.3μm) and minimum loss (1.55μm) of the silica fibre (Li (1985)). Liquid phase epitaxy (LPE) has been widely used for the fabrication of conventional optical devices or for the feasibility studies of new device structures (Ueda et al. (1984b), Chu et al. (1988)). However, LPE suffers from several shortcomings such as graded heterointerfaces, poor thickness control and thickness variation (Dyment (1985)). Since the demand for more sophisticated devices keeps increasing, the future success of optical communication depends critically on the quality and availability of epitaxially grown structures. Molecular beam epitaxy (MBE) has been attracting much attention as one of the alternative thin film growth techniques.

In this chapter, studies on the composition modulation in $In_{1-x}Ga_xAs_yP_{1-y}$ alloy films having a wide range of composition, but lattice-matched to InP, grown with MBE are described. Cross-sectional and plan-view transmission electron microscopy (TEM) was used to investigate the growth features of the films. TEM observations were conducted with a Philips CM12 electron microscope operating at 120kV.

In LPE grown $In_{1-x}Ga_xAs_yP_{1-y}$ films lattice-matched to (001) InP substrates, coarse composition modulations with wavelengths of 1000-1500Å are commonly observed. The modulation usually occurs along two <100> directions parallel to the (001) interface plane (i.e. [100] and [010] directions), which is attributed to elastic "softness"

along the <100> directions in this material (Henoc et al. (1982)). In our lattice-matched MBE films, however, composition modulation occurring only along the [110] direction with small wavelength (~ 100Å) was repeatedly observed.

As reviewed in Section 2.2, incorporation of the strain energy associated with phase modulation significantly affects the theoretical stability of the phase. The strain energy decreases the critical temperature above which a single phase is stable against a small composition fluctuation and this effect is known as strain stabilization (Cahn (1961)). The idea of strain stabilization, first introduced to $In_{1-x}Ga_xAs_yP_{1-y}$ alloys by Stringfellow (1982b), led to a controversial prediction that the alloys are stable at any growth temperature. Glas (1987) pointed that the very low critical temperature estimated from Stringfellow's calculation is caused by an overestimation of the strain energy which was calculated for an infinitely large material. He first derived the strain energy associated with the composition modulation in a thin film deposited epitaxially on a semi-infinite substrate. In Appendix B, Glas' approach is extended to a material with cubic symmetry. Two modulation directions were considered; the conventional modulation along [100] direction commonly observed in LPE material and the newly found [110] modulation. Based on a simple free energy argument, the derived strain energy is used to compare the stability of the $In_{1-x}Ga_xAs_yP_{1-y}$ lattice-matched films against these modulations. The thermodynamic critical temperatures above which the alloy is stabilized against modulation is too low compared with the typical MBE growth temperatures. This suggests that the modulation is not directly caused by the minimization in free energy but is driven by kinetic processes occurring at the growing film surface.

5.2 Results

5.2.1 Structure and composition of the samples

Nineteen samples were examined to study the composition modulation in $In_{1-x}Ga_xAs_yP_{1-y}$ alloy layers. All samples had the same structure shown in Fig.5.2.1. A 3000Å thick $In_{1-x}Ga_xAs_yP_{1-y}$ alloy layer with a composition lattice-matched to the InP (001) substrate was grown on the 500Å thick InP buffer layer. The $In_{1-x}Ga_xAs_yP_{1-y}$ layer was capped with 200 - 400Å thick InP film.

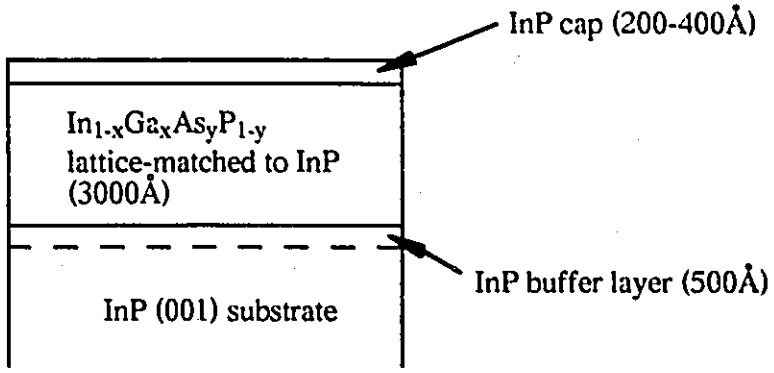

Fig.5.2.1 Structure of the samples with 3000Å thick $In_{1-x}Ga_xAs_yP_{1-y}$ layer lattice-matched to InP.

The nominal composition of the $In_{1-x}Ga_xAs_yP_{1-y}$ layers are shown in Fig.5.2.2 using a composition diagram. A wide range of composition was examined. The deviation of the alloy composition from the exact lattice-match to InP was small. The misfit with respect to InP substrate defined by eq.(1.2) was smaller than 0.1% for all samples except for the sample #940 which has a –0.17% misfit.

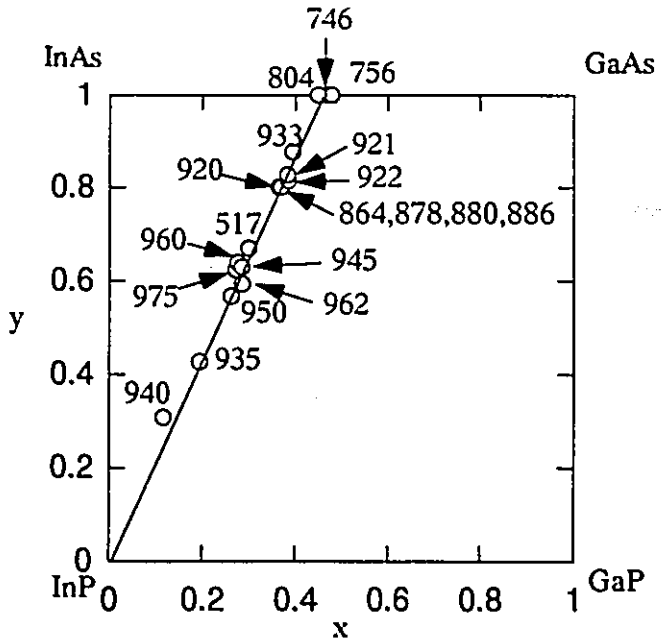

Fig.5.2.2 The nominal composition of the $In_{1-x}Ga_xAs_yP_{1-y}$ layers lattice-matched to InP.

5.2.2 Cross-sectional TEM observation

Six samples are chosen to show how the composition modulation in $In_{1-x}Ga_xAs_yP_{1-y}$ lattice-matched alloy layers varies with their nominal composition; they are #940 (x=0.117, y=0.309), #935 (x=0.194, y=0.427), #950 (x=0.263, y=0.567), #945 (x=0.285, y=0.630), #933 (x=0.395, y=0.876) and #746 (x=0.467, y=1.0). These samples were grown at 470°C. [1 $\bar{1}$0] and [110] cross-sectional TEM photographs for these 6 samples are presented in Fig.5.2.3 and Fig.5.2.4. All micrographs were taken in dark field mode. Reflection vectors **g**=±004 and **g**=±220 were used for [1 $\bar{1}$0] cross-section and **g**=±004 and **g**=±2 $\bar{2}$0 were used for [110] cross-section. Since the image feature is not affected

simply by reversing the direction of g, the direction of the g vector is not presented in each micrograph.

When observed with g=±004, the micrographs reveal a flat interface between the InP cap and $In_{1-x}Ga_xAs_yP_{1-y}$ layer, which indicates that the growth of these lattice-matched layers proceeded in layer-by-layer mode. In addition, the contrast is nearly uniform in the layer and does not show a particular feature. On the other hand, a modulation contrast is clearly seen in both [1 $\bar{1}$0] and [110] cross-sections using g={220} which is parallel to the interface plane, although the feature of the images is not equivalent in the [1 $\bar{1}$0] and [110] cross-sections; the periodic nature of the image is more evident in [1 $\bar{1}$0] cross-sections. This suggests that the modulation does not occur in the conventional <100> directions. This will be verified in TEM plan-view observations in a much clearer manner.

In [1 $\bar{1}$0] cross-sections, the modulation contrast has a regular periodicity, typically about 100Å. The modulations were strongest for the sample #945 (x=0.285, y=0.630) but very weak for #940 (x=0.117, y=0.309) and less pronounced for the lattice-matched ternary sample #746 (x=0.467, y=0). These trends can be correlated with the position of the composition of the film relative to the chemical spinodal for $In_{1-x}Ga_xAs_yP_{1-y}$ alloys, as shown in Fig.2.2.2 calculated by Onabe (1982). At 400-500°C, a composition of #945 (x=0.285, y=0.63) lies deeply within, while #940 (x=0.117, y=0.309) lies outside the chemical spinodal. The magnitude of the composition deviation from the nominal one is considered to be small because virtually no contrast modulation is observed in [1 $\bar{1}$0] cross-sections under g=±004 conditions which should be more sensitive to the composition difference. The periodic modulation contrast under g=±220 may be caused by the relaxation of the lattice at the free surfaces of the TEM foils (Treacy et al. (1985)).

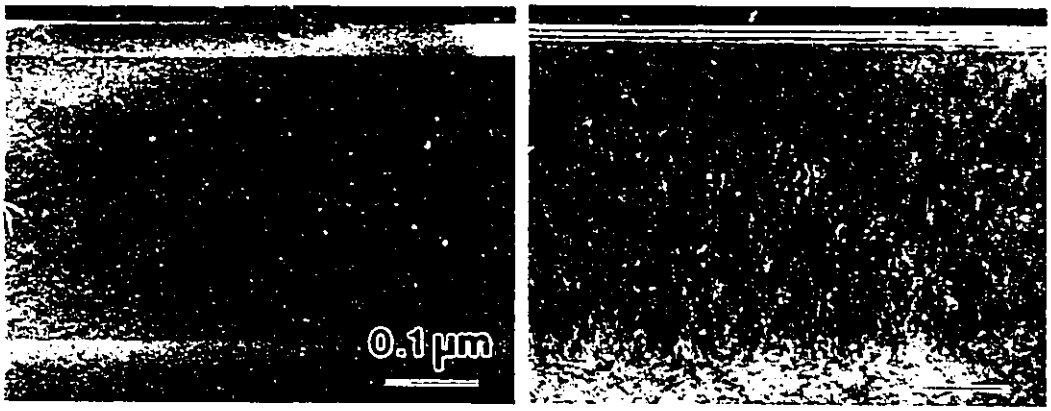

#940 (x=0.117, y=0.309)

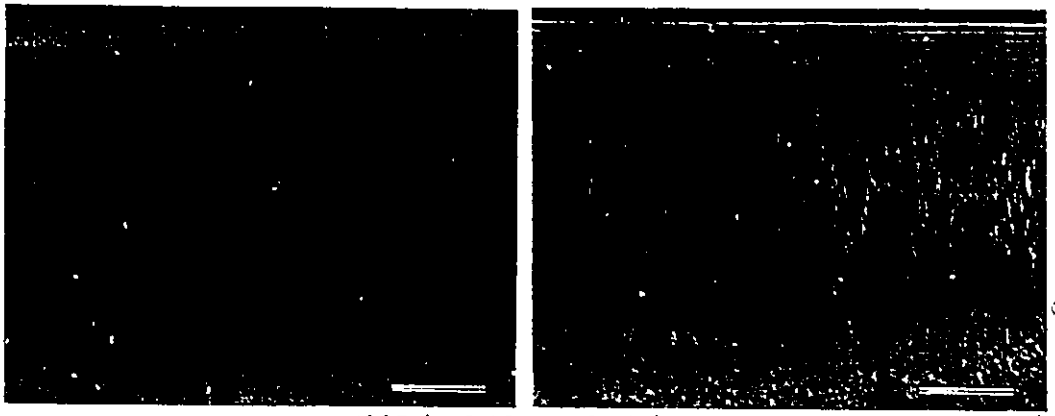

#935 (x=0.194, y=0.427)

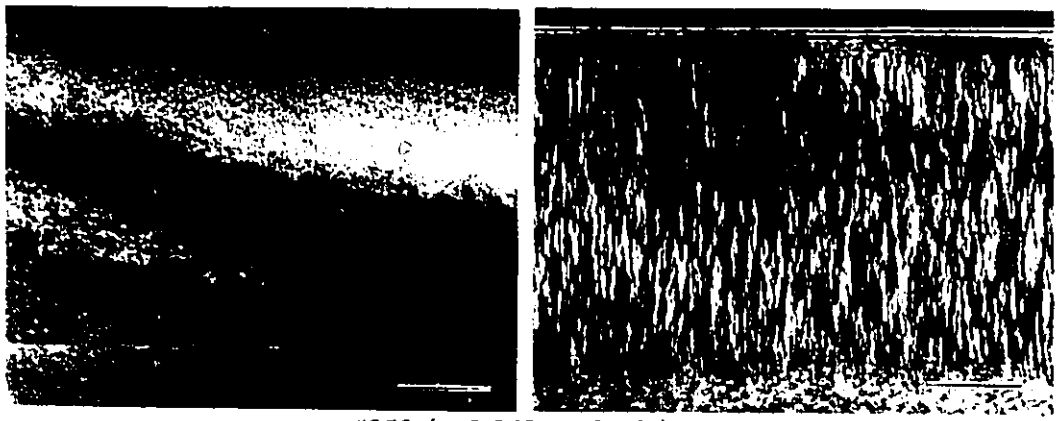

#950 (x=0.263, y=0.567)

Fig.5.2.3 [1 $\bar{1}$0] cross-sectional dark field TEM images of samples #940, #935, #950, #945, #933 and #746. Reflection vectors g=±004 (left side) and g=±220 (right side) were used (marker = 0.1μm).

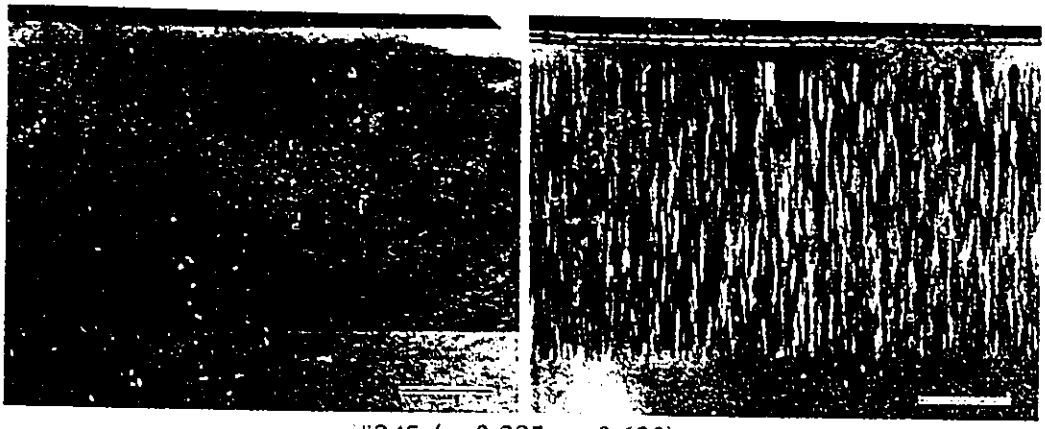

#945 (x=0.285, y=0.630)

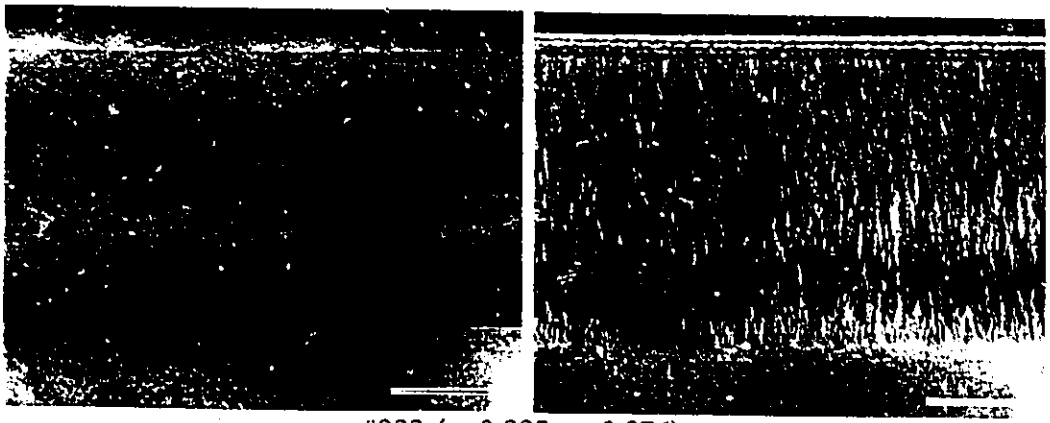

#933 (x=0.395, y=0.876)

#746 (x=0.467, y=1.0)

Fig.5.2.3 (continued)

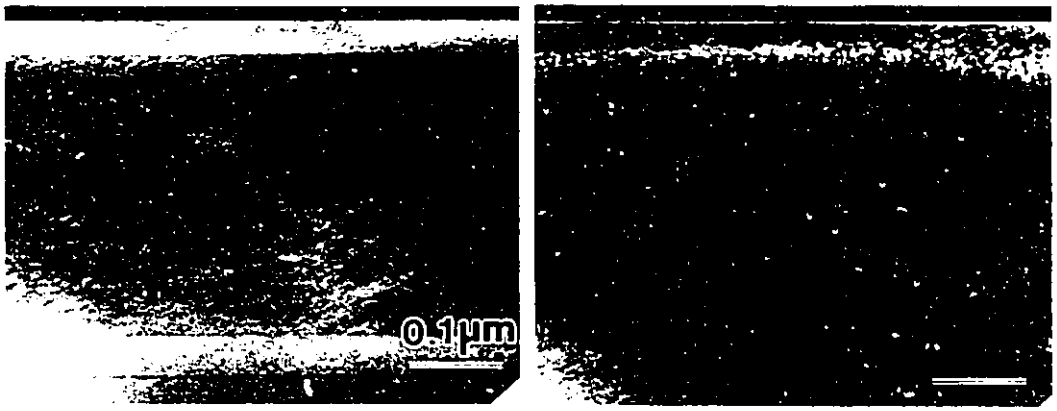

#940 (x=0.117, y=0.309)

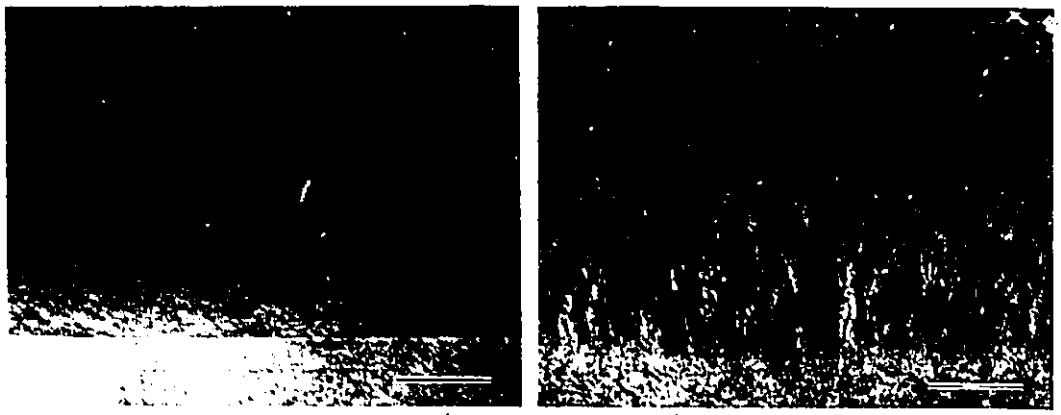

#935 (x=0.194, y=0.427)

#950 (x=0.263, y=0.567)

Fig.5.2.4 [110] cross-sectional dark field TEM images of samples #940, #935, #950, #945, #933 and #746. Reflection vectors g=±004 (left side) and g=±2 $\bar{2}$0 (right side) were used (marker = 0.1μm).

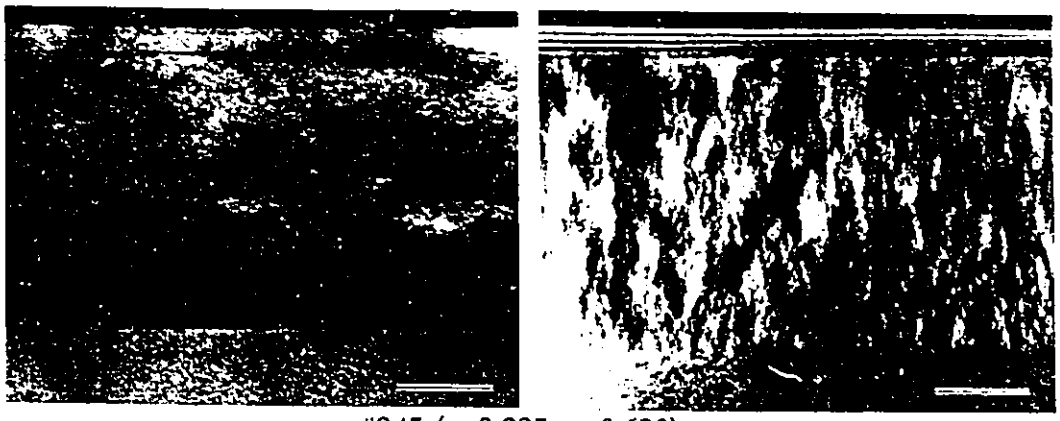

#945 (x=0.285, y=0.630)

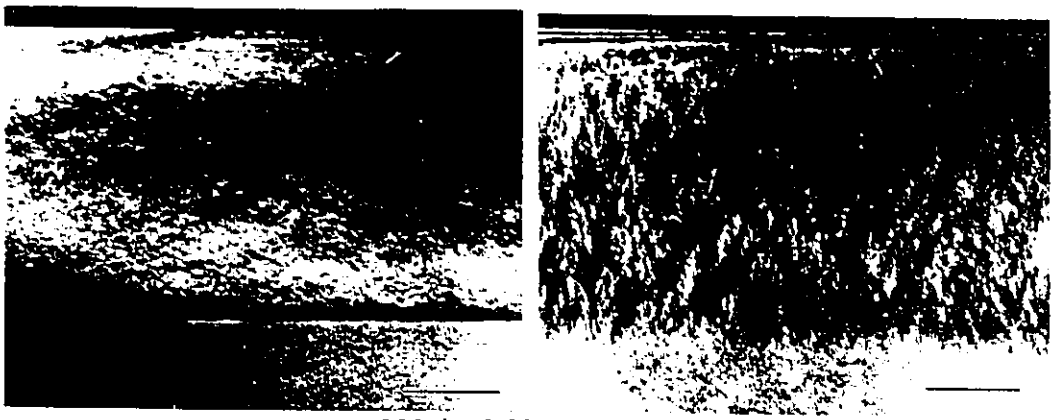

#933 (x=0.395, y=0.876)

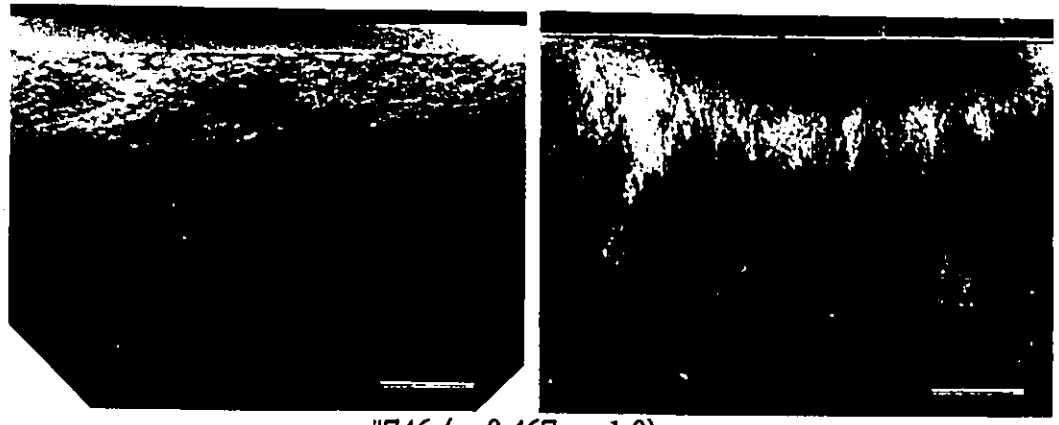

#746 (x=0.467, y=1.0)

Fig.5.2.4 (continued)

Selected area diffraction patterns (SADPs) taken from the above cross-section samples showed no evidence of ordering in these $In_{1-x}Ga_xAs_yP_{1-y}$ alloy layers. This observation distinguishes MBE growth from higher temperature growth processes such as MOCVD used by Follstaedt et al. (1995), where diffraction evidence for ordering was found.

5.2.3 Effect of the growth temperature on composition modulation

In order to examine the effect of the growth temperature on the composition modulation, three samples with the same composition grown at different temperatures were compared. They were #886 (growth temperature 450°C), #878 (470°C) and #880 (490°C) with x=0.37, y=0.80. Figures 5.2.5 and 5.2.6 are the [1 $\bar{1}$0] and [110] cross-sectional micrographs for these samples. As in Fig.5.2.3 and Fig.5.2.4, all micrographs were taken in dark field mode and the direction of the **g** vector is not presented in each micrograph.

The samples #886 and #878 grown at 450°C and 470°C show similar TEM contrast features as the samples studied in the previous subsection. A clear, periodic, fine modulation contrast is observed in [1 $\bar{1}$0] cross-section under **g**=±220. As the growth temperature was raised to 490°C, however, the quality of the sample drastically deteriorated. The $In_{1-x}Ga_xAs_yP_{1-y}$ layer apparently consists of a lower part with relatively better quality and an upper part in which many defects are observed. The composition modulation become more pronounced and can be observed at the lower part of the layer even when the **g** vector is {004} (the left side micrograph of #880). The effect of the growth temperature on the composition modulation along [110] direction again suggests that this new type of modulation is not the "classical" spinodal process, because the classical spinodal decomposition becomes more unlikely to occur at higher temperatures as the driving force decreases.

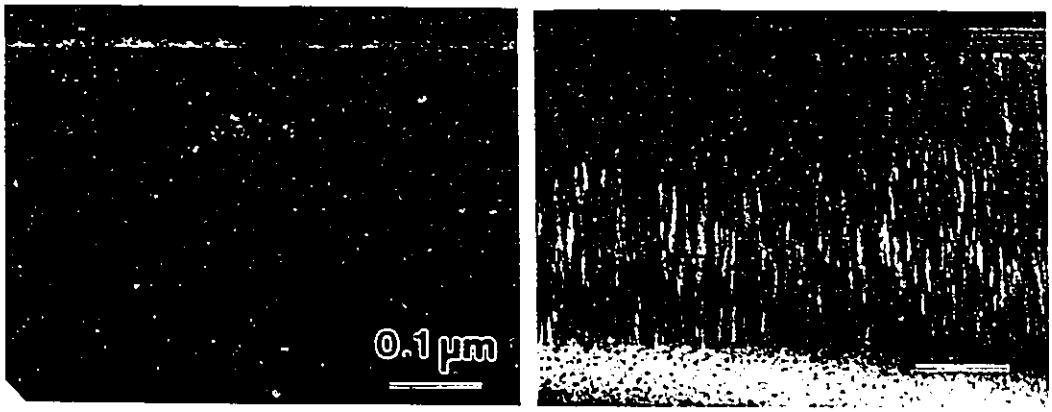

#886 (growth temperature 450°C)

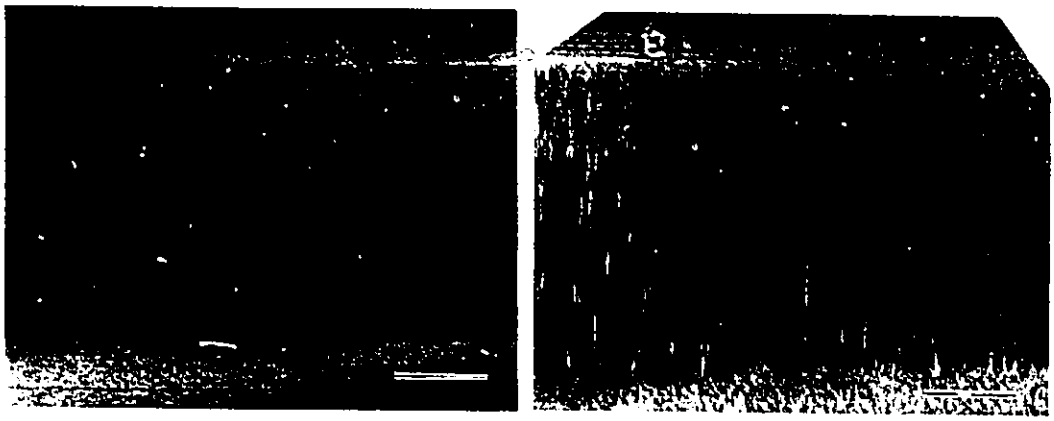

#878 (470°C)

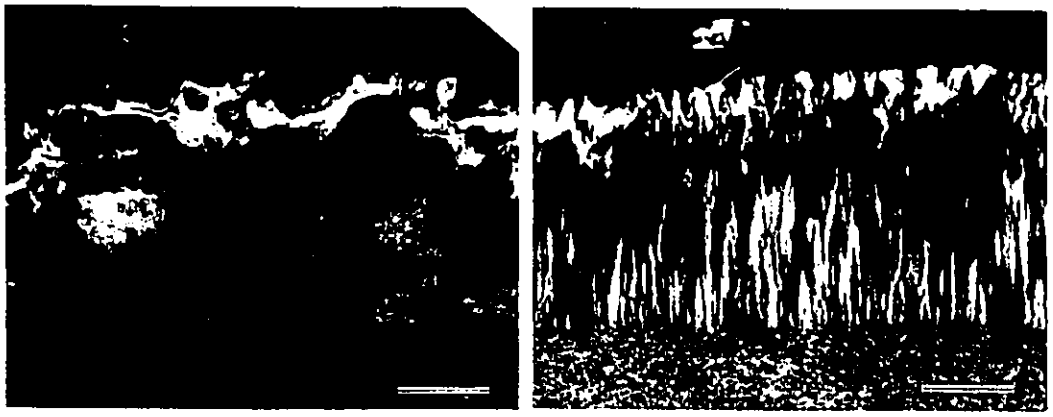

#880 (490°C)

Fig.5.2.5 [1 $\bar{1}$0] cross-sectional dark field TEM images of samples #886, #878 and #880 with x=0.37, y=0.80. Reflection vectors g=±004 (left) and g=±220 (right) were used (marker = 0.1μm).

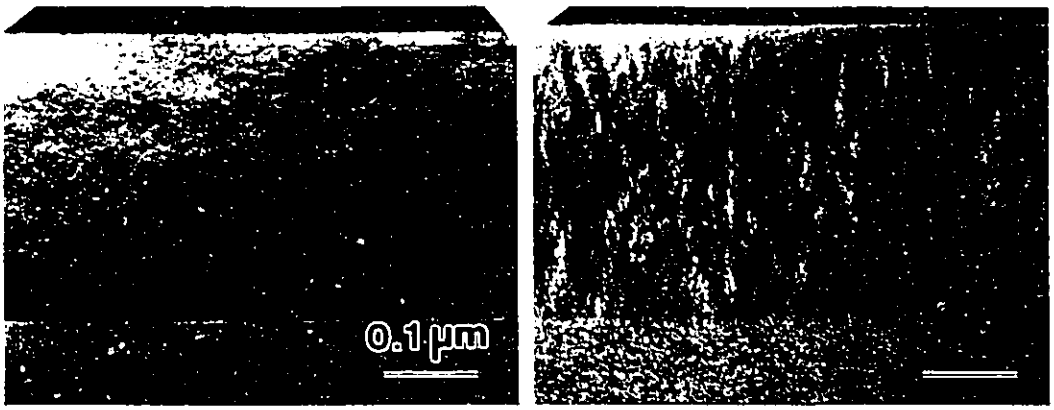

#886 (growth temperature 450°C)

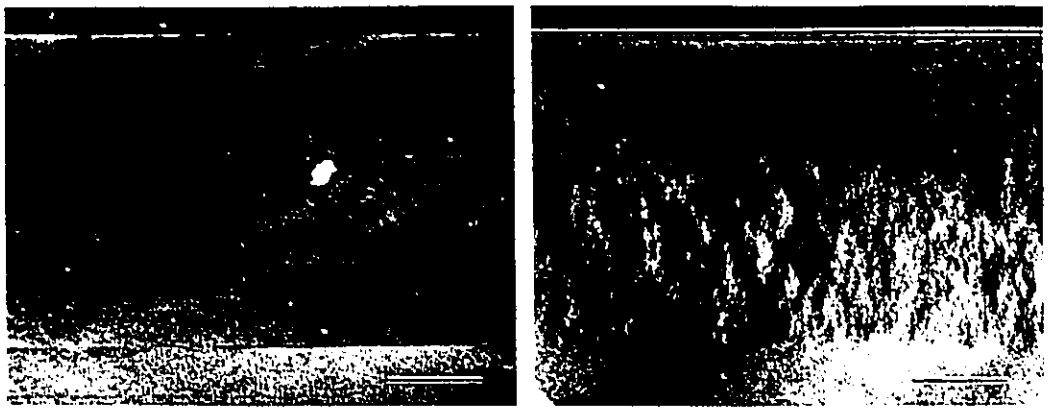

#878 (470°C)

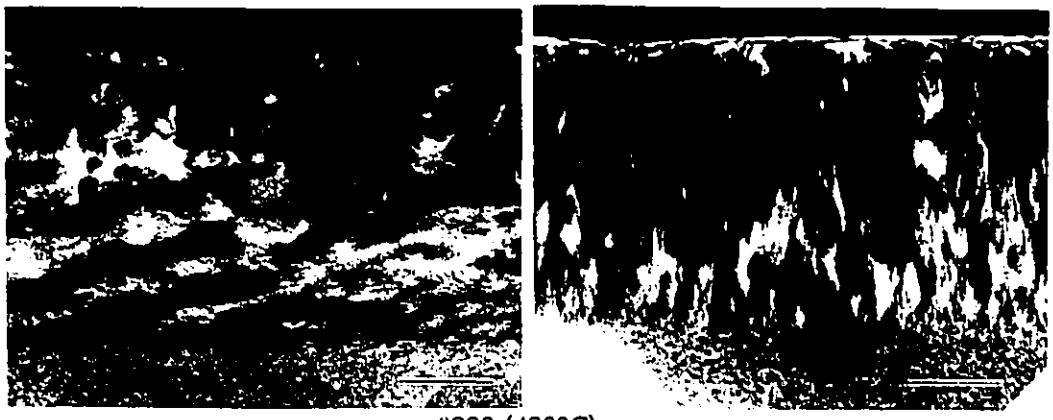

#880 (490°C)

Fig.5.2.6 [110] cross-sectional dark field TEM images of samples #886, #878 and #880. Reflection vectors g=±004 (left) and g=±2 $\bar{2}$0 (right) were used (marker = 0.1μm).

5.2.4 Plan-view TEM observation

The nature of the composition modulation responsible for the diffraction contrast observed in cross-sectional TEM is more clearly recognized in plan-view. Plan-view dark field images of the sample #945 in which the modulations were clearly seen in cross-sectional TEM are shown in Fig.5.2.7. These micrographs were taken with four different g vectors from the same area using an Ar ion-beam damage artifact as a position marker. As clearly seen in Fig.5.2.7 (c), the periodic modulation contrast running approximately along [1 $\bar{1}$0] direction becomes invisible when g vector is taken parallel to the [1 $\bar{1}$0] direction (g=2 $\bar{2}$0 in this figure). This behaviour indicates that the displacement field causing the plan-view modulation contrast is limited to the [110] direction. Thus the contrast feature observed in [110] cross-section, which is much weaker than that observed in the [1 $\bar{1}$0] cross-section, is probably caused by the overlap of small modulated regions with the average size of about 100Å×1000Å×700Å in [110], [1 $\bar{1}$0] and [001] directions, as measured from Fig.5.2.7.

In contrast to the present plan-view TEM results, those from the lattice-matched $In_{1-x}Ga_xAs_yP_{1-y}$ layers grown with LPE look quite different. A large scale modulation, several 1000 Å in wavelength, develops in both [100] and [010] directions in conventional LPE grown films (Henoc et al. (1982)). The modulation forms a basket-weave-like image when observed with g={220}. The modulation becomes invisible if the g vector is perpendicular to its direction, i.e. [100] (or [010]) modulation is invisible when g=±040 (or g=±400).

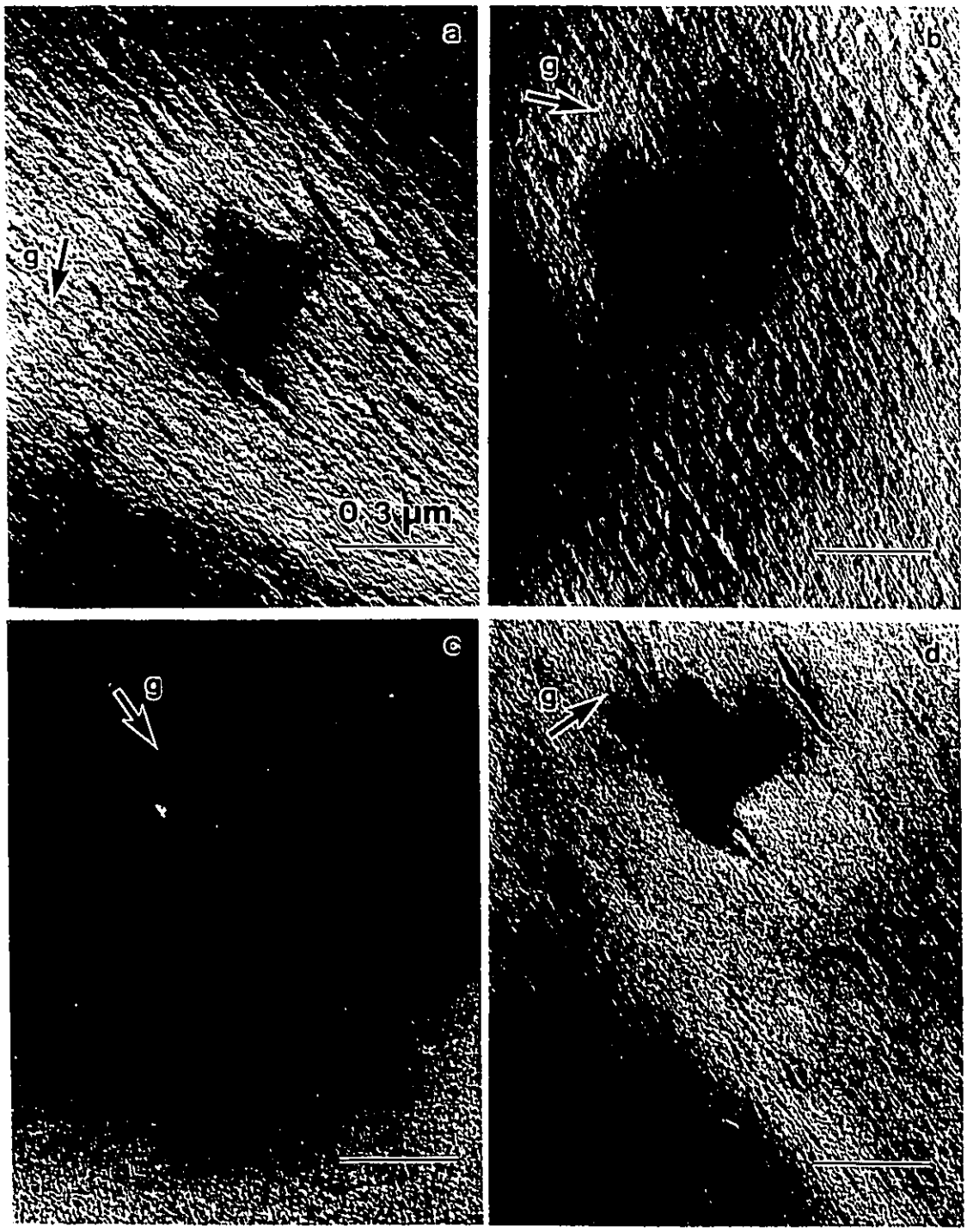

Fig.5.2.7 Plan-view dark field images of #945 (x=0.285, y=0.630) under (a) g=400, (b) g=0 $\bar{4}$0, (c) g=2 $\bar{2}$0 and (d) g= $\bar{2}$ $\bar{2}$0 (marker = 0.3μm).

When observed in more detail, the strain fields associated with the composition modulation are seen to vary in magnitude. The largest of these form regions extending up to 3000 - 5000Å in length along the [1 $\bar{1}$0] direction. They always had a dark field image consistent with local regions in the thin foil which are under compression, characterized by anomalous white strain field contrast on the positive side of the **g** vector (Ashby and Brown (1963)). Figure 5.2.8 (a) is a dark field image of #945 under **g**=400 and the inset is the SADP taken exactly at the [001] zone axis. We note that each diffraction spot is accompanied by a streak extending in or close to the [110] direction and no satellite spots are observed. This suggests that a complete phase separation did not occur in these $In_{1-x}Ga_xAs_yP_{1-y}$ layers. If we assume that the quaternary $In_{1-x}Ga_xAs_yP_{1-y}$ alloys separate into InAs-rich and GaP-rich regions, the coarser areas of black-white contrast in Fig.5.2.8 (a) may correspond to InAs-rich region compressed by the surrounding material. The exact nature of the displacement fields associated with these regions is not known at the present stage.

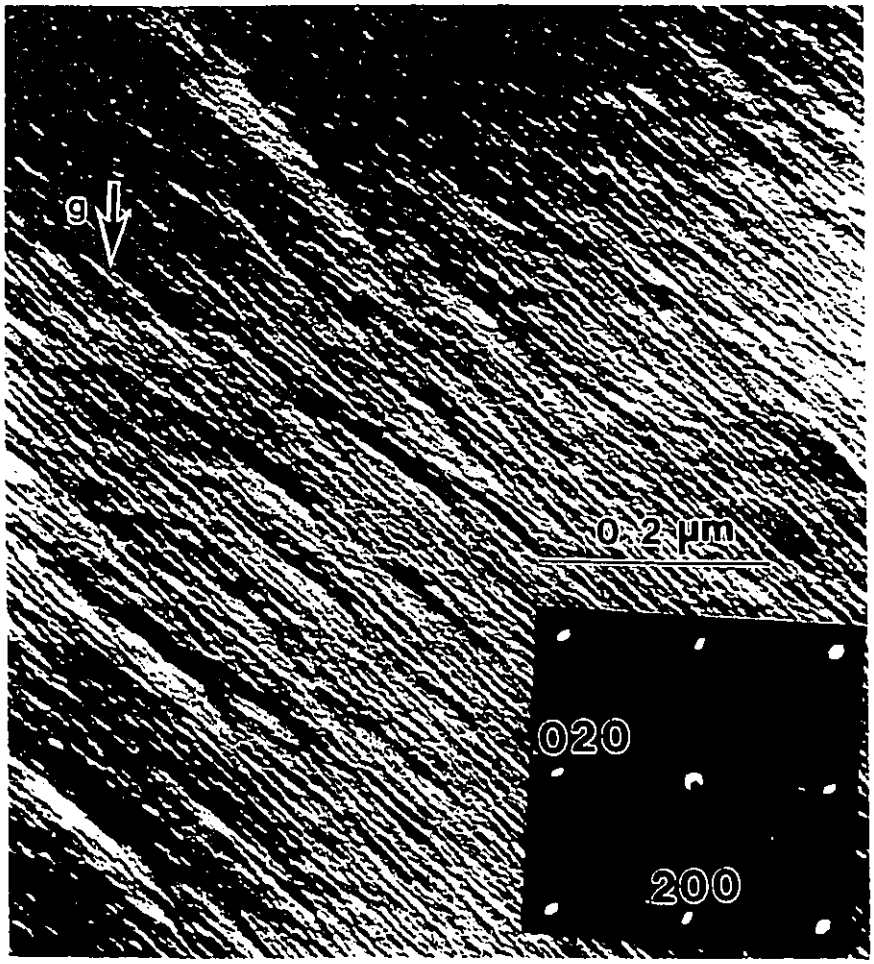

Fig.5.2.8 Dark field image, g=400 of plan-view sample #945 and the selected area diffraction pattern (in the inset) taken exactly at [001] zone axis.

5.3 Discussion

5.3.1 Comparison with photoluminescence measurements

The features of the composition modulation described in the previous section agree well with the results from photoluminescence (PL) measurements. LaPierre (1994) conducted PL experiments for various $In_{1-x}Ga_xAs_yP_{1-y}$ alloy samples including ones I examined using TEM. Figure 5.3.1[a,b] shows the full width at half maximum (FWHM) of PL spectrum and the integrated PL intensity for each lattice-matched $In_{1-x}Ga_xAs_yP_{1-y}$ sample as a function of the As fraction y. Measurements were conducted at room temperature (300K) and low temperature (11K). The points (a) to (f) correspond to the samples #940, #935, #950, #945,#933,#746 in Fig.5.2.3 ([1 $\bar{1}$0] cross-sectional TEM) and Fig.5.2.4 ([110] cross-sectional TEM). Solid lines in Fig.5.3.1[a] are the theoretical PL linewidth in a homogeneous $In_{1-x}Ga_xAs_yP_{1-y}$ alloy. Both thermal and alloy broadening were assumed for 11K, but only the thermal broadening was taken into account at 300K because alloy broadening is not significant at temperatures above 150K. The linewidths for samples with y between 0.5 and 0.9 are much larger than the theoretical value, especially near sample (d) which corresponds to #945 (x=0.285, y=0.630) showing the most significant modulation contrast. The broadening of the PL spectrum suggests that there is a bandgap variation in the sample, which can be attributed to a composition modulation. In addition to the broadening of the spectrum, the integrated PL intensities were significantly reduced (Fig.5.3.1[b]). Both at low and room temperatures, the reduction becomes larger as the degree of composition modulation increases. The reduction was caused by an increase in non-radiative recombination, although the exact nature of the mechanism is not know at the present stage.

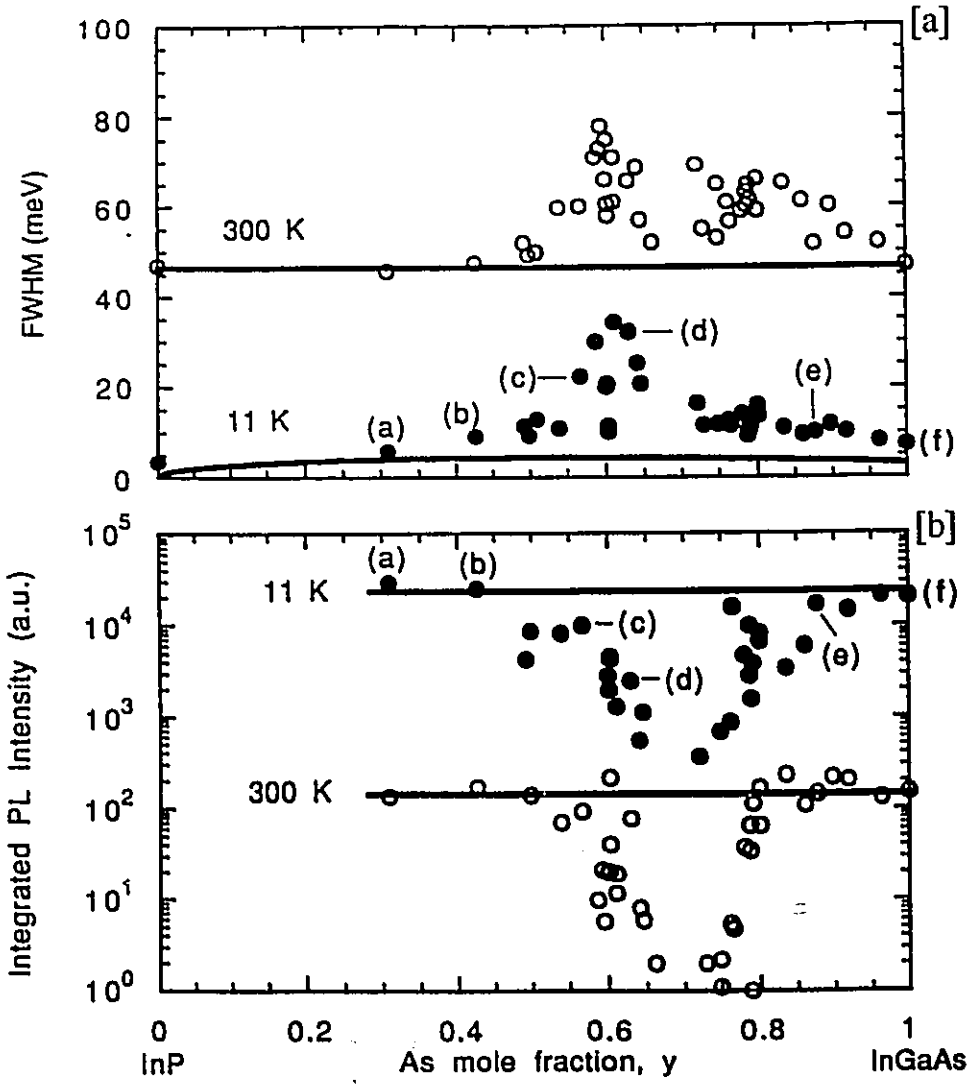

Fig.5.3.1 PL linewidth [a] and integrated intensity [b] as a function of the As content y for various $In_{1-x}Ga_xAs_yP_{1-y}$ lattice-matched layers. Measurements were conducted at room temperature (300K) and low temperature (11K). The solid lines in [a] are theoretical linewidths and the lines in [b] are for reference. The points (a) to (f) correspond to the samples examined using [1 $\bar{1}$0] and [110] cross-section TEM in Section 5.2. (After LaPierre (1994).)

Figure 5.3.2 is the PL spectra for three samples (a)#940, (d)#945 and (f)#746 at various temperatures. The spectra were normalized so that it is easy to compare the difference among these samples. Their intensities were not in the same order as clearly seen from Fig.5.3.1[b]. We can recognize three peaks for the 77K spectrum of the sample #945 which showed the most significant modulation. Here we assume that these three peaks correspond to the electron-hole recombinations in GaP-rich (largest bandgap:peak 3), nominal composition (peak 2) and InAs-rich (smallest bandgap:peak 1) regions. Typical energy differences between the peaks are determined as about 40 meV. If we assume that the phase modulation occurs perpendicular to the lattice-match line, i.e. $\Delta x = -2.1\Delta y$, the composition deviation from the nominal value is estimated using

$$\Delta E_g = \frac{\partial E_g}{\partial x}\Delta x + \frac{\partial E_g}{\partial y}\Delta y = \pm 0.04 \text{ (eV)} \qquad (5.3.1)$$

where E_g is Kuphal's empirical expression for the bandgap in quaternary $In_{1-x}Ga_xAs_yP_{1-y}$ alloy (eq.(3.2.5)). The deviation is estimated to be $\Delta x = 0.028$ and $\Delta y = -0.013$ for the GaP-rich region while for the InAs-rich region, $\Delta x = -0.028$ and $\Delta y = 0.013$. This deviation results in a misfit strain in both GaP-rich and InAs-rich regions having a magnitude of 0.2% with respect to the nominal alloy phase. This very simple estimation does not include the effects of the strain induced in the modulated layer. For a more rigorous analysis, it would be necessary to know the exact elastic field in the modulated film and how this affects the band structure of the film material.

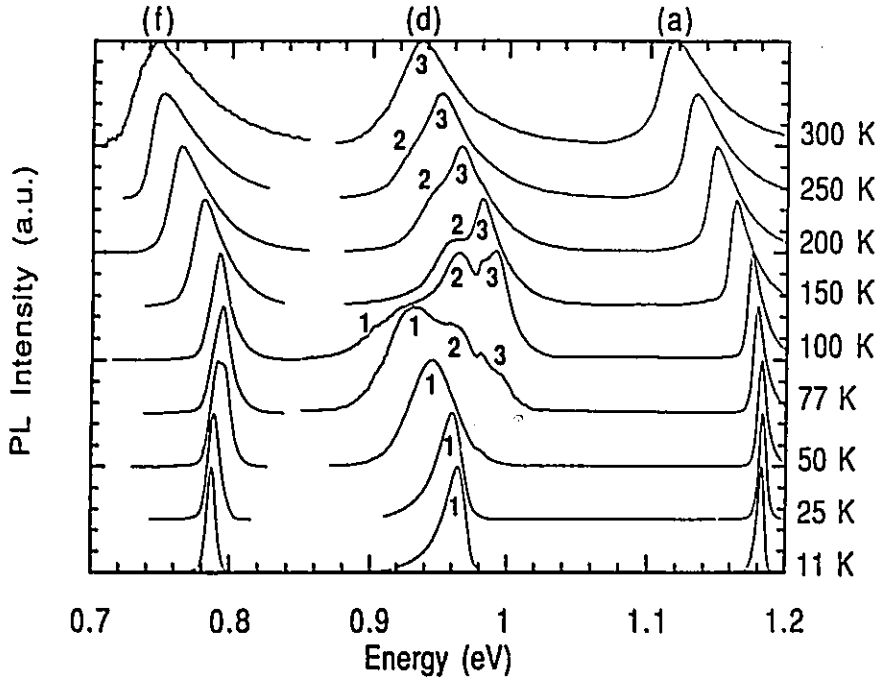

Fig.5.3.2 PL spectra for samples (a)#940, (d)#945 and (f)#746 (after LaPierre (1994)).

5.3.2 Thermodynamic stability against composition modulation

The elastic energies associated with simple sinusoidal lattice-constant modulations along [100] and [110] directions in a thin film material grown on a semi-infinite substrate were derived in Appendix B as eq.(B1.60) and eq.(B2.54), respectively. Figure 5.3.3 shows these energies per unit volume as a function of αh, where $2\pi/\alpha$ is the wavelength of the modulation and h is the thickness of the film. The elastic moduli used for this figure are those of InP: C_{11}=102.2 GPa, C_{12}=57.6 GPa and C_{44}=46.0 GPa (Adachi (1982)). The numbers on the vertical axis of Fig.5.3.3 have to be multiplied by $10^{10} \times \varepsilon_0^{\,2}$ to derive the elastic energy density w_E where ε_0 is the magnitude of the modulation of the strain defined

by eq.(B1.1) and eq.(B2.1). For comparison, the elastic energy density for an elastically isotropic material is also shown as a dotted line. This energy density was calculated by substituting the Voigt average of the elastic constants of InP (μ=36.52 GPa and ν=0.284) into Glas' expression eq.(2.2.28).

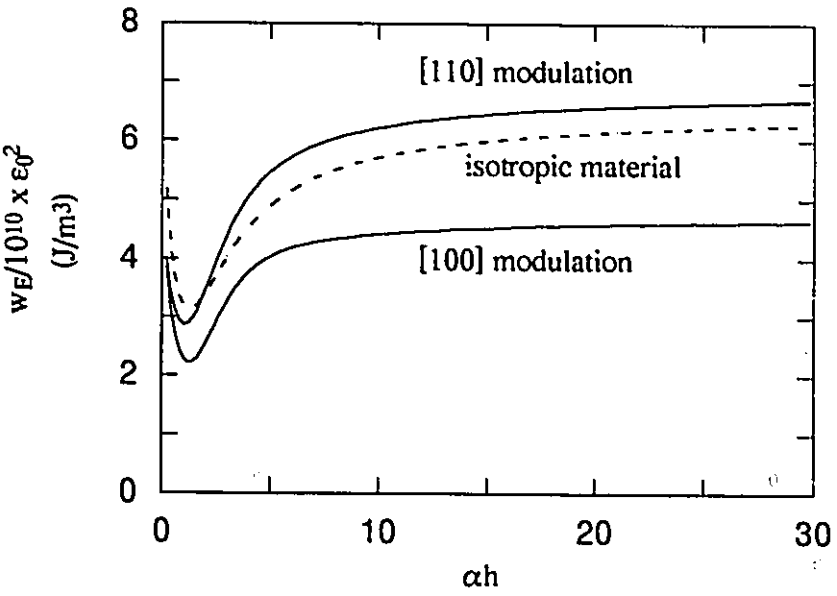

Fig.5.3.3 Strain energy densities for [100] and [110] modulations. The dashed line is calculated for an isotropic material using the Voigt average.

We note that the strain energy density is considerably reduced when the value of αh is about 1. For the modulation wavelength of 100Å, the corresponding film thickness is 16Å. As expected from the elastic moduli, the minimum elastic energy density of the [100] modulation is smaller than that of the [110] modulation, by about 20% around their minima.

Here we define the stability criterion against composition modulation as

$$\frac{\Delta G}{V} = [\text{free energy per unit volume of modulated film}] - [\text{free energy per unit volume of homogeneous film}] = 0 \qquad (5.3.2)$$

where ΔG is the difference in the free energy with and without the modulation and V is the volume of the film. The free energy in the modulated film consists of three terms: the chemical free energy, the mechanical energy and the gradient energy which is proportional to the square of the maximum composition gradient. Since the composition gradient is likely to be small in our case, the gradient term is ignored in the following treatment. The chemical free energy term is calculated using the delta lattice parameter (DLP) model (Stringfellow (1982b)) and the minimum elastic energy per unit volume derived from eq.(B1.60) and eq.(B2.54) is taken as the mechanical energy term.

In the DLP model, the chemical free energy per unit volume is

$$G^{ch} = N_V G^S = N_V[-Ka^{-2.5} + RT\{x \ln x + (1-x)\ln(1-x) + y \ln y + (1-y)\ln(1-y)\}] \qquad (5.3.3)$$

where N_V is the number of moles per unit volume, K is an empirical parameter equal to 1.15×10^7 cal/mol $\text{Å}^{2.5}$, R is the gas constant and T is the absolute temperature. The difference in the chemical free energy ΔG^{ch} can be approximated for a small composition difference between the phases with composition (x,y) and with the starting composition (x_0,y_0) as follows:

$$\Delta G^{ch} = N_V \int \{(x-x_0)\frac{\partial G^S}{\partial x} + (y-y_0)\frac{\partial G^S}{\partial y} + \frac{1}{2}(x-x_0)^2\frac{\partial^2 G^S}{\partial x^2} + (x-x_0)(y-y_0)\frac{\partial^2 G^S}{\partial x \partial y} + \frac{1}{2}(y-y_0)^2\frac{\partial^2 G^S}{\partial y^2}\}dV. \qquad (5.3.4)$$

For a sinusoidal composition modulation following

$$\left.\begin{aligned} x &= x_0 + \Delta x \cos \alpha X \\ y &= y_0 + \Delta y \cos \alpha X \end{aligned}\right\}, \qquad (5.3.5)$$

eq.(5.3.4) is rewritten as

$$\Delta G^{ch} = N_V\{\frac{1}{2}(\frac{\partial^2 G^S}{\partial x^2})(\Delta x)^2 + (\frac{\partial^2 G^S}{\partial x \partial y})(\Delta x)(\Delta y) + \frac{1}{2}(\frac{\partial^2 G^S}{\partial y^2})(\Delta y)^2\}\frac{V}{2} \qquad (5.3.6)$$

where all derivatives are evaluated at $x=x_0$ and $y=y_0$. From eq.(5.3.3), the derivatives become

$$\left.\begin{aligned} (\frac{\partial^2 G^S}{\partial x^2}) &= -8.75K(\frac{\partial a}{\partial x})^2 a_0^{-4.5} + \frac{RT}{x_0(1-x_0)} \\ (\frac{\partial^2 G^S}{\partial x \partial y}) &= -8.75K(\frac{\partial a}{\partial x})(\frac{\partial a}{\partial y}) a_0^{-4.5} \\ (\frac{\partial^2 G^S}{\partial y^2}) &= -8.75K(\frac{\partial a}{\partial y})^2 a_0^{-4.5} + \frac{RT}{y_0(1-y_0)} \end{aligned}\right\} \qquad (5.3.7)$$

where a_0 is the lattice-constant of the starting phase.

The choice of the path of the phase modulation, that is, the ratio of Δx to Δy is not a simple problem. From a thermodynamic point of view, decomposition is expected to occur following the path over which the rate of decrease in the free energy of the system is maximized. In addition, this would probably have to be modified to account for kinetic factors, which might dictate the path during the initial stage of the decomposition although we know little about these factors in our system. In the following, two arbitrary paths $\Delta x = -\Delta y$ and $\Delta x = -2.1\Delta y$ are considered.

First we assume that the modulation occurs following $\Delta x = -\Delta y$. As will be shown later, we should note that the final result of the critical temperature is affected by the direction of modulation, e.g. the ratio of Δx to Δy. Substituting eq.(5.3.7) into eq.(5.3.6), we obtain for the case $\Delta x = -\Delta y$

$$\frac{\Delta G^{ch}}{V} = \frac{N_V}{4}\left[-8.75K\, a_0^{-4.5}\left\{\left(\frac{\partial a}{\partial x}\right)^2 - 2\left(\frac{\partial a}{\partial x}\right)\left(\frac{\partial a}{\partial y}\right) + \left(\frac{\partial a}{\partial y}\right)^2\right\} + RT\left\{\frac{1}{x_0(1-x_0)} + \frac{1}{y_0(1-y_0)}\right\}\right](\Delta x)^2. \qquad (5.3.8)$$

From eq.(2.2.23)

$$\left.\begin{aligned}\frac{\partial a}{\partial x} &= a_{GaP} - a_{InP} + Dy \\ \frac{\partial a}{\partial y} &= a_{InAs} - a_{InP} + Dx\end{aligned}\right\} \qquad (5.3.9)$$

where $D = a_{GaAs} - a_{InAs} - a_{GaP} + a_{InP} = 0.0125$ Å. The magnitude of the strain modulation

ε_0 is

$$\varepsilon_0=\frac{\Delta a}{a}=\frac{1}{a_0}\left(\frac{\partial a}{\partial x}\Delta x+\frac{\partial a}{\partial y}\Delta y\right)=\frac{1}{a_0}\left(a_{GaP}-a_{InAs}+D(y-x)\right)\Delta x. \qquad (5.3.10)$$

Using eqs.(5.3.8), (5.3.9) and (5.3.10), we can rewrite the difference in the chemical free energy using the modulation strain ε_0.

$$\frac{\Delta G^{ch}}{V}=\frac{N_V a_0^2}{4}\left[-8.75Ka_0^{-4.5}+\frac{RT}{\left\{a_{GaP}-a_{InAs}+D(y_0-x_0)\right\}^2}\times\left\{\frac{1}{x_0(1-x_0)}+\frac{1}{y_0(1-y_0)}\right\}\right]\varepsilon_0^2 \qquad (5.3.11)$$

From eq.(5.3.11) and the minimum elastic energy $\langle w_E\rangle_{min}$, we can estimate the critical temperature T_c (x_0,y_0) above which the phase is thermodynamically stabilized against composition modulation. The stability criteria is written as

$$\left(\frac{\Delta G^{ch}}{V}\right)_{x_0,y_0}+\langle w_E\rangle_{min}=0. \qquad (5.3.12)$$

The calculated critical temperatures for [100] and [110] modulations are shown in Fig.5.3.4. The strain stability effect is much larger for the elastically harder [110] modulation, which results in lower critical temperatures. Figure 5.3.5 is the plot of critical temperatures calculated assuming that the modulation occurs perpendicular to the lattice-match line in a composition diagram, that is, $\Delta x=-2.1\Delta y$. We note that the position of the maximum critical temperature is shifted and the critical temperatures are increased for the

alloys close to the lattice-matched $In_{0.533}Ga_{0.467}As$ ternary alloy side.

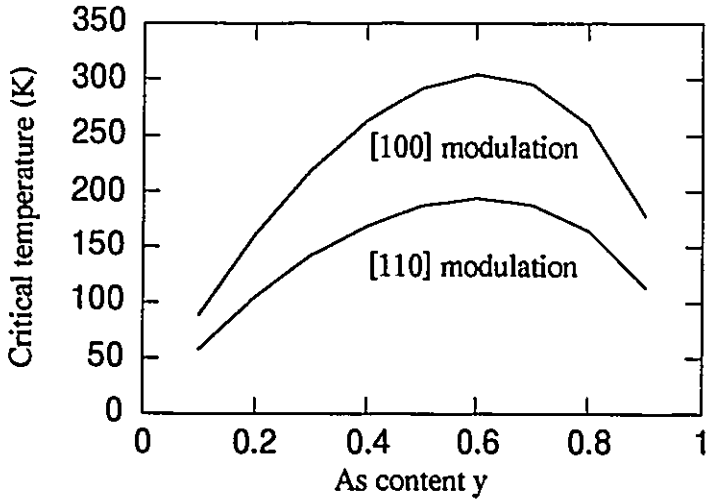

Fig.5.3.4 Thermodynamic critical temperatures of $In_{1-x}Ga_xAs_yP_{1-y}$ alloy film lattice-matched to (001) InP for [100] and [110] modulations. The modulation is assumed to occur along $\Delta x=-\Delta y$.

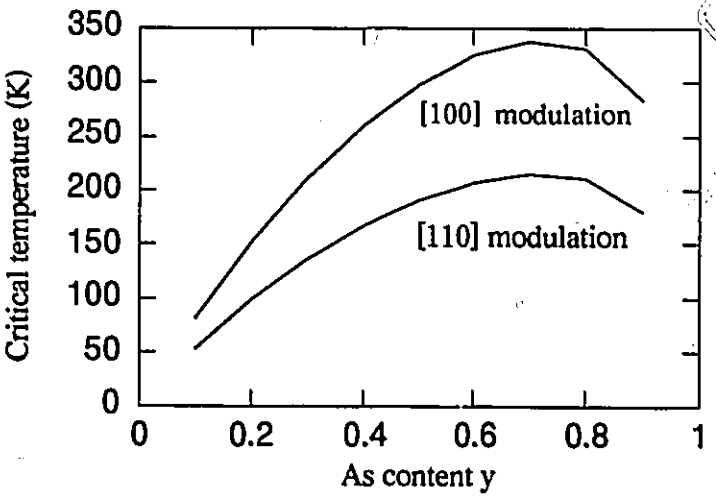

Fig.5.3.5 Critical temperatures when the modulation occurs along $\Delta x=-2.1\Delta y$.

The critical temperature for a ternary alloy can be derived following the same procedures as for a quaternary alloy. The difference in the chemical free energy between the modulated and the homogeneous alloys is written as

$$\frac{\Delta G^{ch}}{V} = \frac{N_V}{4}\{-8.75K(\frac{\partial a}{\partial x})^2 a_0^{-4.5} + \frac{RT}{x_0(1-x_0)}\}(\Delta x)^2. \qquad (5.3.13)$$

The magnitude of the modulation of the strain ε_0 is

$$\varepsilon_0 = \frac{\Delta a}{a_0} = \frac{1}{a_0}(\frac{\partial a}{\partial x})\Delta x = \frac{a_{GaAs} - a_{InAs}}{a_0}\Delta x \qquad (5.3.14)$$

for $In_{1-x}Ga_xAs$ ternary alloy. Substituting eq.(5.3.14) into eq.(5.3.13), we obtain

$$\frac{\Delta G^{ch}}{V} = \frac{N_V a_0^2}{4}\{-8.75K\, a_0^{-4.5} + \frac{RT}{(a_{GaAs} - a_{InAs})^2}\frac{1}{x_0(1-x_0)}\}\varepsilon_0^2. \qquad (5.3.15)$$

Using the stability criteria eq.(5.3.12), the critical temperatures for [100] and [110] modulations are calculated as 305K and 193K, respectively.

As reviewed in Section 2.2, Glas (1987) developed the stability criteria against a composition modulation for III-V ternary alloy thin films with only one composition parameter (pseudo-binary alloy), assuming that the material is elastically isotropic. When analyzing ternary alloys, he used the elastic constants for a <100>-type direction to calculate the critical temperature. The critical temperature 320K he obtained for $In_{1-x}Ga_xAs$ alloy is in good agreement with the present result, 305K for [100] modulation.

Ipatova et al. (1993) derived critical temperatures for various III-V ternary alloy thin

films grown on (001) substrates taking into account the elastic anisotropy of the materials. They considered a composition modulation which occurs both in directions parallel to the substrate and in the growth direction. They found that the elastic energy associated with the composition modulation is minimized for a modulation which is sinusoidal in the [100] direction in the surface plane and decays exponentially with the depth from the surface. In this case the effect of the substrate-film interface can be ignored and the elastic energy corresponding to the modulation is 25% less than that calculated by Glas (1987). This leads to a prediction of higher critical temperature: 430K for $In_{1-x}Ga_xAs$ alloy film. The model proposed by Ipatova et al. (1993) may be applicable to experimental observations in which the modulation enhances as the film grows (Chu et al. (1985)). However, their model is not appropriate for the present observations in which the modulation starts from the very beginning of the film growth with its magnitude virtually unchanged through the film thickness.

Now it is apparent that none of the existing models based on thermodynamic free energy arguments can explain all of our observations of the [110] composition modulation. When the effect of elastic strain energy associated with a composition modulation are included in the analysis, the typical growth temperature (470°C) lies above the coherent miscibility gap for modulations along [100] or [110] directions in the plane of the film. Furthermore [100] rather than [110] modulations would be predicted since the [110] direction is elastically stiffer than [100]. The dimensions of our [110] modulation are observed to be larger in the [1 $\bar{1}$0] direction compared to the [110] direction as clearly shown in plan-view TEM. This anisotropy is consistent with the greater adatom diffusion length in the [1 $\bar{1}$0] direction on the (2×4) reconstructed (001) surface of GaAs where the surface atomic arrangement is anisotropic (Ohta et al. (1989), Hata et al. (1990)).

These results suggest that [110] composition modulations are caused by two-

dimensional phase separation occurring at the growing surface, which is then frozen into the film due to the very low diffusion rate in the bulk state at typical MBE growth temperatures. Just as ordering in $In_{1-x}Ga_xAs_yP_{1-y}$ alloy grown at higher temperatures is controlled by surface reconstruction (Philips et al. (1994)), it is likely that the present results are associated with surface driven phenomena. The future construction of a surface composition model is expected to experience a major difficulty due to the fact that a large number of atoms composing the modulation would have to be involved in any model.

Chapter 6

Morphological instability of strained layer surface

6.1 Introduction

For the application of semiconducting strained layers to optoelectronic devices, it is important to achieve the uniformity of layer thickness everywhere on a flat substrate. Conventionally, it has been assumed that the problem of thickness uniformity is closely related to the growth mode of heteroepitaxy. As reviewed in Section 2.3, the growth mode transition from two-dimensional (2D) layer-by-layer mode to three-dimensional (3D) island forming mode has been attracting much attention from both experimental and theoretical viewpoints. This is because the stress concentration associated with surface undulations (Gao (1991)) and/or the coalescence of 3D islands (Androussi et al. (1995)) provide preferred sites for defect formation e.g. dislocations and stacking faults which may deteriorate the device performance.

Most of the observations reviewed in Section 2.3 are of a single highly strained film deposited on a (001) flat substrate, for example Ge on Si (Eaglesham and Cerullo (1990)), InAs on GaAs (Guha et al. (1991)) or other highly strained systems, e.g. $In_{1-x}Ga_xAs/GaAs$ and $Si_{1-x}Ge_x/Si$, which were designed to have a relatively large misfit strain with a magnitude typically larger than 2%. In these examples Stranski-Krastanov growth was found, i.e. 3D islands isolated from each other were formed on a thin flat strained film composed of 2-3 monolayers. On the other hand, when the magnitude of misfit strain is relatively small (<1%), it is known that an undulation with wavelength of 1000-4000Å can be formed on the strained layer surface. Pidduck et al. (1992) and Dutartre et al. (1994) reported such a long-wavelength surface undulation in $Si_{1-x}Ge_x$ alloy films deposited on Si(001) substrates using chemical vapour deposition.

In this chapter, transmission electron microscopy (TEM) studies on the surface morphology of $In_{1-x}Ga_xAs_yP_{1-y}$ alloy strained layers grown on InP(001) substrates are described. Extensive cross-sectional TEM investigations were conducted using a Philips CM12 electron microscope operating at 120kV. Prominent composition modulations and surface undulations were observed only in the [1 $\bar{1}$0] cross-section, not in the [110] cross-section. The distinctive feature of our findings is that the surface morphology shows clear correlation with the composition modulation occurring predominantly along the [110] direction in the strained layers. Typical wavelength of the surface undulation is about 100-300Å which matches well with the periodicity of the composition modulation contrast. This short-wavelength surface undulation associated with composition modulation is more pronounced in tensile-strained layers than in compressively-strained layers. When the layer is under tension, the surface undulation is observed at relatively small strains (as low as 0.5%); on the other hand, layers with the same magnitude of compressive strain did not exhibit surface undulation. In addition, the surface undulation is composition dependent; the degree of undulation is not the same for all $In_{1-x}Ga_xAs_yP_{1-y}$ layers having the same tensile strain. The surface undulation is enhanced as the degree of composition modulation is increased. Finally, the undulation seems to be unaffected by plastic relaxation due to misfit dislocations. These features make it difficult to explain our findings in the context of the conventional growth mode transition models since the short-wavelength undulation we observe is apparently induced by the inherent composition modulation in $In_{1-x}Ga_xAs_yP_{1-y}$ alloys.

6.2 Results

6.2.1 Effect of strain on surface morphology

A series of samples #421, #501 and #502 were grown to examine the effect of the magnitude and sign of the strain on the surface morphology of the strained layers. In these samples, the In to Ga ratio was fixed (x=0.3) for all strained layers and various tensile and compressive strains were explored by varying the As to P ratio. All growth was conducted at 470°C.

In the sample #421, five strained layers of $In_{0.7}Ga_{0.3}As_{0.2}P_{0.8}$ having 1.5% tensile strain and four marker layers of $In_{0.7}Ga_{0.3}As_{0.468}P_{0.352}$ (20Å thick) being lattice-matched to InP were grown as shown in Fig.6.2.1. These layers were separated from each other by 200Å thick InP layers. By systematically varying the thickness of the $In_{0.7}Ga_{0.3}As_{0.2}P_{0.8}$ layers, we can observe the evolution of the surface undulation with the layer thickness. In Fig.6.2.1, each layer is designated as T1~T5 for the tensile-strained layers or as M1~M4 for the marker layers.

The samples #501 and #502 have the same geometry, shown in Fig.6.2.2. Two different magnitudes of strain (0.5% and 1.0%) were built into the strained layers. In sample #501, all strained layers are under tension; they are 100Å and 460Å thick $In_{0.7}Ga_{0.3}As_{0.5}P_{0.5}$ (0.5% tension) layers and 60Å and 190Å thick $In_{0.7}Ga_{0.3}As_{0.35}P_{0.65}$ (1.0% tension) layers. In the sample #502, all strained layers are under compression; they are 100Å and 460Å thick $In_{0.7}Ga_{0.3}As_{0.8}P_{0.2}$ (0.5% compression) layers and 60Å and 190Å thick $In_{0.7}Ga_{0.3}As_{0.95}P_{0.05}$ (1.0% compression) layers. These strained layers are separated from each other by a 1200Å thick InP layer. In Fig.6.2.2, each layer is designated as T1~T4 for tensile-strained layers in #501 or as C1~C4 for compressively-strained layers in #502.

The composition of each strained layer in samples #421, #501 and #502 is plotted in

the composition diagram of Fig.6.2.3.

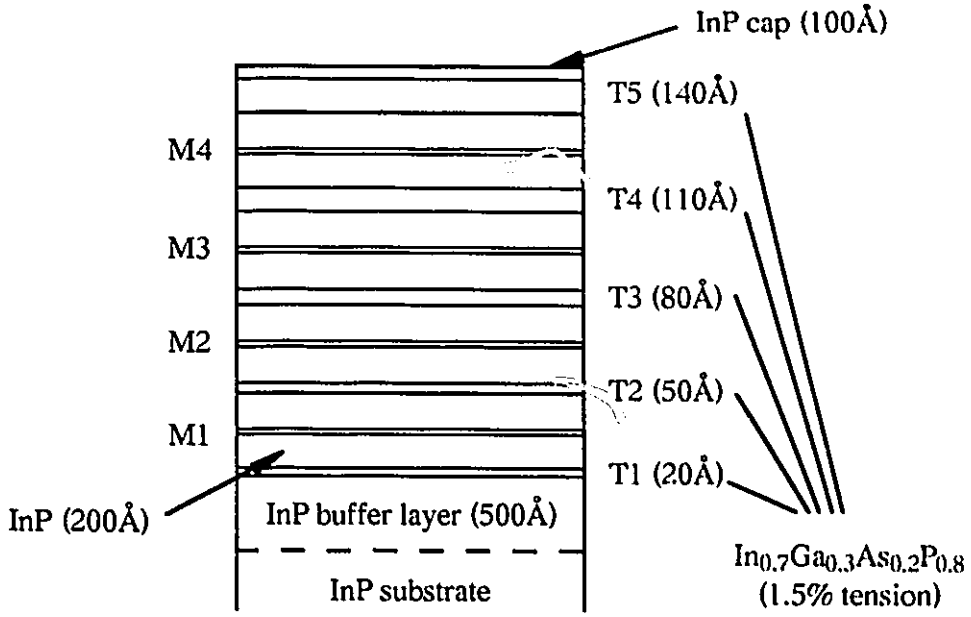

Fig.6.2.1 Structure of #421. The layers T1-T5 with the composition of $In_{0.7}Ga_{0.3}As_{0.2}P_{0.8}$ are under 1.5% tensile strain. The marker layers M1-M4 are 20Å thick $In_{0.7}Ga_{0.3}As_{0.648}P_{0.352}$ being lattice-matched to InP. All layers are separated by 200Å thick InP spacer layers.

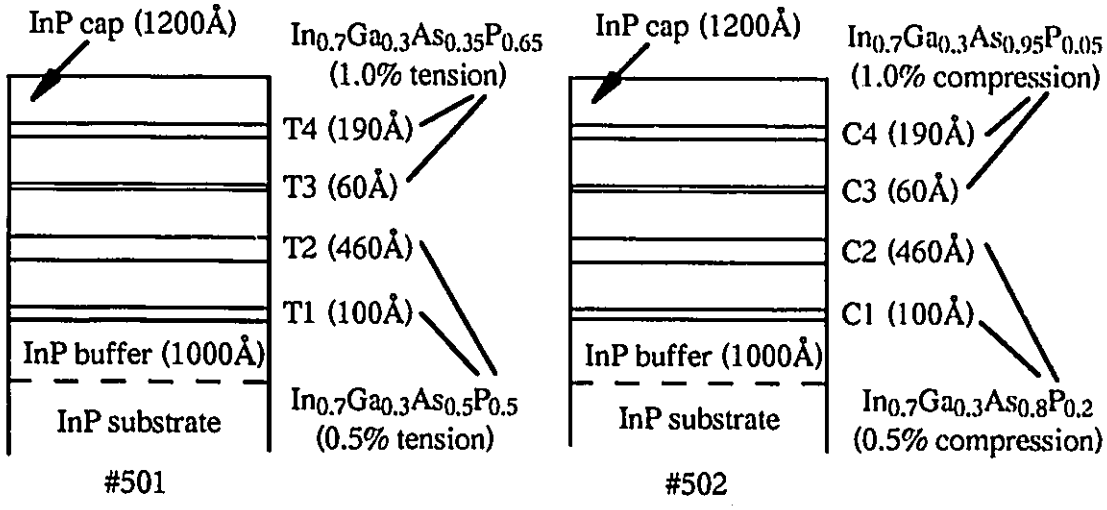

Fig.6.2.2 Structure of samples #501 and #502. All layers are separated by 1200Å thick InP spacer layers.

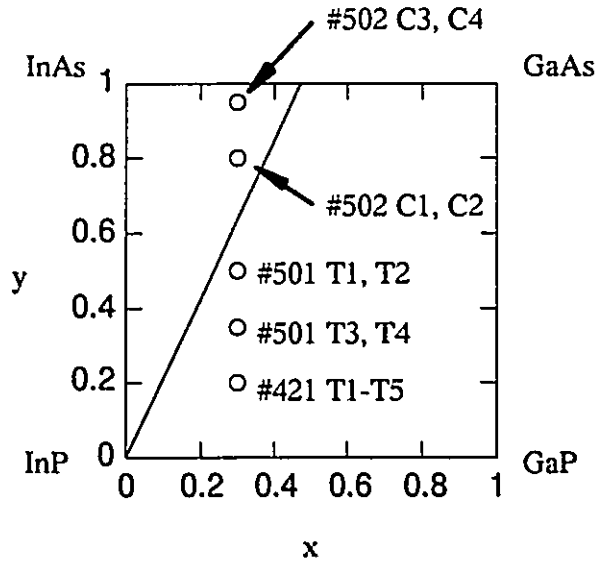

Fig.6.2.3 Composition of strained layers in #421, #501 and #502.

[1 $\bar{1}$0] cross-sectional TEM observations for sample #421 are shown in Fig.6.2.4 (a) and (b). Both micrographs were taken in dark field mode with **g**=00 $\bar{4}$ for (a) and **g**=220 for (b). The surface undulation of the tensile-strained layers seems to have started in the 50Å thick T2 layer and becomes more prominent as the layer thickness increases. In the 140Å thick T5 layer, some parts of the undulated surface consist of well-developed facet planes. The wavelength of the undulation is about 100-150Å and its amplitude is about 20Å. Since the top and bottom interfaces of the lattice-matched marker layers M1~M4 are flat, we know that the flat surface of InP is recovered at least after the growth of 200Å-thick InP. When imaged using a **g** vector parallel to the interface (**g**=220; Fig.6.2.4 (b)), the composition modulation is seen to be constant in all $In_{1-x}Ga_xAs_yP_{1-y}$ layers. The modulation contrast becomes clearer as the layer thickness increases.

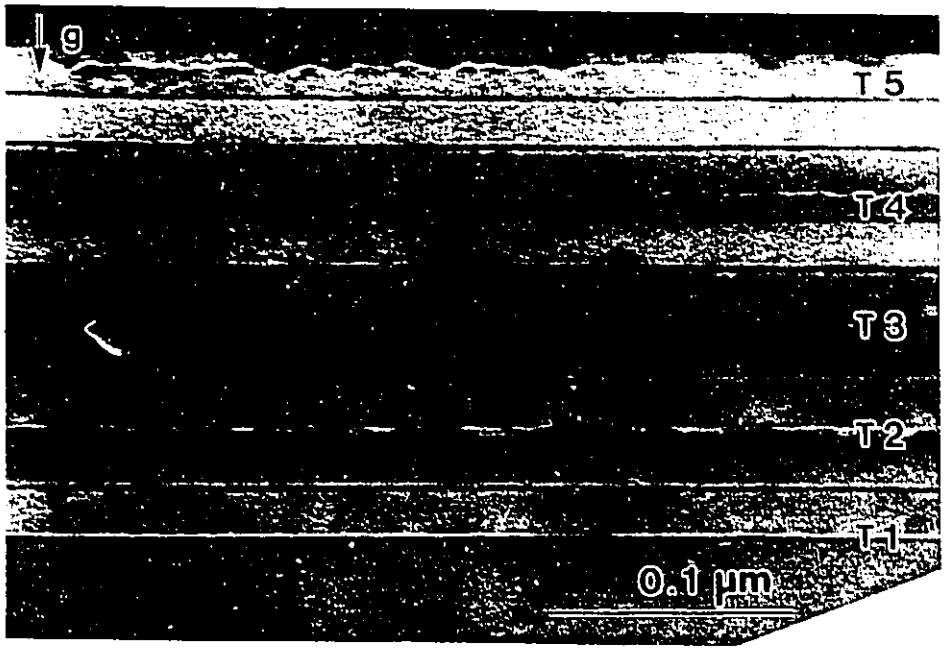

(a) g=00 $\bar{4}$

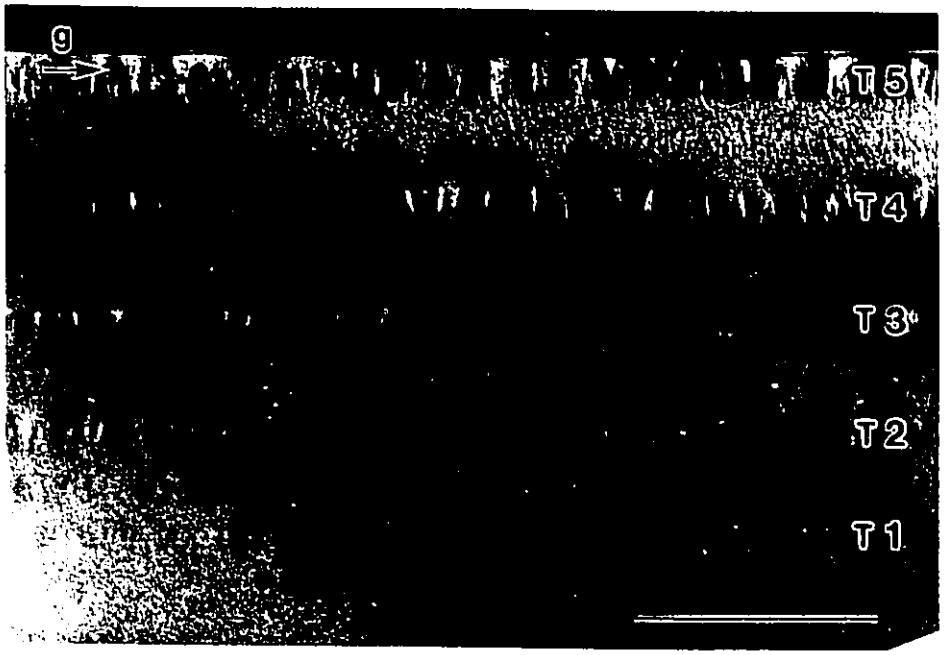

(b) g=220

Fig.6.2.4 [1 $\bar{1}$0] cross-sectional dark field images of #421 taken with g=00 $\bar{4}$ (a) and g=220 (b). The marker is 0.1μm.

(a) g=00 $\bar{4}$

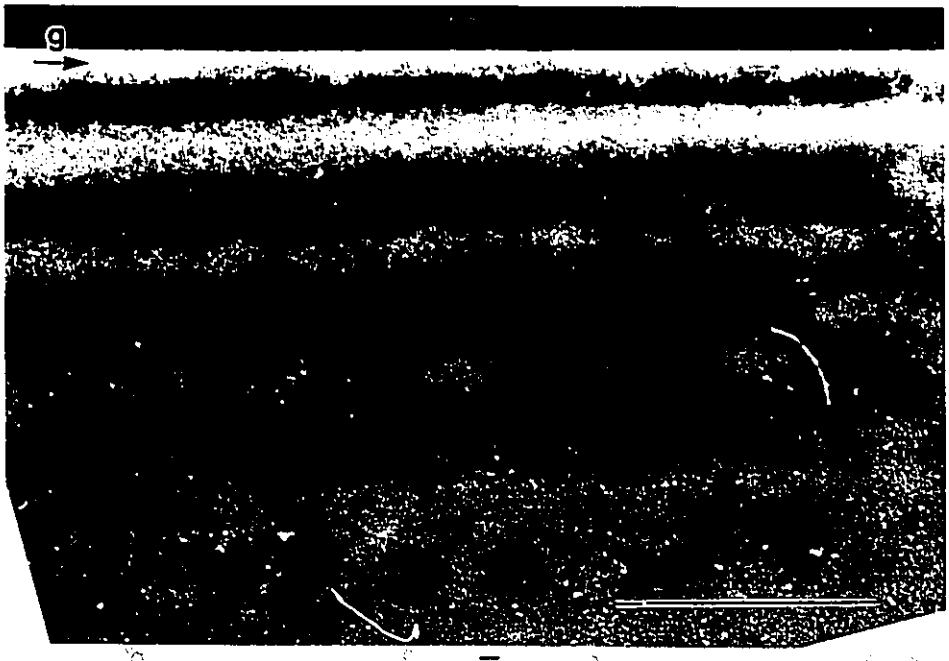

(b) g= $\bar{2}20$

Fig.6.2.5 [110] cross-sectional dark field images of #421 taken with g=00 $\bar{4}$ (a) and g= $\bar{2}20$ (b). The marker is 0.1μm.

The morphological features of the strained layers seen in [110] cross-section are totally different from those observed in [1 $\bar{1}$0] cross-section. Figure 6.2.5 (a) and (b) are the dark field TEM images of the [110] cross-section of sample #421. From the observation under g=00 $\bar{4}$ (Fig.6.2.5 (a)), it is clear that there is no short-wavelength undulation or crystallographic facets at the strained layer surfaces although we can recognize a small irregular long-wavelength undulation. Observations from [1 $\bar{1}$0] and [110] directions indicate that the surface undulation in these 1.5% tensile-strained layers extends only along the [1 $\bar{1}$0] direction.

Similar to the surface morphology, the composition modulation in these layers is also anisotropic in the two <110> directions. In fact, composition modulation contrast does not appear when imaged with a **g** vector parallel to the interface in [110] cross-section (**g**= $\bar{2}$20; Fig.6.2.5 (b)). Therefore, the modulation we observe in the sample #421 is not a classical spinodal decomposition occurring along [100] and [010] directions but, as in the lattice-matched samples (Chapter 5), is a modulation occurring only along the [110] direction.

The 0.5% and 1.0% tensile-strained layers in sample #501 show similar morphological features as observed in sample #421 although the magnitude of the surface undulation is much smaller. Figure 6.2.6 (a) and (b) are the dark field images of the [1 $\bar{1}$0] cross-section of sample #501. At the top surfaces of layers T2 and T4 in Fig.6.2.6 (a), quasi-periodic black-white contrast caused by the short wavelength (100-200Å) surface undulation is observed. The amplitude of the undulation is very small, typically about 5-10Å. When observed with g=220 (Fig.6.2.6 (b)), we can recognize clear periodic composition modulation contrast with a wavelength of 100Å in all tensile-strained layers.

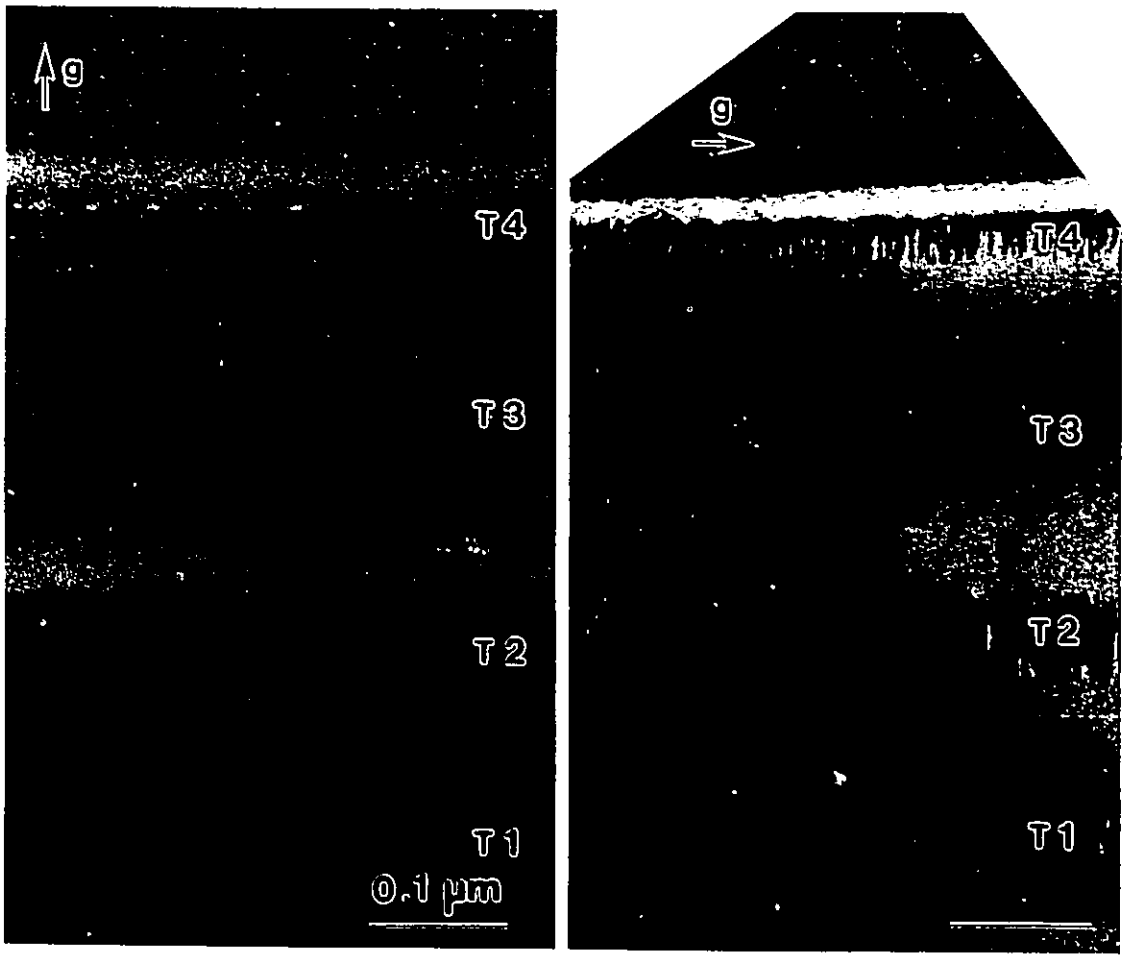

(a) g=004 (b) g=220

Fig.6.2.6 [1 $\bar{1}$0] cross-sectional dark field images of sample #501 taken with g=004 (a) and g=220. The marker is 0.1μm.

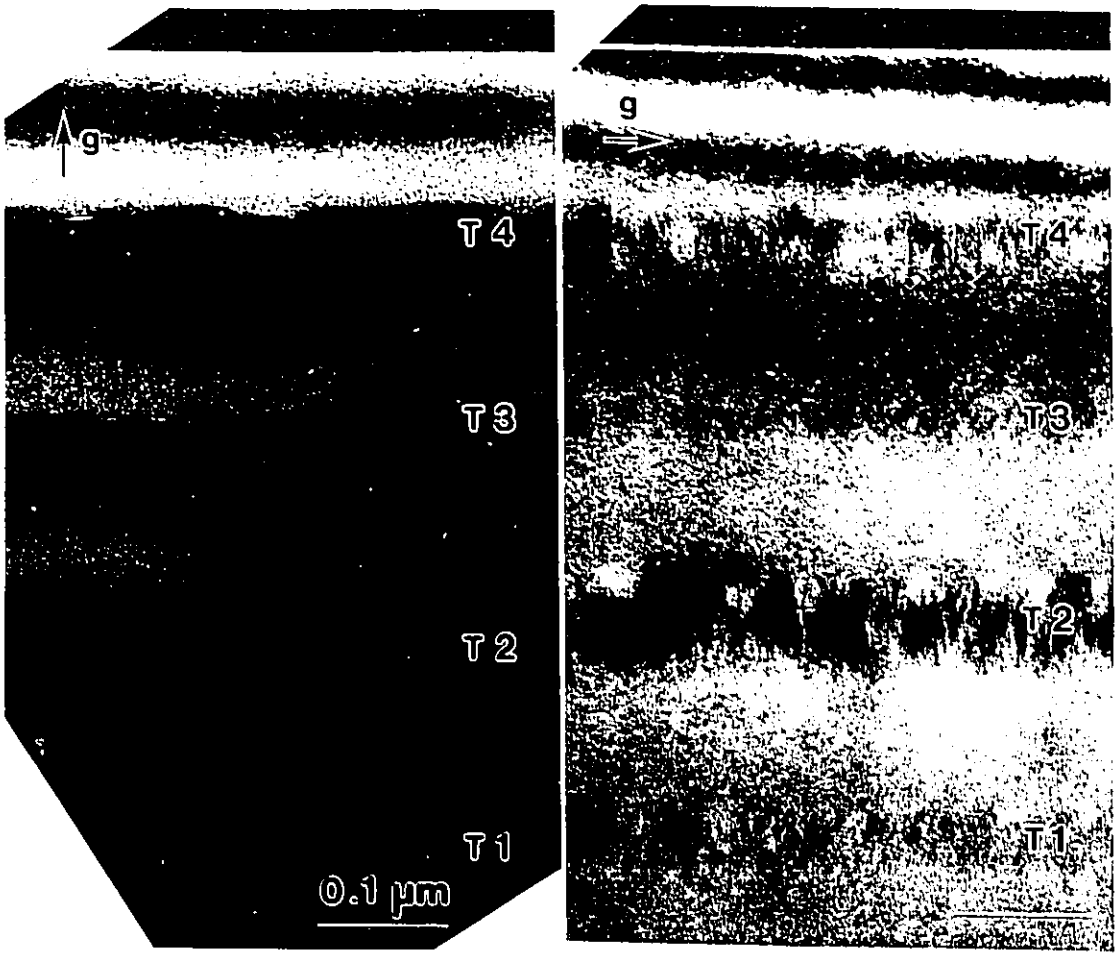

(a) g=004 (b) g= $\bar{2}20$

Fig.6.2.7 [110] cross-sectional dark field images of sample #501 taken with g=004 (a) and g= $\bar{2}20$ (b). The marker is 0.1μm.

[110] cross-sectional micrographs for sample #501 are presented in Fig.6.2.7. Although there is a small and irregular undulation at the layer surfaces, its wavelength is much larger than the undulation wavelength observed in [1 $\bar{1}$0] cross-section. The composition modulation contrast under g=2 $\bar{2}$0 (Fig.6.2.7 (b)) is weaker and less sharp than that observed with g=220 in the [1 $\bar{1}$0] cross-section. There are two possible explanations about how the modulation contrast is formed in the [110] cross-section: the first one is that the overlapped images of the modulated regions extending along the [1 $\bar{1}$0] direction cause a complex contrast in the [110] cross-section; the other possibility is that the modulation occurs both in [1 $\bar{1}$0] and [110] directions but with much weaker intensity along the [1 $\bar{1}$0] direction. Although it is difficult to specify which is the correct model, we can at least conclude that the modulation we observe is not the classical spinodal type occurring in both [100] and [010] directions with much larger wavelength (1000-2000Å). If classical spinodal decomposition had occurred in our samples, the modulation contrast should have been similar in [1 $\bar{1}$0] and [110] cross-sections.

In the compressively-strained layers in sample #502, no surface undulation was observed in either [1 $\bar{1}$0] or [110] cross-sections. Figure 6.2.8 (a) and (b) are the dark field images of the [1 $\bar{1}$0] cross-section of sample #502. As is apparent from Fig.6.2.8 (a), the top surface of each compressively-strained layer C1~C4 is flat. There is no quasi-periodic black-white contrast associated with the surface undulation as observed in Fig.6.2.6 (a). When imaged using g=220 (Fig.6.2.8 (b)), periodic composition contrast is less pronounced than that in the corresponding tensile-strained layers in #501.

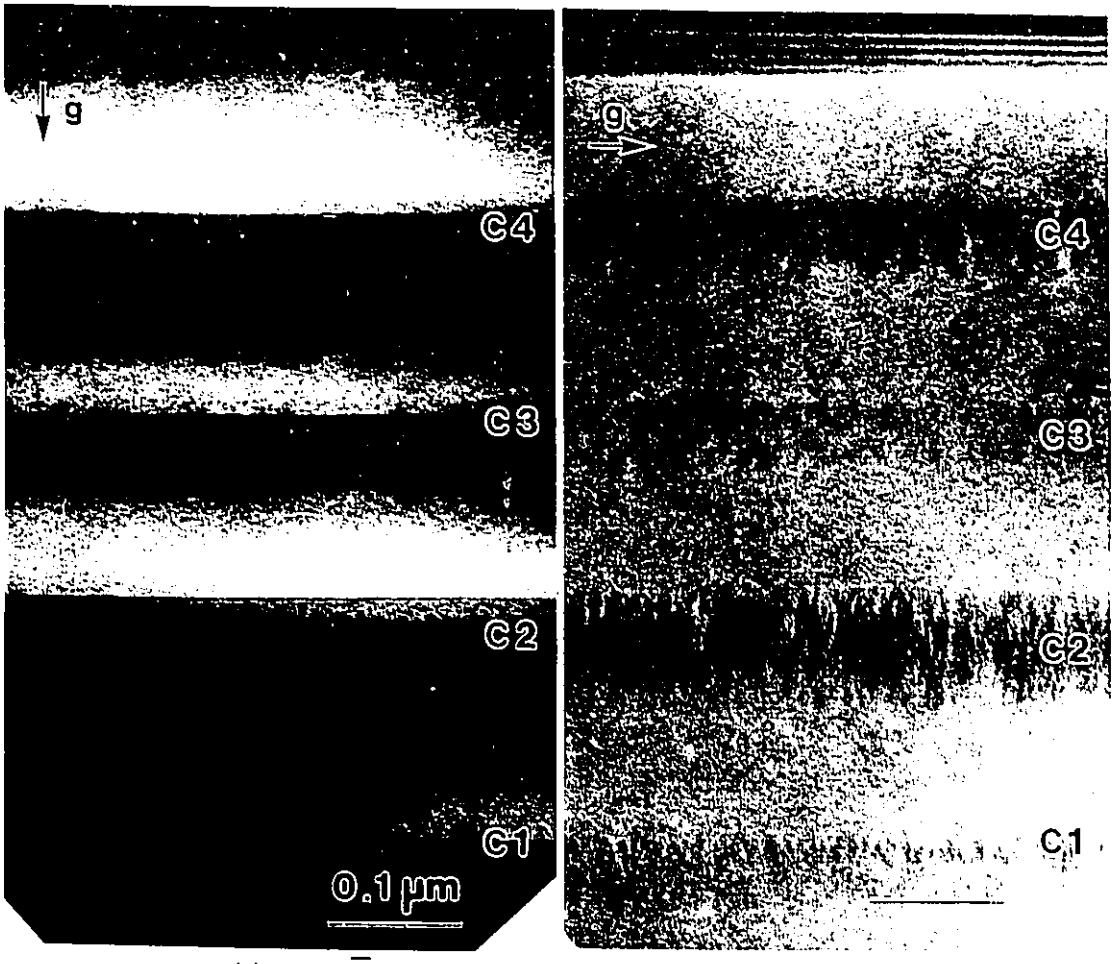

(a) g=00 $\bar{4}$ (b) g=220

Fig.6.2.8 [1 $\bar{1}$0] cross-sectional dark field images of sample #502 taken with g=00 $\bar{4}$ (a) and g=220 (b). The marker is 0.1μm.

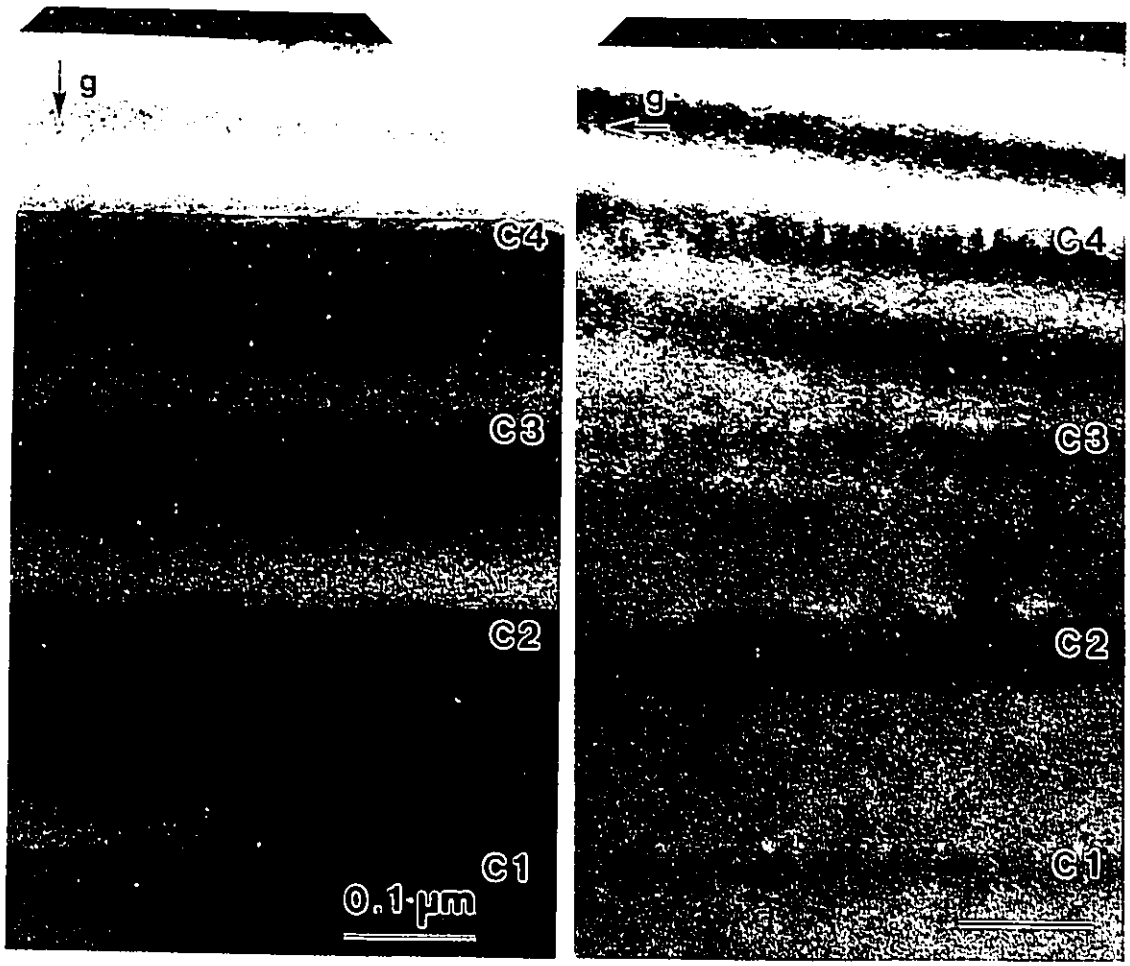

(a) g=00 $\bar{4}$ (b) g=2 $\bar{2}$0

Fig.6.2.9 [110] cross-sectional dark field images of sample #502 taken with g=00 $\bar{4}$ (a) and g=2 $\bar{2}$0 (b). The marker is 0.1μm.

[110] cross-sectional micrographs for the sample #502 are presented in Fig.6.2.9. The top surface is flat for each compressively-strained layer (Fig.6.2.9 (a)). Very weak modulation contrast appears when imaged with g=2 $\bar{2}$0 (Fig.6.2.9 (b)).

The observations in samples #421, #501 and #502 suggest that a composition modulation, predominantly occurring along the [110] direction in tensile-strained layers, helps to promote the surface undulation.

6.2.2 Effect of growth temperature on surface morphology

Samples #899, #900, #901 and #902 were designed to examine the effect of growth temperature (450°C or 490°C) on the surface morphology of tensile- or compressively-strained layers of $In_{1-x}Ga_xAs$ ternary alloy. The $In_{1-x}Ga_xAs$ layers in samples #899 (growth temperature 490°C) and #900 (450°C) are under tension (Fig.6.2.10) while in samples #901 (490°C) and #902 (450°C) they are under compression (Fig.6.2.11). In these samples, all the strained layers are 500Å thick and are separated by a 1000Å thick InP layer. In each sample, the first strained layer (T1 or C1) and second strained layer (T2 or C2) were intended to have (+ or –) 0.6% strain and (+ or –) 0.3% strain, respectively. However, as shown in Fig.6.2.10 and Fig.6.2.11, the layer compositions were shifted slightly from the designed values. We should note that the compressively-strained layers have a larger magnitude of strain than the corresponding tensile-strained layers.

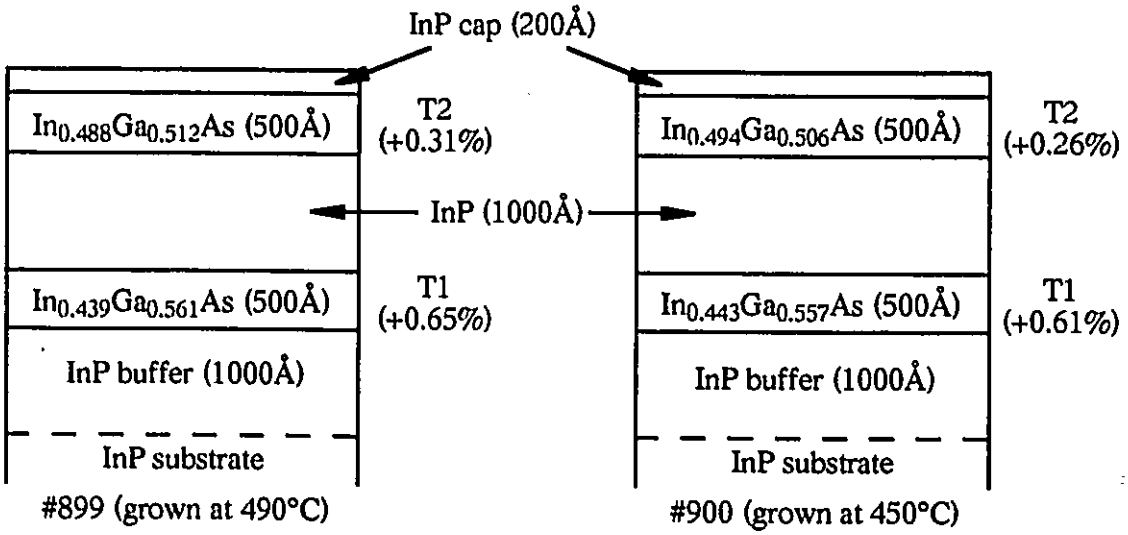

Fig.6.2.10 Structure of samples #899 and #900. All strained layers are under tension (positive strain).

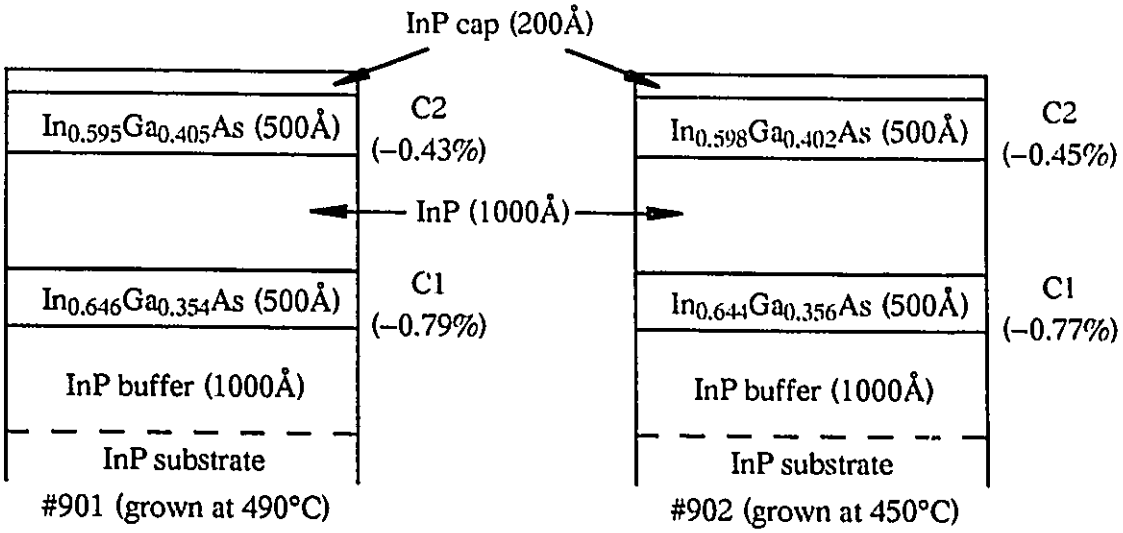

Fig.6.2.11 Structure of samples #901 and #902. All strained layers are under compression (negative strain).

In the following discussion, only the [1 $\bar{1}$0] cross-sectional TEM observations will be presented because, as we have already seen, they can represent the degree of surface undulation and composition modulation well.

[1 $\bar{1}$0] cross-sectional micrographs for these samples are presented in Fig.6.2.12 (#899 and #900) and in Fig.6.2.13 (#901 and #902). All micrographs were taken in dark field using **g**=(±)004 and **g**=(±)220. From these micrographs, it is apparent that clear evidence of surface undulation is only observed at the surface of T1 layer (0.65% tension) of the sample #899 grown at 490°C. There is no undulation at the compressively-strained layer surfaces in spite of the slightly larger magnitude of strain than in the corresponding tensile-strained layers. If we compare the two samples #899 and #900, the suppression of the surface undulation by lowering the growth temperature from 490°C to 450°C is clearly recognized.

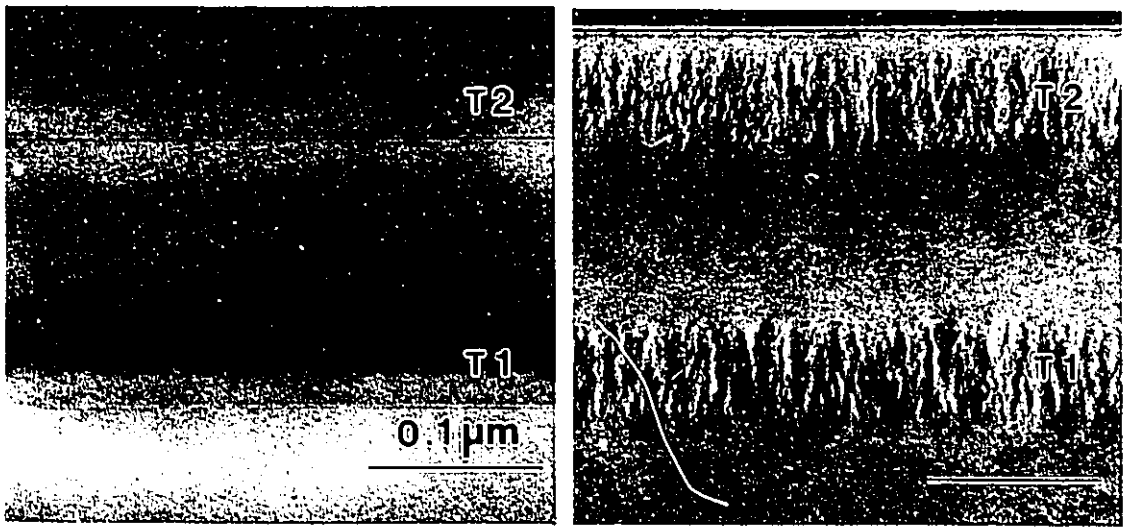

#899 (T1=+0.65%, T2=+0.31%) grown at 490°C

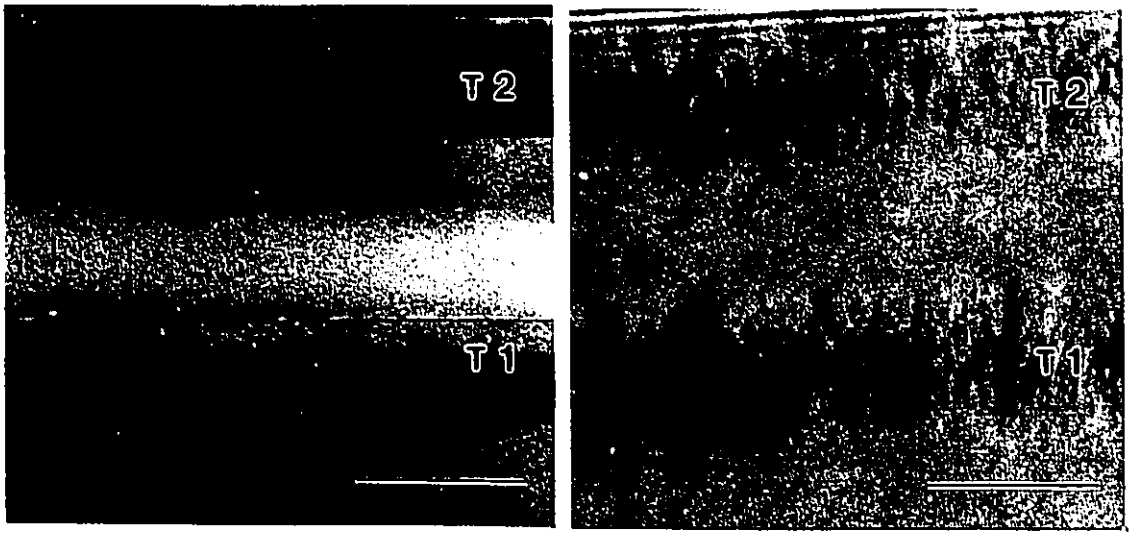

#900 (T1=+0.61%, T2=+0.26%) grown at 450°C

Fig.6.2.12 [1 $\bar{1}$0] cross-sectional dark field TEM images of samples #899 and #900. The diffraction vectors **g**=(±)004 (left) and **g**=(±)220 (right) were used. The marker is 0.1μm.

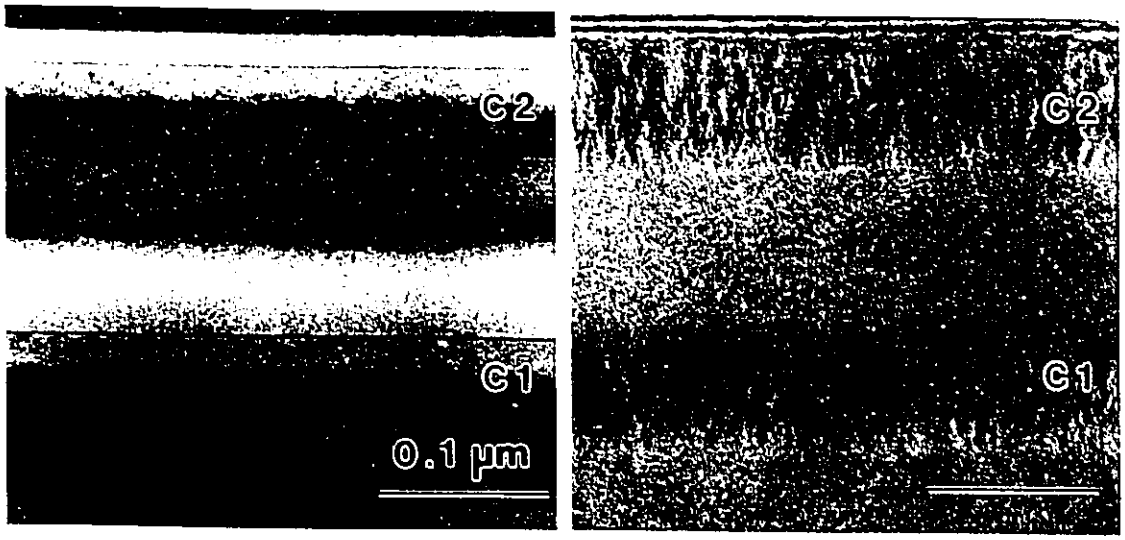

#901 (C1=–0.71%, C2=–0.43%) grown at 490°C

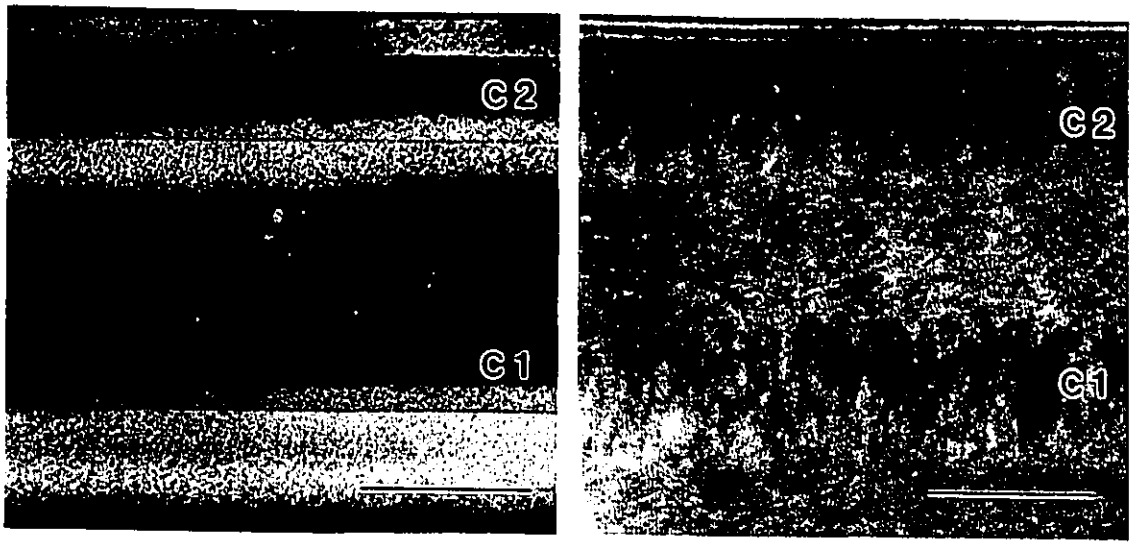

#902 (C1=–0.77%, C2=–0.45%) grown at 450°C

Fig.6.2.13 [1 $\bar{1}$0] cross-sectional dark field TEM images of samples #901 and #902. The diffraction vectors g=(±)004 (left) and g=(±)220 (right) were used. The marker is 0.1μm.

6.2.3 Composition dependence of surface undulation

In order to examine the dependence of strained layer surface morphology on the alloy composition, two series of samples, T(tension)-series and C(compression)-series, were grown. These samples have the same geometry shown in Fig.6.2.14. A 50Å thick $In_{1-x}Ga_xAs_yP_{1-y}$ strained layer was grown on a 1000Å thick InP buffer layer followed by a 500Å thick InP layer and a 1500Å thick $In_{1-x}Ga_xAs_yP_{1-y}$ layer. The structure was capped by a 250Å thick InP layer. Both the 50Å and 1500Å thick $In_{1-x}Ga_xAs_yP_{1-y}$ layers have the same composition. In these T- and C-series samples, all growth was carried out at 450°C. The T-series samples are #1147, #1146, #1141, #1127, #1131, #1137 and #1125 in which the composition of the tensile-strained layers was systematically varied along the 0.5% tensile strain line in a composition diagram (Fig.6.2.15). The C-series samples are #1142, #1126, #1132, #1140 and #1121 in which the composition of compressively-strained layers was systematically varied along the 0.5% compressive strain line (Fig.6.2.15).

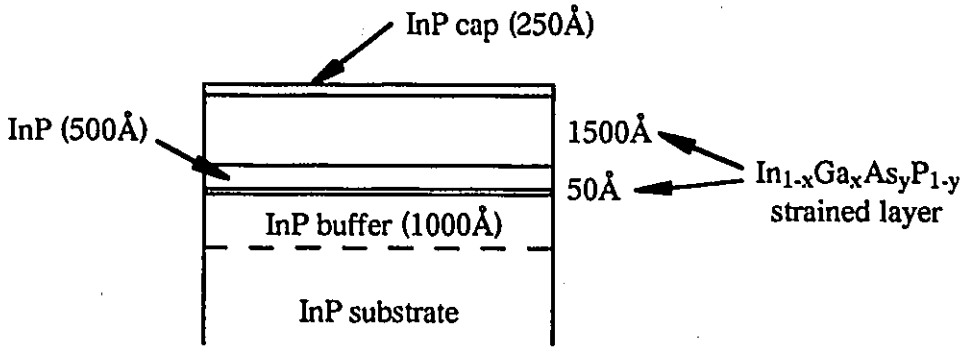

Fig.6.2.14 Structure of T(0.5% tension)- and C(0.5% compression)-series samples.

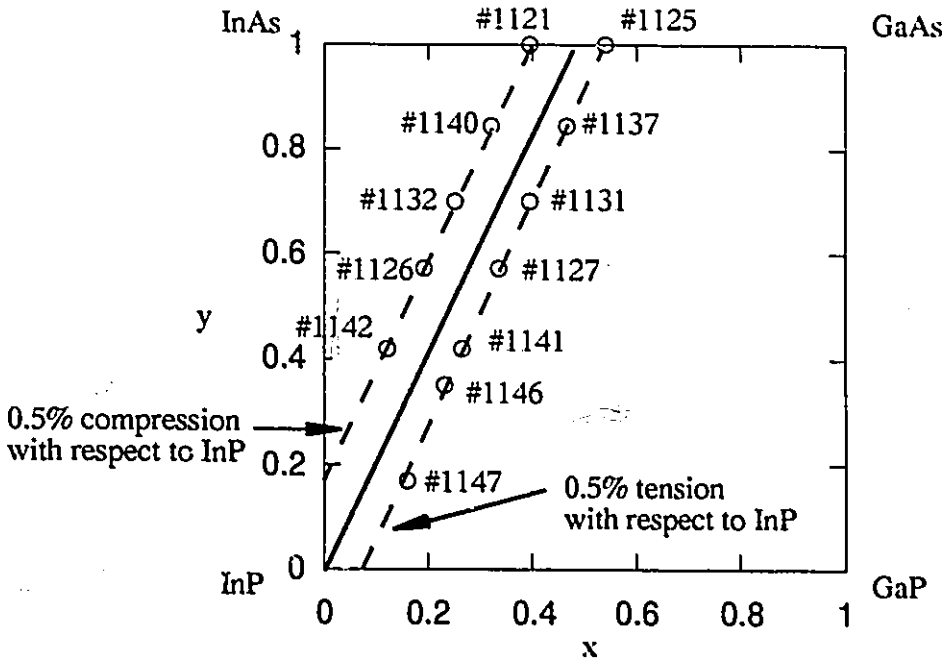

Fig.6.2.15 Composition of $In_{1-x}Ga_xAs_yP_{1-y}$ layers in T-series (tension) samples and C-series (compression) samples.

[1 $\bar{1}$0] cross-sectional TEM photographs of T-series samples taken in dark field mode using **g**=(±)004 and **g**=(±)220 are shown in Fig.6.2.16. The surface of the 1500Å thick 0.5% tensile-strained layer is flat for sample #1147 which is located closest to the InP side of the 0.5% tensile strain line. As the degree of composition modulation increases, a surface undulation starts to develop. A very small undulation is first seen in #1146 and becomes more prominent as the composition approaches the $In_{1-x}Ga_xAs$ ternary alloy side. There is a close correlation between the composition modulation and the surface undulation. We find that lowering the growth temperature to 450°C is not enough to avoid the surface undulation for most of the 0.5% tensile-strained alloys.

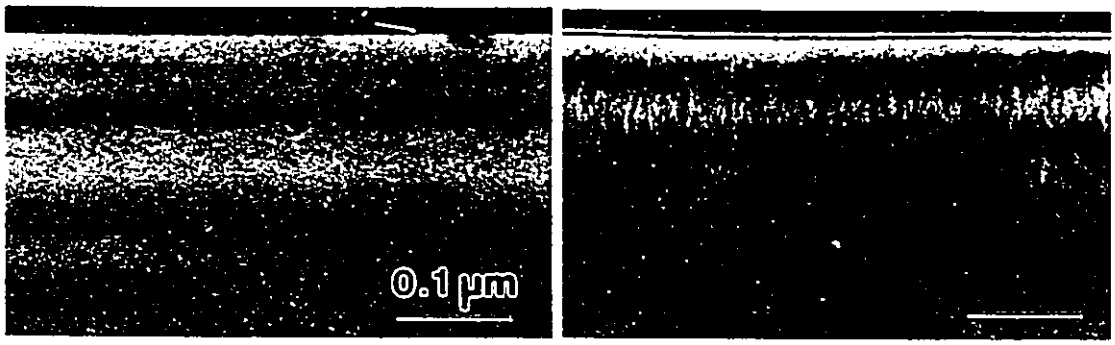

#1147 (x=0.16, y=0.17)

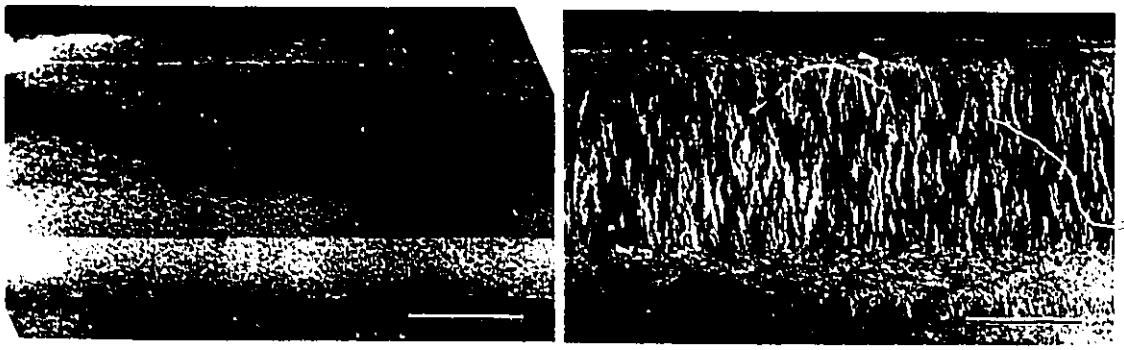

#1146 (x=0.232, y=0.35)

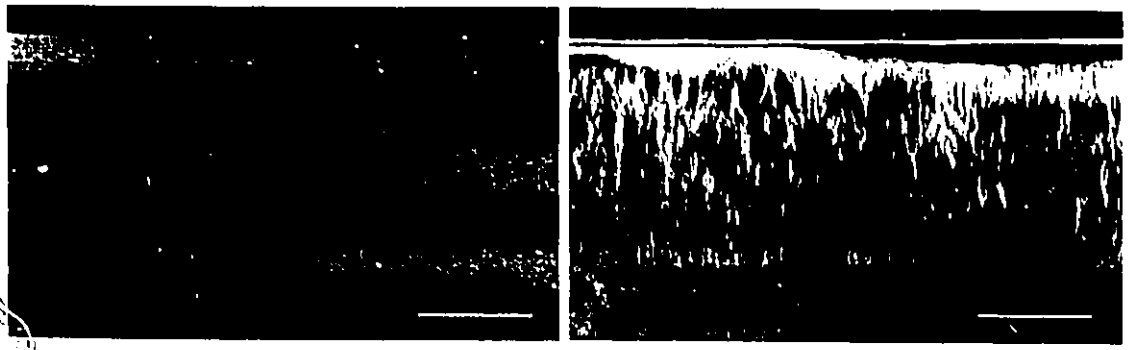

#1141 (x=0.265, y=0.42)

Fig.6.2.16 [1 $\bar{1}$0] cross-sectional dark field images of T-series (0.5% tension) samples taken with **g**=(±)004 (left) and **g**=(±)220 (right). The marker is 0.1μm.

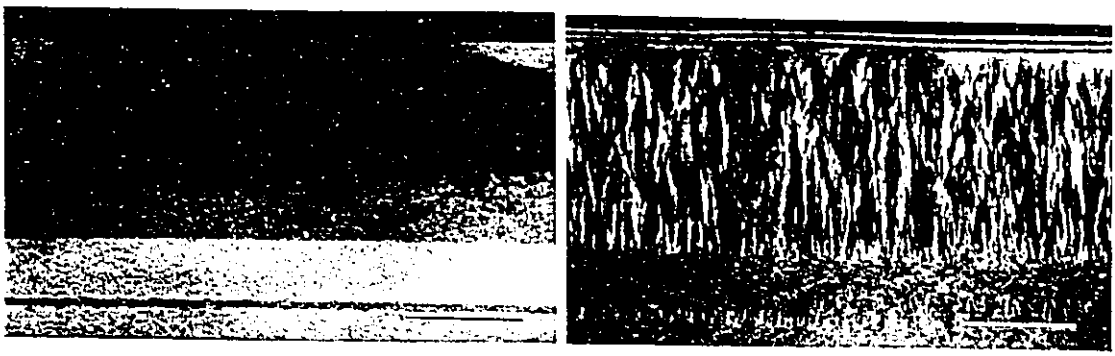

#1127 (x=0.336, y=0.572)

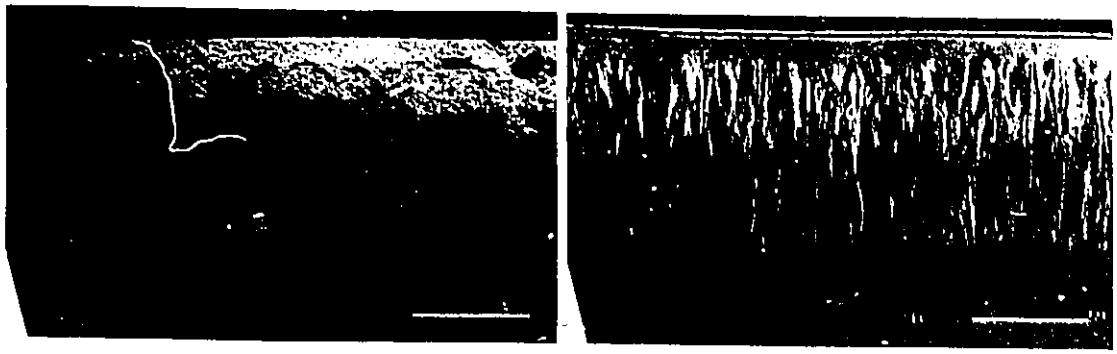

#1131 (x=0.395, y=0.7)

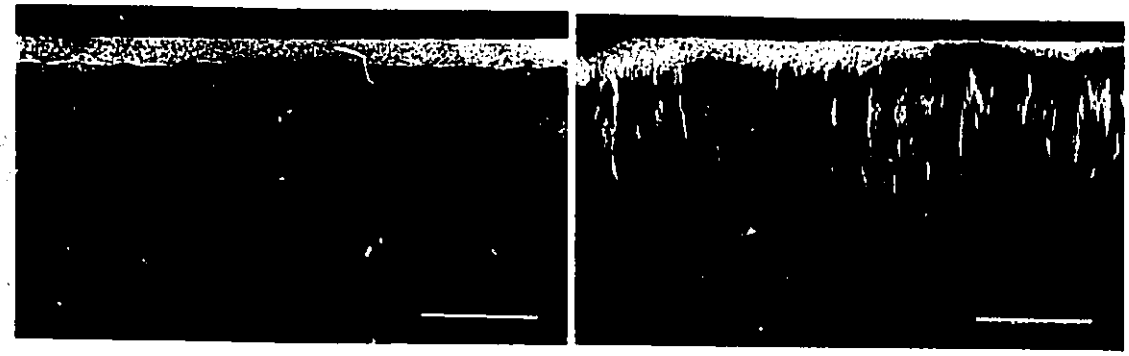

#1137 (x=0.465, y=0.846)

Fig.6.2.16 (continued)

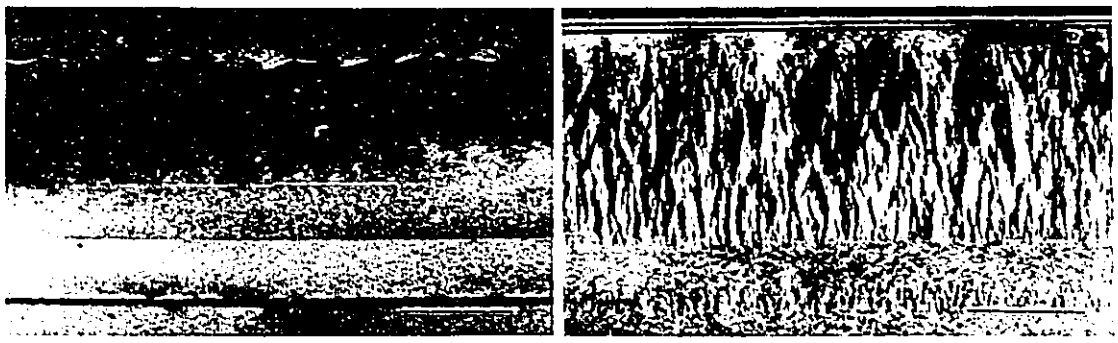

#1125 (x=0.54, y=1.0)

Fig.6.2.16 (continued)

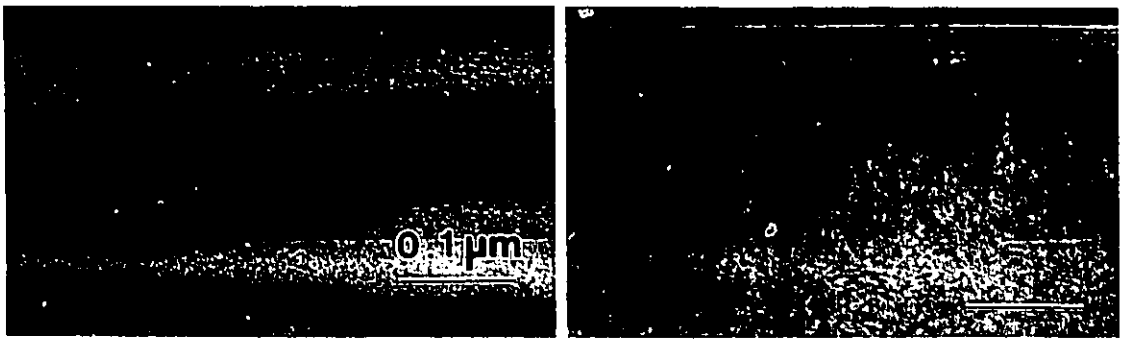

#1142 (x=0.121, y=0.42)

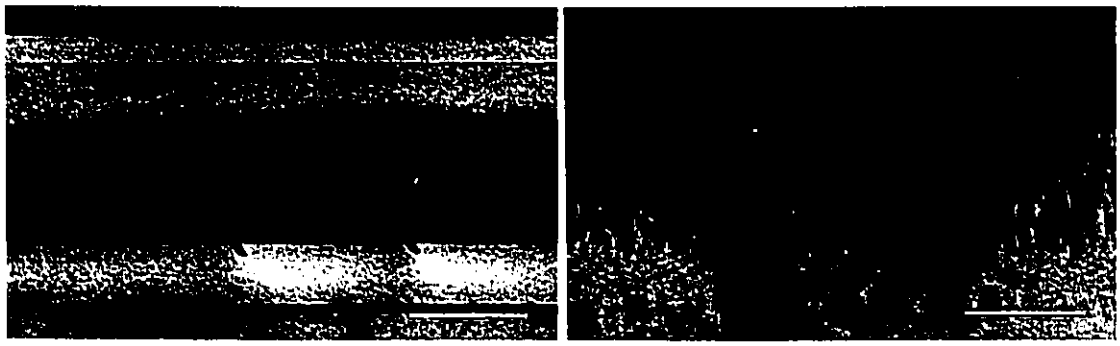

#1126 (x=0.192, y=0.572)

Fig.6.2.17 [1 $\bar{1}$0] cross-sectional dark field images of C-series (0.5% compression) samples taken with g=(±)004 (left) and g=(±)220 (right). The marker is 0.1μm.

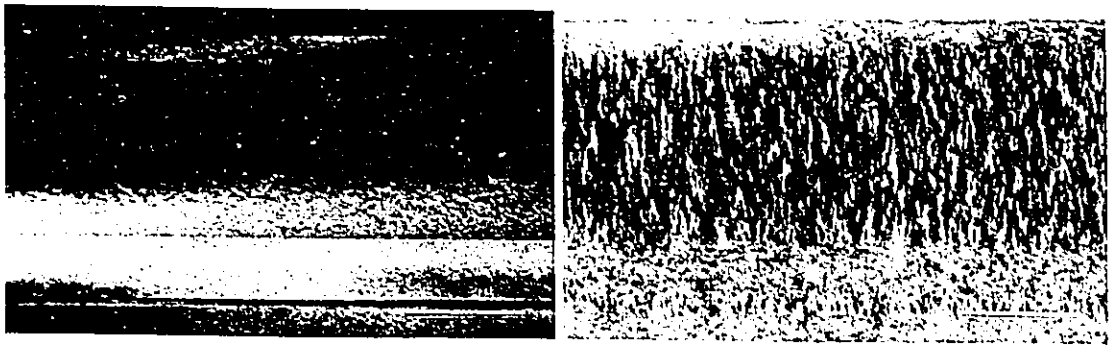

#1132 (x=0.251, y=0.7)

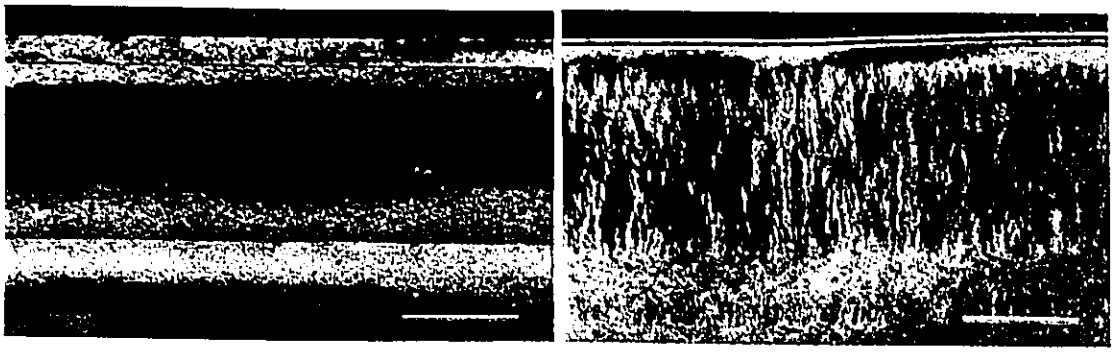

#1140 (x=0.321, y=0.846)

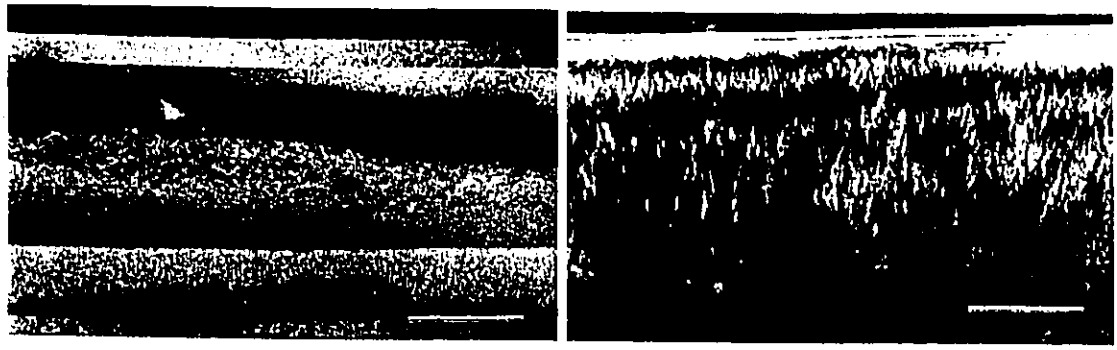

#1121 (x=0.395, y=1.0)

Fig.6.2.17 (continued)

When the layers are under compression, no evidence for surface undulation was found for all the compositions examined in the C-series samples. Dark field images of [1 $\bar{1}$0] cross-sectional TEM for the C-series samples are presented in Fig.6.2.17. Composition modulation contrast in these layers is much weaker or finer than the modulation contrast in some of the T-series samples which showed pronounced surface undulation.

The onset of surface undulation seems to have started from the very early stage of strained layer growth. [1 $\bar{1}$0] cross-sectional high-resolution TEM images for 50Å thick $In_{1-x}Ga_xAs$ ternary alloy layers in samples #1125 (0.5% tension) and #1121 (0.5% compression) are shown in Fig.6.2.18. These high-resolution observations were conducted using a JEOL 2010F field emission TEM operating at 200kV. The top surface of the 50Å thick tensile-strained $In_{0.46}Ga_{0.54}As$ layer in sample #1125 shows a periodic undulation (Fig.6.2.18 (a)). A periodic contrast variation inside the layer which is attributable to composition modulation is also recognized. We should note that this layer is fully constrained because the layer thickness (50Å) is much smaller than the critical thickness (400Å) for the introduction of misfit dislocations at the top and bottom interfaces. The high-resolution image of the 50Å thick compressively-strained $In_{0.605}Ga_{0.395}As$ layer in sample #1121 shows a flat top surface and uniform image intensity inside the layer except for composition transition layers at the interfaces with InP (Fig.6.2.18 (b)). The present results suggest that the surface undulation we observed is induced by the inherent composition modulation occurring along the [110] direction in the strained layer, and the morphological instability of the tensile-strained layer surface starts from the early stage of growth without the help of misfit dislocations at the interfaces.

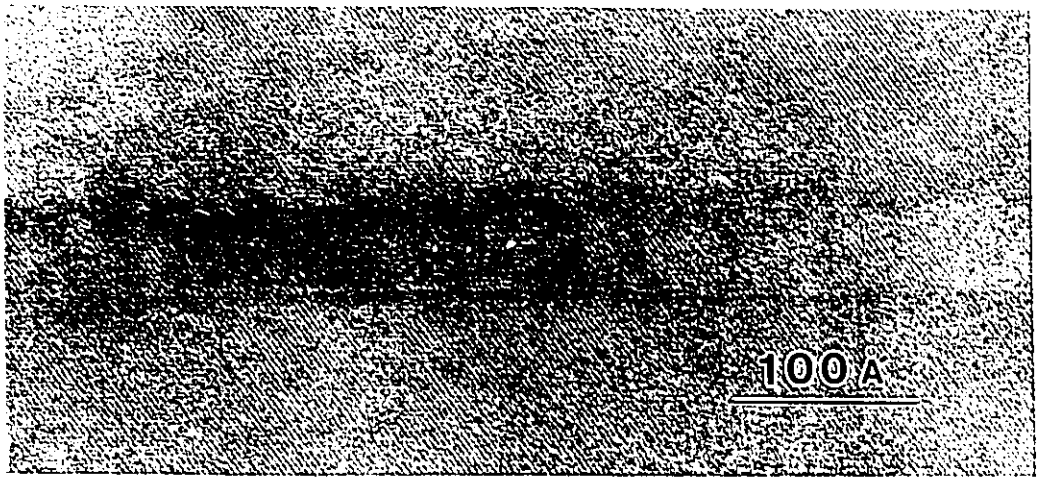

(a) 50Å thick $In_{0.46}Ga_{0.54}As$ (0.5% tension) layer of #1125

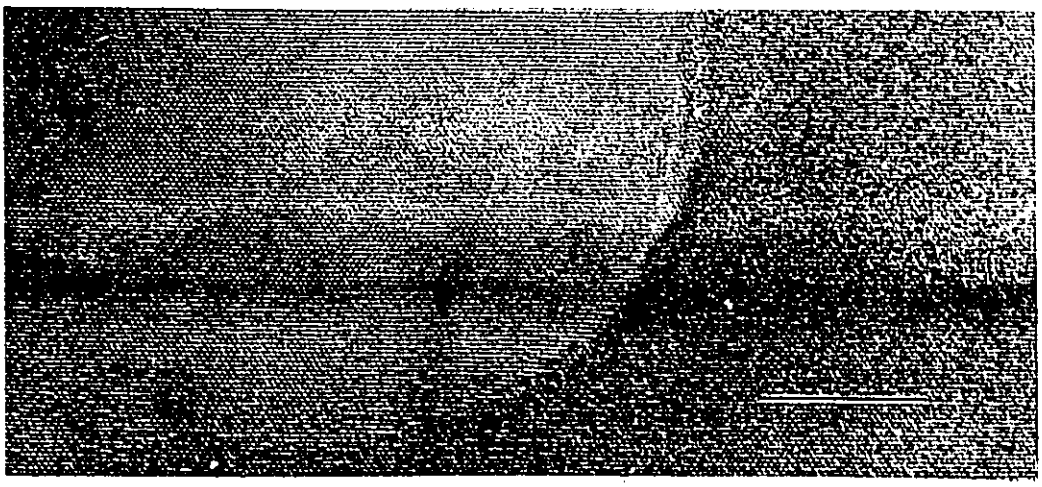

(b) 50Å thick $In_{0.605}Ga_{0.395}As$ (0.5% compression) layer of #1121

Fig.6.2.18 High-resolution images of [1 $\bar{1}$0] cross-section of 50Å thick $In_{1-x}Ga_xAs$ ternary alloy strained layers in #1125 (x=0.54) and #1121 (x=0.395). The circular area of damage in (b) was caused by the electron beam. The marker is 100Å.

6.2.4 Formation of surface faceting

Surface undulations in a thin tensile-strained layer leads to a faceted surface as the thickness of the layer increases. In Fig.6.2.19, [1 $\bar{1}$0] cross-sectional TEM image for sample #745 is shown. In this sample, a single $In_{0.446}Ga_{0.554}As$ alloy film with nominal thickness 3800Å was grown on a 1000Å thick InP buffer layer. The magnitude of tensile strain 0.6% built into this film is almost the same as that in the T1 layer of sample #899 which showed surface undulations (see Fig.6.2.12). As clearly observed in Fig.6.2.19, the surface is composed of distinct facets with plane indices close to (229) and ($\bar{2}$ $\bar{2}$9). When observed under g=(±)220 (Fig.6.2.20), we notice that the composition modulation is not uniform in the layer and its wavelength drastically changes at about 1000Å from the film/buffer layer interface. In the upper part of the film, the large-scale black-white modulation contrast which varies with the periodicity of about 1000Å matches well to the periodic surface faceting. The characteristic black-white modulation contrast reverses as the sign of **g** vector is reversed as shown in Fig.6.2.20 (a) and (b).

When observed in [110] cross-section with g=004 (Fig.6.2.21 (a)), only a small and irregular surface undulation is recognized. The undulation has no crystallographic features. The composition modulation contrast in Fig.6.2.21 (b) also lacks periodic nature.

The anisotropy of surface undulation between the two <110> directions is succeeded by well-developed faceting. However, any model to describe the transition process from the undulation to a well-developed facet is not simple because we have to handle non-uniform growth of undulation and coalescence of the undulation peaks, which results in very complex alloy composition distribution along the growing surface in the transition stage.

Fig.6.2.19 [1 $\bar{1}$0] cross-sectional dark field image of sample #745 taken with g=00 $\bar{4}$. $In_{0.446}Ga_{0.554}As$ film having 0.6% tensile strain is grown on a InP buffer. The nominal thickness of the film is 3800Å.

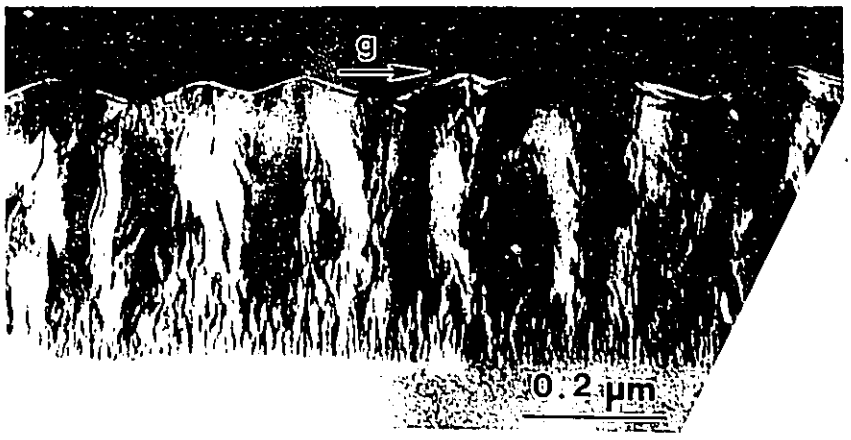

(a) g=220

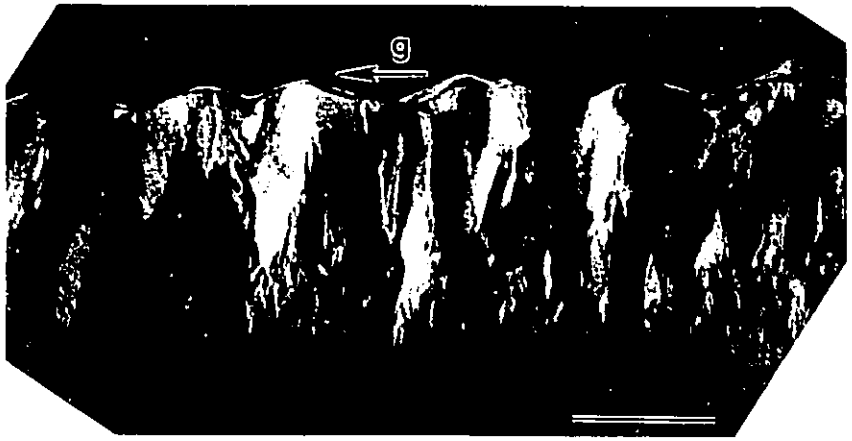

(b) g= $\bar{2}\ \bar{2}0$

Fig.6.2.20 [1 $\bar{1}$0] cross-sectional dark field images of sample #745. Note that the black-white contrast is reversed by reversing the g vector. The marker is 0.2μm.

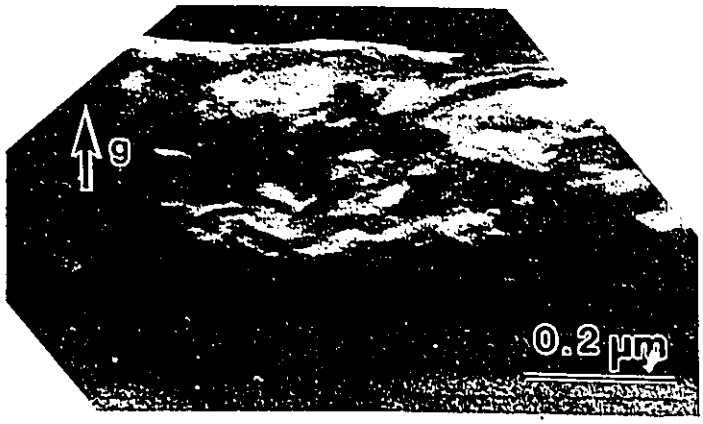

(a) g=004

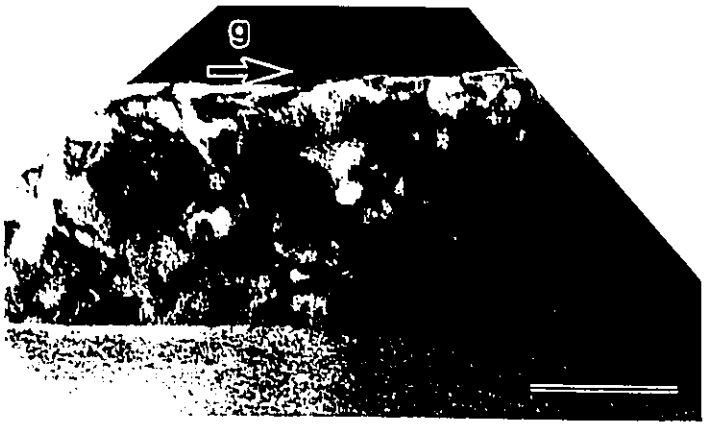

(b) g= $\bar{2}20$

Fig.6.2.21 [110] cross-sectional dark field images of sample #745 taken with g=004 (a) and g= $\bar{2}20$ (b). The marker is 0.2μm.

The variation of the Ga to In ratio along the faceted surface was examined for [1 $\bar{1}$0] cross-sectional TEM sample of #745 using energy dispersive x-ray analysis on the JEOL 2010F field emission TEM. Two series of x-ray data were collected; one for locations about 400Å away from and parallel to the facet planes and the other for deeper locations about 800Å away from the surface and parallel to the film/buffer interface plane. The calculated Ga to In ratio for each position is plotted in Fig.6.2.22. In this figure, V denotes the valley position and P denotes the peak position in the faceted surface. We can clearly recognize the periodic variation of the alloy composition which matches the periodicity of the surface faceting. The peak position is Ga-rich and the valley position is relatively In-rich. This is probably because In atoms, being larger than Ga atoms, tend to be attracted to the stress concentration sites at the valleys under the action of tensile strain in the film.

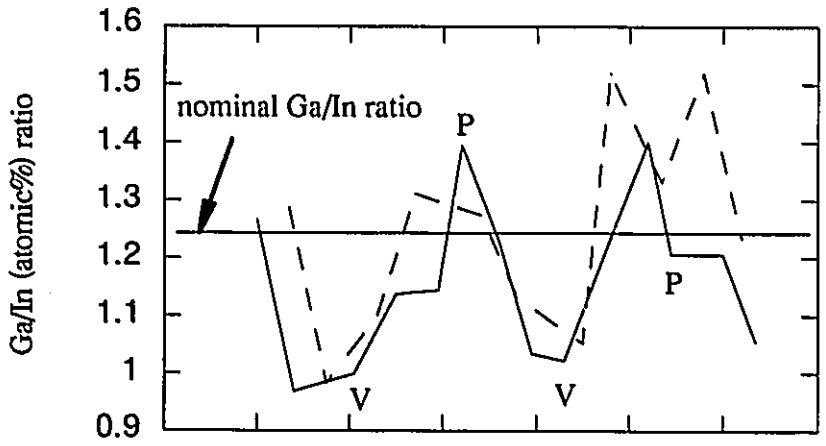

Fig.6.2.22 Variation of Ga/In ratio in the sample #745. The solid line is for the values close to the surface. The dashed line is for the values measured deeper in the film. V denotes valley and P denotes peak position.

From the Ga/In value obtained close to the facet surface, it is estimated that the composition fluctuation is roughly about ±4% and the corresponding variation in the misfit strain is about ±0.3% around the nominal value.

We can summarize our experimental findings as follows:

(1) When a short wavelength (100-400Å) surface undulation is observed at the strained layer surface, it always shows clear anisotropy between the two <1 1 0> directions. The surface undulation extends only along the [1 $\bar{1}$ 0] direction in the (001) surface.

(2) Composition modulation which coexists with the surface undulation is not the classical spinodal decomposition since it predominantly occurs in the [1 1 0] direction.

(3) Surface undulation was observed only in tensile-strained layers. The magnitude of the tensile strain to cause the undulation is as small as 0.5%. On the other hand, the compressively-strained layers show a flat surface. This difference should be attributed not to the sign of the strain in the layer but to the difference in the degree of the composition modulation which depends on the alloy composition.

(4) Surface undulation can occur when the plastic relaxation of the strained layer due to misfit dislocations is very small or even when the layer is fully constrained. Misfit dislocations do not seem to play a significant role in the surface undulation we observed.

6.3 Discussion

6.3.1 Comparison with photoluminescence measurements

LaPierre et al. (1996) conducted photoluminescence (PL) experiments for a series of $In_{1-x}Ga_xAs_yP_{1-y}$ alloy films grown on InP substrates including ones with +0.5% (tension) or -0.5% (compression) strain which correspond to T-series or C-series samples described in subsection 6.2.3. Figure 6.3.1 demonstrates the full width at half maximum (FWHM) of PL spectrum from 1500Å thick $In_{1-x}Ga_xAs_yP_{1-y}$ layers in T-series and C-series samples as a function of As fraction y. PL measurements were conducted at room temperature (300K) and low temperature (11K).

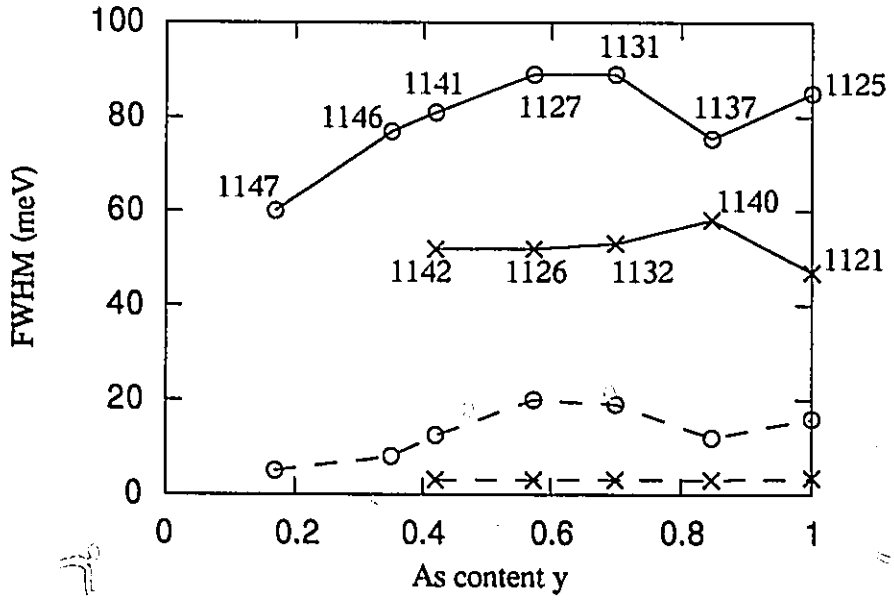

Fig.6.3.1 PL linewidth as a function of As content y for 1500Å thick $In_{1-x}Ga_xAs_yP_{1-y}$ layers having +0.5% (tension) or -0.5% (compression) strain.. Measurements were conducted at room temperature (300K; solid line) and low temperature (11K; dashed line). (After LaPierre et al. (1996).)

As clearly recognized from this figure, the PL spectrum from tensile-strained layers are more broadened than those from compressively-strained layers. This broadening is attributable to a variation in bandgap due to wider composition variation in tensile-strained layers. We also note that the broadening behaviour of the T-series agrees well with our cross-sectional TEM observation of the composition modulation contrast, that is, broadening is a minimum for sample #1147 which is closest to the InP side and increases as the composition approaches the $In_{1-x}Ga_xAs$ ternary side.

The degree of composition modulation can be estimated from the temperature-dependence of the PL peak energy. At low temperatures, the carriers become trapped after diffusing into the smaller bandgap InAs-rich region and subsequent recombination leads to red-shift (longer wavelength) of the PL emission compared to the nominal composition. Therefore we expect the PL peak energy at 11K, E(11K), is smaller than the value corresponding to the nominal composition. As the temperature increases, the carriers can diffuse out of the InAs-rich regions and recombination begins to occur in the nominal and GaP-rich regions. If the recombination occurs in GaP-rich region, the resulting PL emission is blue-shifted (shorter wavelength) and the PL peak energy at 300K, E(300K), is expected to have a larger value than that for the nominal composition. The deviation of E(11K)–E(300K) from Varshni's empirical equation which describes the temperature dependence of the bandgap of homogeneous semiconducting material (Varshni (1967)) can be used to estimate the degree of composition modulation. If we use the values for InP, the bandgap difference between 11K and 300K becomes 70meV.

The PL spectrum from 1500Å thick 0.5% tensile-strained $In_{1-x}Ga_xAs_yP_{1-y}$ layers of samples #1141, #1131 and #1125 at various temperatures are shown in Fig.6.3.2. The value of E(11K)–E(300K) is smaller for samples #1131 and #1125 in which the composition modulation is larger than in #1141. In sample #1125, if we assume that the

red-shift at 11K and the blue-shift at 300K of the PL peak cancel the expected bandgap shift 70meV, we can roughly estimate the magnitude of the composition fluctuation Δx from the nominal value from

$$\frac{\partial E_g}{\partial x}\Delta x = \pm 0.035 \text{ (eV)}. \qquad (6.3.1)$$

By using Kuphal's empirical expression for the bandgap E_g (eq.(3.2.5)), Δx is calculated as 0.032 for the 1500Å thick 0.5% tensile-strained $In_{0.46}Ga_{0.54}As$ layer in #1125. The corresponding misfit strain variation is expressed as $0.5\% \pm 0.22\%$.

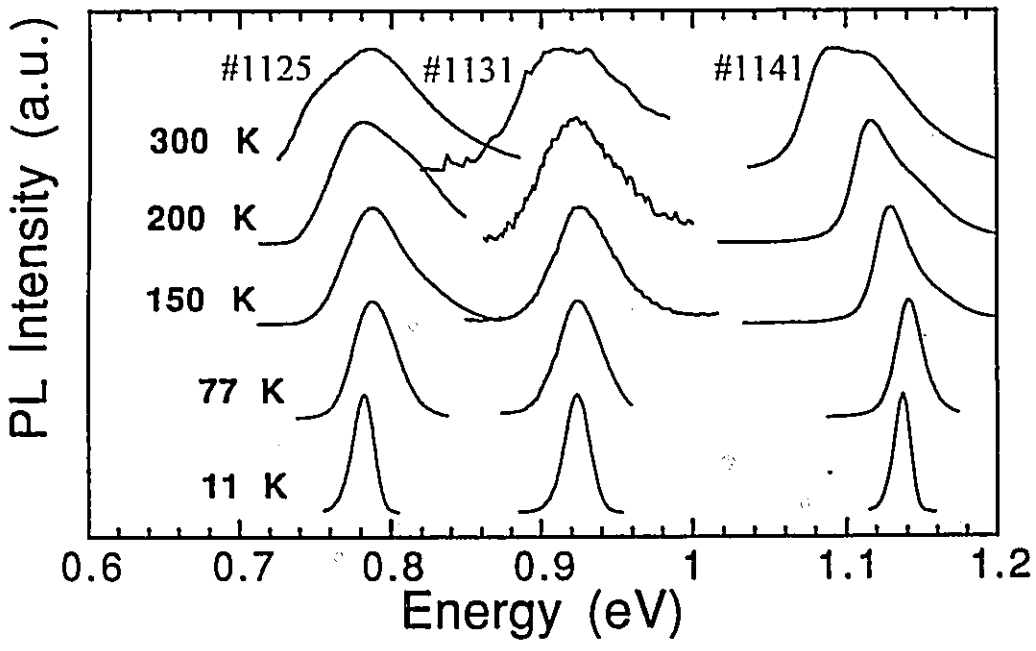

Fig.6.3.2 PL spectrum for 1500Å thick 0.5% tensile-strained $In_{1-x}Ga_xAs_yP_{1-y}$ layers in samples #1141, #1131 and #1125 (after LaPierre et al. (1996)).

6.3.2 Morphological instability caused by composition modulation

It is well known that a small sinusoidal perturbation applied to a strained film surface can lead to unstable growth of a surface undulation when the wavelength of the perturbation is larger than a critical value (Srolovitz (1989), Spencer et al. (1993)). For a static film in which no film growth occurs, the critical wavelength is determined from the balance between the decrease in strain energy and the increase in the surface energy associated with the surface undulation.

A similar discussion may be applicable to the stability of surface morphology of strained layers with an inherent composition modulation. Here we consider a case in which the lattice-constant of the film a_f is modulated along the X-direction following

$$a_f = a_{f0} (1 - \varepsilon_0 \cos \alpha X). \qquad (6.3.2)$$

This type of composition modulation, developing prior to any surface undulation, is suggested by the results presented earlier in this chapter. If the stress-free film material with the average lattice-constant a_{f0} has misfit strain f with respect to the substrate, the resulting elastic field at the film surface (Z=h) is derived as the sum of the elastic fields of a homogeneous strained layer (see Section 2.1) and of a lattice-matched layer having a modulation in lattice-constant. (Glas (1987)).

$$\left.\begin{aligned} \varepsilon_{XX} &= f - \{(1+2\nu) - 2(1+\nu)e^{-\alpha h}\}\varepsilon_0 \cos \alpha X \\ \varepsilon_{YY} &= f + \varepsilon_0 \cos \alpha X \\ \varepsilon_{ZZ} &= -\frac{2\nu}{1-\nu} f + \frac{2\nu}{1-\nu} \{\nu - (1+\nu)e^{-\alpha h}\}\varepsilon_0 \cos \alpha X \end{aligned}\right\} \qquad (6.3.3)$$

The stresses are given by:

$$\left.\begin{aligned}
\sigma_{XX} &= 2\mu\frac{1+\nu}{1-\nu}f - 2\mu\frac{1+\nu}{1-\nu}\varepsilon_0(1-2e^{-\alpha h})\cos\alpha X \\
\sigma_{YY} &= 2\mu\frac{1+\nu}{1-\nu}f + 2\mu\frac{1+\nu}{1-\nu}\varepsilon_0\{(1-2\nu)+2\nu e^{-\alpha h}\}\cos\alpha X \\
\sigma_{ZZ} &= 0
\end{aligned}\right\}. \qquad (6.3.4)$$

And the local hydrostatic stress is

$$p = \frac{1}{3}\sigma_{ii} = 4\mu\frac{1+\nu}{1-\nu}f + 4\mu\frac{1+\nu}{1-\nu}\varepsilon_0\{-\nu+(1+\nu)e^{-\alpha h}\}\cos\alpha X. \qquad (6.3.5)$$

In the above derivation, the film and substrate are assumed to be an elastically isotropic material with the same shear modulus μ and Poisson's ratio ν. The strain energy distribution at the free surface is approximated as

$$w_E = 2\mu\frac{1+\nu}{1-\nu}f^2 - 2\mu\frac{1+\nu}{1-\nu}\{2\nu-2(1+\nu)e^{-\alpha h}\}f\varepsilon_0\cos\alpha X \qquad (6.3.6)$$

where the term of the ε_0^2 is ignored. The second term in eq.(6.3.6) accounts for the elastic interaction between the misfit (f) and the composition modulation. Although the average energy contribution of this term is zero, there are regions of greater than or lower than average p and w_E. Two effects might stem from this. Gradients in chemical potential may

be established, driving surface diffusion. Secondly the rate of incorporation of the different species during growth might depend upon the local value of p, e.g. it might be easier for more dilated regions to accommodate the larger atoms, and vice-versa.

It is difficult to develop these arguments further because we have no knowledge about how the "up-hill" diffusion occurs at the growing film surface to maintain the composition modulation (which predominantly occurs along the [110] direction). At the present stage, we do not know the true nature of this diffusion which is probably driven by surface kinetics. In addition, as clearly seen from our TEM observation, the growth of the undulation leads to the formation of surface facets. All existing theories on the morphological instability of strained layers are based on the assumption that the surface energy is isotropic and an increase in the surface area acts as a stabilizing factor against the development of an undulation (Fig.6.3.3 (a)). However, if the undulation growth proceeds by maintaining low energy facet planes, when the wavelength and amplitude of the surface facet are increased, the total surface area is unchanged as schematically shown in Fig.6.3.3 (b). Therefore, in this case the surface energy term does not act as a stabilizing factor against the facet growth. For a complete model of facet growth, we should also take into account the preferential growth of certain facets at the expense of others. Finally, the surface energy of planes under MBE growth conditions is expected to be different from the (static) equilibrium value. These factors add more complexity to the problem.

Recently, Ponchet and coworkers (Ponchet et al. (1993a,b), Emery et al. (1993), Ponchet et al. (1995)) reported TEM studies on a strong lateral undulation of interfaces with a period of about 500Å in $In_{1-x}Ga_xAs_yP_{1-y}$ multi-layer structures in which tensile-strained layers and compressively strained layers were combined to obtain zero-net-strain structures. They pointed out that the strong modulation was anisotropic in the two <110>

directions and only occurred along the [110] direction. They also reported that a 100Å thick tensile-strained $In_{0.82}Ga_{0.18}As_{0.2}P_{0.8}$ layer with +0.5% strain was responsible for the onset of undulated interfaces in the structure. Since each strained layer was very thin in their samples (for example, 50Å thick compressively-strained layers and 100Å thick tensile-strained layers were combined), the undulation of the interfaces in the upper part of the sample was enhanced by the modulated strained field from the lower layers and the displacement contrast formed a columnar configuration extending throughout the multi-layer structure. I speculate that the morphological instability they observed was induced by the composition modulation in tensile-strained layers, although they did not clearly point out the possibility. This is probably because the composition of the tensile-strained layers they examined was limited to the range in which the composition modulation is relatively small and their sample geometry made it difficult to observe the composition modulation in each layer.

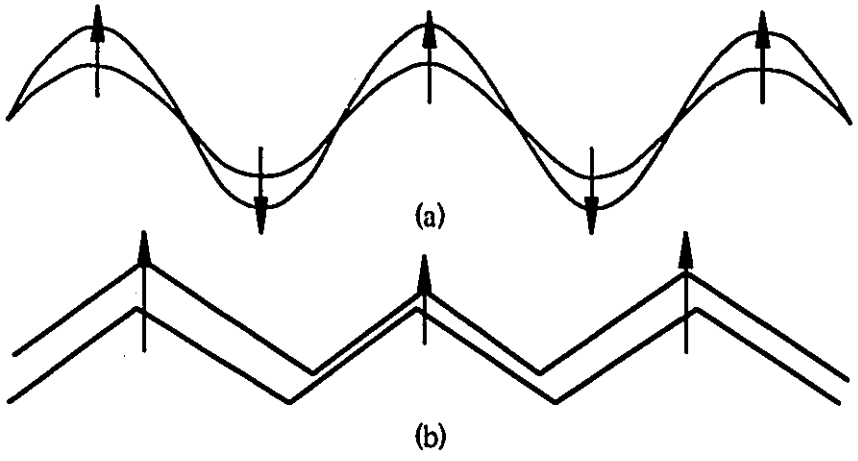

Fig.6.3.3 Schematic representations of development of sinusoidal surface undulation (a) and surface facet (b). Note that the total surface area is increased in (a) but remains unchanged in (b).

Chapter 7

Summary

In the present thesis, some unique growth related phenomena were studied in $In_{1-x}Ga_xAs_yP_{1-y}$ alloy thin films, heteroepitaxially grown on InP (001) substrates with gas-source molecular beam epitaxy. Transmission electron microscopy (TEM) has been extensively used as a major experimental tool. The composition of the $In_{1-x}Ga_xAs_yP_{1-y}$ films is shown in Fig.7.1.

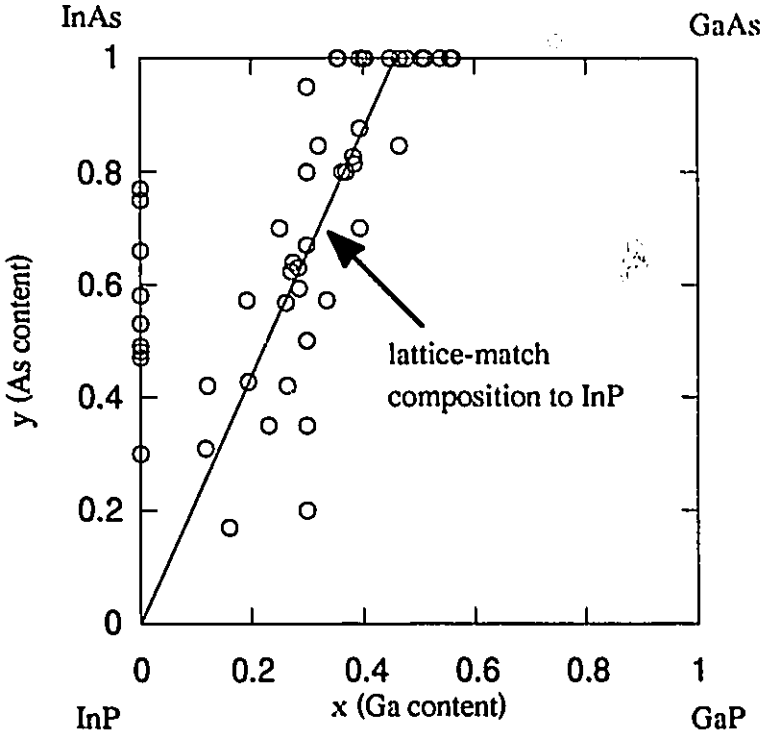

Fig.7.1 Composition of $In_{1-x}Ga_xAs_yP_{1-y}$ thin films examined in this thesis.

The samples can be classified into three groups, that is, compressively-strained $InAs_yP_{1-y}$ ternary alloy films, $In_{1-x}Ga_xAs_yP_{1-y}$ films lattice-matched to InP and tensile- or compressively-strained $In_{1-x}Ga_xAs_yP_{1-y}$ films.

In compressively-strained $InAs_yP_{1-y}$ ternary alloy films, new types of misfit dislocations aligned close to [100] and [010] directions were found, in addition to the expected anisotropic strain relaxation along [1 $\bar{1}$0] and [110] directions. These new types of misfit dislocations were found to be (near-)pure edge in nature formed probably by slip on {011} planes. When analyzing the character of misfit dislocations generated from heterogeneous dislocation sources, contrast intensity profiles for misfit dislocations parallel and adjacent to one of the free surfaces of a plan-view TEM sample were useful. In addition, despite the relatively high compressive strain (–0.96% to –2.43%), the surface of the films was found to be flat and there was no evidence of composition modulation in the $InAs_yP_{1-y}$ films.

In a wide range of $In_{1-x}Ga_xAs_yP_{1-y}$ quaternary alloy films (including $In_{0.533}Ga_{0.467}As$ ternary alloy film) lattice-matched to InP substrates, composition modulation occurring only along the [110] direction with small wavelength (~100Å) was repeatedly observed. The degree of modulation showed a clear correlation with film composition. This modulation is different from "classical" spinodal decomposition along elastically soft [100] and [010] directions with relatively large wavelength (1000-1500Å) which is commonly observed in $In_{1-x}Ga_xAs_yP_{1-y}$ films grown by liquid phase epitaxy. From a simple free energy argument including the effect of constraint by InP substrate, it is suggested that the observed modulation is not directly caused by the minimization of the free energy of the system but is driven by kinetic processes occurring at the growing surface of the film.

Clear correlation was found between the surface morphology of strained films and the degree of composition modulation in tensile- or compressively-strained $In_{1-x}Ga_xAs_yP_{1-y}$ quaternary and $In_{1-x}Ga_xAs$ ternary alloy films. In tensile-strained films with significant composition modulation, the surface undulation may develop even at relatively small strains (as low as 0.5%); on the other hand, films with the same magnitude of compressive strain did not exhibit surface undulation. This instability in surface morphology assisted by composition modulation is different from the "classical" growth mode transition of highly-strained layer from two-dimensional layer-by-layer growth to a three-dimensional island formation mode.

Appendix A

Evaluation of the displacement field of a dislocation in a semi-infinite body

In this appendix the expressions for the local lattice rotation are derived for three types of dislocations aligned parallel to the free surface of an elastically isotropic semi-infinite body. The expressions will be applied to compute the TEM diffraction contrast of a misfit dislocations based on two-beam dynamical theory.

We first resolve the Burgers vector **b** of a dislocation into three components in a coordinate system shown in Fig.A1, following

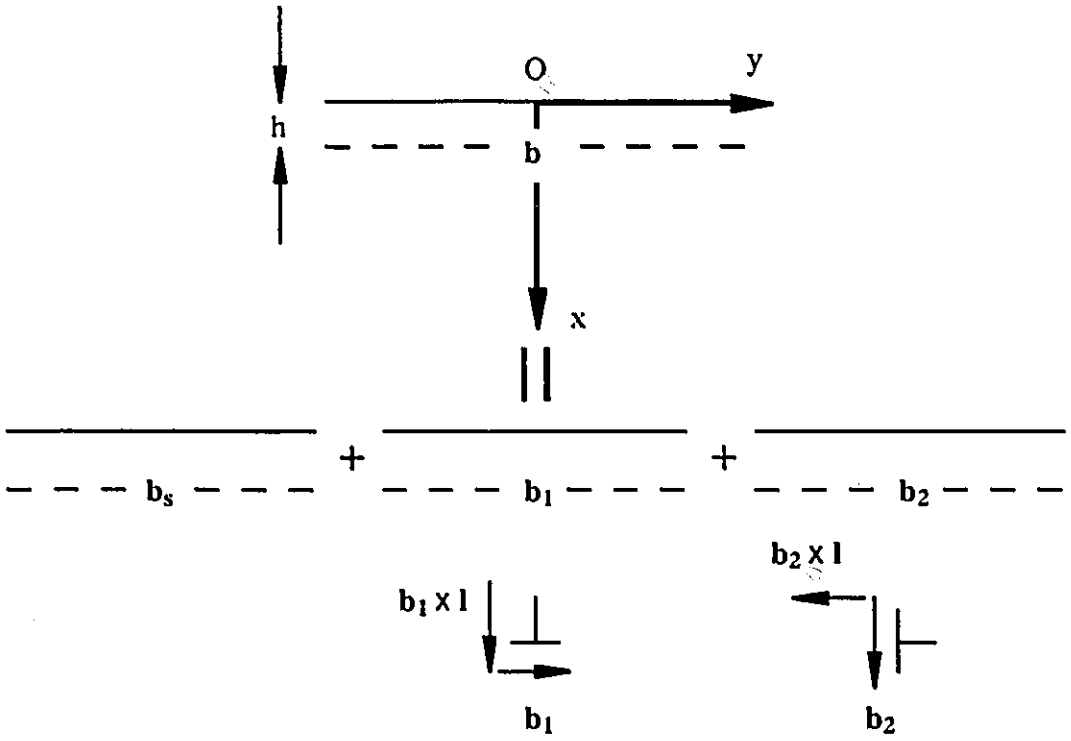

Fig.A1 Burgers vector **b** resolved into 3 components. Note that the dislocation line direction **l** is taken out of the paper.

$$\mathbf{b} = \mathbf{b}_s + \mathbf{b}_1 + \mathbf{b}_2 \qquad (A1)$$

where $\mathbf{b}_s$ is the pure screw component, $\mathbf{b}_1$ is the pure edge component parallel to the free surface and $\mathbf{b}_2$ is the pure edge component perpendicular to the free surface. In Fig.A1 the dislocation line direction is defined as a unit vector **l** taken out the paper and FS/RH convention is used to define the Burgers vector (Hirth and Lothe (1982)). The displacement field $\mathbf{R}_s$ associated with the screw component $\mathbf{b}_s$ which is parallel and adjacent to the free surface separated by the distance h is easily derived by placing an image dislocation with the opposite Burgers vector at the mirror symmetry position (Hirth and Lothe (1982)).

$$\mathbf{R}_s = \frac{\mathbf{b}_s}{2\pi}\{\arctan(\frac{x-h}{y}) - \arctan(\frac{x+h}{y})\} \qquad (A2)$$

The total displacement **R** of the dislocation with Burgers vector **b** is expressed as

$$\mathbf{R} = \mathbf{R}_s + u_y^{(1)}\frac{\mathbf{b}_1}{|\mathbf{b}_1|} + u_x^{(1)}\frac{\mathbf{b}_1\times\mathbf{l}}{|\mathbf{b}_1\times\mathbf{l}|} + u_x^{(2)}\frac{\mathbf{b}_2}{|\mathbf{b}_2|} - u_y^{(2)}\frac{\mathbf{b}_2\times\mathbf{l}}{|\mathbf{b}_2\times\mathbf{l}|} \qquad (A3)$$

where $u_x^{(1)}$ and $u_y^{(1)}$ are the displacements in x and y directions due to the pure edge dislocation $\mathbf{b}_1$ and $u_x^{(2)}$ and $u_y^{(2)}$ are the displacements in x and y directions associated with the second pure edge dislocation $\mathbf{b}_2$. In this study the **g** vectors used to analyze misfit dislocations were limited to the ones within the surface plane (y-z plane in Fig.A1). Therefore, the local lattice rotation term d/dx(**g**.**R**) which appears in the two-beam dynamical theory becomes

$$\frac{d}{dx}(g.R) = \frac{d}{dx}(g.R_s) + \frac{g.b_1}{|b_1|}\frac{du_y^{(1)}}{dx} - \frac{g.b_2 \times l}{|b_2 \times l|}\frac{du_y^{(2)}}{dx}. \qquad (A4)$$

The displacement fields of pure edge dislocations aligned parallel and adjacent to the free surface can not be derived correctly by a simple image dislocation method which is successful only for pure screw dislocations. In the following the expressions for the terms $du_y^{(1)}/dx$ and $du_y^{(2)}/dx$ in eq.(A4) are first derived using Papkovich-Neuber potential method (Weeks et al. (1968)). The results will be shown to agree with the solutions derived from Head's method (Head (1953)).

A.1 Derivation of $du_y^{(1)}/dx$ for a pure edge dislocation with Burgers vector parallel to the free surface

Consider an edge dislocation with Burgers vector $\mathbf{b}_1$ in an infinite body shown in Fig.A2.

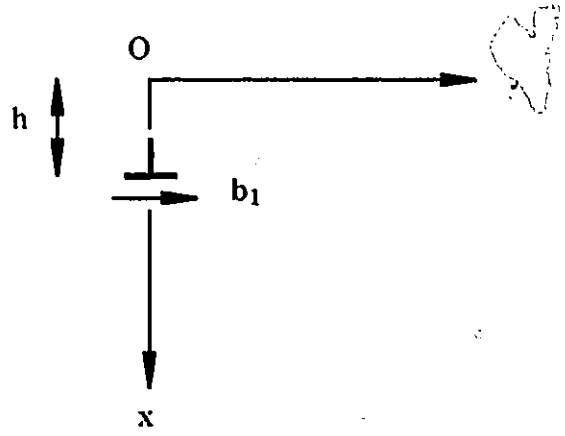

Fig.A2 An edge dislocation $\mathbf{b}_1$ in an infinite body.

The stresses σ_{xx}^* and σ_{xy}^* at the position x=0 are

$$\left.\begin{aligned} \sigma_{xx}^* &= \frac{\mu b_1}{2\pi(1-\nu)}\left\{\frac{h}{h^2+y^2} - \frac{2h^3}{(h^2+y^2)^2}\right\} \\ \sigma_{xy}^* &= \frac{-\mu b_1}{2\pi(1-\nu)}\left\{\frac{y}{h^2+y^2} - \frac{2h^2 y}{(h^2+y^2)^2}\right\} \end{aligned}\right\} \qquad \text{(A5)}$$

where μ and ν are the shear modulus and Poisson's ratio, respectively.

In order to create a traction-free surface at x=0, the stresses σ_{xx}^* and σ_{xy}^* have to be cancelled by an additional loading represented by plane Papkovich-Neuber potentials $\phi_1(x,y)$ and $\psi_1(x,y)$. The formulae for the additional displacements due to these potentials become

$$\left.\begin{aligned} 2\mu u_x^{\Lambda} &= (3-4\nu)\phi_1 - x\frac{\partial \phi_1}{\partial x} - \frac{\partial \psi_1}{\partial x} \\ 2\mu u_y^{\Lambda} &= - x\frac{\partial \phi_1}{\partial y} - \frac{\partial \psi_1}{\partial y} \end{aligned}\right\} \qquad \text{(A6)}$$

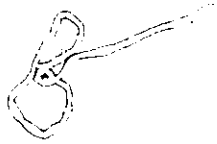

and those for the additional stresses are

$$\left.\begin{aligned} \sigma^{\Lambda}_{xx} &= 2(1-\nu)\frac{\partial \phi_1}{\partial x} - (x\frac{\partial^2 \phi_1}{\partial x^2} + \frac{\partial^2 \psi_1}{\partial x^2}) \\ \sigma^{\Lambda}_{xy} &= (1-2\nu)\frac{\partial \phi_1}{\partial y} - (x\frac{\partial^2 \phi_1}{\partial x \partial y} + \frac{\partial^2 \psi_1}{\partial x \partial y}) \end{aligned}\right\} \qquad (A7)$$

(Sokolnikoff (1956)). The potentials ϕ_1 and ψ_1 are harmonic functions satisfying

$$\nabla^2 \phi_1 = \nabla^2 \psi_1 = 0. \qquad (A8)$$

It is convenient to solve this loading problem by using Fourier transforms defined by the transform and inversion transform formulae (Sneddon (1951))

$$\left.\begin{aligned} \overline{f}(x,\xi) &= \int_{-\infty}^{\infty} f(x,y)\, e^{-i\xi y} dy \\ f(x,y) &= \frac{1}{2\pi}\int_{-\infty}^{\infty} \overline{f}(x,\xi)\, e^{i\xi y} d\xi \end{aligned}\right\}. \qquad (A9)$$

A useful relation is

$$\int_{-\infty}^{\infty} \frac{\partial f(x,y)}{\partial y}\, e^{-i\xi y} dy = i\xi \overline{f}(x,y). \qquad (A10)$$

The condition (A8) leads to the following differential equations about the transforms of the

potentials;

$$\left.\begin{aligned}\left(\frac{d^2}{dx^2} - \xi^2\right)\overline{\phi_1} &= 0\\ \left(\frac{d^2}{dx^2} - \xi^2\right)\overline{\psi_1} &= 0\end{aligned}\right\}. \qquad \text{(A11)}$$

Fourier transforms of σ_{xx}^* and σ_{xy}^* become

$$\left.\begin{aligned}\int_{-\infty}^{\infty}\sigma_{xx}^* e^{-i\xi y}dy &= \frac{-\mu b_1}{2(1-\nu)} h|\xi| e^{-h|\xi|}\\ \int_{-\infty}^{\infty}\sigma_{xy}^* e^{-i\xi y}dy &= i\frac{\mu b_1}{2(1-\nu)}\left(\frac{\xi}{|\xi|} - h\xi\right) e^{-h|\xi|}\end{aligned}\right\}. \qquad \text{(A12)}$$

These transforms of the stresses must be cancelled by the Fourier transforms of the additional loading stresses. From eq.(A11) we assume that the Fourier transforms of the additional potentials have the forms of

$$\left.\begin{aligned}\overline{\phi_1} &= \frac{-\mu b_1}{2(1-\nu)}\frac{A(\xi)}{\xi} e^{-(h+x)|\xi|}\\ \overline{\psi_1} &= \frac{-\mu b_1}{2(1-\nu)}\frac{B(\xi)}{\xi|\xi|} e^{-(h+x)|\xi|}\end{aligned}\right\} \qquad \text{(A13)}$$

where $A(\xi)$ and $B(\xi)$ are unknown variables to be derived from the traction-free condition at the free surface. The Fourier transforms of additional loading stresses σ_{xx}^{A} and σ_{xy}^{A} become

$$\left.\begin{aligned} \int_{-\infty}^{\infty} \sigma_{xx}^{A} e^{-i\xi y} dy &= \frac{\mu b_1}{2(1-\nu)} \{2(1-\nu)A(\xi)\frac{|\xi|}{\xi} + B(\xi)\frac{\xi}{|\xi|}\} e^{-h|\xi|} \\ \int_{-\infty}^{\infty} \sigma_{xy}^{A} e^{-i\xi y} dy &= -i\frac{\mu b_1}{2(1-\nu)} \{(1-2\nu)A(\xi) + B(\xi)\} e^{-h|\xi|} \end{aligned}\right\} \quad \text{(A14)}$$

where we used eqs.(A7) and (A8), and formulae

$$\left.\begin{aligned} \int_{-\infty}^{\infty} \frac{\partial \phi_1}{\partial x} e^{-i\xi y} dy &= \frac{d\,\overline{\phi_1}}{dx} & \int_{-\infty}^{\infty} \frac{\partial^2 \phi_1}{\partial x^2} e^{-i\xi y} dy &= \int_{-\infty}^{\infty} -\frac{\partial^2 \phi_1}{\partial y^2} e^{-i\xi y} dy \\ \int_{-\infty}^{\infty} \frac{\partial \phi_1}{\partial y} e^{-i\xi y} dy &= i\xi\,\overline{\phi_1} & \int_{-\infty}^{\infty} \frac{\partial^2 \phi_1}{\partial y^2} e^{-i\xi y} dy &= -\xi^2\,\overline{\phi_1} \end{aligned}\right\} \quad \text{(A15)}$$

The formulae (A15) also apply to ψ_1. This additional loading problem has to be solved to achieve traction-free surface at x=0, that is,

$$\left.\begin{aligned} \int_{-\infty}^{\infty} \sigma_{xx}^{A} e^{-i\xi y} dy &= -\int_{-\infty}^{\infty} \sigma_{xx}^{*} e^{-i\xi y} dy \\ \int_{-\infty}^{\infty} \sigma_{xy}^{A} e^{-i\xi y} dy &= -\int_{-\infty}^{\infty} \sigma_{xy}^{*} e^{-i\xi y} dy \end{aligned}\right\}. \qquad \text{(A16)}$$

Combining eqs.(A12), (A14) and (A16), we obtain the expressions for $A(\xi)$ and $B(\xi)$ as

$$\left.\begin{aligned} A(\xi) &= -\frac{\xi}{|\xi|} + 2h\xi \\ B(\xi) &= -(3-4\nu)h\xi + 2(1-\nu)\frac{\xi}{|\xi|} \end{aligned}\right\}. \qquad \text{(A17)}$$

Using the inversion formula,

$$\left.\begin{aligned} \phi_1 &= \frac{-\mu b_1}{4\pi(1-\nu)} \int_{-\infty}^{\infty} \frac{A(\xi)}{\xi} e^{-(h+x)|\xi|} e^{iy\xi} d\xi \\ \psi_1 &= \frac{-\mu b_1}{4\pi(1-\nu)} \int_{-\infty}^{\infty} \frac{B(\xi)}{\xi|\xi|} e^{-(h+x)|\xi|} e^{iy\xi} d\xi \end{aligned}\right\}. \qquad \text{(A18)}$$

From eq.(A6)

$$u_y^A = -\frac{1}{2\mu} x \frac{\partial \phi_1}{\partial y} - \frac{1}{2\mu} \frac{\partial \psi_1}{\partial y}$$

$$= i \frac{b_1}{8\pi(1-\nu)} x \int_{-\infty}^{\infty} A(\xi)\, e^{-(h+x)|\xi|}\, e^{iy\xi}\, d\xi$$

$$+ i \frac{b_1}{8\pi(1-\nu)} \int_{-\infty}^{\infty} \frac{B(\xi)}{|\xi|}\, e^{-(h+x)|\xi|}\, e^{iy\xi}\, d\xi \qquad \text{(A19)}$$

and therefore,

$$\frac{du_y^A}{dx} = i \frac{b_1}{8\pi(1-\nu)} \int_{-\infty}^{\infty} \{A(\xi) - B(\xi)\}\, e^{-(h+x)|\xi|}\, e^{iy\xi}\, d\xi$$

$$- i \frac{b_1}{8\pi(1-\nu)} x \int_{-\infty}^{\infty} A(\xi)\, |\xi|\, e^{-(h+x)|\xi|}\, e^{iy\xi}\, d\xi. \qquad \text{(A20)}$$

Substituting (A17) into (A20) and carrying out integrations we obtain the local lattice rotation term due to the additional loading as

$$\frac{du_y^A}{dx} = \frac{-b_1}{4\pi(1-\nu)}\left[2(5-4\nu)\frac{hy(x+h)}{\{(x+h)^2+y^2\}^2} - (3-2\nu)\frac{y}{(x+h)^2+y^2}\right.$$
$$\left. + \frac{2xy(x+h)}{\{(x+h)^2+y^2\}^2} - \frac{12hxy}{\{(x+h)^2+y^2\}^2} + \frac{16hxy^3}{\{(x+h)^2+y^2\}^3}\right]. \qquad (A21)$$

For an edge dislocation in an infinite body shown in Fig.A2

$$u_y = \frac{-b_1}{2\pi}\left[\arctan\left(\frac{x-h}{y}\right) + \frac{(x-h)y}{2(1-\nu)\{(x-h)^2+y^2\}}\right] \qquad (A22)$$

and

$$\frac{du_y}{dx} = \frac{b_1}{4\pi(1-\nu)}\left[\frac{y\{(x-h)^2-y^2\}}{\{(x-h)^2+y^2\}^2} - \frac{2(1-\nu)y}{(x-h)^2+y^2}\right]. \qquad (A23)$$

The local lattice rotation term $du_y^{(1)}/dx$ in the eq.(A4) is the sum of eqs.(A21) and (A23).

A.2 Derivation of $du_y^{(2)}/dx$ for a pure edge dislocation with Burgers vector perpendicular to the free surface

The same procedures as in A.1 can be applied to the other pure edge dislocation $\mathbf{b_2}$.

First, consider an edge dislocation with Burgers vector $\mathbf{b_2}$ in an infinite body shown in Fig.A3.

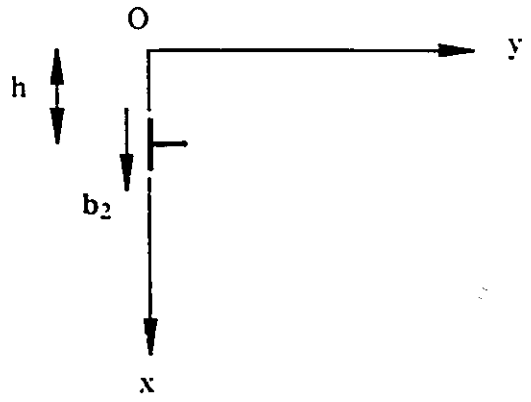

Fig.A3 An edge dislocation b_2 in an infinite body.

The stresses σ_{xx}^* and σ_{xy}^* at x=0 are

$$\left.\begin{aligned}\sigma_{xx}^* &= \frac{-\mu b_2}{2\pi(1-\nu)}\left\{\frac{y}{h^2+y^2}+\frac{2h^2y}{(h^2+y^2)^2}\right\}\\ \sigma_{xy}^* &= \frac{\mu b_2}{2\pi(1-\nu)}\left\{\frac{h}{h^2+y^2}-\frac{2h^3}{(h^2+y^2)^2}\right\}\end{aligned}\right\}. \qquad \text{(A24)}$$

Fourier transforms of these stresses become

$$\left.\begin{aligned}\int_{-\infty}^{\infty}\sigma_{xx}^* e^{-i\xi y}\,dy &= i\frac{\mu b_2}{2(1-\nu)}\left\{\frac{\xi}{|\xi|}+h\xi\right\}e^{-h|\xi|}\\ \int_{-\infty}^{\infty}\sigma_{xy}^* e^{-i\xi y}\,dy &= \frac{-\mu b_2}{2(1-\nu)}h|\xi|\,e^{-h|\xi|}\end{aligned}\right\}. \qquad \text{(A25)}$$

These transforms must be cancelled by an additional loading represented by Papkovich-Neuber potentials ϕ_2 and ψ_2. Here we assume the Fourier transforms of these potentials as

$$\left.\begin{aligned} \overline{\phi_2} &= i\frac{\mu b_2}{2(1-\nu)}\frac{C(\xi)}{\xi}\, e^{-(h+x)|\xi|} \\ \overline{\psi_2} &= i\frac{\mu b_2}{2(1-\nu)}\frac{D(\xi)}{\xi|\xi|}\, e^{-(h+x)|\xi|} \end{aligned}\right\}. \qquad \text{(A26)}$$

The Fourier transforms of the additional loading stresses σ_{xx}^B and σ_{xy}^B are calculated as

$$\left.\begin{aligned} \int_{-\infty}^{\infty} \sigma_{xx}^B\, e^{-i\xi y}\, dy &= -i\frac{\mu b_2}{2(1-\nu)}\{2(1-\nu)C(\xi)\frac{|\xi|}{\xi} + D(\xi)\frac{\xi}{|\xi|}\}\, e^{-h|\xi|} \\ \int_{-\infty}^{\infty} \sigma_{xy}^B\, e^{-i\xi y}\, dy &= \frac{-\mu b_2}{2(1-\nu)}\{(1-2\nu)C(\xi) + D(\xi)\}\, e^{-h|\xi|} \end{aligned}\right\}. \qquad \text{(A27)}$$

From

$$\left.\begin{aligned} \int_{-\infty}^{\infty} \sigma_{xx}^B\, e^{-i\xi y}\, dy &= -\int_{-\infty}^{\infty} \sigma_{xx}^*\, e^{-i\xi y}\, dy \\ \int_{-\infty}^{\infty} \sigma_{xy}^B\, e^{-i\xi y}\, dy &= -\int_{-\infty}^{\infty} \sigma_{xy}^*\, e^{-i\xi y}\, dy \end{aligned}\right\}, \qquad \text{(A28)}$$

we obtain

$$\left.\begin{aligned} C(\xi) &= 1 + 2h|\xi| \\ D(\xi) &= -(3-4\nu)h|\xi| - (1-2\nu) \end{aligned}\right\}. \qquad (A29)$$

Using the Fourier inversion formula

$$\left.\begin{aligned} \phi_2 &= i\frac{\mu b_2}{4\pi(1-\nu)}\int_{-\infty}^{\infty}\frac{C(\xi)}{\xi}\, e^{-(h+x)|\xi|}\, e^{iy\xi}\, d\xi \\ \psi_2 &= i\frac{\mu b_2}{4\pi(1-\nu)}\int_{-\infty}^{\infty}\frac{D(\xi)}{\xi|\xi|}\, e^{-(h+x)|\xi|}\, e^{iy\xi}\, d\xi \end{aligned}\right\}. \qquad (A30)$$

The displacement u_y^B is

$$\begin{aligned} u_y^B &= -\frac{1}{2\mu}\, x\, \frac{\partial \phi_2}{\partial y} - \frac{1}{2\mu}\, \frac{\partial \psi_2}{\partial y} \\ &= \frac{b_2}{8\pi(1-\nu)}\, x \int_{-\infty}^{\infty} C(\xi)\, e^{-(h+x)|\xi|}\, e^{iy\xi}\, d\xi \\ &\quad + \frac{b_2}{8\pi(1-\nu)}\int_{-\infty}^{\infty}\frac{D(\xi)}{|\xi|}\, e^{-(h+x)|\xi|}\, e^{iy\xi}\, d\xi. \end{aligned} \qquad (A31)$$

The differentiation about x gives

$$\frac{du_y^B}{dx} = \frac{b_2}{8\pi(1-\nu)} \int_{-\infty}^{\infty} \{C(\xi) - D(\xi)\} e^{-(h+x)|\xi|} e^{iy\xi} d\xi$$

$$- \frac{b_2}{8\pi(1-\nu)} x \int_{-\infty}^{\infty} C(\xi) |\xi| e^{-(h+x)|\xi|} e^{iy\xi} d\xi. \qquad (A32)$$

Substituting (A29) into (A32) and carrying out integrations the local lattice rotation due to the additional loading becomes

$$\frac{du_y^B}{dx} = \frac{b_2}{4\pi(1-\nu)} [(5-4\nu) \frac{h\{(x+h)^2-y^2\}}{\{(x+h)^2+y^2\}^2} + 2(1-\nu) \frac{x+h}{(x+h)^2+y^2}$$

$$- \frac{x\{(x+h)^2-y^2\}}{\{(x+h)^2+y^2\}^2} - \frac{16hx(x+h)^3}{\{(x+h)^2+y^2\}^3} + \frac{12hx(x+h)}{\{(x+h)^2+y^2\}^2}]. \qquad (A33)$$

For an edge dislocation in an infinite body shown in Fig.A3

$$u_y = \frac{-b_2}{2\pi} [\frac{1-2\nu}{4(1-\nu)} \ln\{(x-h)^2+y^2\} + \frac{(x-h)^2-y^2}{4(1-\nu)\{(x-h)^2+y^2\}}] \qquad (A34)$$

and

$$\frac{du_y}{dx} = \frac{-b_2}{4\pi(1-\nu)} [\frac{(1-2\nu)(x-h)}{(x-h)^2+y^2} + \frac{2(x-h)y^2}{\{(x-h)^2+y^2\}^2}]. \qquad (A35)$$

The local lattice rotation term $du_y^{(2)}/dx$ in eq.(A4) is the sum of (A33) and (A35).

A.3 Derivation of the local lattice rotation terms from Head's solution

The local lattice rotation terms calculated in A.1 and A.2 can also be derived from Head's solution. Head (1953) solved the stress fields of pure edge dislocations which are parallel and adjacent to the free surface of a semi-infinite body. He first placed an image dislocation of pure edge in character at the mirror symmetry position about the free surface and added appropriate potentials to cancel the traction which can not be annihilated by the image dislocation with the opposite Burgers vector.

For an edge dislocation with Burgers vector $\mathbf{b}_1$ parallel to the free surface, the stresses are

$$\left.\begin{aligned}
\sigma_{xx}^{(1)} &= \frac{\mu b_1}{4\pi(1-\nu)}\left[\frac{(x-h)\{(x-h)^2-y^2\}}{\{(x-h)^2+y^2\}^2} - \frac{(x+h)\{(x+h)^2-y^2\}}{\{(x+h)^2+y^2\}^2}\right. \\
&\qquad \left. + 2h\frac{(3x+h)(x+h)^3-6xy^2(x+h)-y^4}{\{(x+h)^2+y^2\}^3}\right] \\
&\text{and} \\
\sigma_{yy}^{(1)} &= \frac{\mu b_1}{4\pi(1-\nu)}\left[\frac{(x-h)\{(x-h)^2+3y^2\}}{\{(x-h)^2+y^2\}^2} - \frac{(x+h)\{(x+h)^2+3y^2\}}{\{(x+h)^2+y^2\}^2}\right. \\
&\qquad \left. - 2h\frac{(x-h)(x+h)^3-6xy^2(x+h)+y^4}{\{(x+h)^2+y^2\}^3}\right]
\end{aligned}\right\}. \quad \text{(A36)}$$

In each expression of eq.(A36), the first term in the square bracket represents the real edge dislocation in an infinite body, the second term is due to the image dislocation and the third term is added to achieve traction-free condition at the surface.

For an edge dislocation with Burgers vector b_2 perpendicular to the free surface,

$$\left.\begin{aligned}\sigma_{xx}^{(2)} &= \frac{\mu b_2}{4\pi(1-\nu)}\left[-\frac{y\{3(x-h)^2+y^2\}}{\{(x-h)^2+y^2\}^2}+\frac{y\{3(x+h)^2+y^2\}}{\{(x+h)^2+y^2\}^2}\right.\\ &\left.\quad +4hxy\frac{\{3(x+h)^2-y^2\}}{\{(x+h)^2+y^2\}^3}\right]\\ \text{and}\\ \sigma_{yy}^{(2)} &= \frac{\mu b_2}{4\pi(1-\nu)}\left[\frac{y\{(x-h)^2-y^2\}}{\{(x-h)^2+y^2\}^2}-\frac{y\{(x+h)^2-y^2\}}{\{(x+h)^2+y^2\}^2}\right.\\ &\left.\quad +4hy\frac{\{(2h-x)(x+h)^2+(3x+2h)y^2\}}{\{(x+h)^2+y^2\}^3}\right]\end{aligned}\right\}. \qquad \text{(A37)}$$

(In Head's original paper, the third term in the square bracket of $\sigma_{xx}^{(2)}$ is misprinted as

$$4hxy\frac{3\{(x+h)^2-y^2\}}{\{(x+h)^2+y^2\}^3}\ .)$$

The displacements $u_y^{(1)}$ and $u_y^{(2)}$ can be derived by integrating $\varepsilon_{yy}^{(1)}$ and $\varepsilon_{yy}^{(2)}$.

$$u_y^{(1)} = \int \varepsilon_{yy}^{(1)}\, dy = \int \frac{1}{2\mu}\{(1-\nu)\sigma_{yy}^{(1)} - \sigma_{xx}^{(1)}\}dy$$

$$= \frac{b_1}{4\pi(1-\nu)}\Big[\frac{(h-x)y}{(x-h)^2+y^2} + 2(1-\nu)\arctan\Big(\frac{y}{x-h}\Big) + \frac{(h+x)y}{(x+h)^2+y^2}$$

$$- 2(1-\nu)\arctan\Big(\frac{y}{x+h}\Big) - \frac{(7+2\nu)hx^2y}{2\{(x+h)^2+y^2\}^2} - \frac{(3+2\nu)h^2xy}{\{(x+h)^2+y^2\}^2}$$

$$+ \frac{(1-2\nu)hy(h^2+y^2)}{2\{(x+h)^2+y^2\}^2} + \frac{3(1-2\nu)hy}{2\{(x+h)^2+y^2\}}\Big] \qquad \text{(A38)}$$

Similarly,

$$u_y^{(2)} = \frac{b_2}{4\pi(1-\nu)}\Big[-\frac{(x-h)^2-y^2}{2\{(x-h)^2+y^2\}} - \frac{1-2\nu}{2}\ln\{(x-h)^2+y^2\} + \frac{(x+h)^2-y^2}{2\{(x+h)^2+y^2\}}$$

$$+ \frac{1-2\nu}{2}\ln\{(x+h)^2+y^2\} + \frac{(1+2\nu)hx^3}{\{(x+h)^2+y^2\}^2} + \frac{2(1+2\nu)h^2x^2}{\{(x+h)^2+y^2\}^2}$$

$$+ \frac{\{(1+2\nu)h^2-(3-2\nu)y^2\}hx}{\{(x+h)^2+y^2\}^2} - \frac{(3-2\nu)hx}{(x+h)^2+y^2} - \frac{4(1-\nu)h^2}{(x+h)^2+y^2}\Big]. \qquad \text{(A39)}$$

By differentiating about x, we obtain the local lattice rotation term of the pure edge dislocation $\mathbf{b}_1$ as

$$\frac{du_y^{(1)}}{dx} = \frac{b_1}{4\pi(1-\nu)}\left[\frac{y\{(x-h)^2-y^2\}}{\{(x-h)^2+y^2\}^2} - \frac{2(1-\nu)y}{(x-h)^2+y^2} - \frac{y\{(x+h)^2-y^2\}}{\{(x+h)^2+y^2\}^2}\right.$$
$$+\frac{2(1-\nu)y}{(x+h)^2+y^2} - \frac{(7+2\nu)hxy\{(x+h)(h-x)+y^2\}}{\{(x+h)^2+y^2\}^3} + \frac{(3+2\nu)h^2y\{(x+h)(3x-h)-y^2\}}{\{(x+h)^2+y^2\}^3}$$
$$\left.-\frac{2(1-2\nu)hy(x+h)(h^2+y^2)}{\{(x+h)^2+y^2\}^3} - \frac{3(1-2\nu)hy(x+h)}{\{(x+h)^2+y^2\}^2}\right]. \qquad \text{(A40)}$$

Although the appearance is different, this local lattice rotation term derived from Head's solution agrees with the sum of (A21) and (A23).

Similarly, the local lattice rotation term of the pure edge dislocation $\mathbf{b}_2$ is

$$\frac{du_y^{(2)}}{dx} = \frac{b_2}{4\pi(1-\nu)}\left[-\frac{2y^2(x-h)}{\{(x-h)^2+y^2\}^2} - \frac{(1-2\nu)(x-h)}{(x-h)^2+y^2} + \frac{2y^2(x+h)}{\{(x+h)^2+y^2\}^2}\right.$$
$$+\frac{(1-2\nu)(x+h)}{(x+h)^2+y^2} + \frac{(1+2\nu)hx^2\{(x+h)(3h-x)+3y^2\}}{\{(x+h)^2+y^2\}^3}$$
$$+\frac{4(1+2\nu)h^2x\{(x+h)(x-h)+y^2\}}{\{(x+h)^2+y^2\}^3} + \frac{\{(1+2\nu)h^2-(3-2\nu)y^2\}h\{(x+h)(h-3x)+y^2\}}{\{(x+h)^2+y^2\}^3}$$
$$\left.-\frac{(3-2\nu)h\{(x+h)(h-x)+y^2\}}{\{(x+h)^2+y^2\}^2} + \frac{8(1-\nu)h^2(x+h)}{\{(x+h)^2+y^2\}^2}\right]. \qquad \text{(A41)}$$

The eq.(A41) agrees with the sum of (A33) and (A35). It is confirmed that both methods starting from Papkovich-Neuber potential and Head's solution provide equivalent solutions to the local lattice rotations for two kinds of pure edge dislocations close to the free surface in a semi-infinite body.

A.4 The local lattice rotation used in image intensity calculation

The plan-view bright or dark field transmission electron microscopy (TEM) observations in Chapter 4 were conducted from the substrate side only, that is, the misfit dislocations were located close to the exit surface of a TEM foil. In order to compute the theoretical image intensity profiles of misfit dislocations, the expression for $(d/dx)(\mathbf{g}.\mathbf{R})$ of eq.(A4) should be rewritten for a new coordinate system in which X=t–x, Y=–y and Z is taken parallel to the dislocation line direction as shown in Fig.A4. Here we take the thickness of the TEM foil as t.

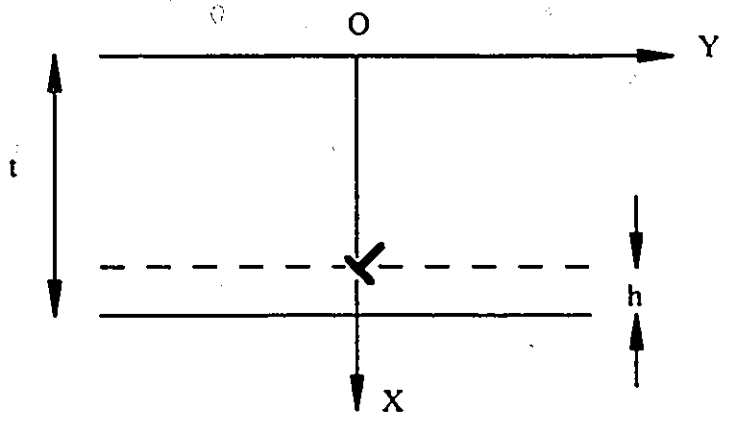

Fig.A4 Coordinate system used to compute TEM diffraction intensity profiles of misfit dislocations.

In this coordinate system (d/dX)(g.R) term becomes

$$\frac{d}{dX}(g.R) = \frac{g.b_s}{2\pi}\beta_s - \frac{g.b_1}{4\pi(1-\nu)}\beta_1 + \frac{g.b_2 \times l}{4\pi(1-\nu)}\beta_2. \qquad (A42)$$

Using TS and TL for t –h and t + h, respectively, the β terms are

$$\beta_s = \frac{Y}{(TS-X)^2+Y^2} - \frac{Y}{(TL-X)^2+Y^2}$$

$$\beta_1 = \frac{-Y\{(TS-X)^2-Y^2\}}{\{(TS-X)^2+Y^2\}^2} + \frac{2(1-\nu)Y}{(TS-X)^2+Y^2} + \frac{Y\{(TL-X)^2-Y^2\}}{\{(TL-X)^2+Y^2\}^2} - \frac{2(1-\nu)Y}{(TL-X)^2+Y^2}$$
$$+ \frac{(7+2\nu)hY(t-X)\{(TL-X)^2+Y^2-2(t-X)(TL-X)\}}{\{(TL-X)^2+Y^2\}^3}$$
$$+ \frac{(3+2\nu)h^2Y\{(TL-X)^2+Y^2-4(t-X)(TL-X)\}}{\{(TL-X)^2+Y^2\}^3}$$
$$+ \frac{2(1-2\nu)hY(h^2+Y^2)(TL-X)}{\{(TL-X)^2+Y^2\}^3} + \frac{3(1-2\nu)hY(TL-X)}{\{(TL-X)^2+Y^2\}^2}$$

$$\beta_2 = \frac{-2(TS-X)Y^2}{\{(TS-X)^2+Y^2\}^2} - \frac{(1-2\nu)(TS-X)}{(TS-X)^2+Y^2} + \frac{2(TL-X)Y^2}{\{(TL-X)^2+Y^2\}^2} + \frac{(1-2\nu)(TL-X)}{(TL-X)^2+Y^2}$$
$$+ (1-2\nu)h\frac{(t-X)^2\{3(TL-X)^2+3Y^2-4(t-X)(TL-X)\}}{\{(TL-X)^2+Y^2\}^3}$$
$$+ 4(1+2\nu)h^2(t-X)\frac{(TL-X)^2+Y^2-2(t-X)(TL-X)}{\{(TL-X)^2+Y^2\}^3}$$
$$+ \{(1+2\nu)h^2-(3-2\nu)Y^2\}h\frac{(TL-X)^2+Y^2-4(t-X)(TL-X)}{\{(TL-X)^2+Y^2\}^3}$$
$$- (3-2\nu)h\frac{(TL-X)^2+Y^2-2(t-X)(TL-X)}{\{(TL-X)^2+Y^2\}^2} + \frac{8(1-\nu)h^2(TL-X)}{\{(TL-X)^2+Y^2\}^2}. \qquad (A43)$$

Appendix B

Elastic fields associated with phase modulation

In this appendix, the strain energy is derived for a system composed of a semi-infinite substrate and a coherently grown film whose stress-free lattice-constant is periodically modulated along a direction within the film/substrate interface. The Eshelby-like approach first introduced by Glas (1987) for an elastically isotropic material is extended to a material having cubic symmetry. The surface normal of the system is taken as [001] and two different modulations are considered; the first is a modulation along [100] and the second is along [110] direction; these are treated in sections B.1 and B.2, respectively. The modulation along elastically soft <100> directions is expected to have the smallest elastic energy and is commonly observed in $In_{1-x}Ga_xAs_yP_{1-y}$ alloy films grown with liquid phase epitaxy, as reviewed in Section 2.2. In our study, however, we found a modulation which occurs only along the [110] direction in $In_{1-x}Ga_xAs_yP_{1-y}$ thin films deposited by molecular beam epitaxy. In Chapter 5, the strain energies derived in this appendix are used to calculate the critical temperatures above which the homogeneous phase is stabilized against a small composition modulation, by using a simple free energy argument.

B.1 Modulation along [100] direction

In this section the elasticity problem is solved when the stress-free intrinsic lattice-constant of an epitaxial film (thickness h) grown on a (001) substrate is sinusoidally modulated along one of the <100> directions within the interface plane following,

$$a(X,Y,Z) = a_0(1 - \varepsilon_0 \cos \alpha X) \qquad (B1.1)$$

where a_0 is the lattice-constant of the substrate and $2\pi/\alpha$ is the period of modulation. The coordinate system X,Y,Z used in this calculation with respect to the crystallographic coordinate system is shown in Fig.B1.1.

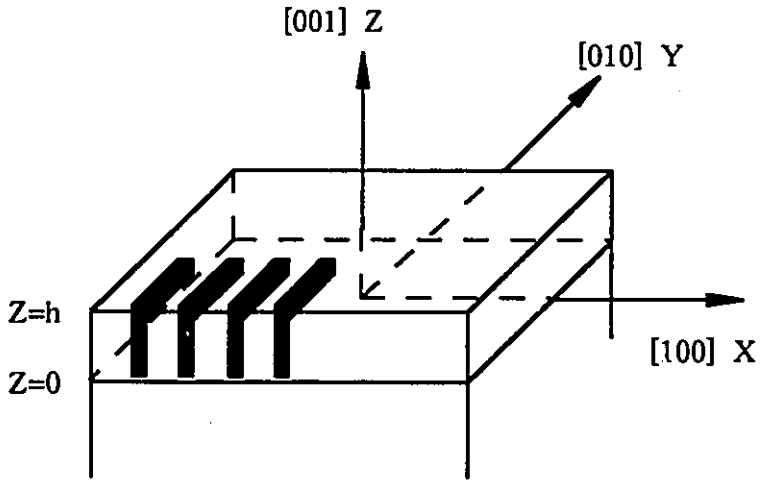

Fig.B1.1 Coordinate system X,Y,Z used for elasticity calculation of [100] modulation. The periodic lines schematically represent the modulation occurring along the X-direction ([100] in the crystal).

As clearly shown in the figure, axes X,Y and Z are parallel to [100],[010] and [001] in the crystal and the modulation occurs along the [100] direction. The film/substrate interface is taken at Z=0. For simplicity, both film and substrate material are assumed to have the same elastic moduli expressed in a matrix form;

$$\begin{pmatrix} C_{11} & C_{12} & C_{12} & 0 & 0 & 0 \\ C_{12} & C_{11} & C_{12} & 0 & 0 & 0 \\ C_{12} & C_{12} & C_{11} & 0 & 0 & 0 \\ 0 & 0 & 0 & C_{44} & 0 & 0 \\ 0 & 0 & 0 & 0 & C_{44} & 0 \\ 0 & 0 & 0 & 0 & 0 & C_{44} \end{pmatrix}. \qquad \text{(B1.2)}$$

In order to find the mechanically equilibrium state of the system, a step-by-step method similar to the one given by Glas (1987) for an elastically isotropic material is followed.

(1) External strain stage (superscript e)

First the film material is divided into independent cubes having the stress-free intrinsic lattice-constant represented by eq.(B1.1). Then external forces are applied to each cube to give it the lattice-constant of the substrate a_0. The strain and stress fields developed at this stage are;

$$\varepsilon^e_{XX}=\varepsilon^e_{YY}=\varepsilon^e_{ZZ}=\frac{a_0-a_0(1-\varepsilon_0\cos\alpha X)}{a_0(1-\varepsilon_0\cos\alpha X)}\approx\varepsilon_0\cos\alpha X \qquad \text{(B1.3)}$$

$$\sigma^e_{XX}=\sigma^e_{YY}=\sigma^e_{ZZ}=(C_{11}+2C_{12})\,\varepsilon_0\cos\alpha X. \qquad \text{(B1.4)}$$

(2) Assemble stage (superscript a)

The "cubes" described in the previous stage are assembled. This process changes only the nature of some of the external forces.

At the film/substrate interface (Z=0), the traction changes into a density of body force given as

$$f_Z^a = [-(C_{11}+2C_{12})\,\varepsilon_0 \cos \alpha X]\,\delta(Z) \qquad \text{(B1.5)}$$

where $\delta(Z)$ is Dirac's delta function.

Inside the modulated film, a density of body force appears following

$$\left.\begin{aligned} &f_i^a = -\sigma^e_{ij,j} \quad \text{that is,} \\ &f_X^a = -(\sigma^e_{XX,X}+\sigma^e_{XY,Y}+\sigma^e_{XZ,Z}) = (C_{11}+2C_{12})\,\varepsilon_0 \alpha \sin \alpha X \\ &f_Y^a = f_Z^a = 0. \end{aligned}\right\} \qquad \text{(B1.6)}$$

where the symbol (,) represents partial differential.

(3) Relaxation stage (superscript r)

The mechanical equilibrium is achieved by suppressing the applied forces in the first external stage.

At the free surface (Z=h), a traction

$$F_Z^r = -(C_{11}+2C_{12})\,\varepsilon_0 \cos \alpha X \qquad \text{(B1.7);}$$

at the film/substrate interface (Z=0), a density of body force

$$f_Z^r = [(C_{11}+2C_{12})\,\varepsilon_0 \cos \alpha X]\,\delta(Z) \qquad \text{(B1.8);}$$

and in the modulated film, a density of body force

$$f_X^r = -(C_{11}+2C_{12})\,\varepsilon_0 \alpha \sin \alpha X \qquad \text{(B1.9)}$$

are applied for relaxation.

The final state of the system (superscript E) is obtained by adding the strain and

stress fields in the external stage (e) and the relaxation stage (r), that is,

$$\varepsilon_{ij}^{E} = \varepsilon_{ij}^{e} + \varepsilon_{ij}^{r} \qquad \text{(B1.10)}$$

$$\sigma_{ij}^{E} = \sigma_{ij}^{e} + \sigma_{ij}^{r}. \qquad \text{(B1.11)}$$

Here we divide the solution for the relaxation stage (r) into a particular solution (superscript P) and a general solution (superscript G) for a two-dimensional elasticity problem without body forces.

$$\varepsilon_{ij}^{r} = \varepsilon_{ij}^{P} + \varepsilon_{ij}^{G} \qquad \text{(B1.12)}$$

$$\sigma_{ij}^{r} = \sigma_{ij}^{P} + \sigma_{ij}^{G} \qquad \text{(B1.13)}$$

If we take the particular solution (P) as

$$u_X^P = -\frac{C_{11}+2C_{12}}{C_{11}} (\varepsilon_0/\alpha) \sin \alpha X \qquad \text{(B1.14)}$$

$$\varepsilon_{XX}^P = -\frac{C_{11}+2C_{12}}{C_{11}} \varepsilon_0 \cos \alpha X \qquad \text{(B1.15)}$$

$$\left.\begin{aligned} \sigma_{XX}^P &= -(C_{11}+2C_{12})\varepsilon_0 \cos \alpha X \\ \sigma_{YY}^P = \sigma_{ZZ}^P &= -\frac{C_{12}(C_{11}+2C_{12})}{C_{11}} \varepsilon_0 \cos \alpha X \end{aligned}\right\} \qquad \text{(B1.16)}$$

for a plane strain problem, the condition for the body force in the modulated film

(eq.(B1.9)) is satisfied ($-\sigma^{P}_{XX,X} = -(C_{11}+2C_{12})\,\varepsilon_0\alpha \sin \alpha X$).

The problem which remains to be solved is to find the general solution so that the sum of the particular (P) and the general (G) solutions satisfies the boundary conditions (BCs) at the relaxation stage which can be summarized as follows. The quantities related to the substrate are distinguished by suffixes (') on their superscripts.

At the free surface (Z=h)

BC(1)

$$\sigma^{r}_{ZZ} = \sigma^{P}_{ZZ} + \sigma^{G}_{ZZ} = -(C_{11}+2C_{12})\,\varepsilon_0 \cos \alpha X \qquad \text{(B1.17)}$$

BC(2)

$$\sigma^{r}_{XZ} = \sigma^{P}_{XZ} + \sigma^{G}_{XZ} = \sigma^{G}_{XZ} = 0. \qquad \text{(B1.18)}$$

At the film/substrate interface (Z=0)

BC(3)

$$(\sigma^{G'}_{ZZ} - \sigma^{r}_{ZZ})\,\delta(Z) = [(C_{11}+2C_{12})\,\varepsilon_0 \cos \alpha X]\,\delta(Z)$$

$$\Rightarrow \sigma^{G'}_{ZZ} - (\sigma^{P}_{ZZ}+\sigma^{G}_{ZZ}) = (C_{11}+2C_{12})\,\varepsilon_0 \cos \alpha X \qquad \text{(B1.19)}$$

BC(4)

$$\sigma^{G'}_{XZ} = \sigma^{r}_{XZ}$$

$$\Rightarrow \sigma^{G'}_{XZ} = \sigma^{G}_{XZ}. \qquad \text{(B1.20)}$$

Because the substrate is not disturbed by the modulation at infinity,

BC(5)

$$\lim_{Z\to-\infty} u_i^{G'} = 0. \qquad \text{(B1.21)}$$

Coherency is maintained at the interface (Z=0),

$$u_i^{G'} = u_i^{r}$$

which is equivalent to

BC(6)

$$\varepsilon_{XX}^{G'} = \varepsilon_{XX}^{P} + \varepsilon_{XX}^{G} \qquad \text{(B1.22)}$$

and

BC(7)

$$u_{Z,X}^{r'} (= u_{Z,X}^{G'}) = u_{Z,X}^{r}. \qquad \text{(B1.23)}$$

We should note that there is no particular solution for the substrate.

We introduce Airy's stress functions χ for the film and χ' for the substrate from which the general solutions of the stresses are derived following

$$\sigma_{XX}^{G}=\frac{\partial^2\chi}{\partial Z^2},\ \sigma_{XZ}^{G}=-\frac{\partial^2\chi}{\partial Z\partial X},\ \sigma_{ZZ}^{G}=\frac{\partial^2\chi}{\partial X^2} \qquad \text{(B1.24)}$$

for a plane strain problem with $\varepsilon_{YY}=\varepsilon_{XY}=\varepsilon_{YZ}=0$. The above definitions also apply to the stresses in the substrate. The stresses defined by eq.(B1.24) automatically satisfy the two-dimensional equilibrium conditions

$$\frac{\partial \sigma_{XX}}{\partial X}+\frac{\partial \sigma_{XZ}}{\partial Z}=0, \quad \frac{\partial \sigma_{XZ}}{\partial X}+\frac{\partial \sigma_{ZZ}}{\partial Z}=0. \qquad \text{(B1.25)}$$

For this plane strain problem, the only remaining compatibility equation for the strain is

$$\frac{\partial^2 \varepsilon_{ZZ}}{\partial X^2} + \frac{\partial^2 \varepsilon_{XX}}{\partial Z^2} = 2\frac{\partial^2 \varepsilon_{ZX}}{\partial Z \partial X}. \qquad \text{(B1.26)}$$

Substituting the strain-stress relationships

$$\left.\begin{aligned} \varepsilon_{ZZ} &= \frac{-C_{12}}{C_{11}^2-C_{12}^2}\sigma_{XX} + \frac{C_{11}}{C_{11}^2-C_{12}^2}\sigma_{ZZ} \\ \varepsilon_{XX} &= \frac{C_{11}}{C_{11}^2-C_{12}^2}\sigma_{XX} - \frac{C_{12}}{C_{11}^2-C_{12}^2}\sigma_{ZZ} \\ \varepsilon_{ZX} &= \frac{1}{2C_{44}}\sigma_{ZX} \end{aligned}\right\} \qquad \text{(B1.27)}$$

into the compatibility equation (B1.26), we obtain

$$\begin{aligned} &\left(\frac{-C_{12}}{C_{11}^2-C_{12}^2}\frac{\partial^2 \sigma_{XX}}{\partial X^2}+\frac{C_{11}}{C_{11}^2-C_{12}^2}\frac{\partial^2 \sigma_{ZZ}}{\partial X^2}\right) \\ &+ \left(\frac{C_{11}}{C_{11}^2-C_{12}^2}\frac{\partial^2 \sigma_{XX}}{\partial Z^2}-\frac{C_{12}}{C_{11}^2-C_{12}^2}\frac{\partial^2 \sigma_{ZZ}}{\partial Z^2}\right) = 2\frac{1}{2C_{44}}\frac{\partial^2 \sigma_{ZX}}{\partial Z \partial X}. \end{aligned} \qquad \text{(B1.28)}$$

Using eq.(B1.24), eq.(B1.28) can be rewritten in the form

$$\frac{\partial^4\chi}{\partial Z^4} + \frac{2\{A(C_{11}+C_{12})-C_{12}\}}{C_{11}}\frac{\partial^4\chi}{\partial Z^2\partial X^2} + \frac{\partial^4\chi}{\partial X^4} = 0 \qquad \text{(B1.29)}$$

where $A=(C_{11}-C_{12})/2C_{44}$. The same equation was derived by Treacy and Gibson (1986), but the coefficient of the second term of eq.(B1.29) was mistakenly quoted by them as $2\{A(C_{11}+2C_{12})-C_{12}\}/(C_{11}+C_{12})$.

If we assume $\chi=G(Z)\cos\alpha X$, eq.(B1.29) becomes

$$\left(\frac{d^4G}{dZ^4} - B\alpha^2\frac{d^2G}{dZ^2} + \alpha^4G\right)\cos\alpha X = 0 \qquad \text{(B1.30)}$$

where

$$B = \frac{2\{A(C_{11}+C_{12})-C_{12}\}}{C_{11}}. \qquad \text{(B1.31)}$$

Solutions for G generally take the form

$$G(Z) = \sum_{k=1}^{4} A_k \exp(\lambda_k Z). \qquad \text{(B1.32)}$$

Substitution of eq.(B1.32) into eq.(B1.30) leads to

$$\sum_{k=1}^{4} (\lambda_k^4 - B\alpha^2\lambda_k^2 + \alpha^4)\, A_k \exp(\lambda_k Z) = 0. \qquad \text{(B1.33)}$$

Therefore

$$\lambda_k = \pm\frac{\alpha}{2}(\sqrt{2+B} \pm i\sqrt{2-B}) = \pm(\beta \pm i\gamma) \qquad \text{(B1.34)}$$

where

$$\beta = \frac{\alpha}{2}\sqrt{2+B} \text{ and } \gamma = \frac{\alpha}{2}\sqrt{2-B}. \qquad \text{(B1.35)}$$

The general solutions for stresses in the film σ_{ij}^{G} (or in the substrate $\sigma_{ij}^{G'}$) can be expressed using eq.(B1.24), the definition of G (χ=G(Z) cos αX) and

$$G(Z) = A_1\exp(\beta+i\gamma)Z + A_2\exp(\beta-i\gamma)Z + A_3\exp(-\beta+i\gamma)Z + A_4\exp(-\beta-i\gamma)Z$$

or

$$G'(Z) = A'_1\exp(\beta+i\gamma)Z + A'_2\exp(\beta-i\gamma)Z + A'_3\exp(-\beta+i\gamma)Z + A'_4\exp(-\beta-i\gamma)Z. \qquad \text{(B1.36)}$$

We have to determine the unknown coefficients A_1~A_4 and A'_1~A'_4 from the boundary conditions.

The boundary conditions BC(1)~(6) can be rewritten using A_i and A'_i as follows.

BC(1)

$$\alpha^2\{A_1\exp(\beta+i\gamma)h + A_2\exp(\beta-i\gamma)h + A_3\exp(-\beta+i\gamma)h + A_4\exp(-\beta-i\gamma)h\} = \frac{(C_{11}-C_{12})(C_{11}+2C_{12})}{C_{11}}\varepsilon_0 \qquad \text{(B1.37)}$$

BC(2)

$$(\beta+i\gamma)A_1\exp(\beta+i\gamma)h + (\beta-i\gamma)A_2\exp(\beta-i\gamma)h$$
$$+(-\beta+i\gamma)A_3\exp(-\beta+i\gamma)h + (-\beta-i\gamma)A_4\exp(-\beta-i\gamma)h = 0 \qquad \text{(B1.38)}$$

BC(3)

$$-\alpha^2(A'_1+A'_2+A'_3+A'_4)+\alpha^2(A_1+A_2+A_3+A_4)=\frac{(C_{11}-C_{12})(C_{11}+2C_{12})}{C_{11}}\varepsilon_0 \qquad \text{(B1.39)}$$

BC(4)

$$(\beta+i\gamma)A'_1+ (\beta-i\gamma)A'_2+ (-\beta+i\gamma)A'_3+ (-\beta-i\gamma)A'_4$$
$$= (\beta+i\gamma)A_1+ (\beta-i\gamma)A_2+ (-\beta+i\gamma)A_3+ (-\beta-i\gamma)A_4 \qquad \text{(B1.40)}$$

From BC(5)

$$A'_3 = A'_4 = 0 \qquad \text{(B1.41)}$$

BC(6)

$$\frac{C_{11}}{C_{11}^2-C_{12}^2}\left[\{(\beta+i\gamma)^2(A'_1-A_1)+(\beta-i\gamma)^2(A'_2-A_2)+(-\beta+i\gamma)^2(A'_3-A_3)\right.$$
$$\left.+(-\beta-i\gamma)^2(A'_4-A_4)\}+\alpha^2\{(A'_1-A_1)+(A'_2-A_2)+(A'_3-A_3)+(A'_4-A_4)\}\right]$$
$$=-\frac{C_{11}+2C_{12}}{C_{11}}\varepsilon_0 \qquad \text{(B1.42)}$$

BC(7) states that $u^r_{Z,X}$ is continuous at the interface (Z=0). We can rewrite the displacements u^r_Z as

$$u^r_Z(X,Z) = \int_{-\infty}^{Z} \varepsilon^r_{ZZ}(X,\varsigma)\, d\varsigma \qquad \text{for the substrate} \qquad (B1.43)$$

$$u^r_Z(X,Z) = \int_{h}^{Z} \varepsilon^r_{ZZ}(X,\varsigma)\, d\varsigma + u^r_Z(X,Z=h) \qquad \text{for the film.} \qquad (B1.44)$$

Here we assume the displacement at the free surface (Z=h) as

$$u^r_Z(X,Z=h) = N\cos\alpha X. \qquad (B1.45)$$

From

$$2\varepsilon^r_{XZ,X} = \varepsilon^r_{XX,Z} + (u^r_{Z,X})_{,X} \text{ and } \varepsilon^r_{XZ}(Z=h) = 0$$

we obtain

$$\varepsilon^r_{XX,Z} + (u^r_{Z,X})_{,X} = 0 \text{ at } Z=h. \qquad (B1.46)$$

Substituting eqs.(B1.27) and (B1.45) into eq.(B1.46) with the stresses expressed using $A_1 \sim A_4$, N is derived as

$$N=\frac{1}{\alpha^2(C_{11}^2-C_{12}^2)}[(\beta+i\gamma)\{(\beta+i\gamma)^2C_{11}+\alpha^2C_{12}\}A_1\exp(\beta+i\gamma)h$$
$$+(\beta-i\gamma)\{(\beta-i\gamma)^2C_{11}+\alpha^2C_{12}\}A_2\exp(\beta-i\gamma)h$$
$$+(-\beta+i\gamma)\{(-\beta+i\gamma)^2C_{11}+\alpha^2C_{12}\}A_3\exp(-\beta+i\gamma)h$$
$$+(-\beta-i\gamma)\{(-\beta-i\gamma)^2C_{11}+\alpha^2C_{12}\}A_4\exp(-\beta-i\gamma)h]. \quad (B1.47)$$

Carrying out the integrations in eqs.(B1.43) and (B1.44) and the subsequent differentiation by X, the condition of the continuity of $u^r_{Z,X}$ at the interface becomes

$$-N+\frac{1}{C_{11}^2-C_{12}^2}\left[\frac{C_{12}(\beta+i\gamma)^2+C_{11}\alpha^2}{\beta+i\gamma}\{1-\exp(\beta+i\gamma)h\}A_1\right.$$
$$+\frac{C_{12}(\beta-i\gamma)^2+C_{11}\alpha^2}{\beta-i\gamma}\{1-\exp(\beta-i\gamma)h\}A_2$$
$$+\frac{C_{12}(-\beta+i\gamma)^2+C_{11}\alpha^2}{-\beta+i\gamma}\{1-\exp(-\beta+i\gamma)h\}A_3$$
$$\left.+\frac{C_{12}(-\beta-i\gamma)^2+C_{11}\alpha^2}{-\beta-i\gamma}\{1-\exp(-\beta-i\gamma)h\}A_4\right]$$
$$=\frac{1}{C_{11}^2-C_{12}^2}\left\{\frac{C_{12}(\beta+i\gamma)^2+C_{11}\alpha^2}{\beta+i\gamma}A'_1+\frac{C_{12}(\beta-i\gamma)^2+C_{11}\alpha^2}{\beta-i\gamma}A'_2\right\} \quad (B1.48)$$

where $A'_3 = A'_4 = 0$ (eq.(B1.41)) is used. Substituting eq.(B1.47) into eq.(B1.48), BC(7) is finally written as

$$\left[\frac{-I_1}{\alpha^2}(I_1^2C_{11}+\alpha^2C_{12})\exp(I_1h)+\frac{I_1^2C_{12}+\alpha^2C_{11}}{I_1}\{1-\exp(I_1h)\}\right]A_1$$
$$+\left[\frac{-I_2}{\alpha^2}(I_2^2C_{11}+\alpha^2C_{12})\exp(I_2h)+\frac{I_2^2C_{12}+\alpha^2C_{11}}{I_2}\{1-\exp(I_2h)\}\right]A_2$$
$$+\left[\frac{-I_3}{\alpha^2}(I_3^2C_{11}+\alpha^2C_{12})\exp(I_3h)+\frac{I_3^2C_{12}+\alpha^2C_{11}}{I_3}\{1-\exp(I_3h)\}\right]A_3$$
$$+\left[\frac{-I_4}{\alpha^2}(I_4^2C_{11}+\alpha^2C_{12})\exp(I_4h)+\frac{I_4^2C_{12}+\alpha^2C_{11}}{I_4}\{1-\exp(I_4h)\}\right]A_4$$
$$=\frac{I_1^2C_{12}+\alpha^2C_{11}}{I_1}A'_1+\frac{I_2^2C_{12}+\alpha^2C_{11}}{I_2}A'_2 \qquad \text{(B1.49)}$$

where I_1, I_2, I_3 and I_4 are $\beta+i\gamma$, $\beta-i\gamma$, $-\beta+i\gamma$ and $-\beta-i\gamma$, respectively.

The boundary conditions are the combined equations of (B1.37)~(B1.42) and (B1.49). A_1~A_4 are solved as

$$A_1 = [(-i\gamma F_1^2 F_2)\exp(-2\beta)h + \beta\{\alpha^4 F_1 - 2\beta(\beta - i\gamma)(\beta^2+\gamma^2)^2 - 2(\beta - i\gamma)^2 F_1 F_2\}$$
$$\times \exp(-\beta - i\gamma)h + \{-(\beta - i\gamma)\alpha^4 F_1 + 2\beta(\beta^2+\gamma^2)^3 + 2\beta(\beta^2+\gamma^2)F_1 F_2\}\exp(-\beta + i\gamma)h$$
$$-4i\alpha^4\beta(\beta - i\gamma)\gamma]D_0 \;/\; 4i\alpha\beta\gamma[F_1 F_2\{(\beta - i\gamma)\exp(-\beta - i\gamma)h - (\beta + i\gamma)\exp(-\beta + i\gamma)h\}$$
$$+2i\alpha^4\gamma]\exp(\beta + i\gamma)h \qquad \text{(B1.50)}$$

$$A_2 = [i\gamma(\beta - i\gamma)F_1^2 F_2\exp(-2\beta)h - (\beta^2+\gamma^2)\{\alpha^4 F_1 - 2\beta(\beta - i\gamma)(\beta^2+\gamma^2)^2 - 2\beta(\beta - i\gamma)$$
$$\times F_1 F_2\}\exp(-\beta - i\gamma)h + \beta\{(\beta - i\gamma)\alpha^4 F_1 - 2\beta(\beta^2+\gamma^2)^3 - 2(\beta + i\gamma)(\beta^2+\gamma^2)F_1 F_2\}$$
$$\times \exp(-\beta + i\gamma)h + 4i\alpha^4\beta(\beta^2+\gamma^2)\gamma]D_0 / 4i\alpha\beta\gamma(\beta - i\gamma)[F_1 F_2\{(\beta - i\gamma)\exp(-\beta - i\gamma)h$$
$$-(\beta + i\gamma)\exp(-\beta + i\gamma)h\} + 2i\alpha^4\gamma]\exp(\beta - i\gamma)h \qquad \text{(B1.51)}$$

$$A_3 = \frac{(\beta - i\gamma)F_1^2 F_2\exp(-\beta - i\gamma)h + 2\beta(\beta^2+\gamma^2)^3 - \alpha^4(\beta - i\gamma)F_1}{4\alpha\beta(\beta - i\gamma)[F_1 F_2\{(\beta - i\gamma)\exp(-\beta - i\gamma)h - (\beta + i\gamma)\exp(-\beta + i\gamma)h\} + 2i\alpha^4\gamma]} D_0$$
$$\text{(B1.52)}$$

$$A_4 = \frac{-F_1^2 F_2\exp(-\beta + i\gamma)h + \alpha^4 F_1 - 2\beta(\beta - i\gamma)(\beta^2+\gamma^2)^2}{4\alpha\beta[F_1 F_2\{(\beta - i\gamma)\exp(-\beta - i\gamma)h - (\beta + i\gamma)\exp(-\beta + i\gamma)h\} + 2i\alpha^4\gamma]} D_0 \qquad \text{(B1.53)}$$

where

$$\left.\begin{aligned} F_1 &= \alpha^2 + \beta^2 + \gamma^2 \\ F_2 &= \alpha^2 - \beta^2 - \gamma^2 \\ D_0 &= \frac{(C_{11}-C_{12})(C_{11}+2C_{12})}{C_{11}}\frac{\varepsilon_0}{\alpha} \end{aligned}\right\}. \qquad \text{(B1.54)}$$

A'_1 and A'_2 need not be derived because they are not necessary to calculate the elastic energy in the modulated film.

The elastic energy stored in a volume V_1 of the modulated film is

$$W_E = \frac{1}{2}\int_{V_1} \varepsilon^e_{ij}\sigma^E_{ij}\,dv = \frac{1}{2}\varepsilon_0 \int_{V_1} (\sigma^E_{XX}+\sigma^E_{YY}+\sigma^E_{ZZ}) \cos \alpha X\, dv. \qquad \text{(B1.55)}$$

Using

$$\left.\begin{aligned} \sigma^E_{XX} &= \sigma^e_{XX} + \sigma^P_{XX} + \sigma^G_{XX} \\ \sigma^E_{YY} &= \sigma^e_{YY} + \sigma^P_{YY} + \sigma^G_{YY} = \sigma^e_{YY} + \sigma^P_{YY} + \frac{C_{12}}{C_{11}+C_{12}}(\sigma^G_{XX}+\sigma^G_{ZZ}) \\ \sigma^E_{ZZ} &= \sigma^e_{ZZ} + \sigma^P_{ZZ} + \sigma^G_{ZZ} \end{aligned}\right\} \qquad \text{(B1.56)}$$

we obtain

$$\sigma^E_{XX}+\sigma^E_{YY}+\sigma^E_{ZZ}$$
$$=\{\frac{2(C_{11}-C_{12})(C_{11}+2C_{12})}{C_{11}}\varepsilon_0+(1+\frac{C_{12}}{C_{11}+C_{12}})(\frac{d^2G}{dZ^2}-\alpha^2G)\}\cos\alpha X. \quad (B1.57)$$

The elastic energy w_E per unit volume is

$$w_E=\frac{\varepsilon_0}{4h}[\frac{2(C_{11}-C_{12})(C_{11}+2C_{12})}{C_{11}}\varepsilon_0 h$$
$$+\frac{(1+\frac{C_{12}}{C_{11}+C_{12}})D_0}{8\alpha\beta\gamma(\beta^2+\gamma^2)\{-\alpha^4\gamma+F_1F_2(\beta\sin\gamma h+\gamma\cos\gamma h)\exp(-\beta h)\}\exp(2\beta)h}\sum_{k=1}^{8}E_k \quad (B1.58)$$

where

$$E_1=-2\alpha^4F_1\{\alpha^2(\beta^2-\gamma^2)-(\beta^2+\gamma^2)^2\}$$

$$E_2=4\beta^2(\beta^2+\gamma^2)F_2\{(\beta^2+\gamma^2)^2+F_1F_2\}$$

$$E_3=-2\gamma F_1^2F_2(\gamma F_1\cos\gamma h+\beta F_2\sin\gamma h)\exp(-\beta h)$$

$$E_4=2\beta^2[\alpha^4F_1F_2-2(\beta^2+\gamma^2)^2\{\alpha^2(\beta^2-\gamma^2)-(\beta^2+\gamma^2)^2\}$$
$$-2F_1F_2\{(\beta^2-3\gamma^2)\alpha^2-(\beta^2+\gamma^2)^2\}]\cos 2\gamma h$$

$$E_5 = -2\beta\gamma[\alpha^4 F_1^2 - 4\alpha^2\beta^2(\beta^2+\gamma^2)^2 + 2F_1F_2\{(-3\beta^2+\gamma^2)\alpha^2 + (\beta^2+\gamma^2)^2\}] \sin 2\gamma h$$

$$E_6 = 2\gamma^2(F_1^3F_2 - 16\alpha^6\beta^2)\exp(\beta h)\cos\gamma h$$

$$E_7 = -2\beta\gamma[4\alpha^4\{(\beta^2-\gamma^2)\alpha^2 - (\beta^2+\gamma^2)^2\} - 4\alpha^6F_1 + 8\alpha^6\beta^2 + F_1^2F_2^2]\exp(\beta h)\sin\gamma h$$

$$E_8 = 2\alpha^2\gamma^2[8\alpha^4\beta^2 + 4\beta^2(\beta^2+\gamma^2)^2 - \alpha^2F_1^2]\exp(2\beta h).$$

(B1.59)

Using eq.(B1.35) the expression for w_E is simplified as

$$w_E = \frac{\varepsilon_0^2}{2}\frac{(C_{11}-C_{12})(C_{11}+2C_{12})}{C_{11}}\left[1 - \frac{1+\dfrac{C_{12}}{C_{11}+C_{12}}}{2\alpha h\sqrt{2+B}\exp(\alpha h\sqrt{2+B})}\right.$$

$$\times\{2+\frac{1}{2}(2+B)\cos(\alpha h\sqrt{2-B}) - \frac{1}{2}\sqrt{4-B^2}\sin(\alpha h\sqrt{2-B})$$

$$-2(2+B)\exp(\frac{\alpha h}{2}\sqrt{2+B})\cos(\frac{\alpha h}{2}\sqrt{2-B})$$

$$\left.+2\sqrt{4-B^2}\exp(\frac{\alpha h}{2}\sqrt{2+B})\sin(\frac{\alpha h}{2}\sqrt{2-B}) + \frac{1}{2}(2+3B)\exp(\alpha h\sqrt{2+B})\}\right].$$

(B1.60)

If we substitute 2 for B in eq.(B1.60) and replace $(C_{11}-C_{12})(C_{11}+2C_{12})/C_{11}$ and

$C_{12}/(C_{11}+C_{12})$ with $E/(1-\nu)$ and ν, the elastic energy density w_E reduces to eq.(2.2.28) for an elastically isotropic material, as first calculated by Glas (1987).

B.2 Modulation along [110] direction

In this section the elasticity problem is solved when the modulation occurs along [110] direction. The step-by-step procedures used in the previous section are also adopted. First, we introduce a coordinate system shown in Fig.B2.1.

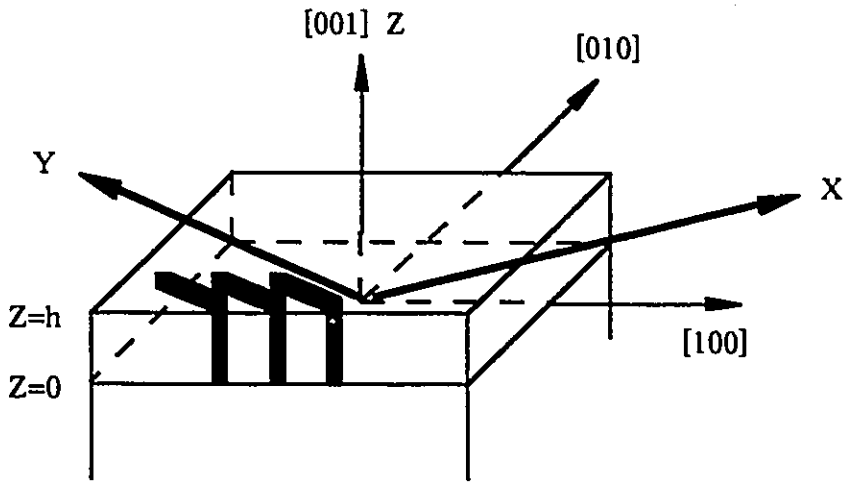

Fig.B2.1 Coordinate system X,Y,Z used for elasticity calculation of [110] modulation. The periodic lines schematically represent the modulation occuring along the X-direction ([110] in the crystal).

The modulation of lattice-constant occurs along the X-direction following

$$a(X,Y,Z) = a_0(1 - \varepsilon_0 \cos \alpha X). \qquad (B2.1)$$

In this coordinate system, the X- and Y-axes and Z-axis are no longer crystallographicaily equivalent, because X- and Y-axes are parallel to <110> directions and Z-axis is parallel to

[001] direction. The elasticity problem associated with the [110] modulation can be solved by treating the new X,Y,Z axes as if they were the basis axes in a crystal with tetragonal symmetry.

In the new tetragonal system, the elastic moduli can be expressed with the matrix:

$$\begin{pmatrix} C_{11} & C_{12} & C_{13} & 0 & 0 & 0 \\ C_{12} & C_{11} & C_{13} & 0 & 0 & 0 \\ C_{13} & C_{13} & C_{33} & 0 & 0 & 0 \\ 0 & 0 & 0 & C_{44} & 0 & 0 \\ 0 & 0 & 0 & 0 & C_{44} & 0 \\ 0 & 0 & 0 & 0 & 0 & C_{66} \end{pmatrix}. \qquad \text{(B2.2)}$$

The independent elastic moduli in the tetragonal system C_{11}, C_{12}, C_{44}, C_{33}, C_{13} and C_{66} are correlated with the elastic moduli in the original cubic system through a coordinate transformation (Nye (1985)):

$$\left.\begin{aligned} C_{11}(\text{tetragonal}) &= \tfrac{1}{2}C_{11}(\text{cubic}) + \tfrac{1}{2}C_{12}(\text{cubic}) + C_{44}(\text{cubic}) \\ C_{12}(\text{tetragonal}) &= \tfrac{1}{2}C_{11}(\text{cubic}) + \tfrac{1}{2}C_{12}(\text{cubic}) - C_{44}(\text{cubic}) \\ C_{44}(\text{tetragonal}) &= C_{44}(\text{cubic}) \\ C_{33}(\text{tetragonal}) &= C_{11}(\text{cubic}) \\ C_{13}(\text{tetragonal}) &= C_{12}(\text{cubic}) \\ C_{66}(\text{tetragonal}) &= \tfrac{1}{2}C_{11}(\text{cubic}) - \tfrac{1}{2}C_{12}(\text{cubic}). \end{aligned}\right\} \qquad \text{(B2.3)}$$

In the following analysis, all the elastic moduli and other related quantities are the values in this tetragonal system unless otherwise mentioned.

The step-by-step procedures similar to Section B.1 are followed.

(1) External strain stage (e)

The film is divided into independent cubes having the stress-free lattice-constant represented by eq.(B2.1). Then external forces are applied to each cube to give it the lattice-constant of the substrate a_0. The strain and stresses developed in this stage are:

$$\varepsilon^e_{XX} = \varepsilon^e_{YY} = \varepsilon^e_{ZZ} = \varepsilon_0 \cos \alpha X \qquad \text{(B2.4)}$$

$$\left.\begin{aligned} \sigma^e_{XX} &= \sigma^e_{YY} = (C_{11}+C_{12}+C_{13})\,\varepsilon_0 \cos \alpha X \\ \sigma^e_{ZZ} &= (C_{33}+2C_{13})\,\varepsilon_0 \cos \alpha X \end{aligned}\right\}. \qquad \text{(B2.5)}$$

Since $C_{11}+C_{12}+C_{13} = C_{33}+2C_{13}$ in our "tetragonal" notation, $\sigma^e_{XX} = \sigma^e_{YY} = \sigma^e_{ZZ}$.

(2) Assemble stage (a)

After assembling the cubes in the previous stage the nature of the some of the applied forces changes.

At the film/substrate interface (Z=0),

$$f^a_Z = [-(C_{33}+2C_{13})\,\varepsilon_0 \cos \alpha X]\,\delta(Z). \qquad \text{(B2.6)}$$

Inside the modulated film the traction changes into a density of body force

$$\left.\begin{aligned} f^a_X &= -\sigma^a_{Xj,j} = (C_{11}+C_{12}+C_{13})\,\varepsilon_0 \alpha \sin \alpha X \\ f^a_Y &= f^a_Z = 0 \end{aligned}\right\}. \qquad \text{(B2.7)}$$

(3) Relaxation stage (r)

The mechanical equilibrium is achieved by applying the following forces to cancel the external forces.

At the free surface (Z=h), a traction

$$F_Z^r = -(C_{33}+2C_{13})\,\varepsilon_0 \cos \alpha X \qquad \text{(B2.8)};$$

at the interface (Z=0), a density of body force

$$f_Z^r = [(C_{33}+2C_{13})\,\varepsilon_0 \cos \alpha X]\,\delta(Z) \qquad \text{(B2.9)};$$

in the modulated film, a density of body force

$$f_X^r = -(C_{11}+C_{12}+C_{13})\,\varepsilon_0 \alpha \sin \alpha X \qquad \text{(B2.10)}$$

are applied for relaxation.

The final state of the system (E) is obtained as the sum of the strain or stress field of the external stage (e) and the relaxation stage (r).

$$\varepsilon_{ij}^E = \varepsilon_{ij}^e + \varepsilon_{ij}^r \qquad \text{(B2.11)}$$

$$\sigma_{ij}^E = \sigma_{ij}^e + \sigma_{ij}^r \qquad \text{(B2.12)}$$

The solution for the relaxation stage can be written as the sum of a particular solution (P) and a general solution (G) for a two-dimensional elasticity problem without body forces.

$$\varepsilon_{ij}^r = \varepsilon_{ij}^P + \varepsilon_{ij}^G \qquad \text{(B2.13)}$$

$$\sigma_{ij}^r = \sigma_{ij}^P + \sigma_{ij}^G \qquad \text{(B2.14)}$$

Here we assume the particular solution as

$$u_X^P = -\frac{C_{11}+C_{12}+C_{13}}{C_{11}}(\varepsilon_0/\alpha)\sin\alpha X \qquad \text{(B2.15)}$$

$$\varepsilon_{XX}^P = -\frac{C_{11}+C_{12}+C_{13}}{C_{11}}\varepsilon_0\cos\alpha X \qquad \text{(B2.16)}$$

$$\left.\begin{aligned}
\sigma_{XX}^P &= -(C_{11}+C_{12}+C_{13})\varepsilon_0\cos\alpha X \\
\sigma_{YY}^P &= -\frac{C_{12}(C_{11}+C_{12}+C_{13})}{C_{11}}\varepsilon_0\cos\alpha X \\
\sigma_{ZZ}^P &= -\frac{C_{13}(C_{11}+C_{12}+C_{13})}{C_{11}}\varepsilon_0\cos\alpha X
\end{aligned}\right\} \qquad \text{(B2.17)}$$

for plane strain problem. This particular solution satisfies the condition for the body force in the modulated film at the relaxation stage (eq.(B2.10)). The problem to be solved is to find the general solution (G) so that the sum of the particular (P) and the general (G) solutions satisfies the boundary conditions at the relaxation stage.

The boundary conditions (BCs) are summarized below. Suffixes are put on the quantities related to the substrate.

At the free surface (Z=h)

$$\text{BC(1)} \quad \sigma_{ZZ}^r = \sigma_{ZZ}^P + \sigma_{ZZ}^G = -(C_{33}+2C_{13})\varepsilon_0\cos\alpha X \qquad \text{(B2.18)}$$

$$\text{BC(2)} \quad \sigma_{XZ}^r = (\sigma_{XZ}^P +)\,\sigma_{XZ}^G = 0. \qquad \text{(B2.19)}$$

At the film/substrate interface (Z=0)

$$\text{BC(3)} \quad (\sigma^{G'}_{ZZ} - \sigma^{r}_{ZZ})\,\delta(Z) = [(C_{33}+2C_{13})\varepsilon_0 \cos\alpha X]\,\delta(Z)$$

$$\Rightarrow \sigma^{G'}_{ZZ} - (\sigma^{P}_{ZZ} + \sigma^{G}_{ZZ}) = (C_{33}+2C_{13})\varepsilon_0 \cos\alpha X \qquad \text{(B2.20)}$$

$$\text{BC(4)} \quad \sigma^{G'}_{XZ} = \sigma^{G}_{XZ}. \qquad \text{(B2.21)}$$

Substrate is not disturbed by the modulation at infinity, that is,

$$\text{BC(5)} \quad \lim_{Z\to-\infty} u_i^{G'} = 0. \qquad \text{(B2.22)}$$

Coherency is maintained at the interface (Z=0)

$$u_i^{G'} = u_i^{r}$$

which is equivalent to

$$\text{BC(6)} \quad \varepsilon^{G'}_{XX} = \varepsilon^{P}_{XX} + \varepsilon^{G}_{XX} \qquad \text{(B2.23)}$$

$$\text{BC(7)} \quad u^{G'}_{Z,X} = u^{r}_{Z,X}. \qquad \text{(B2.24)}$$

We should note that there is no particular solution for the substrate.

Stress functions χ for the film and χ' for the substrate are introduced from which the general solutions of the stresses are derived following,

$$\sigma^{G}_{XX} = \frac{\partial^2\chi}{\partial Z^2},\ \sigma^{G}_{XZ} = -\frac{\partial^2\chi}{\partial X\partial Z},\ \sigma^{G}_{ZZ} = \frac{\partial^2\chi}{\partial X^2} \qquad \text{(B2.25)}$$

for the plane strain problem with $\varepsilon_{YY} = \varepsilon_{XY} = \varepsilon_{YZ} = 0$. The above definition also applies to the stresses in the substrate. The stresses defined by eq.(B2.24) automatically satisfy the two-dimensional equilibrium conditions

$$\frac{\partial \sigma_{XX}}{\partial X} + \frac{\partial \sigma_{XZ}}{\partial Z} = 0, \quad \frac{\partial \sigma_{XZ}}{\partial X} + \frac{\partial \sigma_{ZZ}}{\partial Z} = 0. \qquad \text{(B2.26)}$$

For this plane strain problem, the only remaining compatibility condition is

$$\frac{\partial^2 \varepsilon_{ZZ}}{\partial X^2} + \frac{\partial^2 \varepsilon_{XX}}{\partial Z^2} = 2\frac{\partial^2 \varepsilon_{ZX}}{\partial Z \partial X}. \qquad \text{(B2.27)}$$

Substituting the strain-stress relationships

$$\left.\begin{aligned} \varepsilon_{ZZ} &= \frac{-C_{13}}{C_{11}C_{33}-C_{13}^2}\sigma_{XX} + \frac{C_{11}}{C_{11}C_{33}-C_{13}^2}\sigma_{ZZ} \\ \varepsilon_{XX} &= \frac{C_{33}}{C_{11}C_{33}-C_{13}^2}\sigma_{XX} - \frac{C_{13}}{C_{11}C_{33}-C_{13}^2}\sigma_{ZZ} \\ \varepsilon_{ZX} &= \frac{1}{2C_{44}}\sigma_{ZX} \end{aligned}\right\} \qquad \text{(B2.28)}$$

into the compatibility equation (B2.27), we obtain

$$\left(\frac{-C_{13}}{C_{11}C_{33}-C_{13}^2}\frac{\partial^2\sigma_{xx}}{\partial X^2}+\frac{C_{11}}{C_{11}C_{33}-C_{13}^2}\frac{\partial^2\sigma_{zz}}{\partial X^2}\right)$$

$$+\left(\frac{C_{33}}{C_{11}C_{33}-C_{13}^2}\frac{\partial^2\sigma_{xx}}{\partial Z^2}-\frac{C_{13}}{C_{11}C_{33}-C_{13}^2}\frac{\partial^2\sigma_{zz}}{\partial Z^2}\right)=2\frac{1}{2C_{44}}\frac{\partial^2\sigma_{zx}}{\partial Z\partial X}. \qquad \text{(B2.29)}$$

Using eq.(B2.25), eq.(B2.29) can be rewritten in the form

$$\frac{\partial^4\chi}{\partial Z^4}+B_1\frac{\partial^4\chi}{\partial Z^2\partial X^2}+B_2\frac{\partial^4\chi}{\partial X^4}=0 \qquad \text{(B2.30)}$$

where

$$B_1=\frac{C_{11}C_{33}-C_{13}^2}{C_{33}}\left(\frac{1}{C_{44}}-\frac{2C_{13}}{C_{11}C_{33}-C_{13}^2}\right) \text{ and } B_2=\frac{C_{11}}{C_{33}}. \qquad \text{(B2.31)}$$

If we assume $\chi=G(Z)\cos\alpha X$, the eq.(B2.30) becomes

$$\left(\frac{d^4G}{dZ^4}-B_1\,\alpha^2\frac{d^2G}{dZ^2}+B_2\,\alpha^4G\right)\cos\alpha X=0. \qquad \text{(B2.32)}$$

Solutions for G generally take the form

$$G(Z)=\sum_{k=1}^{4}A_k\exp(\lambda_k Z) \qquad \text{(B2.33)}$$

which leads to

$$\sum_{k=1}^{4} (\lambda_k^4 - B_1 \alpha^2 \lambda_k^2 + B_2 \alpha^4) A_k \exp(\lambda_k Z) = 0. \qquad \text{(B2.34)}$$

Therefore

$$\lambda_k = \pm \frac{\alpha}{2} \{ \sqrt{2\sqrt{B_2} + B_1} \pm i\sqrt{2\sqrt{B_2} - B_1} \} = \pm (\beta \pm i\gamma) \qquad \text{(B2.35)}$$

where

$$\beta = \frac{\alpha}{2}\sqrt{2\sqrt{B_2} + B_1} \quad \text{and} \quad \gamma = \frac{\alpha}{2}\sqrt{2\sqrt{B_2} - B_1}\,. \qquad \text{(B2.36)}$$

The general solution for stresses in the film σ^G_{ij} (or in the substrate $\sigma^{G'}_{ij}$) can be expressed using eq.(B2.25), the definition of G (χ=G(Z) cos αX) and

$$G(Z) = A_1 \exp(\beta + i\gamma)Z + A_2 \exp(\beta - i\gamma)Z + A_3 \exp(-\beta + i\gamma)Z + A_4 \exp(-\beta - i\gamma)Z$$

or

$$G'(Z) = A'_1 \exp(\beta + i\gamma)Z + A'_2 \exp(\beta - i\gamma)Z + A'_3 \exp(-\beta + i\gamma)Z + A'_4 \exp(-\beta - i\gamma)Z. \qquad \text{(B2.37)}$$

The boundary conditions (1)~(7) can be rewritten using A_i and A'_i.

BC(1)

$$\alpha^2\{A_1\exp(\beta+i\gamma)h+A_2\exp(\beta-i\gamma)h+A_3\exp(-\beta+i\gamma)h+A_4\exp(-\beta-i\gamma)h\}$$
$$=\frac{(C_{11}-C_{13})(C_{33}+2C_{13})}{C_{11}}\varepsilon_0 \qquad \text{(B2.38)}$$

BC(2)

$$(\beta+i\gamma)A_1\exp(\beta+i\gamma)h+(\beta-i\gamma)A_2\exp(\beta-i\gamma)h$$
$$+(-\beta+i\gamma)A_3\exp(-\beta+i\gamma)h+(-\beta-i\gamma)A_4\exp(-\beta-i\gamma)h=0 \qquad \text{(B2.39)}$$

BC(3)

$$-\alpha^2(A'_1+A'_2+A'_3+A'_4)+\alpha^2(A_1+A_2+A_3+A_4)=\frac{(C_{11}-C_{13})(C_{33}+2C_{13})}{C_{11}}\varepsilon_0$$
(B2.40)

BC(4)

$$(\beta+i\gamma)A'_1+(\beta-i\gamma)A'_2+(-\beta+i\gamma)A'_3+(-\beta-i\gamma)A'_4$$
$$=(\beta+i\gamma)A_1+(\beta-i\gamma)A_2+(-\beta+i\gamma)A_3+(-\beta-i\gamma)A_4 \qquad \text{(B2.41)}$$

From BC(5)

$$A'_3=A'_4=0. \qquad \text{(B2.42)}$$

BC(6)

$$\frac{C_{33}}{C_{11}C_{33}-C_{13}^2}\{(\beta+i\gamma)^2(A'_1-A_1)+(\beta-i\gamma)^2(A'_2-A_2)+(-\beta+i\gamma)^2(A'_3-A_3)$$

$$+(-\beta-i\gamma)^2(A'_4-A_4)\}+\frac{C_{13}}{C_{11}C_{33}-C_{13}^2}\alpha^2\{(A'_1-A_1)+(A'_2-A_2)+(A'_3-A_3)$$

$$+(A'_4-A_4)\} = -\frac{C_{33}+2C_{13}}{C_{11}}\varepsilon_0 \qquad \text{(B2.43)}$$

BC(7) can be derived in a similar manner as in Appendix B.1.

$$[\frac{-I_1}{\alpha^2}(I_1^2C_{33}+\alpha^2C_{13})\exp(I_1h)+\frac{I_1^2C_{13}+\alpha^2C_{11}}{I_1}\{1-\exp(I_1h)\}]A_1$$

$$+[\frac{-I_2}{\alpha^2}(I_2^2C_{33}+\alpha^2C_{13})\exp(I_2h)+\frac{I_2^2C_{13}+\alpha^2C_{11}}{I_2}\{1-\exp(I_2h)\}]A_2$$

$$+[\frac{-I_3}{\alpha^2}(I_3^2C_{33}+\alpha^2C_{13})\exp(I_3h)+\frac{I_3^2C_{13}+\alpha^2C_{11}}{I_3}\{1-\exp(I_3h)\}]A_3$$

$$+[\frac{-I_4}{\alpha^2}(I_4^2C_{33}+\alpha^2C_{13})\exp(I_4h)+\frac{I_4^2C_{13}+\alpha^2C_{11}}{I_4}\{1-\exp(I_4h)\}]A_4$$

$$=\frac{I_1^2C_{13}+\alpha^2C_{11}}{I_1}A'_1+\frac{I_2^2C_{13}+\alpha^2C_{11}}{I_2}A'_2 \qquad \text{(B2.44)}$$

where I_1, I_2, I_3 and I_4 are $\beta+i\gamma$, $\beta-i\gamma$, $-\beta+i\gamma$ and $-\beta-i\gamma$, respectively.

A_1~A_4 are solved as:

$$A_1=[-i\gamma JH\exp(-2\beta)h+\beta\{\alpha^4C_{11}H-2\beta(\beta-i\gamma)(\beta^2+\gamma^2)^2C_{33}^2-2(\beta-i\gamma)^2JC_{33}\}$$
$$\times\exp(-\beta-i\gamma)h+\{-(\beta-i\gamma)\alpha^4C_{11}H+2\beta(\beta^2+\gamma^2)^3C_{33}^2+2\beta(\beta^2+\gamma^2)JC_{33}\}$$
$$\times\exp(-\beta+i\gamma)h-4i\alpha^4\beta(\beta-i\gamma)\gamma C_{11}C_{33}]D_0/4i\alpha\beta\gamma C_{33}G\exp(\beta+i\gamma)h \qquad \text{(B2.45)}$$

$$A_2=[i\gamma JH\exp(-2\beta)h-(\beta+i\gamma)\{\alpha^4C_{11}H-2\beta(\beta-i\gamma)(\beta^2+\gamma^2)^2C_{33}^2-2\beta(\beta-i\gamma)JC_{33}\}$$
$$\times\exp(-\beta-i\gamma)h+\{\beta\alpha^4C_{11}H-2\beta^2(\beta+i\gamma)(\beta^2+\gamma^2)^2C_{33}^2-2\beta(\beta+i\gamma)^2JC_{33}\}$$
$$\times\exp(-\beta+i\gamma)h+4i\alpha^4\beta(\beta+i\gamma)\gamma C_{11}C_{33}]D_0/4i\alpha\beta\gamma C_{33}G\exp(\beta-i\gamma)h \qquad \text{(B2.46)}$$

$$A_3=\frac{-\alpha^4C_{11}H+2\beta(\beta+i\gamma)(\beta^2+\gamma^2)^2C_{33}^2+JH\exp(-\beta-i\gamma)h}{4\alpha\beta C_{33}G}D_0 \qquad \text{(B2.47)}$$

$$A_4=\frac{\alpha^4C_{11}H-2\beta(\beta-i\gamma)(\beta^2+\gamma^2)^2C_{33}^2-JH\exp(-\beta+i\gamma)h}{4\alpha\beta C_{33}G}D_0 \qquad \text{(B2.48)}$$

where

$$\left.\begin{aligned} J &= \alpha^4 C_{11} - (\beta^2+\gamma^2)^2 C_{33} \\ G &= -2i\{J(\beta \sin \gamma h + \gamma \cos \gamma h) \exp(-\beta h) - \alpha^4 \gamma C_{11}\} \\ H &= \frac{\alpha^2 C_{11}(C_{33}-C_{13}) + (\beta^2+\gamma^2) C_{33}(C_{11}-C_{13})}{C_{11}-C_{13}} \\ D_0 &= \frac{(C_{11}-C_{13})(C_{33}+2C_{13})}{C_{11}} \frac{\varepsilon_0}{\alpha} \end{aligned}\right\}. \qquad \text{(B2.49)}$$

The elastic energy stored in a volume V_1 of the modulated film is

$$W_E = \frac{1}{2} \int_{V_1} \varepsilon_{ij}^e \sigma_{ij}^E \, dv = \frac{1}{2} \varepsilon_0 \int_{V_1} (\sigma_{XX}^E + \sigma_{YY}^E + \sigma_{ZZ}^E) \cos \alpha X \, dv. \qquad \text{(B2.50)}$$

Using

$$\left.\begin{aligned} \sigma_{XX}^E &= \sigma_{XX}^e + \sigma_{XX}^P + \sigma_{XX}^G \\ \sigma_{YY}^E &= \sigma_{YY}^e + \sigma_{YY}^P + \left(\frac{C_{12}C_{33}-C_{13}^2}{C_{11}C_{33}-C_{13}^2} \sigma_{XX}^G + \frac{C_{11}C_{13}-C_{12}C_{13}}{C_{11}C_{33}-C_{13}^2} \sigma_{ZZ}^G\right) \\ \sigma_{ZZ}^E &= \sigma_{ZZ}^e + \sigma_{ZZ}^P + \sigma_{ZZ}^G \end{aligned}\right\}, \qquad \text{(B2.51)}$$

$$\sigma^E_{XX}+\sigma^E_{YY}+\sigma^E_{ZZ}=\frac{(C_{33}+2C_{13})(2C_{11}-C_{12}-C_{13})}{C_{11}}\varepsilon_0\cos\alpha X+(1+K)\sigma^G_{XX}$$
$$+(1+KL)\sigma^G_{ZZ} \qquad (B2.52)$$

where

$$K=\frac{C_{12}C_{33}-C_{13}^2}{C_{11}C_{33}-C_{13}^2} \quad \text{and} \quad L=\frac{C_{11}C_{13}-C_{12}C_{13}}{C_{12}C_{33}-C_{13}^2}. \qquad (B2.53)$$

The elastic energy per unit volume w_E can then be written as

$$w_E=\frac{\varepsilon_0^2}{2}\{\frac{(C_{33}+2C_{13})(2C_{11}-C_{12}-C_{13})}{2C_{11}}+\frac{\frac{(C_{11}-C_{13})(C_{33}+2C_{13})}{C_{11}}}{D_T}(\sum_{k=1}^{7}E_k)\}$$

(B2.54)

where

$$D_T=2\alpha hC_{33}\sqrt{B_2(4B_2-B_1^2)}\,[(C_{11}-B_2C_{33})\{\sqrt{2\sqrt{B_2}+B_1}\sin(\frac{\alpha h}{2}\sqrt{2\sqrt{B_2}-B_1})$$
$$+\sqrt{2\sqrt{B_2}-B_1}\cos(\frac{\alpha h}{2}\sqrt{2\sqrt{B_2}-B_1})\}\exp(-\frac{\alpha h}{2}\sqrt{2\sqrt{B_2}+B_1})$$
$$-C_{11}\sqrt{2\sqrt{B_2}-B_1}\,]\exp(\alpha h\sqrt{2\sqrt{B_2}+B_1})$$

$$E_1 = C_{11}\{2(1+K)B_2(MC_{11}+\sqrt{B_2}\,C_{33}) - (1+K)(2\sqrt{B_2}+B_1)B_2C_{33}$$
$$-(1+KL)(MC_{11}+\sqrt{B_2}\,C_{33})B_1 + (1+KL)(2\sqrt{B_2}+B_1)\sqrt{B_2}\,C_{33}\}$$

$$E_2 = \frac{1}{2}(2\sqrt{B_2}-B_1)\exp(\frac{\alpha h}{2}\sqrt{2\sqrt{B_2}+B_1})\Big[-4(1+KL)(2\sqrt{B_2}+B_1)C_{11}C_{33}$$
$$+(C_{11}-B_2C_{33})(MC_{11}+\sqrt{B_2}\,C_{33})\{(1+KL)+(1+K)\sqrt{B_2}\}\Big]$$
$$\times\cos(\frac{\alpha h}{2}\sqrt{2\sqrt{B_2}-B_1})$$

$$E_3 = -\frac{1}{2}\sqrt{4B_2-B_1^2}\exp(\frac{\alpha h}{2}\sqrt{2\sqrt{B_2}+B_1})\Big[-4(1+KL)\{C_{11}(MC_{11}+\sqrt{B_2}\,C_{33})$$
$$-\frac{1}{2}(2\sqrt{B_2}+B_1)B_2C_{33}^2\} + 2(1+KL)(2\sqrt{B_2}+B_1)(C_{11}-B_2C_{33})C_{33}$$
$$-4C_{11}C_{33}\{(1+K)B_2-(1+KL)\frac{B_1}{2}\} - (C_{11}-B_2C_{33})$$
$$\times(MC_{11}+\sqrt{B_2}\,C_{33})\{(1+K)\sqrt{B_2}-(1+KL)\}\Big]\sin(\frac{\alpha h}{2}\sqrt{2\sqrt{B_2}-B_1})$$

$$E_4=\frac{1}{2}(2\sqrt{B_2}-B_1)\left[2(1+KL)(2\sqrt{B_2}+B_1)C_{11}C_{33}-(1+K)\sqrt{B_2}\,(MC_{11}\right.$$
$$\left.+\sqrt{B_2}\,C_{33})C_{11}-(1+KL)(MC_{11}+\sqrt{B_2}\,C_{33})C_{11}+(1+KL)B_2(2\sqrt{B_2}\right.$$
$$\left.+B_1)C_{33}^2\right]\exp(\alpha h\sqrt{2\sqrt{B_2}+B_1})$$

$$E_5=-\frac{1}{2}(C_{11}-B_2C_{33})(MC_{11}+\sqrt{B_2}\,C_{33})\exp(-\frac{\alpha h}{2}\sqrt{2\sqrt{B_2}+B_1})\left[(2\sqrt{B_2}-B_1)\right.$$
$$\times\{(1+K)\sqrt{B_2}+(1+KL)\}\cos(\frac{\alpha h}{2}\sqrt{2\sqrt{B_2}-B_1})-\sqrt{4B_2-B_1^2}$$
$$\left.\times\{(1+K)\sqrt{B_2}-(1+KL)\}\sin(\frac{\alpha h}{2}\sqrt{2\sqrt{B_2}-B_1})\right]$$

$$E_6=-\frac{1}{2}(2\sqrt{B_2}+B_1)\left[(1+K)\sqrt{B_2}\,(MC_{11}+\sqrt{B_2}\,C_{33})C_{11}-2(1+K)B_2^2C_{33}^2\right.$$
$$-2(1+K)B_2(C_{11}-B_2C_{33})C_{33}-(1+KL)(MC_{11}+\sqrt{B_2}\,C_{33})C_{11}$$
$$\left.+(1+KL)B_1B_2C_{33}^2+2(1+KL)(B_1-\sqrt{B_2})(C_{11}-B_2C_{33})C_{33}\right]$$
$$\times\cos(\alpha h\sqrt{2\sqrt{B_2}-B_1})$$

$$E_7=\frac{1}{2}\sqrt{4B_2-B_1^2}\,[-(1+K)\sqrt{B_2}\,(MC_{11}+\sqrt{B_2}\,C_{33})C_{11}-2(1+K)B_2$$
$$\times(C_{11}-B_2C_{33})C_{33}-(1+KL)(MC_{11}+\sqrt{B_2}\,C_{33})C_{11}+(1+KL)$$
$$\times(2\sqrt{B_2}+B_1)B_2C_{33}^2+2(1+KL)(\sqrt{B_2}+B_1)(C_{11}-B_2C_{33})C_{33}]$$
$$\times\sin(\alpha h\sqrt{2\sqrt{B_2}-B_1}\,).$$

(B2.55)

In the above expression

$$M=\frac{C_{33}-C_{13}}{C_{11}-C_{13}}. \qquad \text{(B2.56)}$$

If we replace C_{33} and C_{13} with C_{11} and C_{12}, the elastic energy per unit volume w_E (eq.(B2.54)) for a [110] modulation agrees with eq.(B1.60) which is the expression of the elastic energy for a [100] modulation.

References

M.S.Abrahams, J.Blanc and C.J.Buiocchi, Appl.Phys.Lett. **21** (1972) 185

S.Adachi, J.Appl.Phys. **53** (1982) 8775

M.Albrecht, H.P.Strunk, R.Hull and J.M.Bonar, Appl.Phys.Lett. **62** (1993) 2206

T.Anan, K.Nishi and S.Sugou, Appl.Phys.Lett. **60** (1992) 3159

Y.Androussi, A.Lefebvre, B.Courboulès, N.Grandjean, J.Massies, T.Bouhacina and J.P.Aimé, Appl.Phys.Lett. **65** (1994) 1162

Y.Androussi, A.Lefebvre, C.Delamarre, L.P.Wang, A.Dubon, B.Courboulès, C.Deparis and J.Massies, Appl.Phys.Lett. **66** (1995) 3450

H.Asai and K.Oe, J.Appl.Phys. **54** (1983) 2052

M.F.Ashby and L.M.Brown, Philo.Mag. **8** (1963) 1083

E.Bauer, Z.Kristallogr. **110** (1958) 372

J.M.Bonar, R.Hull, R.Malik, R.Ryan and J.F.Walker, Proc.XIIth Int.Cong.Electron Microscopy (1990) p.602

J.M.Bonar, R.Hull, J.F.Walker and R.Malik, Appl.Phys.Lett. **60** (1992) 1327

J.W.Cahn, Acta.Metall. **9** (1961) 795

S.N.G.Chu, S.Nakahara, K.E.Strege and W.D.Johnston,Jr., J.Appl.Phys. **57** (1985) 4610

S.N.G.Chu, S.Nakahara, M.E.Twigg, L.A.Koszi, E.J.Flynn, A.K.Chin, B.P.Segner and W.D.Johnston,Jr., J.Appl.Phys. **63** (1988) 611

A.Claverie, J.Crestou and J.C.Garcia, Appl.Phys.Lett. **62** (1993) 1638

D.J.H.Cockaye and A.Hons, J.de Phys. **40** (1979) C6-11

B.C.De Cooman and C.B.Carter, Acta. Metall. **37** (1989) 2765

B.C.De Cooman, C.B.Carter, K.T.Chan and J.R.Shealy, Acta. Metall. **37** (1989) 2779

B.W.Dodson, Appl.Phys.Lett. **53** (1988) 394

D.Dutartre, P.Warren, F.Chollet, F.Gisbert, M.Bérenguer and I.Berbézier, J.Cryst.Growth **142** (1994) 78

J.C.Dyment, Can.J.Phys. **63** (1985) 651

M.Dynna, T.Okada and G.C.Weatherly, Acta.Metall.Mater. **42** (1994) 1661

D.J.Eaglesham and M.Cerullo, Phys.Rev.Lett. **64** (1990) 1943

B.Elman, E.S.Koteles, P.Melman, C.Jagannath, J.Lee and D.Dugger, Appl.Phys.Lett. **55** (1989) 1659

J.-Y.Emery, C.Starck, L.Goldstein, A.Ponchet and A.Rocher, J.Cryst.Growth **127** (1993) 241

J.D.Eshelby, Proc.R.Soc.London Ser.**A241** (1957) 376

D.M.Follstaedt, R.P.Schneider,Jr. and E.D.Jones, J.Appl.Phys. **77** (1995) 3077

H.Gao, J.Mech.Phys.Solids **39** (1991) 443

F.Glas, J.Appl.Phys. **62** (1987) 3201

J.Grilhe, Acta.Metall.Mater. **41** (1993) 909

S.Guha, A.Madhukar and K.C.Rajkumar, Appl.Phys.Lett. **57** (1990) 2110

S.Guha, K.C.Rajkumar and A.Madhukar, J.Cryst.Growth **111** (1991) 434

J.E.Guyer and P.W.Voorhees, Phys.Rev.Lett. **74** (1995) 4031

P.O.Hansson, M.Albrecht, H.P.Strunk. E.Bauser and J.H.Werner, Thin Solid Films **216** (1992) 199

M.Hata, T.Isu, A.Watanabe and Y.Katayama, J.Vac.Sci.Technol. **B8** (1990) 692

A.K.Head, Proc.Phys.Soc. **B66** (1953) 793

A.K.Head, P.Humble, L.M.Clarebrough, A.J.Morton and C.T.Forwood, Computed Electron Micrographs and Defect Idntification (North-Holland, Amsterdam, 1973)

P.Henoc, A.Izrael, M.Quillec and H.Launois, Appl.Phys.Lett. **40** (1982) 963

P.B.Hirsch, A.Howie and M.J.Whelan, Philo.Trans. **A252** (1960) 499

J.P.Hirth and A.G.Evans, J.Appl.Phys. **60** (1986) 2372

J.P.Hirth and J.Lothe, Theory of Dislocations, 2nd ed. (Krieger, FL, 1982)

P.G.Hofstra, D.A.Thompson, B.J.Robinson and R.W.Streater, J.Vac.Sci.Technol. **B11** (1993) 985

A.Howie and M.J.Whelan, Proc.Roy.Soc. **A263** (1961) 217

A.Howie and M.J.Whelan, Proc.Roy.Soc. **A267** (1962) 206

D.Huet and M.Lambert, J.Electro.Mater. **15** (1986) 37

I.P.Ipatova, V.G.Malyshkin and V.A.Shchukin, J.Appl.Phys. **74** (1993) 7198

M.Ishikawa, T.Onda, N.Ogasawara and R.Ito, Jpn.J.Appl.Phys. **29** (1990) 2332

S.C.Jain, T.J.Gosling, J.R.Willis, D.H.J.Totterdell and R.Bullough, Philo.Mag. **A65** (1992) 1151

W.A.Jesser and J.W.Matthews, Philo. Mag. **15** (1967) 1097

W.A.Jesser and J.W.Matthews, Philo. Mag. **17** (1968) 461

A.S.Jordan and M.Ilegems, J.Phys.Chem.Solids **36** (1975) 329

K.L.Kavanagh. M.A.Capano, L.W.Hobbs, J.C.Barbour. R.M.J.Marée, W.Schaff, J.W.Mayer, D.Pettit, J.M.Woodall, J.A.Stroscio and R.M.Feenstra, J.Appl.Phys. **64** (1988) 4843

P.Kightley, G.Aragon-Herranz, P.J.Goodhew and R.C.Pond, Int.Phys.Conf.Ser.No.117 (1991) p.603

K.-H.Kuesters, B.C.De Cooman and C.B.Carter, Philo.Mag. **A53** (1986) 141

E.Kuphal, J.Cryst.Growth **67** (1984) 441

M.Lambert, L.Goldstein, A.Perales, F.Gaborit, C.Starck and J.-L.Lievin, J.Cryst.Growth **111** (1991) 495

R.R.LaPierre, Master's Dissertation, McMaster University (1994)

R.R.LaPierre, T.Okada, B.J.Robinson, D.A.Thompson and G.C.Weatherly, J.Cryst. Growth **158** (1996) 6

T.Li, Physics Today (May 1995) p.24

A.T.Macrander and S.Lau, J.Electrochem.Soc. **138** (1991) 1147

S.Mahajan, B.V.Dutt, H.Temkin, R.J.Cava and W.A.Bonner, J.Cryst.Growth **68** (1984) 589

M.J.Marcinkowski and E.S.P.Das, Int.J.Fracture **10** (1974) 181

P.M.J.Marée, J.C.Barbour, J.F. van der Veen, K.L.Kavanagh, C.W.T.Bulle-Lieuwma and M.P.A.Viegers, J.Appl.Phys. **62** (1987) 4413

J.W.Matthews, Epitaxial Growth, Part B (Academic Press, New York, 1975)

J.W.Matthews and A.E.Blakeslee, J.Cryst.Growth **27** (1974) 118

J.W.Matthews and A.E.Blakeslee, J.Cryst.Growth **29** (1975) 273

J.W.Matthews, A.E.Blakeslee and S.Mader, Thin Solid Films **33** (1976) 253

J.W.Matthews, S.Mader and T.B.Light, J.Appl.Phys. **41** (1970) 3800

T.L.McDevitt, S.Mahajan, D.E.Laughlin, W.A.Bonner and V.G.Keramidas, Phys.Rev. **B45** (1992) 6614

J.L.Meijering, Philips Res.Rep. **5** (1950) 333

M.Mihara and T.Ninomiya, Phys.Stat.Sol. **(a)32** (1975) 43

D.Morris, Q.Sun, C.Lacelle, A.P.Roth, J.L.Brebner, M.Simard-Normandin and K.Rajan, J.Appl.Phys. **71** (1992) 2321

W.W.Mullins, J.Appl.Phys. **28** (1957) 333

R.E.Nahory, M.A.Pollack, W.D.Johnston,Jr. and R.L.Barns, Appl.Phys.Lett. **33** (1978) 659

H.Nakao and T.Yao, Jpn.J.Appl.Phys. **28** (1989) L352

A.G.Norman and G.R.Booker, J.Appl.Phys. **57** (1985) 4715

J.F.Nye, Physical Properties of Crystals (Oxford University Press, 1985)

K.Ohta, T.Kojima and T.Nakagawa, J.Cryst.Growth **95** (1989) 71

K.Onabe, Jpn.J.Appl.Phys. **21** (1982) 797

E.P.O'Reilly, Semicond. Sci. Technol. **4** (1989) 121

M.B.Panish and M.Ilegems, Progress in Solid State Chemistry (Pergamon Press, Oxford, 1972) Vol.7, p.39

M.B.Panish and S.Sumski, J.Appl.Phys. **55** (1984) 3571

F.Peiró, A.Cornet, J.R.Morante, S.Clark and R.H.Williams, Appl.Phys.Lett. **59** (1991) 1957

F.Peiró, A.Cornet, A.Herms, J.R.Morante, S.A.Clark and R.H.Williams, J.Appl.Phys. **73** (1993) 4319

D.D.Perovic, G.C.Weatherly and D.C.Houghton, Philo.Mag. **A64** (1991) 1

B.A.Philips, A.G.Norman, T.Y.Seong, S.Mahajan, G.R.Booker, M.Skowronski, J.P.Harbison and V.G.Keramidas, J.Cryst.Growth **140** (1994) 249

A.J.Pidduck, D.J.Robbins, A.G.Cullis, W.Y.Leong and A.M.Pitt, Thin Solid Films 222 (1992) 78

A.Ponchet, A.Rocher, J.-Y.Emery, C.Starck and L.Goldstein, J.Appl.Phys. 74 (1993a) 3778

A.Ponchet, A.Rocher, J.-Y.Emery, C.Starck and L.Goldstein, Mat.Sci.Eng. **B21** (1993b) 241

A.Ponchet, A.Rocher, J.-Y.Emery, C.Starck and L.Goldstein, J.Appl.Phys. 77 (1995) 1977

A.P.Roth, D.Morris, Q.Sun, C.Lacelle, Z.Wasilewski, P.Maigné and A.Bensaoula, J.Cryst.Growth **120** (1992) 212

I.N.Sneddon, Fourier Transforms (McGraw-Hill, New York, 1951)

C.W.Snyder, B.G.Orr, D.Kessler and L.M.Sander, Phys.Rev.Lett. **66** (1991) 3032

I.S.Sokolnikoff, Mathematical Theory of Elasticity (McGraw-Hill, New York, 1956)

B.J.Spencer, P.W.Voorhees and S.H.Davis, J.Appl.Phys. **73** (1993) 4955

D.J.Srolovitz, Acta.Metall. **37** (1989) 621

G.B.Stringfellow, J.Cryst.Growth **58** (1982a) 194

G.B.Stringfellow, J.Electro.Mat. **11** (1982b) 903

K.Tappura, T.Hakkarainen, K.Rakennus, M.Hovinen and H.Asonen, J.Cryst.Growth **112** (1991) 27

M.M.J.Treacy and J.M.Gibson, J.Vac.Sci.Technol. **B4** (1986) 1458

M.M.J.Treacy, J.M.Gibson and A.Howie, Phil.Mag. **51** (1985) 389

O.Ueda, S.Isozumi and S.Komiya, Jpn.J.Appl.Phys. **23** (1984a) L241

O.Ueda, S.Komiya, S.Yamazaki, Y.Kishi, I.Umebu and T.Kotani, Jpn.J.Appl.Phys. **23** (1984b) 836

J.H.van der Merwe, Interface Sci. **1** (1993) 77

Y.P.Varshni, Physica **34** (1967) 149

R.Weeks, J.Dundurs and M.Stippes, Int.J.Eng.Sci. **6** (1968) 365

W.Wegscheider and H.Cerva, J.Vac.Sci.Technol. **B11** (1993) 1056

G.J.Whaley and P.I.Cohen, Appl.Phys.Lett. **57** (1990) 144

I.Yonenaga and K.Sumino, J.Cryst.Growth **126** (1993a) 19

I.Yonenaga and K.Sumino, J.Appl.Phys. **74** (1993b) 917

M.Zafrany, F.Voillot, J.P.Peyrade, D.Caillard, A.Couret and R.Coquille, Philo.Mag. **A65** (1992) 195

J.Zou and D.J.H.Cockayne, J.Appl.Phys. **74** (1993) 925

J.Zou, C.T.Chou, D.J.H.Cockayne, A.Sikorski and M.R.Vaughan, Appl.Phys.Lett. **65** (1994) 1647